Electron transfer and spin injection in C_{60}-ferromagnetic composites

Timothy Moorsom

School of Physics and Astronomy

University of Leeds

Submitted in accordance with the requirements for the degree of

Doctor of Philosophy

August 2016

"Nature is trying very hard to make us succeed, but nature does not depend on us. We are not the only experiment."

-R. Buckminster Fuller (for whom the carbon allotrope Buckminster Fullerene is named).

Intellectual Property Statement

The candidate confirms that the work submitted is his own and that appropriate credit has been given where reference has been made to the work of others.

In all cases, Dr Oscar Cespedes provided guidance and concepts for experiments and interpretation of data. Design and optimisation of the C_{60} deposition system was performed by Dr May Wheeler and Dr Oscar Cespedes.

The following publications are used in this work:

T Moorsom, M Wheeler, M T Khan, F Al Ma'Mari, C Kinane, S Langridge, D Ciudad, A Bedoya-Pinto, L Hueso, G Teobaldi, V K. Lazarov, D Gilks, G Burnell, B J Hickey and O Cespedes, *Spin-polarized electron transfer in ferromagnet/*C_{60} *interfaces*, Phys. Rev. B, **90**, 125311, 2014.

T Moorsom, M Wheeler, M T Khan, F Al Ma'Mari, G Brunell, B J Hickey, V K Lazarov, D Gilks and O Cespedes. *Effects of spin doping and spin injection in the luminescence and vibrational spectrum of* C_{60}, Appl. Phys. Lett. **105**, 022408, 2014.

XMCD and XAS was performed by the candidate with the aid of D Ciudad, A Bedoya-Pinto and M Valvidares. PNR was performed by the candidate with the aid of O Cespedes, C Kinane and S Langridge. PL quenching experiments were performed by the candidate and O Cespedes. Raman and PL spectroscopy during transport was performed by the candidate using samples developed by M Wheeler and using protocols and equipment developed by the same. Analysis was performed by the candidate with the exception of the Fe and Ni volume magnetization data presented in figure 4.1 which was performed by O Cespedes and the PL quenching map presented in figure 6.2 which was made by O Cespedes.

Acknowledgements

Firstly, I would like to thank my supervisor Dr Oscar Cespedes with whom it has been a pleasure to work and whose creativity, insight and dedication were the genesis of this work. In addition, the tenacity, composure and aplomb displayed by Fatma Al Ma'Mari has been instrumental in making this work possible. Dr May Wheeler's extensive work in setting up and optimising the growth systems and protocols used in this work and her advice and guidance in the early stages of my studentship provided the foundation for my research. The advice and interest of Professors Bryan J Hickey and Christopher Marrows as well as the advice of Dr Gavin Burnell, Dr Mannan Ali and Dr Thomas Moore has been invaluable.

I would like to thank Dr Christy Kinane for teaching me to use the POLREF and CRISP beamlines and Dr Manuel Valvidares for going above and beyond the call of duty in helping me to secure the data in section 6.5.

I am grateful to Dr James De Lisle for his camaraderie and friendship during this process.

I thank my family for their support and guidance and for always being just one call away.

Most importantly, I would like to thank Emma Bourne for her enduring support, calm understanding and patience during the difficult process of producing this thesis.

Abstract

The magnetic properties of spin doped fullerenes are investigated in hybrid organic/inorganic structures with the aim of establishing the extent to which magnetic states can be induced and controlled in these materials.

Volume magnetometry is used to measure a reduction of net magnetization and an increase in coercivity in cobalt which can be understood in terms of a transfer of majority spin electrons from the transition metal d-band into spin polarized hybrid interface states. This is supported by PNR and XAS studies of Co/C_{60} which reveal AF coupling between Co metal films and a hybrid interfacial region where magnetic ground states are induced in fullerenes through charge transfer.

Investigations of hybridization between C_{60} and the RE-TM alloy CoGd show that the compensation temperature of the ferrimagnet is altered by the presence of C_{60}. PNR measurements of $CoGd/C_{60}$ MLs reveal interfacial coupling which creates an AF region 1.5 ± 0.1 nm thick. Magnetometry of Gd/C_{60} bilayers indicates that hybridization between the metal conduction bands and the C_{60} LUMO modifies magnetic ordering in Gd. This is supported by the observation of novel features in the temperature dependence of magnetization and resistivity in the composite. XAS of Gd/C_{60} bilayers shows a large peak in the carbon K-edge at 282 eV which is attributed to interfacial hybridization.

It is shown that PL quenching in C_{60} is greater over Co than Au which is attributed to the greater electron transfer between Co and C_{60}. PL quenching is proposed as an effective way to measure magnetic coupling and electron transfer in interfaces. Raman spectra are recorded in C_{60} junctions during spin polarised transport. The Ag(2) peak splitting is shown to depend on the polarisation of injected current acting as an effective probe of triplet formation in C_{60}. Finally, XAS at the carbon K-edge is recorded during spin transport. A suppression of the LUMO to zero and increase in the intensity of the 282 eV peak occurs after removal of external bias and is shown to be reversible and repeatable under cycles of grounding and charge injection. A proposed mechanism involving the redistribution of charge following the removal of bias which causes electrons to become trapped in interfacial states is suggested.

Abbreviations

AF	Anti-ferromagnetic	AC	Alternating Current
CCD	Charge Coupled Device	CPL	Circularly Polarized Luminescence
DC	Direct Current	DFT	Density Functional Theory
DOS	Density of States	FCC	Face Centred Cubic
FM	Ferromagnetic	FOM	Figure of Merit
FWHM	Full width half maximum	HOMO	Highest Occupied Molecular Orbital
IV	Current vs Voltage	LUMO	Lowest Unoccupied Molecular Orbital
ML	Monolayer	MR	Magnetoresistance
NEXAFS	Near Edge X-ray Absorption Fine Structure	NPL	Negative Photo-luminescence
OFET	Organic Field Effect Transistor	PES	Photo-electron spectroscopy
PL	Photo-luminescence	PNR	Polarized Neutron Reflectivity
PVD	Physical Vapour Deposition	PY	Permalloy
RE	Rare-earth	RF	Radio Frequency
RKKY	Ruderman-Kittel-Kasuya-Yosida	RMS	Root-mean-square
SC	Simple Cubic	SCCM	Standard Cubic Centimetres per Minute
SHIPS	Spin Hybridization Induced Polarized States	SLD	Scattering Length Density
SQUID	Superconducting Quantum Interference Device	TEY	Total Electron Yield
UHV	Ultra High Vacuum	UV	Ultra-violet
VSM	Vibrating Sample Magnetometry	VTI	Variable Temperature Insert
XAS	X-Ray Absorption Spectroscopy	XMCD	X-ray Magnetic Circular Dichroism
XRR	X-ray reflectivity	ZFC-FC	Zero Field Cooled - Field Cooled

Contents

Chapter 1

Introduction

1.1 Molecular Innovation

The attraction of molecular and organic electronics is the promise of a technological future radically different to our past, in which the artificial constructs of our technology and the naturally occurring constructs of living things are built from the same fundamental components. Whether it is the development of the steel plough in 1837, the emergence of anti-biotics in 1928 or the development of Colossus, the first digital computer; human history, or at least modern history, can be seen as the continual innovation of new solutions to the challenges of life. In the past century, the exponential growth of computer technology has propelled an unprecedented expansion of human capability. However, it is quite probable that the next century will prove unusually challenging and new innovation is the key to our survival. Our society and global economy is now dependent on computational technologies but the environmental and economic cost of meeting demand using currently available materials is becoming unmanageable. [1]

For now and for the foreseeable future, metal-oxide-semiconductor technology will dominate the electronic market, [2] especially with the recent emergence of commercially viable, sub-5nm nanowire FETs. [3] However, molecular electronics allows for more than mere imitation of MOSFETs. The use of diverse species of molecules and molecular solids allows devices to be fabricated with a wide range of properties not possible in inorganic counterparts. Perhaps the most successful application of molecular electronics has been the creation of organic light emitting diodes (OLEDs) [4] which have now enabled novel technologies such as flexible displays to be constructed. [5] Recently, the goal of many researchers in this field has been to build a single molecule transistor: a device which achieves transistor-like behaviour using a single molecule and a manipulation mechanism, be it light, gate voltage or other means. [6] This is primarily an exercise in miniaturisation wherein the use of a single molecule in the basic unit of a logic circuit could lead to an extension of Moore's Law. Several examples of possible single molecule transistors exist, perhaps the most famous being based on a carbon nanotube (CNT) and, more recently, a single pthalocyanine molecule. [7, 8] Graphene has also received world-wide attention as a new basis for transistors, [9] although these devices come with many problems of their own. [10]

The encroaching hard limit of Moore's Law has prompted the rise of spintronics, which achieves greater functionality by utilizing the spin degree of freedom in addition

to, or instead of, the motion of charge, gaining data density while reducing heat dissipation and power requirements. [11] In the past decade, molecules have emerged as potential components in this new spintronic generation of devices. Molecular spintronics, sometimes subsumed under the title organic spintronics, focuses on using molecular solids or single molecules in place of inorganic materials in spin-based logic and memory devices. [12] The field emerged as the result of attempts to improve the performance of organic light emitting diodes (OLEDs) by injecting spin polarised electrons from ferromagnetic electrodes. The measurement of a high magneto-resistance ratio in the organic sexithienyl prompted a rush of investigation into various molecular and organic materials for use in spintronic devices. [13] [14]

Choosing the best molecules for a given application is difficult due to the complexity and variety of possible species and research in this field has, so far, involved a few families of molecules which have been shown to exhibit desirable properties such as good mobility, long spin diffusion lengths, simple processing and low toxicity. A few common materials are cyano-group molecules such as pthalocyanines [15] or tetracyanoethylene [16] with a variety of dopant atoms, Alq_3 [17], aromatic molecules such as rubrene [18] and carbon fullerenes such as C_{60} [19] and carbon nanotubes. [20]

1.2 Buckminsterfullerene: C_{60}

Buckminsterfullerene was first isolated as a constituent of carbon vapour by Richard Smalley and Harold Kroto in 1985. [21] They and their team used a pulsed Nd:YAG laser to produce a vapour of carbon atoms from a graphite disc which was then quenched in a high density He gas. The original experiment aimed to reproduce the conditions in which carbon clusters might form in interstellar space. Surprisingly, the carbon vapour produced stable geometric structures with the most common being C_{60} (>50% of the evaporated mass) and C_{70} (5% of evaporated mass). However, the original goal of the experiment has been vindicated by the observation of C_{60} in interstellar space. [22] Five years after its discovery, C_{60} was isolated in bulk from carbon soot using a benzene dispersal method. [23] This allowed large quantities of C_{60} to be produced for the first time and thus wholesale experimentation on its properties began with the swift discovery of metallic behaviour [24] and superconductivity in C_{60} doped with alkali metal atoms [25], which occurred at far higher temperatures than predicted. While fullerene superconductors could not compete with the cuprates, interest in C_{60}

remained despite the crisis in fullerene research brought about by one of the most famous cases of academic fraud in recent history. [26]

As organic spintronics gained momentum at the turn of the second decade of the new millennium, C_{60} came forward as an ideal candidate for the development of organic devices. In addition to the low spin orbit coupling characteristic of the light atoms in organic materials, it also lacked hydrogen atoms which were a source of hyperfine scattering of spins. This indicated that C_{60} should have a very long spin diffusion length, the mean distance an electron will diffuse before undergoing a spin-flip. In 2012, the spin diffusion length in bulk C_{60} crystals was found to exceed 100 nm [27] allowing C_{60} based spin valves to show excellent MR ratios at room temperature. [19] In this work, the high first electron affinity of C_{60}, 2.7 eV [28], also makes it an ideal candidate for charge transfer studies. To date, a large body of work exists detailing C_{60} charge transfer complexes and surface interactions which will be discussed in section 2.2 and 2.4.

1.3 Molecular Spintronics and Spinterface Physics

In order to utilise molecules in spintronics, materials had to be chosen carefully such that polarized carriers could be injected and transported with high fidelity. This requires molecular solids with long spin diffusion lengths and lifetimes. Initial observations, such as the experiments by Dediu et al [13] were very promising since molecules generally comprise light elements: C, N, O, H; with low spin orbit coupling, reducing the scattering of spin polarised electrons. However, use of organic and molecular materials present particular challenges, not least understanding the processes involved in spin injection.

Any device which aims to have spins reside within an organic layer has to consider how spin polarised carriers will move between this organic layer and electrodes. [29] This is challenging due to the difference in electronic structure between metals or semi-conductors with extended band structures and molecular systems where electronic states are highly localised [30] and because of the complex interfacial interactions between molecules and electrode materials, such as the emergence of spin hybridization induced polarized states and the transfer of charge or formation of interfacial dipoles. [17] [31] The study of interfacial hybridization and its impact on the field of organic and molecular spintronics has been dubbed 'spinterface science'. [32]

As with other aspects of organic and molecular spintronics, these interfacial interactions offer not a hindrance to easy manufacture, but a method of manipulating device properties to gain new functionality. That is, provided we have sufficient understanding to control and predict their behaviour. The observation by Cespedes et al that contact with ferromagnetic substrates can induce a magnetic ground state in carbon nanotubes through spin polarized charge transfer offers one such possibility. [33] The engineering of magnetic interface states has also been applied to the development of molecular memory [34] and the development of novel ferromagnetic composites using copper and manganese. [35] In this work, the properties of interfaces between C_{60} and ferromagnetic metals will be analysed in order to explore the idea that molecules can be used to influence and control the magnetic behaviour of other materials and that these interfaces can be engineered to control spin transport in a new generation of molecular spintronic devices.

1.4 Thesis Layout

This thesis studies the properties of C_{60}-ferromagnetic composites with a spintronics perspective. The research herein aims to establish the effects of ferromagnets on the molecule C_{60} and the reciprocal effects of C_{60} on ferromagnets as well as discussing the interactions of spin polarised electrons in C_{60} films of the type used in spintronic devices.

Chapter 2 discusses pertinent theoretical background from first principles. The origin of itinerant, indirect and molecular ferromagnetic exchange is discussed and the dependences of each form of magnetic exchange on band structure are introduced, section 2.1 and 2.2, such that the changes in the magnetic properties of the materials in chapters 4 and 5 can be understood in terms of spin polarized electron transfer and band distortions due to hybridization. A brief overview is provided of the role of fullerenes as semiconductors in the field of molecular electronics, section 2.3, before the modern science of molecular spintronics is introduced. A discussion of the importance of interfacial interactions in metal-organic hybrid materials is provided with reference to current research into spinterface physics, section 2.4. An overview of anisotropy and exchange bias is provided, section 2.5, for comparison to the observtion of hysterisis loop asymmetry in Co/C_{60} presented in section 4.5. The physical origins of SQUID magnetometry are discussed, section 2.6, to provide context for one of the key tech-

niques used in this work for characterisation of ferromagnetic thin films. The equations governing X-ray and neutron reflectivity are explained, sections 2.7 and 2.8, in order to justify the use of the polarised neutron reflectivity technique as a probe of depth dependent magnetisation in multi-layer hybrid structures in sections 4.4 and 5.2. The technique of X-ray absorption spectroscopy is introduced, section 2.9, with the details of the carbon K-edge, transition metal L edge and rare earth M edge discussed to aid interpretation of the results in sections 4.3, 5.5 and 6.5. The techniques of photoluminescence and Raman spectroscopy are covered, sections 2.10 and 2.11, to provide the necessary context for the results presented in chapter 6.

Chapter 3 introduces the experimental details for equipment and samples used in this work. Section 3.1 presents the deposition of hybrid layers in detail, including a description of the steps taken to prevent oxygen intercalation, the deposition of caps and metal over-layers without metal diffusion, the co-deposition of rare-earth transition-metal alloys and the use of shadow masks to create junctions for spin injection. The instruments used for magnetometry, both conventional and SQUID-VSM, are detailed, section 3.2. The use of laser light to study the Raman and photoluminescence spectra of C_{60} is discussed, including considerations of photo-induced polymerization, section 3.3. The beamlines used in this work are briefly introduced: the I1011 and BOREAS beamlines used for XMCD, section 3.4, and the CRISP and POLREF beamlines used for PNR, section 3.5. The cryostat used for low temperature transport is presented in section 5.4 is briefly introduced, section 3.6.

In chapter 4, C_{60} films are deposited on thin films of the three transition metal ferromagnets, section 4.2. Transfer of spin polarized electrons, spin doping, is determined by observing the bulk magnetization of the ferromagnetic films. These results indicate that there is a transfer of majority spin electrons from Co and Fe into C_{60} which causes a magnetization reduction up to 270 ± 10 emu/cc in 5 nm thick Co films. Further detail is obtained using the XAS, XMCD and PNR techniques, section 4.3. XAS identifies a shoulder which emerges below the LUMO in the NEXAFS of C_{60} thin films which can be attributed to hybridized interface states near the Fermi energy. [36] [37] PNR supports this interpretation of the interfacial coupling, section 4.4. [32] A hybrid interfacial region, 1.5 ± 0.1 nm thick is identified in fits of the reflectivity spectrum which is anti-ferromagnetically coupled to the underlying cobalt substrate. Finally, the impact of interfacial hybridization on the anisotropy of cobalt is studied using SQUID magne-

tometry and AC susceptibility, section 4.5. Asymmetry is identified in the hysteresis loops of hybrid CoC_{60} bilayers indicative of some uniaxial anisotropy. AC susceptibility identifies time evolution which hints at some frustrated magnetic order at the hybrid interface. These results are tentatively attributed to frustration of magnetic moments in the hybrid interface due to variations in interfacial coupling. Frustrated interfacial moments are expected to freeze into a disordered state at low temperatures. [38]

In chapter 5, the interactions between C_{60} and rare earth ferromagnets are studied. Heavy rare earths also exhibit ferromagnetic ordering but with a very different exchange mechanism with localised moments interacting via an indirect, RKKY exchange process. [39] Ferrimagnetic alloys of CoGd are prepared using a composite target so that the magnetization of alloy, interface and molecular layers can be measured above and below the alloy's compensation temperature, section 5.2. The molecular layer is found to reverse the sign of its magnetization as the alloy is cooled through the compensation temperature, indicating that spin doped fullerenes couple preferentially to the cobalt sublattice. The compensation temperature and compensated fraction of a CoGd alloy is found to be modified by the presence of C_{60}. Magnetometry of GdC_{60} bilayers finds unexpected changes in magnetization as a function of temperature, section 5.3. Resistance vs temperature measurements are compared with magnetometry to suggest an intermediate disordered state which emerges between the ferromagnetic and paramagnetic phases of Gd induced by the presence of C_{60}, section 5.4. XAS is used to identify evidence of hybridization in GdC_{60} bilayers, section 5.5. This behaviour is interpreted as a change in the band structure and population of the conduction bands of Gd and a corresponding change in the periodicity of RKKY coupling resulting in a chiral or anti-ferromagnetic phase analogous to those found in Er, Ho and Dy. [40]

In chapter 6: photoluminescence, Raman and x-ray absorption spectroscopy are used to identify the effects of spin injection on the vibrational spectrum and electronic structure of C_{60} molecules. A study of photo-luminescence at metal-molecule interfaces shows that photoluminescence quenching is enhanced by spin doping and hybridization and is proposed as a probe of interfacial charge transfer, section 6.2. [41] Measurements of the Raman spectrum of C_{60} during spin injection show an increase in the low energy variant of the Ag(2) vibron peak, confirming its association with the formation of spin triplets [42] and indicating it is an effective probe of spin injection, section 6.4. Photoluminescence is also shown to reduce during spin injection and this is attributed to

the spin-forbidding of recombination pathways and a corresponding increase in carrier lifetime, section 6.4. [43] Finally, XAS at the carbon K-edge is recorded during spin injection in a tunnel junction, section 6.5. While limited changes in the C 1s - LUMO transition are observed, significant changes in the NEXAFS of C_{60} are observed when an external bias is removed after transport. The LUMO is supressed to effectively zero while a lower energy feature becomes dominant. This altered edge is persistent for time periods in excess of 30 minutes and can be reversed by connecting the junction electrodes to an external ground. This effect is attributed to interfacial charge trapping which occurs when the charge density of the C_{60} layer is redistributed in order to achieve equilibrium following transport.

Chapter 2

Theoretical Background

2.1 Magnetism in Metals

2.1.1 Origin of Ferromagnetism

Ferromagnet, a portmanteau of the Latin word *ferrum* (iron) and Greek *magnetes* (Magnesia, the primary source of lodestone in antiquity), refers to any material which exhibits spontaneous magnetization at zero field. The origin of ferromagnetism is the exchange interaction which occurs between the spins of electrons whose wave-functions overlap and leads to increased order in collections of spins. The exchange interaction is quantum mechanical in origin and can be described by considering two electrons which can interact but are spatially separate such that they have a total state

$$\Psi_{1,2} = \psi_{\mathrm{a}}(\mathbf{r}_1)\psi_{\mathrm{b}}(\mathbf{r}_2), \tag{2.1}$$

where $\Psi_{1,2}$ is the total wavefunction describing state 1 and 2 and $\psi_{\mathrm{a,b}}(\mathrm{r}_{1,2})$ describes the individual wavefunctions of electron a or b at spatial site r_1 or r_2. According to the Pauli Exclusion principle, the overall wavefunction must be anti-symmetric under particle exchange such that

$$\psi_{\mathrm{a}}(\mathbf{r}_1)\psi_{\mathrm{b}}(\mathbf{r}_2) = -\psi_{\mathrm{a}}(\mathbf{r}_2)\psi_{\mathrm{b}}(\mathbf{r}_1). \tag{2.2}$$

This can be achieved with anti-symmetric, spin, χ, or spatial, φ, components

$$\Psi(\mathbf{r}) = \varphi(\mathbf{r})\chi(\mathbf{s}) \tag{2.3}$$

$$\text{where } \varphi(\mathbf{r}) = -\varphi(\mathbf{r}) \tag{2.4}$$

$$\text{or } \chi(\mathbf{s}) = -\chi(\mathbf{s}), \tag{2.5}$$

where $\mathbf{s}$ describes spin coordinate. In the case where the spatial component is symmetric, the result is a spin singlet χ_{s}

$$\Psi_{\mathrm{s}} = \frac{1}{\sqrt{2}}\big[(\varphi(\mathbf{r}_1)\varphi(\mathbf{r}_2) + \varphi(\mathbf{r}_2)\varphi(\mathbf{r}_1))\chi_{\mathrm{s}}(\mathrm{s})\big], \tag{2.6}$$

or, if the spatial component is anti-symmetric, the result is a spin triplet χ_{t}

$$\Psi_{\mathrm{t}} = \frac{1}{\sqrt{2}}\big[(\varphi(\mathbf{r}_1)\varphi(\mathbf{r}_2) - \varphi(\mathbf{r}_2)\varphi(\mathbf{r}_1))\chi_{\mathrm{t}}(\mathrm{s})\big]. \tag{2.7}$$

The energy of either state can be calculated from the expectation value

$$E_{s,t} = \int \Psi^*_{s,t} \mathcal{H} \Psi_{s,t} d\mathbf{r}_1 d\mathbf{r}_2, \tag{2.8}$$

where * denotes the complex conjugate. The potential energy operator, $V_{1,2}$ will describe interactions between the states

$$V_{1,2} = k \frac{e^2}{\Delta \mathbf{r}_{1,2}}, \tag{2.9}$$

where e is the electron charge, k the Coulomb constant and $\Delta r_{1,2}$ the spatial separation of states 1 and 2. The cross coupling terms between different states can be divided into a Coulomb term, E_c

$$E_c = \int \frac{e^2}{k \Delta \mathbf{r}_{1,2}} \sum |\psi_a(\mathbf{r}_{1,2})|^2 |\psi_b(\mathbf{r}_{2,1})|^2 d\mathbf{r}_1 d\mathbf{r}_2, \tag{2.10}$$

and an exchange term, E_j

$$E_j = \int \frac{e^2}{k \Delta \mathbf{r}_{1,2}} \sum \psi^*_a(\mathbf{r}_{1,2}) \psi^*_b(\mathbf{r}_{2,1}) \psi_a(\mathbf{r}_{2,1}) \psi_b(\mathbf{r}_{1,2}) d\mathbf{r}_1 d\mathbf{r}_2. \tag{2.11}$$

This second integral is the energy difference between the singlet and triplet state. The integral in equation 2.11 can be denoted $J_{i,j}$, where i and j are any two spatially separate spins, and is referred to as the exchange integral. A spin dependent Hamiltonian describing the energy of nearest neighbour spins whose spin vectors are denoted $s_{i,j}$, called the Heisenberg Hamiltonian, can be constructed where

$$\mathcal{H} = -\sum_{i,j} J_{ij} s_i \cdot s_j. \tag{2.12}$$

From this it can be seen that when the exchange integral has a value greater than 0, energy is minimized by maximizing the dot product of the two spins, thus allowing the two spin system to minimize its energy by adopting a triplet configuration, giving rise to spontaneous magnetization. If the exchange integral has a value less than 0, energy is minimized by minimizing the dot product, favouring a singlet state. [44]

In real metals, delocalised electronic states can be described macroscopically according to the free-electron model. In transition metals, the partially filled 3d band intersects the Fermi energy. In order to describe the itinerant ferromagnetism of the transition metals, it is necessary to consider the effect of the exchange interaction on the 3d band.

All but three metals in the d-transition block do not exhibit ferromagnetism though seventeen are paramagnetic. Paramagnetic materials have a magnetic moment which aligns to an applied field but retains no spontaneous magnetization. In the band picture of transition metals, this can be understood by dividing the 3d band into spin up and spin down populations. When a field is applied, the energy of a given state which is anti-aligned to the field is raised by the Zeeman energy for a single electron moment, μ_B, in a field B while the energy of a given aligned state is lowered by the same amount. Since the Fermi energy, E_F is the same for both bands, this will result in a change in population for the up and down 3d bands. If the total density of states is described by a function g(E) the total imbalance of the spin population (the total number of 'up' spins minus the total number of 'down' spins) will be

$$n_u - n_d = \int_0^{E_F} g(E)\mu_B B dE. \tag{2.13}$$

If we assume the change in energy is small with respect to the size of the band, we can limit discussion to the states in the vicinity of the Fermi energy. Counting each imbalanced electron as contributing μ_B to the macroscopic moment, a magnetization, M, can be defined

$$M = g(E_F)\mu_B^2 B = \mu_B(n_u - n_d). \tag{2.14}$$

In a ferromagnet, magnetization is retained even in the absence of an external field. From the above discussion, this can be described by considering that the exchange interaction creates some inherent imbalance of the spin population which follows the magnetization rather than the applied field. This inherent imbalance is described as the action of a molecular field. That is, an internal field generated by the magnetization which maintains the magnetization. The feedback of magnetization generating a field which maintains the magnetization is an intuitive way of understanding spontaneous magnetization. Before the determination of the Heisenberg Hamiltonian, equation 2.12, the Weiss molecular field allowed ferromagnetism to be interpreted using classical physics.

Consider that the molecular field causes an energy shift δE which can be viewed as the range of states below the Fermi energy which are shifted from the minority spin band to the majority spin band. The total change in energy ΔE_k can be stated as

$$\Delta E_K = \frac{1}{2} g(E_f) \delta E^2. \tag{2.15}$$

The molecular field must offset this cost. The proportionality of the molecular field, H_m, to the magnetization can be described in terms of a scalar, λ, which is related to the Coulomb potential, U, between delocalised electrons by $\lambda = \frac{U}{\mu_0 \mu_B^2}$

$$H_m = \mu_0 \lambda M. \tag{2.16}$$

The energy of the molecular field acting on the magnetization is

$$\Delta E_m = -\frac{1}{2} \mu_0 \lambda M^2 = -\frac{1}{2} \mu_0 \mu_B^2 \lambda (n_u - n_d)^2. \tag{2.17}$$

Assuming the magnetization is the sum of the imbalanced spins each contributing μ_B. The molecular field is related to the Coulomb interaction, U, which, from equation 2.8, is related to the exchange interaction. The energy of the molecular field acting on the spins in the ferromagnet can be rewritten in terms of the density of states by assuming that the excess population of spin up electrons is equal to the density of states at the Fermi level multiplied by a small variation in energy δE

$$\Delta E_m = -\frac{1}{2} U (g(E_F) \delta E)^2. \tag{2.18}$$

The sum of the two energy contributions is

$$\Delta E_K + \Delta E_m = \frac{1}{2} g(E_F) (\delta E)^2 (1 - U g(E_F)). \tag{2.19}$$

Whether or not the spin imbalance is favourable, $\Delta E_m > \Delta E_K$, or unfavourable, $\Delta E_m < \Delta E_K$, depends on the sign of the last bracket, which provides the famous stoner criterion

$$U g(E_F) \geq 1, \tag{2.20}$$

often stated in terms of the exchange integral as

$$J g(E_F) \geq 1, \tag{2.21}$$

where J is the exchange integral for a given set of states.

Thus, whether spontaneous magnetization emerges or not is determined by comparing the decrease in energy of a collection of electrons whose spins are aligned due to the action of the exchange integral to the increase of kinetic energy when polarized electrons shift to higher energy states in a given band. [44, 45]

In real metals, the stability of ferromagnetism is related to the band structure via the density of states and the molecular field. Changes to the band structure can thus be expected to affect the macroscopic magnetic properties, such a magnetisation, of a material. Chapter 4 looks at how surface interactions and resultant changes to the spin dependent DOS of the ferromagnet cobalt change its macroscopic magnetic properties.

2.1.2 Anisotropy

With only the above arguments, one might imagine that a ferromagnet would be described by one macroscopic vector, **M**, indicative of a magnetization which could simply follow any applied field, **B**, with no energy cost. Particles of sufficiently small size can behave in this manner; [46] however, most ferromagnetic materials will preferentially maintain magnetization in a particular direction or plane. This property is due to the presence of an energy cost associated with the rotation of the magnetization vector into particular axes, called anisotropy. This barrier has multiple sources which can vary in significance depending on the material. The first and most obvious anisotropy arises from a magnets shape. The magnetostatic energy, E, of a dipole in an external field can be described as

$$\mathrm{E} = -\frac{\mu_0}{2}\int \mathbf{M}\cdot\mathbf{H}\mathrm{dV}, \tag{2.22}$$

where **M** and **H** are the magnetization vector and total internal field respectively and V is the object volume. The total internal field is described as a combination of external $\mathbf{H}_{\mathrm{ext}}$ and demagnetizing fields $\mathbf{H}_{\mathrm{d}}$

$$\mathbf{H} = \mathbf{H}_{\mathrm{ext}} + \mathbf{H}_{\mathrm{d}}. \tag{2.23}$$

Since the demagnetizing field is proportional to magnetization and demagnetizing factor, N

$$\mathbf{H}_{\mathrm{d}} = -\mathrm{N}\mathbf{M}. \tag{2.24}$$

The magnetostatic energy will be higher when the sample is oriented to maximize the demagnetizing factor. Depending on the sample shape, the demagnetization factor can make it more favourable for the magnetization to remain perpendicular to applied fields of several tesla. [47]

Another important source of anisotropy is the interaction of the spins in a material lattice with the lattice itself through the spin-orbit interaction. The spin-orbit interaction couples the spin moment of an electron to the magnetic field produced by its orbital motion

$$\mathcal{H}_{SO} = \frac{-e\hbar^2}{2m_e^2c^2r}\frac{d\varphi}{dr}\mathbf{S}\cdot\mathbf{L}, \tag{2.25}$$

where $\mathcal{H}_{SO}$ is the spin-orbit Hamiltonian, $\hbar$ the reduced Planck constant, m_e the electron mass, $\frac{d\varphi}{dr}$ is the gradient of the nuclear potential and $\mathbf{S}$ and $\mathbf{L}$ are spin and angular momentum vectors. The spin orbit coupling can be described as an effective field acting only on orbital moments

$$\mathcal{H}_{SO} = -m_l \cdot \mathbf{H}_{orb}, \tag{2.26}$$

where m_l is the orbital moment and

$$\mathbf{H}_{orb} = \frac{-e\hbar^2\hat{\mathbf{M}}}{4m_e^2c^2r\mu_B}, \tag{2.27}$$

where $\hat{\mathbf{M}}$ is the unit vector for the magnetization. The projection of the orbital moment can then be described simply as the susceptibility of orbital moments, χ_{orb} to this effective spin orbit field

$$\mathbf{m}_l = \chi_{orb}\cdot\mathbf{H}_{orb}. \tag{2.28}$$

The susceptibility, χ_{orb} is a rank 2 tensor whose elements are dependent on the crystal structure. Depending on the symmetry of the crystal, the susceptibility will vary for different crystallographic planes. Where crystals are more symmetric, such as Fe and Ni which exhibit bcc and fcc structures respectively, there is little difference between the diagonal terms of the orbital susceptibility tensor and the total susceptibility varies little for different planes. For less symmetric crystals such as hcp Co, there is significant variation between planes which can be observed experimentally. [48, 49]

It is useful to note that significant changes occur in the symmetry and anisotropy of magnetic layers near their boundaries. This surface anisotropy was first described by Néel. [50] Simply, the loss of symmetry created by the boundary at a ferromagnet surface means the anisotropy constants, K, are modified close to the surface. The total anisotropy energy, E_{ani}, of a material can then be treated as the sum of these three contributions: shape anisotropy, magneto-crystalline anisotropy and surface anisotropy

$$E_{ani} = K\sin^2\Theta = \left(-\mu_0 M^2 + \frac{2K_s}{t} + K_v \right)\sin^2\Theta, \tag{2.29}$$

where K is the total anisotropy, $K_{s,v}$ are the anisotropy constants for the surface and volume respectively, M the magnitude of the magnetization vector, t the thickness of the magnetic film and Θ is the angle between the anisotropy axis and magnetization assuming the anisotropy is symmetric about one axis, known as uniaxial anisotropy.

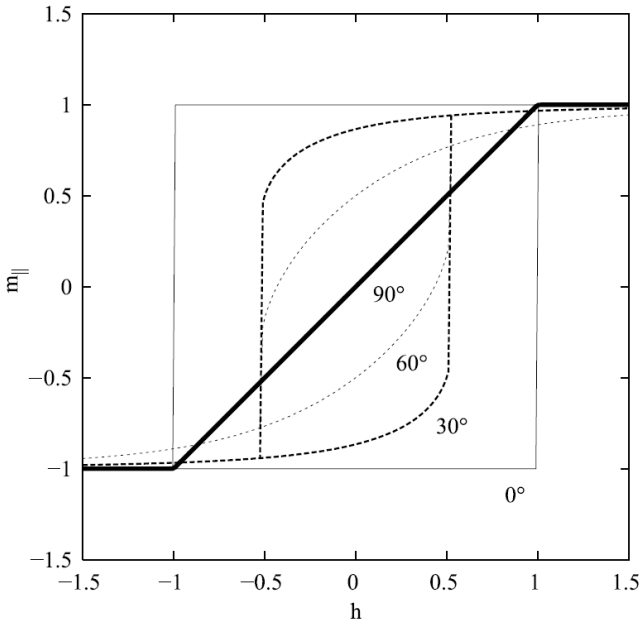

Figure 2.1: Hysterisis loops showing the projection of the magnetization vector on to the anisotropy axis for various Θ values, angles of applied field. Figure adapted from [51].

This now provides a more realistic depiction of the behaviour of ferromagnets: spontaneous magnetization is maintained by the molecular field and magnetization, the magnetization vector will align to external fields subject to the effects of anisotropy which preferentially maintains the magnetization in one or more axes (usually called easy

axes). However, there remains the issue that such a material is expected to exhibit a uniform magnetization throughout with no local variation. Such 'single-domain' objects do occur under certain conditions where domain formation is energetically unfavourable and are called Stoner-Wohlfarth particles after the physicists who first described their behaviour with the eponymous model. [52]

In the Stoner-Wohlfarth model, the energy of a ferromagnetic material with uniaxial anisotropy can be defined as function of two angles, Θ and φ, which represent the angles between the magnetization vector and the anisotropy axis and between the applied field and anisotropy axis respectively

$$E = K\sin^2(\Theta) - \mu_0 H M_s \cos(\Theta - \varphi), \tag{2.30}$$

where M_s is the saturation magnetization of the object and H the magnitude of the applied field. Minimizing the energy for a given field allows the magnetization direction to be determined. Plotting the projection of the magnetization vector on to the axis of the applied field for increasingly large fields maps the well known hysteresis loop of a ferromagnetic material. The squareness of the hysteresis loop is determined then by the angle Θ between the applied field and the easy axis with a completely square loop achieved when $\Theta = 0$, figure 2.1.

2.1.3 RE Ferromagnetism

Apart from the three 3d ferromagnets (Co, Ni and Fe), the only elements to exhibit bulk ferromagnetism are in the Lanthanide series, period 6. An initial examination of these materials would indicate that it should be impossible, given the arguments of the prior sections, for these materials to be ferromagnetic. The 4f shell in the lanthanides is progressively filled with gadolinium containing the half full shell. From Hund's rule, this is where maximum multiplicity should give rise to a large spin moment per atom. However, unlike the 3d shell in transition metals, the 4f shell is highly localised. As the nuclear charge increases for heavier atoms, the screening of this charge by inner electrons becomes less effective and the attraction between outer electrons and nucleus becomes greater. This leads to Lanthanide contraction, the property of successive lanthanides that their atomic radii decrease as the 4f shell is filled. In particular, the 4f electrons lie within the 5d- and 6s-orbitals, screening them from exterior potentials. [39] Since the exchange, equation 2.11, is dependent on the overlap between the

two spin states i and j, this localization should mean nearest neighbour atoms cannot exhibit ferromagnetic order since their unpaired 4f electrons are non-interacting. However, heavy lanthanides (those with a more than half full 4f shell) exhibit a number of magnetic behaviours with gadolinium exhibiting bulk ferromagnetism below 293 K, Terbium below 219 K, dysprosium below 85 K and Holmium below 19 K with the latter having the highest magnetic moment of any naturally occurring element. Lanthanides exhibit exotic ordering such as helical anti-ferromagnetism (Dysprosium, Erbium, and Holmium) which are not seen outside the lanthanide series. [53]

Explaining this magnetic behaviour relies on the realisation that direct exchange is not the only method by which spin correlation can occur. In the lanthanides, the unpaired electrons in the 4f shell are able to interact via the itinerant conduction electrons. Considering equation 2.12, the exchange interaction between a localised 4f-orbital and 6s conduction electrons can be written as

$$\mathcal{H}_{sf} = -J\mathbf{s}\sum_{i}\cdot\mathbf{S}_{i}, \tag{2.31}$$

where $\mathbf{s}$ represents a single conduction electron spin and $\mathbf{S}_i$ are the unpaired 4f spins. The 4f spins for a collection of rare earth ions at positions $\mathbf{R}_i$ can be described as a collection of localised fields, $\mathbf{H}_i(\mathbf{R}_i)$, which act on a delocalised moment, $\mu(r)$, which describes the spins of the conduction electrons

$$\mathcal{H}_{sf} = -\int \mathbf{H}_i(\mathbf{R}_i)\cdot\mu(\mathbf{r})d\mathbf{r}. \tag{2.32}$$

The moment of a conduction electron moving between two locations $\mathbf{r}$ and $\mathbf{r'}$ can be described as the product of the susceptibility of that electron to the local field produced by the 4f electrons at another point, $\mathbf{H}_j(\mathbf{R}_j)$

$$\mu(\mathbf{r}) = \int \chi(\mathbf{r}-\mathbf{r'})H_j(\mathbf{R}_j)d\mathbf{r'}. \tag{2.33}$$

The susceptibility $\chi(\mathbf{r}-\mathbf{r'})$ is the susceptibility of an electron scattering from position $\mathbf{r}$ to $\mathbf{r'}$. This definition is convenient since, under a Fourier transformation, it is possible to express the susceptibility in terms of a scattering wavevector q, involving ion centres at $\mathbf{R}_i$ and $\mathbf{R}_j$, equation 2.38. Inserting this definition into equation 2.32, the coupling between two sites i and j is expressed as the product of their local fields and the susceptibility of conduction electrons to those fields

$$\mathcal{H}_{ij} = -\int\int H_i(\mathbf{R}_i)\chi(\mathbf{r}-\mathbf{r'})H_j(\mathbf{R}_j).d\mathbf{r}d\mathbf{r'} \tag{2.34}$$

If the conduction electron moment arises from N conduction electrons contributing μ_B, the effective field can be defined as

$$\mathbf{H}(\mathbf{R}_i) = \frac{1}{N\mu_B}J(r-R_i)\mathbf{S}_i. \tag{2.35}$$

It is useful to restate this relationship in terms of the scattering vector, $\mathbf{q}$, which describes the scattering of a conduction electron between two points on the Fermi surface. Under a Fourier transformation, the susceptibility becomes

$$\chi(\mathbf{r}) = \frac{1}{(2\pi)^3}\int \chi(\mathbf{q})e^{i\mathbf{q}\cdot\mathbf{r}}d\mathbf{q}, \tag{2.36}$$

and the exchange integral becomes

$$J(\mathbf{r}) = \frac{1}{(2\pi)^3}\int J(\mathbf{q})e^{i\mathbf{q}\cdot\mathbf{r}}d\mathbf{q}. \tag{2.37}$$

Reverting then to the version of the Heisenberg Hamiltonian in equation 2.31, the coupling between two 4f spins $\mathbf{S}$ at sites i and j can be described as the product of the exchange integral for a scattering event, $\mathbf{q}$ between i and j and -$\mathbf{q}$ between j and i multiplied by the susceptibility of the conduction electrons to the local fields at site i and j

$$\mathcal{H}_{ff} = -\frac{1}{N^2\mu_B^2(2\pi)^3}\sum_{ij}\int \chi(\mathbf{q})J(\mathbf{q})J(\mathbf{-q})e^{i\mathbf{q}\cdot(\mathbf{R}_i-\mathbf{R}_j)}\mathbf{S}_i\cdot\mathbf{S}_j d\mathbf{q}, \tag{2.38}$$

where $\mathbf{R}_{ij}$ are the positions of two rare earth ions which we now assume are equivalent to the conduction electron coordinates $\mathbf{r}$ and $\mathbf{r'}$. This can be simplified to a more familiar form

$$\mathcal{H}_{ff} = -\sum_{ij}\mathcal{J}(ij)\mathbf{S}_i\mathbf{S}_j, \tag{2.39}$$

where $\mathcal{J}$ is the exchange integral for ions i and j which is related to the 4f-6s exchange integral by the relationships

$$\mathcal{J}(ij) = \frac{1}{(2\pi)^3}\sum_{q}\mathcal{J}(\mathbf{q})e^{i\mathbf{q}\cdot(\mathbf{R}_i-\mathbf{R}_j)}, \tag{2.40}$$

and

$$\mathcal{J}(\mathbf{q}) = \frac{1}{N^2 \mu_b^2} |J(\mathbf{q})|^2 \chi(\mathbf{q}). \tag{2.41}$$

The susceptibility of the conduction electrons to the 4f field, $\chi(\mathbf{q})$, can be defined as

$$\chi(\mathbf{q}) = \mu_B^2 \int \frac{f_k - f_{k-q}}{E(k) - E(k-q)} dk, \tag{2.42}$$

where f_k is the Fermi-Dirac distribution for conduction electrons and f_{k-q} is the Fermi-dirac distribution following scattering through a wavevector q. E(k) takes the form, $E = \frac{\hbar^2 k^2}{2m^*}$ where m* is the electron effective mass. Thus, the coupling between two 4f electrons is sensitive to the band structure of the conduction electrons via their susceptibility to the field produced by 4f spins. This is, perhaps, easier to see in the original Hamiltonian suggested by Ruderman and Kittel for the coupling of nuclear moments via conduction electrons [54]

$$\mathcal{H}(\mathbf{R}_{i,j}) = \frac{\mathbf{I}_i \cdot \mathbf{I}_j}{4} \frac{|\Delta_{k_F k_F}|^2 m^*}{(2\pi)^3 R_{i,j}^4 \hbar^2} [2k_F R_{i,j} \cos(2k_m R_{i,j}) - \sin(2k_F R_{i,j})], \tag{2.43}$$

where $I_{i,j}$ are the nuclear spins of atoms i and j, $\Delta_{k_F k_F}$ is the hyperfine coupling constant for conduction electrons with wavevector, k_F scattering from ions i and j. The term $|\Delta_{k_F k_F}|^2$ comes from the double scattering of an electron from $k \rightarrow k'$ and $k' \rightarrow k$ with the assumption that all scattering involves small deviations from the Fermi wavevector such that $k \sim k' \sim k_F$. R_{ij} is the distance between ion centres i and j. Changes in the effective mass, band bending or alterations in the distribution of conduction electrons affects the susceptibility of conduction electrons to the local, 4f fields thus changing the magnitude and periodicity of the interaction.

An interesting behaviour arises when the exchange integral is determined for various values of q. For all the magnetic rare earths apart from Gd, there is a peak in the exchange integral for some non-zero value of q. This peak arises due to the resonant scattering of pairs of states on parallel components of the Fermi surface separated by a wavevector q, a phenomenon known as Fermi surface nesting, which gives rise to peaks in the exchange at this wavevector, known as Kohn anomalies. Under Fourier transformation, this peak at a non-zero q gives rise to an oscillation of the exchange integral with ion separation $\mathbf{R}$ known as Friedel oscillations, such that the sign of the

exchange integral oscillates depending on ion separation. The competition between FM and AF interactions between ions with different separations gives rise to the well known periodic order observed in RE ferromagnets such as Ho, Er and Dy. The lack of Kohn anomalies in Gd also explains why Gd is not observed to produce periodic magnetic coupling. [39]

2.2 Molecular Magnetism

Molecules, unlike metals, have, as individual units, collections of atoms bonded in complex structures rather than individual atoms in a regular lattice. This increased complexity makes it hard to describe global properties for molecular solids but allows for a far wider variety of magnetic and electronic behaviours to be engineered. Recent investigation has led to the development of many molecular magnets for use in various applications despite the fact that light elements were, until a few decades ago, thought to be unable to exhibit ferromagnetism. [55, 56]

The exchange interaction described in section 2.1.1 would apply equally to degenerate, orthogonal orbitals on a single light atom or nearest neighbour orbitals on two bonded atoms since we can simply assign the spin pair ij to any two electrons in spatially separate, degenerate orbitals. Thus, a triplet state can be stabilized by the exchange interaction to create unpaired spins on molecules with degenerate, orthogonal orbitals. This can be used to explain the paramagnetism of molecular oxygen, which has unpaired electrons in its 2p-orbitals. However, as seen in the transition metals, unpaired electrons at a single lattice site does not necessarily lead to ferromagnetism. Molecules tend to be weakly bonded together, reducing the strength of inter-molecular interactions, and are largely composed of light elements dominated by s- and p-orbitals which tend to couple anti-ferromagnetically. The Heisenberg model has it that only metals from the transition block with partially full 3d-orbitals can meet the Stoner criterion for direct exchange and Lanthanides with partially (but greater than half) full 4f shell for indirect exchange. [39, 57]

Molecules containing transition metal ions can exhibit ferromagnetic coupling and several examples were prevalent long before the advent of pure organic magnetism. [58, 59] Even in such materials, the weak inter-molecular interactions and wide spacing between nearest neighbours means there is little opportunity for direct exchange and magnetic interactions occur via superexchange at low temperatures. Such exchange

occurs when metal radicals couple together via ligands, commonly oxygen atoms, and is usually anti-ferromagnetic with a few exceptions. [60]

Ferromagnetic interactions between high-spin atoms in purely organic materials, without transition metal ions, are observed in several molecules such as galvinoxyl [61] and tanol suberate [62]; but these materials were found not to exhibit bulk organic ferromagnetism, being a one dimensional ferromagnet and a meta-magnetic state emerging from an otherwise paramagnetic system respectively. [63, 64] Bulk, 3D organic magnetism was first observed in nitronyl nitroxides, experimentally confirmed at 1.48 K in 1993. [65, 66] In these nitroxides, ferromagnetism emerges due to charge transfer, delocalization of uncompensated spins and the arrangement of positive and negative spin concentrations through particular stacking orientations. In the nitrogen-oxygen bond, an unpaired electron can exist in two degenerate configurations on either the nitrogen or oxygen atom meaning it is effectively delocalized in the N-O pair. In biradicals with two nitrogen or oxygen atoms, the delocalization of uncompensated spins leads to polarization of terminal radicals which can couple ferro or anti-ferromagnetically depending on the configuration of the p-orbitals. Where there is significant overlap between all the p-orbitals in a planar group, the coupling is anti-ferromagnetic while it becomes ferromagnetic when one of the p-orbitals is perpendicular to the others. This demonstrates that molecular symmetry is vital in determining magnetic properties. [67]

The coupling between nitroxides in a lattice occurs due to the McConnel mechanism. [68] This is a special case of the exchange interaction considered for aromatic radicals. In this model, the Heisenberg Hamiltonian is re-written to approximate the coupling between two π electrons, i and j, on aromatic rings, A and B

$$\mathcal{H} = -\sum_{ij} J_{ij}^{AB} \mathbf{S}_i^A \cdot \mathbf{S}_j^B. \tag{2.44}$$

The spin operators can be written as total spin densities for the two rings, $\rho_{i,j}^{A,B}$

$$\mathcal{H} = -\sum_{ij} J_{ij}^{AB} \rho_i^A \rho_j^B. \tag{2.45}$$

The exchange integral between two overlapping p-orbitals is almost universally negative and would stabilize anti-ferromagnetic coupling between the delocalized electrons on stacked aromatic rings and, by extension, other planar molecules with delocalized, uncompensated spins. However, certain configurations allow areas of positive spin

density and negative spin density to overlap. The negative exchange integral and negative product of the two spin densities then give overall positive coupling leading to ferromagnetic interaction. This explains why para-nitrophenyl nitronyl nitroxide was shown to undergo a ferromagnetic transition at sub-Kelvin temperatures when none of its other phases did. [69]

A second McConnell model was applied to describing triplet states in charge transfer complexes where a triplet emerged in the excitations of electrons between a donor and acceptor molecule. [70] This model was extended by Yamaguchi to describe how the negative exchange interactions for a donor-acceptor pair and the negative exchange interaction between a chain of donor-acceptor pairs could, for certain structures, produce charge transfer complexes with ferri- or ferromagnetic order and a net magnetic moment. [71] The importance of structure is highlighted when considering the case of the first charge transfer complex which showed evidence of ferromagnetism: tetrakis(dimethylamino)ehtylene(TDAE)C_{60}. While initial studies of this material found a ferromagnetic transition at 16 K, though it was noted that it may be super-paramagnetic due to the lack of clear remanence in DC magnetometry, [72] it took almost a decade before it was shown that annealing TDAE-C_{60} crystals above 350 K solved the issue of reproducibility and confirmed the existence of ferromagnetism. It was realised that the necessity of annealing was due to the conformational restrictions on the emergence of magnetism. [73]

2.3 Fullerenes as Semiconductors

In bulk, C_{60} forms a face-centred-cubic structure in which individual molecules continuously rotate between degenerate configurations via a ratcheting mechanism. Below 249 K, it undergoes a structural transition to a simple cubic structure due to the orientational ordering of the molecules. [74] Ratcheting between low energy orientations continues down to 90 K, below which the rotational degree of freedom becomes frozen. [75]

The weak, van der Waals bonding between fullerenes means the solid retains much of the band characteristics of the isolated molecules with narrow HOMO and LUMO bands, $\approx$ 0.5 eV wide. In an isolated fullerene, the band gap is 1.9 eV. The measured bandgap is 1.69 eV in the solid due to the formation of a Frenkel exciton, see section 2.10. The true band gap is 2.3 eV if on fullerene Coulomb interactions between electrons

and holes are ignored. [76, 77, 78] Inter-molecular charge transfer occurs via a hopping mechanism with an activation energy of 0.58 eV at room temperature, aided by the formation of mid-gap states. [79, 80]

Molecular hopping can be visualised as the process by which an electron, which is localized on a single charged molecule, can scatter from the intra-molecular vibrations, vibrons, in order to overcome the energy barrier for it to move to an adjacent molecule. The transfer rates, $\frac{1}{\tau}$ are usually described at high temperature by the Marcus electron transfer theorem [81, 82]

$$\frac{1}{\tau} = \frac{V^2}{\hbar}\sqrt{\frac{\pi}{\lambda k_B T}}\exp\Big(-\frac{(\Delta G^0+\lambda)^2}{4\lambda k_B T}\Big), \tag{2.46}$$

where, ΔG^0 is the free energy gap between the initial and final states of an electron moving between two molecular sites, λ is the reorganization energy which can be defined as the energy cost associated with the geometric distortions of the molecule and its environment which occur when a molecule goes from being neutral to being charged. V is sometimes referred to as the electron transfer integral and describes the intermolecular coupling strength.

When an electric field, E, is applied, the Marcus expression becomes

$$\frac{1}{\tau} = \frac{V^2}{\hbar}\sqrt{\frac{\pi}{\lambda k_B T}}\exp\Big(-\frac{(\Delta G^0+eEa+\lambda)^2}{4\lambda k_B T}\Big), \tag{2.47}$$

where e is the electron charge and a is the intersite distance, such that the hopping time, and therefore conductivity, varies non-linearly with applied field. In a system where all molecular sites are identical, such as a single crystal of C_{60} the free energy difference can be assumed to be zero such that the key components are the charge transfer integral V, the reorganization energy λ and the thermal energy. The charge carrier mobility μ can be calculated using the single step model in which it is assumed that the hopping event is driven by the thermal energy and that a single hopping event can be extended to describe diffusive behaviour over the whole system. The Einstein relation provides a description of the carrier mobility in terms of a diffusion constant D

$$\mu = \frac{e}{k_B T}D, \tag{2.48}$$

where D can be given by

$$D = \frac{1}{2d}\frac{\langle l(t)^2 \rangle}{t}, \tag{2.49}$$

where l(t) is expectation value for the distance between the charges position at time 0 and t and d is the dimensionality of the system (1,2 or 3). The distance between the charges position at time 0 and t can be approximated as the intermolecular distance a and the time as the hopping rate k

$$D = a^2 k. \tag{2.50}$$

Using equations 2.47, 2.48 and 2.50, it can be seen that the mobility can be expressed in terms of temperature as

$$\mu = \frac{ea^2V^2}{\hbar k_B T^{3/2}}\sqrt{\frac{\pi}{\lambda k_B}}\exp\Big(-\frac{(eEa+\lambda)^2}{4\lambda k_B T}\Big), \tag{2.51}$$

giving the characteristic $T^{-3/2}$ dependence of mobility at high temperatures and inverse exponential dependence at low temperatures. [83] Since this form of hopping transport is entirely mediated by thermal energy, it is sometimes known as thermally activated hopping. In the case of a molecule such as C_{60}, we can thus consider the transport of electrons as a sequence of short jumps between localised states which relies on thermal energy.

In organic and molecular semiconductors, the reorganisation potential can create a distortion of the molecular structure which couples to the charge carrier as it moves through a solid. This coupling of distortion and charge carrier is usually described as a quasi-particle called a polaron. [84] In organic or molecular solids where small, local distortions are involved in polaron formation, the Holstein "small polaron" model can be applied. [85] The small polaron model describes hopping in terms of a tight binding model where the local band structure, in this case the molecular orbitals, require only a small correction to describe the global band structure. In this approximation, the correction defines the width of a narrow conduction band derived from the molecular LUMO. This width is defined by the activation energy for a polaron, i.e the energy required to cause a hopping event and form a small polaron. In the case of C_{60}, this gives rise to a narrow conduction band ($E_a \approx 0.5$ eV)just above the Fermi energy. [86] [77]

Photoconductivity measurements of solid C_{60}, in which a laser was used to create excitons and the decay of conductivity following the excitation used as a measure of recombination time, showed weak temperature dependence and strong transfer integral dependence compatible with a hopping transport mechanism between 100 and 400 K. [80] The structural transition in C_{60} at $\approx$ 250 K is clearly evident in conductivity measurements and can be explained in a hopping model by recognising the change in inter-molecular distance which occurs as a result of the change from FCC to SC crystal structure. [79] C_{60} has demonstrated good field effect mobility amoung molecular semiconductors and has been successfully incorporated into OFETs. In pure, well ordered crystals, C_{60} can have electron mobilities as high as 11 $cm^2V^{-1}s^{-1}$. [87]

In studies of spin injection and transport in C_{60}, hopping is treated as a chain of intermolecular tunnelling events. This provides good agreement with experiment, particularly in modelling the long spin diffusion lengths of C_{60} layers, since each inter-molecular tunnelling event is spin conserving. [19] [88] C_{60} shows a long spin diffusion length, 110 nm at room temperature. [27]

2.4 Interfacial Charge Transfer and Spinterface Physics

More recently, organic molecules have been invoked as a potentially revolutionary alternative to inorganic semiconductors in spintronics. [29] [12] However, interfacial effects and charge transfer were increasingly acknowledged as a vital consideration for organic spintronic devices as the field gained momentum. [89, 90, 13] Following the observation by O Cespedes et al that contact with a ferromagnet could induce magnetism in carbon nanotubes, a focus of research became the spin polarization which could occur in various carbon allotropes due to interfacial hybridization with ferromagnetic substrates. [91, 33] In 2010, Clement Barraud and colleagues used the idea of a magnetic, hybrid interface to explain hitherto mysterious anomalies in the sign of magneto-resistance in $(La, Sr)MnO_3$/tris[8 – hydroxyquinoline]aluminium/Co, LSMO/Alq_3/Co, spin valves, naming this phenomenon spin hybridization induced interface polarized states (SHIPS). [17] This phenomenon was applied by K V Raman et al to create intrinsic spin filter layers in organic materials in 2013. [34] The study of SHIPs and the inclusion of this understanding in future engineering of organic spintronic devices was named by Stefano Sanvito, who coined the term Spinterface physics. [32]

Consider the interface formed between a semiconductor with electron affinity E_a

and conduction band E_c above the Fermi energy and a metal with workfunction φ. Where these materials are in contact, the Fermi energy becomes a universal reference in both systems. However, aligning the Fermi energies at the surface means the vacuum levels are not the same since $E_a + E_c \neq \varphi$.

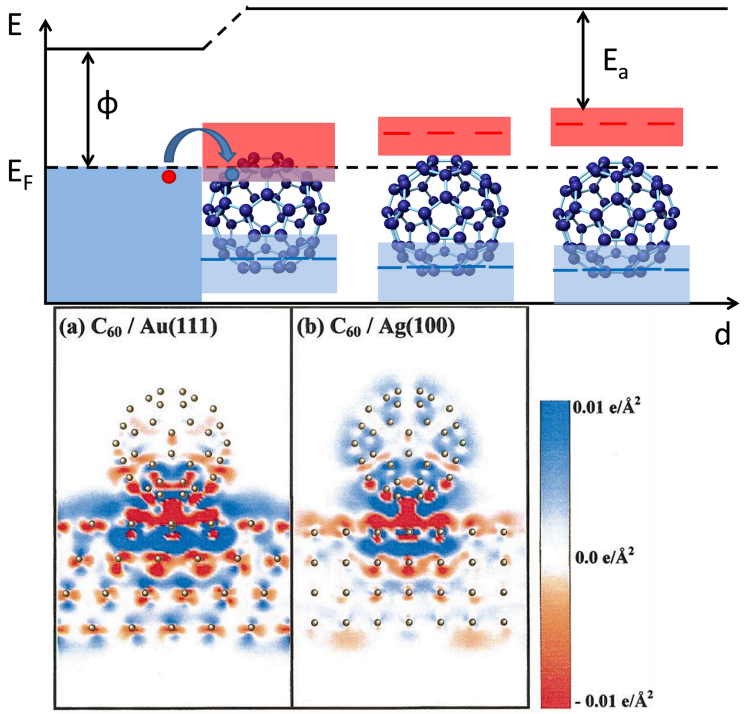

Figure 2.2: Illustration of the interfacial coupling between a metal and C_{60}. The solid state band gap of C_{60} is 2.3 eV and the electron affinity is around 4.6 eV. The LUMO states define a narrow band due to phonon-electron coupling with a width of 0.5 eV. [77][92] [86] Near the surface, polarization of the metal substrate, hybridization of molecular orbitals and redistribution of surface charge causes the gap to narrow and the LUMO derived band to broaden. This moves the LUMO closer to the Fermi energy through the process known as Fermi level pinning. Depending on the degree of hybridization and charge redistribution, the bottom of the LUMO derived band can shift below the Fermi energy allowing electrons from the metal to occupy metallic hybrid interface states. [93] [37]. The bottom panel shows a DFT simulation of a C_{60}/Au and C_{60}/Ag contact with the resulting redistribution of charge mapped over a small region. Figure reproduced from [94].

The difference between their Fermi levels creates an effective potential between the two systems called the contact potential. This potential causes an interfacial dipole

to emerge at the interface between metal and semiconductor due to the action of this electric field. In the semiconductor, this potential means that electrons near the interface are at a higher energy with respect to the vacuum level, effectively distorting the band structure so that the conduction band is closer to the vacuum level the closer one moves toward the interface. When contact is established between semiconductor and metal, the vacuum levels at the contact are identical and the distortion of the band structure is a maximum. This 'band-bending' and the resultant change in the energy difference between conduction states in the semiconductor and metallic states, the Schottky barrier height, is well established in inorganic-metal contacts and is a key consideration in the engineering of semiconductor devices. [95] However, the simplistic model presented here does not describe observed Schottky barrier heights well. Metal work function is found, in reality, to be far less influential than expected in determining interfacial band distortions. This weak dependence is referred to as Fermi-level pinning, because the valence and conduction bands in the semiconductor preferentially maintain their alignment to the Fermi level rather than the vacuum level. [96] Understanding Fermi-level pinning requires bonding, hybridization and interfacial charge distribution to be considered in the model.

If we consider the case of a molecular semiconductor like C_{60}, the valence and conduction bands are made up from the localised, degenerate HOMO and LUMO. The measured ionization potential in C_{60} is 6.9 eV and the band gap is 2.3 eV. [77] [92] The LUMO lies just above the Fermi energy such that the workfunction for C_{60} should fall between 4.6 eV and 4.85 eV given a band width of $\approx$ 0.5 eV. This is confirmed by Photoelectron/photoemission spectroscopy (PES) in the study of Lof et al. [92] We might expect, therefore, that metals with work functions below about 4.6 eV should create sufficient contact potential with solid C_{60} to push the LUMO below the Fermi energy, resulting in charge mixing between the metal and molecular semiconductor.

While charge transfer is observed for metals such as Mg (φ = 3.6 eV), it is also observed in metals such as Au (φ = 5.1 eV), and Co (φ = 5 eV) and appears not to depend on vacuum level alignment for metals with a range of workfunctions 1.5 eV wide. [37] This Fermi-level pinning in organic-metal interfaces is key to understanding the formation of a spinterface. PES of C_{60} films on metal substrates shows that adsorption reduces the molecular band gap. [97] This is interpreted in theory as the result of two effects. First, a molecule such as C_{60} adsorbed to a metal will exhibit some overlap

of π-orbitals and the extended, delocalised 3d-orbitals of the metal. Hybridization between these discrete, localised orbitals and extended, delocalised orbitals broadens the molecular orbitals into a hybrid band. Second, the reorganization of charge at the interface which occurs due to the adsorption of the molecule creates a polarization in the metal. The molecular band gap includes a Coulomb term which affects the energy of electrons or holes in the LUMO or HOMO as seen in the case of the Frenkel exciton.[77] Polarization of the metal increases the attraction between electrons and holes in the HOMO and LUMO bands reducing the observed band gap at the interface. [93] In C_{60}, this shifting and broadening of interfacial orbitals aligns the LUMO, at least partially, below the Fermi energy for a wide range of different transition metals, irrespective of their work function, allowing charge mixing in which the LUMO at the interface is partially filled by electrons from the metal, figure 2.2.

Where the metal substrate has a net spin polarization, the coupling between molecular orbitals and metal orbitals is also different for spin up and spin down. [98] Spinterface interactions are, in many ways, similar to the ideas outlined in the McConnel and Yamaguchi mechanisms in that they concern the overlap between molecular orbitals, the excitation of transferred charge between different parts of the system and the stabilization of different spin configurations due to the coupling between spin polarized electrons. However, while McConnel and Yamaguchi consider donor and acceptor atoms in a molecule or molecules in a complex; the donor and acceptor here are a bulk ferromagnet and a molecule. A simple, general picture relies on considering how the DOS of the two systems will change as they interact.

As described above, hybridization and dipole formation causes the molecular orbitals to broaden into hybrid interface states and narrows the band gap so that they are moved closer to the Fermi level. This hybridization is dependent on the symmetry and population of the partially filled metal orbitals. Where exchange splitting means the population of spin up and spin down bands in the metal substrate is not equal, broadening and Fermi-level pinning of the molecular orbitals is also not equal leading to a net spin polarization of the LUMO close to ferromagnetic interfaces, figure 2.3.[99] Measurements of spin valves with hybrid organic-ferromagnet interfaces demonstrated this spinterface model of the interfacial interaction could explain the observed MR. It was determined that the spin polarization of the interface dominates spin injection into molecular semiconductors prompting some researchers to start including tunnel barri-

ers between FM electrodes and molecular layers where a spinterface was not desired or designing new structures which included the spinterface as an active component. [98, 100, 101, 34, 102] Thus far, the metal in this model is treated as an infinite pool of electrons in which any interfacial effects are strongly screened and do not affect bulk properties. Chapters 4 and 5 specifically analyse the effect of such interfaces on the metal.

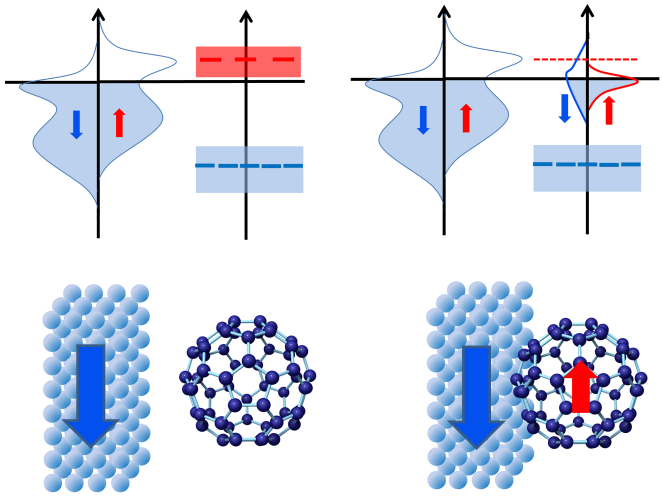

Figure 2.3: Illustration of the interfacial coupling between molecule and magnet reproduced in the manner of [32]. In isolated molecules, the molecular LUMO is a discrete, degenerate multiplet. As they are brought into contact, the interfacial coupling between the two materials broadens the LUMO and shifts its energy to align the Fermi levels at the interface. A spin-split orbital can emerge due to unequal population of the spin up and spin down bands in the metal producing a polarization at the interface. This may even be inverse to the FM polarization depending on the choice of materials.

2.5 Frustration, Disorder and Exchange Bias

In 1957, Meiklejohn and Bean noticed that the hysteresis loops obtained from oxidized cobalt nano-particles were not symmetric in field, figure 2.4. The hysteresis loop could be described accurately by the Stoner Wohlfarth model as given in equation 2.30, save that there appeared to be an additional component of the anisotropy which acted unidirectionally rather than uniaxially. [103]

Using equation 2.30, we can state the offset as though an additional field H_b were

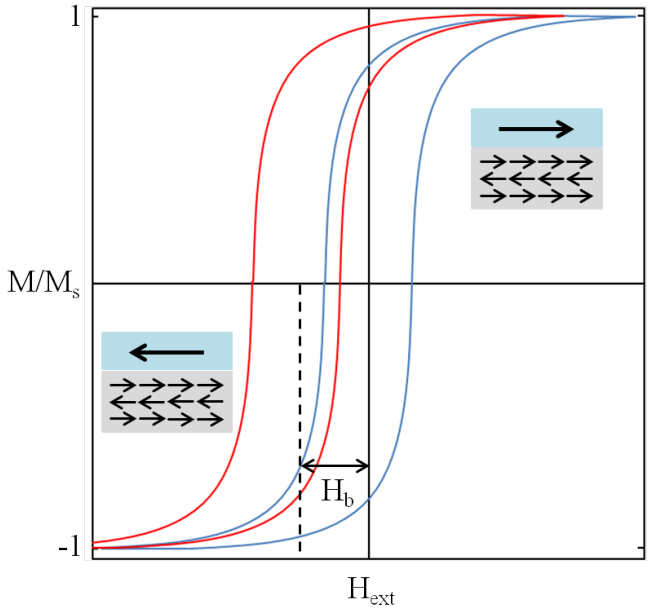

Figure 2.4: Illustration of the same magnetic material with (red) an without (blue) exchange anisotropy. Simplistically, the bias field, H_b would perfectly offset the hysteresis loop from zero without changing its reversal dynamics. For real interfaces, the mechanisms by which domain walls form in exchange biased systems can make the loop highly asymmetric around H_b. [104] Also, disorder and frustration at real interfaces will often result in a significant increase in the corrected coercivity (half width) of the loop. [105]

acting on the magnet to maintain its direction

$$E = K\sin^2\Theta - \mu_0(H + H_b)M_s\cos(\Theta - \varphi). \tag{2.52}$$

It is worth noting that for the simple case that the field is applied entirely perpendicular to the anisotropy axis we have

$$E = K\sin^2\Theta - \mu_0(H + H_b)M_s\cos(\Theta - \frac{\pi}{2}). \tag{2.53}$$

Minimization of the first term occurs when the magnetization vector lies on the anisotropy axis, minimization of the second term occurs when the magnetization vector points in the direction of the applied field. For the magnetization vector to lie completely along the direction of the applied field it must be great enough that

$$K \leq \mu_0(H + H_b)M_s. \tag{2.54}$$

This creates a convenient notation where, in the absence of domains or any other deviation from the Stoner-Wohlfarth model, the anisotropy contributions can be expressed as effective fields

$$H_k = \frac{K_a}{\mu_0 M_s}, \tag{2.55}$$

and

$$H_b = \frac{K_d}{\mu_0 M_s}, \tag{2.56}$$

where K_a and K_d are the uniaxial and unidirectional components of the anisotropy respectively. As can be seen from equation 2.30, the uniaxial anisotropy has axial symmetry because its sign is determined by magnetization vector. Thus, if the magnetization vector changes sign, the anisotropy follows it. Unidirectional anisotropy does not reverse if the sign of the magnetization changes. In order for anisotropy to be unidirectional, it must be independent of the magnetization direction of the sample. Meiklejohn and Bean quickly realised that this could be explained by the anti-ferromagnetic phase of CoO. In an antiferromagnet, as described in section 2.1.1, nearest neighbour spins couple with opposite sign. In a crystal lattice, this opposite coupling produces a material with no net magnetization and therefore no susceptibility. This would be precisely true in an infinite single crystal. However, in a film spins at the surface will be compensated on one side only leaving an uncompensated plane. A ferromagnet which interacts with this uncompensated plane will couple to the surface spins. If the anti-ferromagnet is raised above its Néel temperature, the surface spins will spontaneously align to the magnetization of the ferromagnet. When cooled again, this direction will be set as the anti-ferromagnet orders and will define a unidirectional anisotropy. Because the susceptibility of the anti-ferromagnet is nominally zero, the unidirectional anisotropy will not reverse with field.

In reality, anti-ferromagnets are not perfect single crystals and the interface between two films is not a perfectly flat plane. These deviations from the ideal model presented by Mieklejohn and Bean are evident from the apparent weakness of the exchange field compared to its theoretical value.

If the energy for two interfacial spins is simply given by the 1D solution to the Heisenberg Hamiltonian (equation 2.12), then the exchange energy per unit cell for interfacial spins is

$$E = -\frac{2J_{i,j}\mathbf{s}_i\mathbf{s}_j}{a^2}, \tag{2.57}$$

where a is the cubic lattice parameter assuming both lattices are simple cubic with exact lattice matching. The magnetostatic energy for the volume element of the ferromagnet which is being held opposite to the applied field is

$$E = -HMa^2t, \tag{2.58}$$

or, per unit cell,

$$E = -HMt. \tag{2.59}$$

At the point where these two energies are exactly equal, we recover the behaviour of the isolated ferromagnet with an offset in applied field given by the bias field

$$H_b = \frac{2J_{i,j}\mathbf{s}_i\mathbf{s}_j}{a^2M_{FM}t_{FM}}, \tag{2.60}$$

where a is the the cubic lattice constant, M_{FM} the ferromagnet magnetization and t_{FM} the ferromagnet thickness. Giving an estimate for the magnitude of the bias field which is proportional to the exchange stiffness: $J\frac{\langle s\rangle^2}{a^2}$ and inversely proportional to magnetization and thickness of the ferromagnet.

This model seems intuitively accurate and the 1/t proportionality is consistently observed in exchange biased systems. [106] However, reasonable estimates for the interfacial exchange are two or three orders of magnitude lower than experimentally obtained values. [107]

Understanding the interfacial coupling remained a challenge for decades and a number of different models were proposed. [108] It is now understood that the coupling in real interfaces is influenced by random defects, geometrical disorder and the influence of multiple sub-lattices at the boundary which all act to modify the exchange energy. [104] In a model which attempted to account for random interfacial defects, Malozemoff stated the exchange field as

$$H_b = \frac{2}{M_{FM}t_{FM}}\sqrt{\frac{JK_{AF}}{a}}, \tag{2.61}$$

which provides closer agreement with observation but still lacks realistic depictions of interfacial defects. [109] [110] Further modifications to models of exchange bias based

on interfacial disorder were made in the early millennium such as the Schulthess-Butler model. [111]

In addition, where coupling is strong at a surface, it is predicted that the exchange field will still be reduced due to the formation of partial anti-ferromagnetic domain walls as ferromagnet spins exert a torque on the uncompensated surface spins. A detailed description of this model was given by Mauri [107] and a further description including spin-flop transitions which can occur when partial domain walls are rotated up to some critical angle was described by Stiles and McMichael. [112]

The complexity of the relationship between interfacial roughness, defects and bias field means that theoretical models still lack generality. More recently, exchange bias has been investigated using a number of different materials which demonstrate different forms of magnetic order including disordered systems such as spin glasses. [38] Exchange bias has been observed in molecule-metal hybrids where anti-ferromagnetic stacks of 2D Pthalocyanine molecules were layered on top of the ferromagnetic substrate and C_{60} films have been observed to modify perpendicular magnetic anisotropy in cobalt. [113] [114] As yet unexplored is the use of interfacial hybridization and charge transfer to create this kind of unidirectional anisotropy without any intrinsic AF order. This idea is the subject of section 4.5.

2.6 SQUID Magnetometry

While Vibrating Sample Magnetometry has been common since its inception in 1959, [115] the more recent application of Josephson junctions to magnetic sensing [116] has created a new generation of magnetometers. These instruments utilize the properties of Superconducting Quantum Interference Devices (SQUIDs) which provide far higher sensitivity and additional measurement capability such as measuring AC susceptibility. [117] [118]

A SQUID consists of two Josephson junctions set in a loop of superconducting material. The superconducting loop will expel any flux applied to the loop as would be expected from the Meissner effect. A screening current, J_s, flows around the loop in order to expel the flux which would penetrate the loop.

In a single Josephson junction, the current flow between the two superconducting regions can be defined in terms of the critical current of the junction, J_c and the phase difference of the superconducting wavefunction across the weak link, φ

$$J_s = J_c \sin(\varphi). \tag{2.62}$$

If a flux flows through the loop, a screening current flows around the loop. The Aharanov-Bohm effect describes how a charged particle, described by a wavefunction ψ, following a path around a non zero vector potential, $\mathbf{A}$, acquires some phase, φ

$$\psi = e^{i\varphi}\psi. \tag{2.63}$$

The phase can be related to the total magnetic flux through the loop, Φ, by recognising that the phase can be defined

$$\varphi = \frac{q}{\hbar}\int \mathbf{A}\cdot d\mathbf{l}, \tag{2.64}$$

where q is the particle charge and $\mathbf{l}$ is a vector describing the path. If the path is a closed path around the whole loop, Stokes theorem can be used to show this phase is equivalent to the total flux in the loop

$$\oint \mathbf{A}\cdot d\mathbf{l} = \frac{q}{\hbar}\int \mathbf{B}\cdot d\mathbf{S} = \frac{q}{\hbar}\Phi. \tag{2.65}$$

The Born condition stipulates that the wavefunction describing this charged particle must be singly valued everywhere. In the superconducting ring the supercurrent is described by a macroscopic wavefunction, such that for a closed path around the ring

$$\psi e^{i\varphi_0} = \psi e^{i\varphi_0+\varphi}, \tag{2.66}$$

which is achieved where $\varphi = 2\pi n$, where n is an integer. Using equation 2.64, this shows that the total flux flowing through the superconducting loop must be quantized

$$\varphi = \frac{q}{\hbar}\oint_c \mathbf{A}\cdot d\mathbf{l} = \frac{q}{\hbar}\Phi = 2\pi n. \tag{2.67}$$

Which, since a cooper pair has charge 2e, allows the definition of a flux quantum, Φ_0

$$\Phi_0 = \frac{h}{2e} \quad \frac{J}{A}(\mathrm{Wb}). \tag{2.68}$$

If we now define the two Josephson junctions as A and B, we can define two paths for charge carriers through the SQUID, a and b. The phase change due to this motion is defined as

$$\varphi_{a,b} = \frac{q}{\hbar}\int_{a,b} \mathbf{A}\cdot d\mathbf{l}. \tag{2.69}$$

The phase difference between these paths can be defined trivially as

$$\varphi_a - \varphi_b = \frac{q}{\hbar}\int_a \mathbf{A}\cdot d\mathbf{l} - \frac{q}{\hbar}\int_b \mathbf{A}\cdot d\mathbf{l}, \tag{2.70}$$

These two paths, a and b, also describe the same closed path as in equation 2.65

$$\varphi_a - \varphi_b = \frac{q}{\hbar}\oint \mathbf{A}\cdot d\mathbf{l} \tag{2.71}$$

$$\varphi_a - \varphi_b = \frac{q}{\hbar}\Phi. \tag{2.72}$$

This can be redefined in terms of the flux quantum defined in equation 2.68

$$\varphi_a - \varphi_b = \pi\frac{\Phi}{\Phi_0}. \tag{2.73}$$

The phase difference across either junction can now be described as the intrinsic phase difference modified by the phase change due to the screening current. The total current in the loop between the branching and meeting point of the paths a and b can then be described by the sum of the currents J_a and J_b

$$J_a + J_b = 2J_c\left(\sin\left(\varphi_{avg} + \frac{\pi\Phi}{\Phi_0}\right) + \sin\left(\varphi_{avg} - \frac{\pi\Phi}{\Phi_0}\right)\right), \tag{2.74}$$

where $\varphi_{avg} = \frac{\varphi_a+\varphi_b}{2}$. This can be simplified to

$$J_{tot} = 2J_c\sin\varphi_{avg}\cos\left(\frac{\pi\Phi}{\Phi_0}\right). \tag{2.75}$$

If we concern ourselves only with the phase difference between junction A and B, taking the intrinsic phase φ_{avg} as a constant with flux, it can be seen that the total current flowing through the SQUID oscillates with flux as

$$J_{tot} = 2J_c\cos\left(\frac{\pi\Phi}{\Phi_0}\right). \tag{2.76}$$

If the SQUID used is operated close to the critical current, the screening current can cause the current density in one Josephson junction to become super critical current

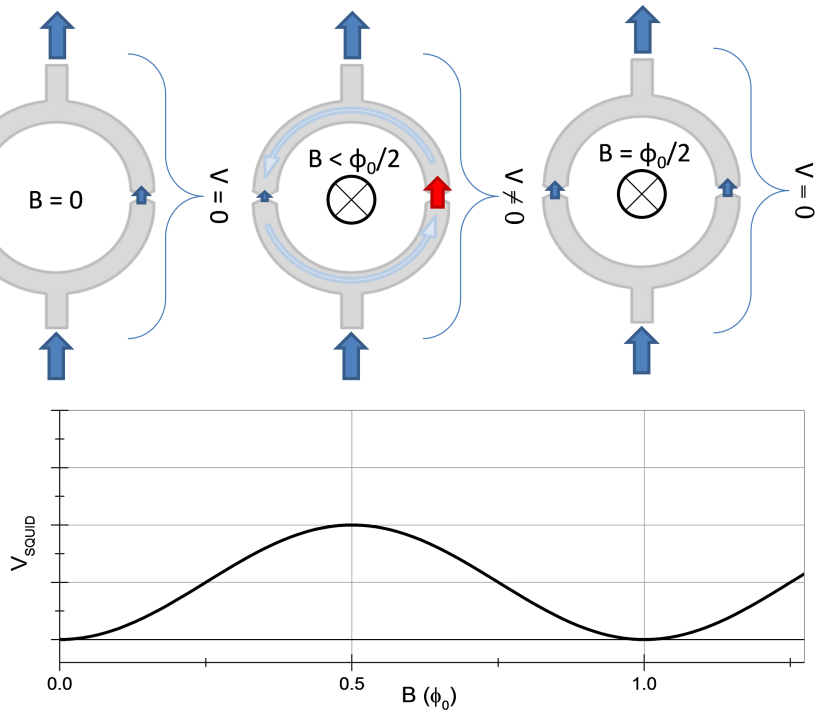

Figure 2.5: Illustration of SQUID device showing the current flow through the two JJ branches. Applied field increases the current in one of the branches causing an oscillation in the measured voltage across the junction with a period of Φ_0.

such that the loop becomes a resistively shunted Josephson junction. The voltage measured across one junction, V_0, is now given as

$$V_0^2 = R^2(J_0^2 - J_c^2), \tag{2.77}$$

where R is the junction resistance when normal, J_0 is the current density through the junction in normal mode and J_c the critical current density. Assuming that the current flow in one of the junctions is half the total in 2.76

$$V_0^2 = R^2\left(J_c^2\cos^2\left(\frac{\pi\Phi}{\Phi_0}\right) - J_c^2\right). \tag{2.78}$$

Since the voltage across the normal junction is the total voltage between points a and b

$$V_{SQUID}^2 = R^2 J_c^2 \sin^2\frac{\pi\Phi}{\Phi_0}, \tag{2.79}$$

such that V_{SQUID} is non-zero and oscillates with a period Φ_0. This oscillating voltage

provides the SQUID its high sensitivity. In reality, the dimensions of the junction cannot be ignored but, in a simple picture, this provides an explanation for the SQUIDs high resolution as flux sensor.

2.7 X-Ray Reflectivity

Probing structures on an atomic level requires radiation with a characteristic wavelength of similar magnitude to interatomic distances: 10^{-10} m. This is at the boundary between hard and soft X-Rays. Most commonly, X-Ray investigations of atomic structure are undertaken using radiation at 1.54 Å, the wavelength of copper Kα emission. This wavelength is largely used because of the simplicity of its production via X-Ray tubes. Electrons are accelerated from an anode to a cathode of a chosen material, in this case copper. As hot electrons impact the surface they rapidly lose energy through the Bremsstrahlung mechanism, producing a continuous spectrum of X-Rays. Additionally, scattering between hot electrons and core shell electrons results in a core-hole, recombination of the core hole with an outer shell electron emits peak radiation at wavelengths characteristic for the material such as the copper Kα. The resultant radiation can be collimated and used to probe thin film samples. [119]

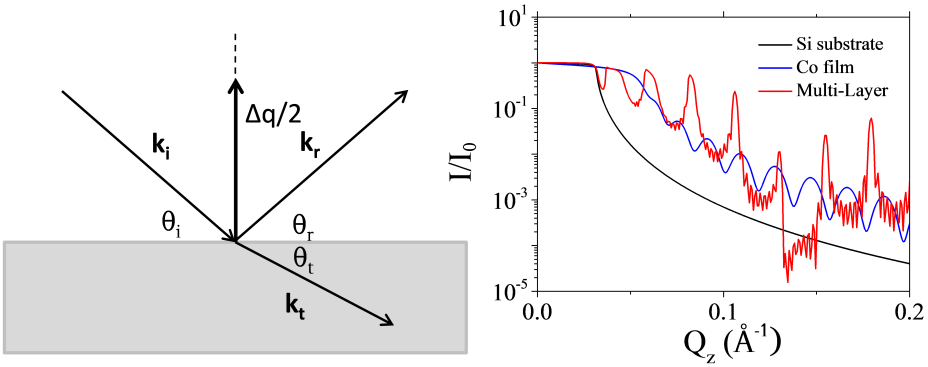

Figure 2.6: Representation of X-Ray scattering from the surface of an ideally smooth thin film [Left]. [Right] Graph showing simulations of a plain, ideally flat Si surface showing the characteristic q^{-4} behaviour (black), an ideal metal film showing the Kiessig fringes (blue) and a ten repeat multilayer of Cobalt and C_{60} similar to those used in this research showing Bragg peaks (red).

The information obtainable from small angle scattering of X-Rays is four-fold: the

critical edge provides information about the average electron density of sample interfaces; the super-critical dependence of reflected intensity on incident angle tells us about the homogeneity and roughness of an interface; Kiessig fringes tell us about the total thickness of a thin film and Bragg peaks tell us about the correlation length of structures in a film, figure 2.6.

At very small angles, many materials act like near perfect mirrors even if their reflectivity is poor at higher angles. This can easily be seen by observing a mirage. This phenomenon is generally referred to in optics as total external reflection and is defined as near unity reflectivity of a surface at sub-critical incident angles. The critical angle for a surface is derived from Snell's Law by considering that total external reflection will occur whenever the angle of refraction is greater than or equal to $\frac{\pi}{2}$

$$\alpha_{\text{critical}} = \arcsin(n_2). \tag{2.80}$$

For X-Rays the refractive index is, by convention, written as a small modification δ to unity

$$n = 1 - \delta. \tag{2.81}$$

In order to take advantage of the small angle approximation, we can state the critical angle in terms of ϑ, angle between incident light and the surface, and simplify

$$\vartheta_c = \sqrt{2\delta}. \tag{2.82}$$

We may then restate δ as a dispersion term related to scattering of X-Rays from electrons, we can assume elastic scattering for soft X-Rays

$$\delta = \frac{r_0 n_e \lambda^2}{2\pi}, \tag{2.83}$$

where r_0 is the Bohr radius, λ the X-Ray wavelength and n_e the electron density. Since the density of atoms in a solid varies only slightly with atomic number while n_e scales directly with Z

$$\vartheta_c \propto \lambda\sqrt{Z}. \tag{2.84}$$

The critical angle for X-Ray reflectivity is an excellent probe of atomic number in thin films. [120]

Above this critical angle, the reflected intensity drops with a characteristic $(\sin\vartheta)^{-4}$ behaviour. The scattering process at small angles can be considered in terms of a partial reflection from a perfectly smooth interface. The incident and reflected angles must be equal, $\vartheta_i = \vartheta_r$ and, since the scattering is elastic, the wave-vectors k_i and k_r must also be equal. On reflection, there is a change in momentum perpendicular to the surface, q_z

$$q_z = 2k\sin\vartheta, \tag{2.85}$$

or, in terms of wavelength

$$q_z = \frac{4\pi}{\lambda}\sin\vartheta. \tag{2.86}$$

Using the Born approximation for scattering cross-section, assuming a perfectly smooth surface and specular reflection, the reflectivity of the surface is described by Sinha et al, reference [121], as

$$|R|^2 = \frac{16\pi^2 r_0^2 n_e^2 \lambda^2 b}{q_z^4}, \tag{2.87}$$

where q_z is the z component of the photon momentum and b the x-ray scattering length for a given atom which is related the more commonly used scattering cross-section by: $4\pi b^2 = \sigma$. This is sometimes referred to as Porod's Law. As well as demonstrating the typical dependence of X-Ray reflectivity on angle, it is worth noting that materials with higher electron densities are predicted here to have higher reflectivity across all angles. It is, therefore, more difficult to use XRR to investigate lighter elements. However, this approximation is only valid when the surface is smooth and the specular condition in the differential scattering cross section, $\frac{d\sigma}{d\Omega}$, is met

$$\frac{d\sigma}{d\Omega} = \frac{4\pi^2}{q_z^2} r_0^2 n_e^2 L_x L_y \delta(q_x)\delta(q_y). \tag{2.88}$$

Here, σ represents the scattering cross-section, Ω is solid scattering angle, L_x and L_y defines the probed area of the sample plane. The two delta functions express the specular condition, requiring that only the z component of the momentum scattering not be zero. This can be assumed to be the case where $\frac{r}{\lambda} << 1$ i.e where the length scale of roughness and inhomogeneity, r, is much smaller than the wavelength of the X-Rays. If the specular conditions are not met, the differential scattering cross section must be

modified to take account of off-specular scattering. Deriving the exact dependence of the off-specular components on surface roughness is unnecessary here save to note that rougher surfaces cause significantly faster loss of reflected intensity in ϑ.

When X-Rays scatter coherently from multiple surfaces, interference can occur. By observing interference maxima in a reflectivity spectrum, one can determine the spacing of the layers. In order for this to be a useful probe, the path difference between X-Rays reflected from two surfaces must be on the order of λ for small angles.

The interference of X-Rays from interfaces can be described by Bragg's Law

$$m\lambda = 2d\sin\vartheta, \tag{2.89}$$

where X-Rays reflect from a periodic structure, the intensity peaks which occur due to constructive interference are referred to as Bragg peaks. These peaks can be modelled using a modified Bragg equation

$$m\lambda = 2\sin\vartheta_n\Lambda\Big[1 - \frac{\delta}{\sin^2\vartheta_n}\Big], \tag{2.90}$$

where Λ is the period of the superlattice and ϑ_n is the angular position of the n^{th} interference maximum. Where such maxima occur, the superposition of many reflections can result in unity reflectivity. Because the reflectivity of multi-layer structures can be unity at Bragg peaks, they are often employed as high efficiency mirrors for X-Rays otherwise known as Göbel mirrors. In this research, Bragg peaks are used to determine the periodicity of superlattices. [122]

2.8 Polarized Neutron Reflectivity

Neutrons can be used to probe materials in a manner analogous to x-rays. X-rays scatter with different amplitudes from materials of different Z allowing them to probe layered structures by scanning reflected amplitude above the critical angle. Neutrons can, similarly, be scattered from material interfaces but the mechanism of scattering is very different. Neutrons scatter from both the atomic nucleus and electron cloud where X-rays are principally scattered by the electron cloud. Thus, neutrons are more sensitive to different nuclear composition even for elements with similar Z. The neutron spin can interact with the internal field of an atom as well as the nucleus. This means that, for neutrons, magnetic and structural scattering can be deconvoluted. As a

result, polarized neutron reflectivity (PNR) is a powerful tool for probing microscopic magnetism. [123]

From reference [124], the scattering of a neutron from a given nucleus can be defined in terms of the potential $V(\mathbf{r})$

$$V(\mathbf{r}) = \frac{2\pi\hbar^2}{m_n} b_j \delta(\mathbf{r} - \mathbf{r}_j), \tag{2.91}$$

where m_n is the neutron mass and $\delta(\mathbf{r} - \mathbf{r}_j)$ is the Dirac delta function for the neutron coordinate r and nuclear coordinate r_j with scattering length b_j where scattering length and cross-section, σ are related for low energy scattering by: $4\pi b_j^2 = \sigma$. Because the wavelength of the neutron, ≈ 1Å, is far greater than the radius of the nucleus, ≈ 5 fm the nucleus can be treated as a point such that the delta function is nonzero for a radius r_0. Rearranging for the scattering length, taking the fourier transform of the potential and integrating over the scattering volume, the scattering length can be defined as

$$b = \frac{m_n}{2\pi\hbar^2} a \left(\frac{4}{3}\pi r_0^3 \right), \tag{2.92}$$

where a is the value of the potential within the radius r_0. For a collection of N atoms, the potential is written

$$V = \frac{2\pi\hbar^2}{m_n} Nb, \tag{2.93}$$

where Nb is the scattering length density (SLD). For a neutron impacting a surface, total reflection will occur if the kinetic energy of the neutron is less than the potential

$$E_\perp = V = \left(\frac{\hbar^2 (k \sin\vartheta_i)^2}{2m_n} \right) = \frac{2\pi\hbar^2}{m_n} Nb. \tag{2.94}$$

Rearranging, this becomes

$$\sin^2\vartheta_i = 4\pi\lambda^2 Nb, \tag{2.95}$$

where $\lambda = \frac{1}{k}$. The critical momentum, Q_c can be defined as

$$Q_c = \sqrt{16\pi Nb}, \tag{2.96}$$

where the momentum $Q_c = \frac{4\pi}{\lambda}\sin\vartheta_c$. This is the same dependence as observed for the critical angle of x-ray reflection. However, as can be seen from equation 2.92, it

is dependent on the nuclear scattering cross section rather than Z, making it more sensitive to changes in density even in isotopes of the same element. Other than these adjustments, neutrons can be treated in the same manner as scattered x-rays with a wavelength given by the de Broglie wavelength.

Finally, as mentioned, the total scattering of neutrons contains both nuclear and magnetic terms. The magnetic potential is simply defined by the neutron moment, μ and the magnetic field of the atom, $\mathbf{B}$

$$V_m = -\mu \cdot \mathbf{B}. \tag{2.97}$$

The total potential is thus modified by the alignment of the neutron moment to the local magnetic field and, thus, the scattering length has a polarization dependence. Probing a given material with polarized neutrons aligned or anti-aligned with the sample magnetization provides two different reflectivity spectra from which can be extracted the alignment of the magnetization of each layer to the neutron beam polarization.

2.9 X-Ray Absorption Spectroscopy

It is convenient in complexes involving many different materials and involving unknown atomic interactions to look at element specific band structures and magnetism. This can be achieved through resonant excitation of core-hole excitons. An electron in an inner shell can be excited to an empty state above the Fermi level at a resonant energy which is unique to the atomic orbital structure and, therefore, can be isolated from its environment. The energies required for these excitations vary depending on the element and the initial and final states but generally range between 50 - 2000 eV. This energy range corresponds to soft x-ray emission such as those produced from synchrotron radiation. The use of x-rays in probing these resonances gives the name X-ray absorption spectroscopy to this technique.

In this work the carbon K-edge, transition metal L-edges and rare earth M-edges are all probed in different contexts. The carbon K-edge appears at 280-290 eV and involves the excitation of an electron from the 1s-orbital to the 2p-orbital. The carbon K-edge exhibits a high degree of near-edge x-ray absorption fine structure (NEXAFS) due to the different bonding symmetries and energies in carbon molecules. These are generally divided into the π^* and σ^* resonances occurring between 280 - 289 eV and

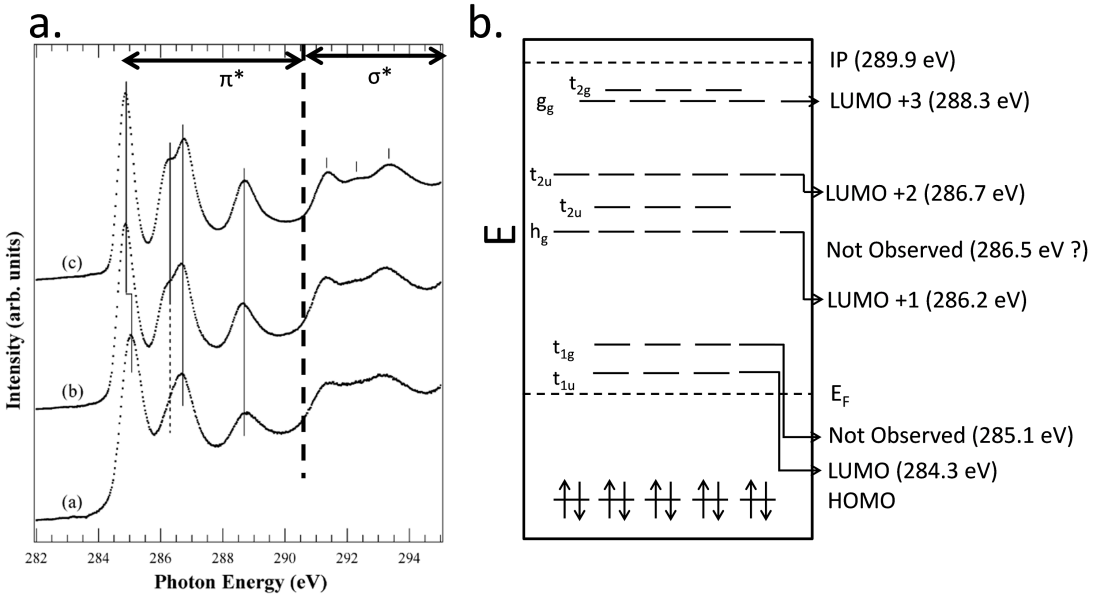

Figure 2.7: a. Diagram of C_{60} NEXAFS reproduced from [126] to show a typical NEXAFS in pristine solid C_{60}. The separate curves show the spectra for (a) 0.25 ML, (b) 1 ML and (c) 5 ML. b. Shows a Huckel diagram for all molecular orbitals below the ionization potential (IP) and above the HOMO with their symmetry labels and degeneracy. [127] The energy of the resonant excitations for each orbital in NEXAFS are labelled on the right hand side. Localisation of the core-hole exciton causes a reduction of the exciton energy which is greatest for the LUMO (-1.8 eV) and is progressively less for higher energy excitations due to weaker localisation (LUMO +1 0.35 eV, LUMO +2 0.15 eV). [128] Note that the t_{1g} and t_{2u} are not usually observed as their resonance overlaps significantly with the more dominant LUMO and LUMO+1 transitions. Because they were not observed experimentally in early NEXAFS observations, they are, by convention, not counted in the numbering of resonances above the LUMO.

290 - 310 eV respectively. The number and position of the π* peaks is indicative of the molecular orbital structure and can be used to distinguish different carbon allotropes. [125]

It is notable that, as in the PL spectra (section 2.10) , the core-hole exciton appears at a lower than expected energy in many carbon allotropes due to the effect of the core hole. The LUMO peak observed in the carbon K-edge for C_{60} exists 2.2 eV below the expected position derived from PES. [128] [129] The energy for the various resonant transitions expected in the NEXAFS of C_{60} are presented in figure 2.7 using values recorded in C_{60} on an Si substrate found in [130]. Excluded are transitions

to delocalised σ*-orbitals above the ionization potential. Unlike the narrow, localised core-hole excitons associated with the π*-orbitals below the ionization potentials, these transitions to delocalised states create a broad resonance between 290 eV and 310 eV. Some resonant peaks exist within this region and a bound σ* exciton is sometimes observed at the onset of the σ* resonance. [126] This exciton remains localised due to Coulomb attraction between the core hole and excited electron. It has been studied extensively in graphite. [131]

It is not possible to apply the principles of XMCD, described below, to carbon because the K-transition probes only the orbital moment. [132] Despite this, magnetism in K-edges can still be detected where there is strong spin-orbit coupling. [133] In light elements such as carbon, measurement of magnetic dichroism in the K-edge is challenging but has been achieved in a few cases. [134] [135] [36] In C_{60}, spin-orbit coupling is increased compared to other carbon allotropes due to the curvature of the molecule which makes measurements of spin moment more feasible than in a 2D carbon system such as graphene. [136]

The transition metal L-edges involve the excitation of an electron from the 2p-orbital to the 3d-orbital. In transition metals, the 2p-orbitals are split via the spin orbit interaction into two sub-orbitals corresponding to total angular momentum, j, of $\frac{3}{2}$ and $\frac{1}{2}$ giving rise to the labels $p_{\frac{3}{2}}$ and $p_{\frac{1}{2}}$. The transitions from these orbitals into the d-band are respectively labelled L_3 and L_2. The splitting of the 2p-orbital in transition metals allows the spin population of the d band to be probed by using different helicities of circularly polarized light to pump the exciton.

The selection rules for possible excitations for circularly polarized light can be stated as

$$\Delta j = 0, \pm 1, \Delta s = 0, \Delta l = \pm 1, \Delta m = +1(\mu^+), -1(\mu^-), \tag{2.98}$$

where j is the total angular momentum quantum number, s the spin, l the orbital moment and m the azimuthal quantum number. $\Delta m = +1$ corresponds to right handed helicity and $\Delta m = -1$ to left handed helicity. Note that in either case the spin is unaffected.

The one electron transition probabilities for all allowed transitions can be calculated using Wigner Eckhart theorem and are presented in detail in [137]. Summed over all spin states for + and - helicities, the L_3 transition occurs with probability $P_{+-} = \frac{2}{3}$

while the L_2 transition occurs with $P_{+-} = \frac{1}{3}$. If the d band is exchange split and has an unequal population of spin up and spin down states, the transition probability for spin-up and spin-down states will be different in both L_2 and L_3 transitions. For left handed helicity (-), the transition of a spin up electron from the p-orbitals occurs with $P_- = \frac{5}{8}$ from the L_3 edge and $P_- = \frac{1}{4}$ from the L_2 edge. A transition involving a spin down electron occurs with $P_- = \frac{3}{8}$ from the L_3 orbital and $P_- = \frac{3}{4}$ from the L_2 orbital. This is inverse for right handed helicity (+). Thus, if the available states in the d-band are not equal for spin up and spin down, the sum of both spin up and spin down transitions for left and right helicities at the L_2 and L_3 peaks will not be equal. The difference in intensity for left and right helicity at the two peaks is indicative of exchange splitting in the d-band. [138]

The spin and orbital moment (m_{spin} and m_{orb} respectively) of a transition metal atom can be extracted from the inequality of the left and right helicity edges using the sum rules developed by Thole et al. [140] These rules were found to match experimental data in the study of iron and cobalt by Chen et al [139]

$$m_{orb} = -\frac{4\int_{L_3+L_2}(\mu_+ - \mu_-)dE}{3\int_{L_3+L_2}(\mu_+ + \mu_-)dE}(10 - n_{3d}) \tag{2.99}$$

$$m_{spin} = -6\frac{\int_{L_3}(\mu_+ - \mu_-)dE - 4\int_{L_3+L_2}(\mu_+ - \mu_-)dE}{\int_{L_3+L_2}(\mu_+ + \mu_-)dE} \times (10 - n_{3d})\left(1 + \frac{7\langle T_z\rangle}{2\langle S_z\rangle}\right)^{-1}. \tag{2.100}$$

The integrals can be found by taking the area of the dichroism within the limits of the L_2, L_3 or entire edge, the difference between the signal with left and right helicity. $\langle T_Z\rangle$ and $\langle S_z\rangle$ are the expectation values of the magnetic dipole and spin operators for the transition and n_{3d} is the number of d-band holes. While it is quite possible to apply these rules to well known systems such as pure cobalt and iron, in novel systems it is difficult to determine exact values for n_{3d}. Where the ratio $\frac{7\langle T_z\rangle}{2\langle S_z\rangle}$ is small, this term can be neglected. Chen at al discuss in reference [139] the contribution of this correction to Co and Fe. If this term is negelcted, the number holes, n_{3d}, need not be known if calculating the ratio of spin and orbital moment

$$\frac{m_{orb}}{m_{spin}} = \frac{2q}{9p - 6q}, \tag{2.101}$$

where p and q are integrals of the dichroism defined in figure 2.8. The rare earth M transitions involve the excitation of an electron from the 3d-orbital to the 4f-orbital.

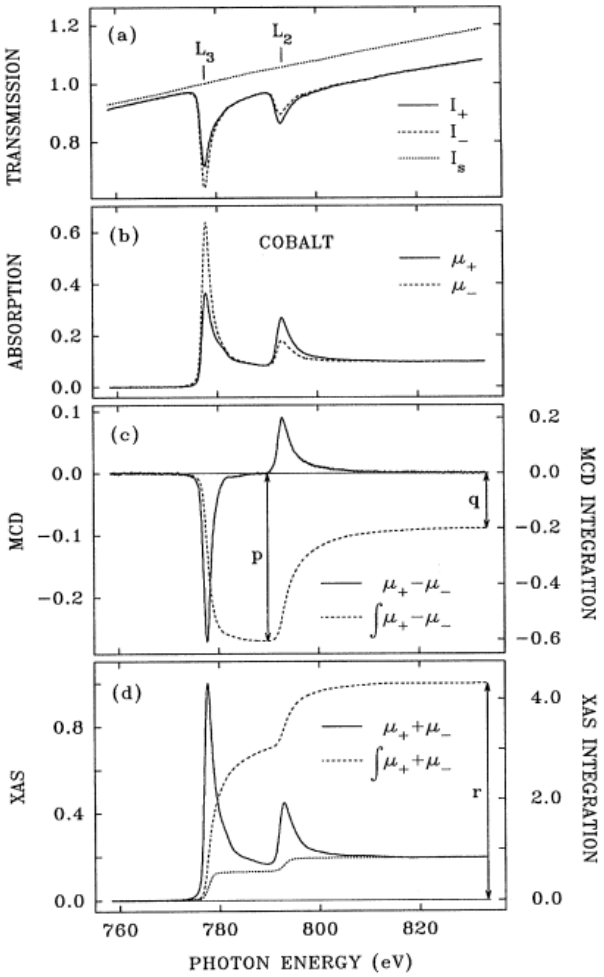

Figure 2.8: Example of the applied sum rules for the $L_{2,3}$ edge fo cobalt. Figure reproduced from [139]

The 3d-orbital is similarly split by spin orbit coupling, this time between states with $j = \frac{5}{2}, \frac{3}{2}$ labelled $M_{4,5}$. The sum rules can be derived using a similar method but require a correction factor C which takes into account the orbital mixing of the split 3d-orbitals due to strong Coulomb interactions in the rare-earths [141]

$$\frac{m_{orb}}{m_{spin}} = \frac{2C}{5\frac{p}{q} - 3}\left(1 + \frac{6\langle T_z\rangle}{m_{spin}}\right), \tag{2.102}$$

where p and q have the same values as in figure 2.8. [141]

Various methods can be used to measure the absorption of X-rays. The most obvious

and, arguably, most accurate method is transmission spectroscopy. This measures the transmitted intensity of an X-ray beam passed through a thin film of material enabling the experimenter to calculate the exact absorption cross section. [137] However, this method is limited in practice since one must ensure a film is thin enough to allow a detectable intensity of beam to pass through to the detector. Thick substrates such as the 1 mm thick Si wafers used in this work are, thus prohibited.

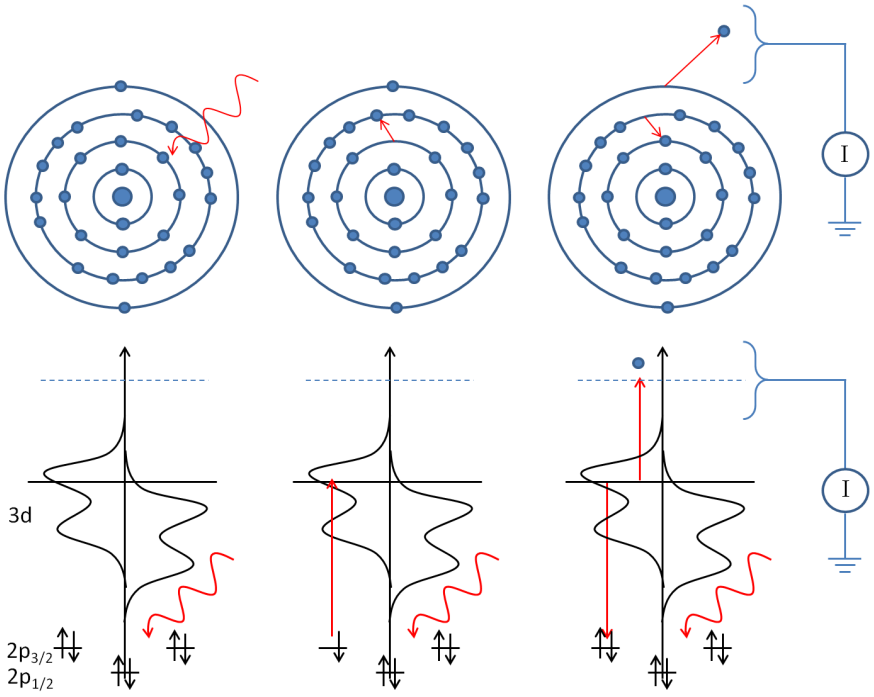

Figure 2.9: Cartoon of the Auger process in TEY. [From left to right] an x-ray is absorbed during an inner electron transition. The core hole exciton recombines and the energy loss causes an outer electron to be ejected to the vacuum level which is then measured as a drain current.

Other methods rely on measuring the result of recombination rather than direct absorption. Flourescence measures the photons emitted through radiative recombination processes. [142] However, flourescence yields tend to be low in carbon due to non-radiative, multielectron recombination mechanisms. [143]

In this work, the primary detection method is total electron yield (TEY). This measures the secondary electrons emitted during the decay of the core-hole exciton, particularly Auger electrons, figure 2.9. In the Auger process, the de-excitation of the core-hole exciton scatters with an electron in the outer orbitals of the atom, causing

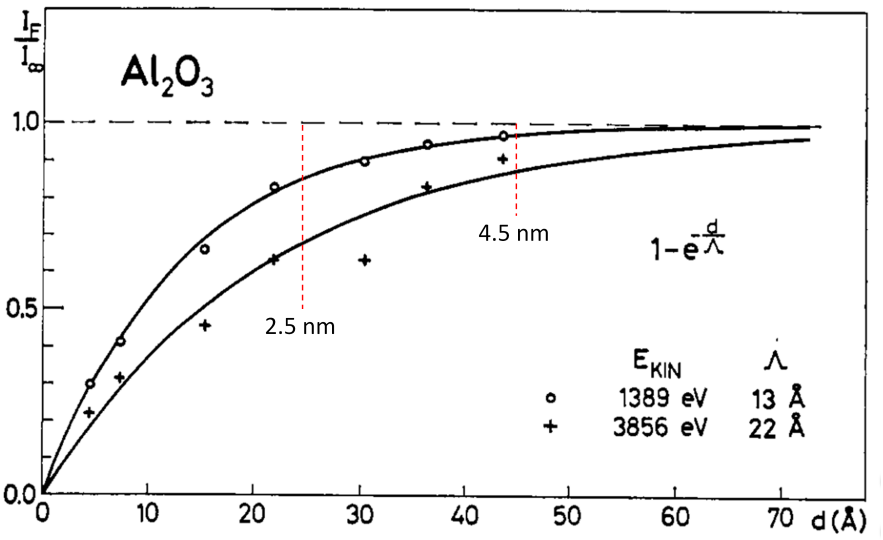

Figure 2.10: Figure reproduced from [144] showing the fractional peak intensity reduction for Auger electrons produced in a chromium 1s transition passing through an alumina film of varying depth. The thicknesses of the caps used in section 4.3 and 6.5 are shown.

it to be raised above the vacuum level and emitted as a free electron. A conducting contact attached to the film surface will allow these emitted electrons to drain to ground and be detected as a current which is proportional to photon absorption. [137] The key limitation of TEY is the limited escape depth of secondary electrons. Secondary electrons scatter from sample atoms and lose energy, eventually being recaptured before detection if the emitting atom is too far from the drain contact, see figure 2.10. In C_{60}, the escape depth is expected to be very shallow. Rotenberg et al predict only 3 ML. [145] For aluminium oxide, the escape depth of Auger electrons is $\approx$ 2.2nm limiting possible cap thickness. [144]

2.10 Photo-Luminescence

In many non-metals, the gap between valence and conduction bands is of a similar order to visible light. When a photon of energy greater than or equal to the direct band gap is incident on the material it can create an exciton (electron-hole pair). This pair will relax via Coulomb or electron phonon scattering until it occupies the band minimum before recombining, releasing a photon of energy exactly equal to the semi-

conducting band gap. This allows light to be used as a probe of the band structure of a semiconductor. Excitations across the bandgap or recombinations can also occur through scattering with phonons. These multi-particle recombination processes can lead to phonon emission at energies other than that of the direct band-gap. Such emission is called a phonon replica and can reveal information about the phonon-electron interactions in semiconductors. [95]

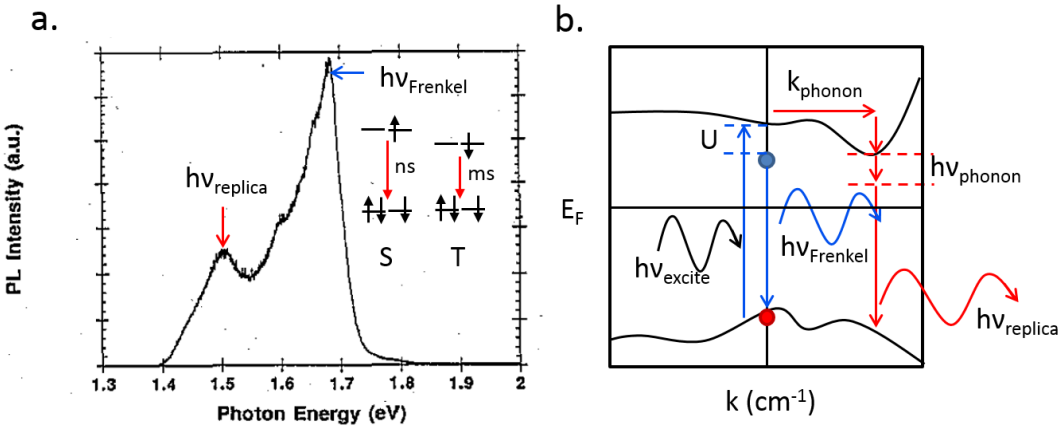

Figure 2.11: a. Example of PL spectrum of C_{60} recorded at 10 K showing the main peak (1.69 eV) created by recombination across the direct bandgap and the key phonon replicas, especially the strong phonon replica peak at 1.5 eV. Figure replicated from [146] The singlet (S) and triplet (T) exciton configurations are included. The singlet state has a lifetime of the order of ns while the more stable triplet has a lifetime of ms. Thus, the PL spectrum is mostly due to singlet recombination. b. Diagram of excitations in an arbitrary semiconductor. Where excitons are highly localised, the Coulomb interaction, U, lowers the exciton energy. If the excited electron scatters with a phonon, it can move to another region of the band in k-space as well as changing the energy of the recombination.

This description of excitation and recombination might be suitable for discussing excitons in materials where bands are broad and excitons are delocalised. However, C_{60} and many other molecular semiconductors, as discussed in section 2.2, are described in a tight binding model in which the band structure of the isolated molecule is well preserved as a narrow band in the solid and motion of charge carriers occurs via short hops between localised states. If one measures the band structure of C_{60} by photo-electron or inverse-photo-electron spectroscopy (PES, IPES) in which electrons are excited to vacuum from valence bands, a band gap of 2.3 eV is observed. [77] However,

if one measures photo-luminescence from C_{60} the luminescence peak is clearly observed at 1.69 eV, fig 2.11. This inconsistency is solved by invoking the concept of a Frenkel exciton.

In a simplified picture, a Frenkel exciton occurs in localised or poorly screened systems where there is strong Coulomb interaction between the electron-hole pair that make up the exciton. This attraction serves to lower the energy of the excitation such that it lies within the semi-conducting band gap. The recombination of excitons in C_{60} is not a trivial problem. For a start, electric dipole recombination of the singlet excitons has been shown to be forbidden with recombination occurring through inter-system coupling via a Herzberg-Teller mechanism. [147] In addition, a triplet exciton (aligned spins in HOMO and LUMO) can be accessed through inter-molecular interactions which is more stable than the singlet exciton (anti-aligned spins in HOMO and LUMO). The singlet has a short lifetime of 1.2 ns while the triplet exciton exhibits a long lifetime on the order of ms. [148] The dynamics of recombination are discussed in detail in both [149] and [150] with reference to the triplet transition and the lifetime of singlet excitons responsible for the fluorescence spectrum.

2.11 The Raman Effect

Molecules vibrate when at finite temperatures. These vibrations can be imagined simply by picturing a molecule as a collection of spheres linked by rigid springs. When energy is imparted to the molecule, the springs flex and oscillate in a complex manner dependent on the positions and relative masses of the different spheres and the 'flexibility' of the bonds. Through this analogy, it is easy to see that molecular vibrations will occur at various frequencies which build up a characteristic spectrum unique to every molecular structure. Taking a structure as simple as an H_2O molecule, three non-degenerate vibrational modes can be identified.

Where charge is not evenly distributed around a molecule, such as in the H-O bond in water, such oscillations constitute an oscillating dipole. In 1928, C.V. Raman determined that the coupling between these dipole oscillations and light could produce a change in the frequency of light which has passed through a material containing such oscillating dipoles: named Raman scattering. [151] In short, Raman scattering can be described as the inelastic scattering of light from polarisable molecules. The inelastic scattering can be partially explained by classical electromagnetism. [152] The

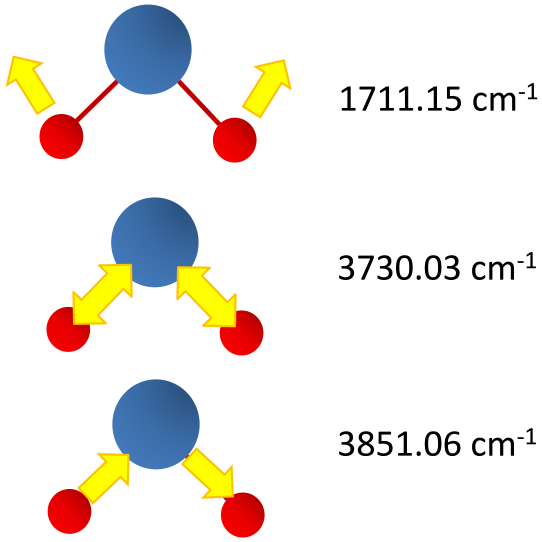

Figure 2.12: The three non-degenerate vibrations of water molecules.

oscillation of a molecule in one mode can described by a displacement Q_k

$$Q_k(t) = Q_k^0 cos2\pi\nu_k t, \tag{2.103}$$

where Q_k^0 is the displacement amplitude and ν_k the frequency of mode k. The induced electric dipole moment, μ, can be described as

$$\mu = \alpha E = \alpha E_0 cos2\pi\nu_0 t, \tag{2.104}$$

where E is the oscillating field of a coherent beam of light, such as a laser, at frequency ν_0 and α the polarizability. Because the electric dipole moment of the molecule is proportional to the displacement of the charges, the change of the polarizability can be described with respect to the displacement vector (shown to a first order approximation here)

$$\alpha = \alpha_0 + \left(\frac{\partial\alpha}{\partial Q_k}\right)_0 Q_k + ... \tag{2.105}$$

Thus

$$\alpha E = \mu = \alpha_0 E + \left(\frac{\partial\alpha}{\partial Q_k}\right)_0 Q_k E. \tag{2.106}$$

Substituting equation 2.103 and 2.104

$$\mu = \alpha_0 E_0 \cos 2\pi\nu_0 t + E_0 Q_k^0 \Big(\frac{\partial\alpha}{\partial Q_k}\Big)_0 \cos 2\pi\nu_0 t \cos 2\pi\nu_k t, \tag{2.107}$$

which, expanded, becomes

$$\mu = \alpha_0 E_0 \cos 2\pi\nu_0 t + \frac{1}{2} E_0 Q_k^2 \Big(\frac{\partial\alpha}{\partial Q_k}\Big)_0 [\cos 2\pi(\nu_0 + \nu_k)t + \cos 2\pi(\nu_0 - \nu_k)t]. \tag{2.108}$$

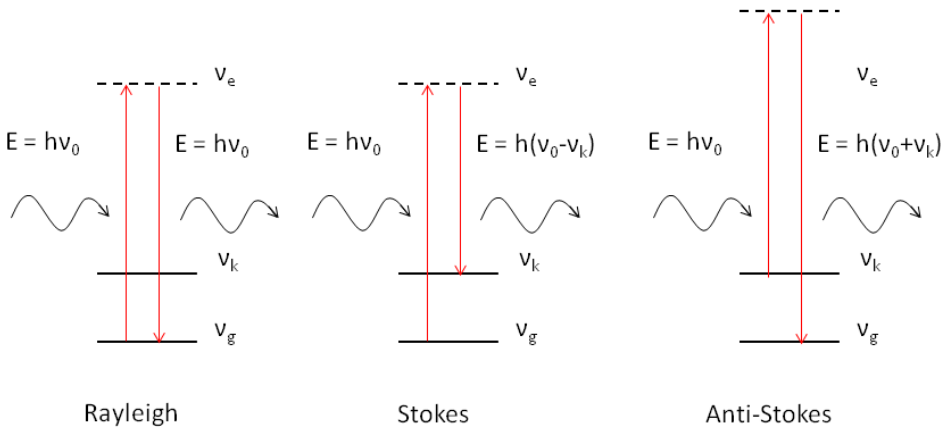

Figure 2.13: The three processes of dipole scattering of light (Left) elastic scattering which dominates. (Middle) Stokes scattering which reduces the energy of scattered photons and can be shown to dominate in-elastic scattering when considering thermal population of different states. (Right) Anti-Stokes scattering: the molecule begins in an excited state and scatters with the incident photon to a higher energy virtual state. Relaxation to the ground state thus results in the emission of a photon at higher energy than the incident photon.

The first term here describes the fully elastic component of the scattering where the dipole oscillation occurs at the same frequency as the incident light, the Rayleigh scattering. The two terms in the square bracket refer to the inelastic components where the scattered light has its frequency altered by interaction with the dipole oscillations. Where the scattering occurs from a higher frequency to a lower frequency producing a photon with a higher energy than the incident photon, $(\nu_0 + \nu_k)$ the scattering is called anti-Stokes. Where the scattering occurs from a lower frequency to a higher frequency, $(\nu_0 - \nu_k)$, this is called Stokes. The Stokes and anti-Stokes processes can be more easily visualized by considering a band diagram with a virtual excited state comprising the superposition of the incident light and internal vibration of the molecule, figure 2.13.

This derivation relies on a 1D approximation and ignores thermal effects on the population of different vibrational states and quantum mechanical effects on the polarizability. These corrections show that Stokes scattering will significantly outweigh Anti-Stokes scattering due to different populations of higher energy states. In C_{60} there are ten non-degenerate, Raman active vibration modes. [153] These are separated into two categories based on the symmetry of the oscillation. The two symmetries are labelled with the characters H_g and A_g, with H and A representing single and quintuple degeneracy and the g subscript inversion symmetry. [154] Two A_g modes can be observed in the Raman spectrum of C_{60} and eight H_g modes. The Ag(2) mode at 1470 cm^{-1} is the dominant mode.

Chapter 3

Experimental Methods

3.1 Deposition Methods

3.1.1 DC Magnetron Sputtering

In order to study the properties of materials, especially magnetic materials, it is necessary to create material samples with strictly controlled parameters. The parameters most crucial to this research are physical dimensions, crystallinity, stoichiometry, contaminant/impurity concentration, surface morphology and roughness. Controlling all of these, especially surface morphology and crystallinity, would require an epitaxial growth method. While this might produce mono-crystalline samples, it is a time-intensive technique.

The C_{60} molecule is 7 Å in diameter. This means any layer of C_{60}, even deposited in an ideal mono-crystalline form, would have a root mean square (RMS) roughness of approximately half this diameter. C_{60} layers deposited using the evaporation method have typical roughness between 7-20 Å, as measured by XRR and AFM. While epitaxially grown metal layers may have roughness on the order of one unit cell (a few Å). Thus, epitaxial methods would be redundant due to the intrinsic roughness introduced by C_{60}. Control over physical dimensions, contaminant/impurity concentration and stoichiometry can be obtained by DC magnetron sputtering to a sufficient degree.

DC magnetron sputtering is a Physical Vapour Deposition (PVD) method for thin film growth. PVD uses a physical process such as heating or ion bombardment, unlike CVD where volatile reactants are included, to produce a vapour of material which can be directed toward a substrate for deposition. As with all vapour deposition techniques, PVD relies on strict control of the atmosphere and is usually performed under high vacuum (HV) conditions ($10^{-8} < \mathrm{P} < 10^{-6}$ Torr).

Sputtering uses accelerated ions to liberate atoms from a target in order to create the vapour. A gas, usually an inert gas to prevent reaction between the sputter gas and material vapour, is injected into the space between an anode and a cathode. A high voltage is created between the electrodes in order to produce a strong electric field. When the voltage becomes high enough, a breakdown occurs in the gas.

Electrons are stripped from the gas to create a conducting pathway between the electrodes, otherwise known as an arc. If the current sourced across the electrodes is sufficient to balance the flow through the arc, a stable plasma can be created as the ionized gas and free electrons are accelerated by the voltage and continue to collide,

producing further ions in a cascade. A plume of stable plasma can thus be formed between the electrodes. The ionized atoms and free electrons have opposite charge and will thus be accelerated toward opposite electrodes. However, the lower mass electrons will not transfer momentum to the anode as efficiently as the high mass ions will to the cathode. Deceleration of the electrons will create thermal excitations in the anode causing heating but, unless the acceleration voltage is in the range of tens of kilovolts, it will not cause sufficient heating to significantly evaporate the anode material. However, the heavier ions will collide with atoms in the cathode and transfer momentum fairly elastically to the similar mass atoms in the cathode material. The transfer of momentum to those atoms near the surface of the cathode will provide sufficient energy for them to overcome their binding energy in the lattice and release them into vacuum. These released atoms can then be transferred to any substrate simply by placing it in the vapour, figure 3.1.

Sputtering in this manner is limited by low deposition rates (typically hundredths of Å per second), high required gas pressure (10^{-2} mbar) and high operating voltages (2-3 kV). Magnetron sputtering, developed in the 70's, solves many of these problems allowing higher deposition rates (Ås per second), operating voltages of a few hundred volts and operating pressures of 10^{-3} mbar. [155]

When a magnetron is present, the ions which move close to the anode surface follow a circular path due to the Lorentz force. The magnet poles are arranged such that one polarity forms a ring around the cathode circumference while the other is a point in the centre, this confines the spiralling ions to the region of the cathode. In this region, the acceleration and confinement induced by the field causes a significant increase in the number of collisions between ions and un-activated neutrals. These collisions release further free electrons which follow a similar but opposite circular path causing further collisions. This increase in collision and ionization means the plasma in the region close to the cathode surface is significantly more dense than elsewhere in the gap. The toroidal region of high density plasma preferentially erodes a circular region on the sputter target known as a racetrack.

Many variants of the magnetron sputtering system exist for a host of different applications. One of the most common industrial usages is the unbalanced magnetron where the magnetic field is stronger in one part of the cathode than others producing very high deposition rates for commercial applications. However, because this research

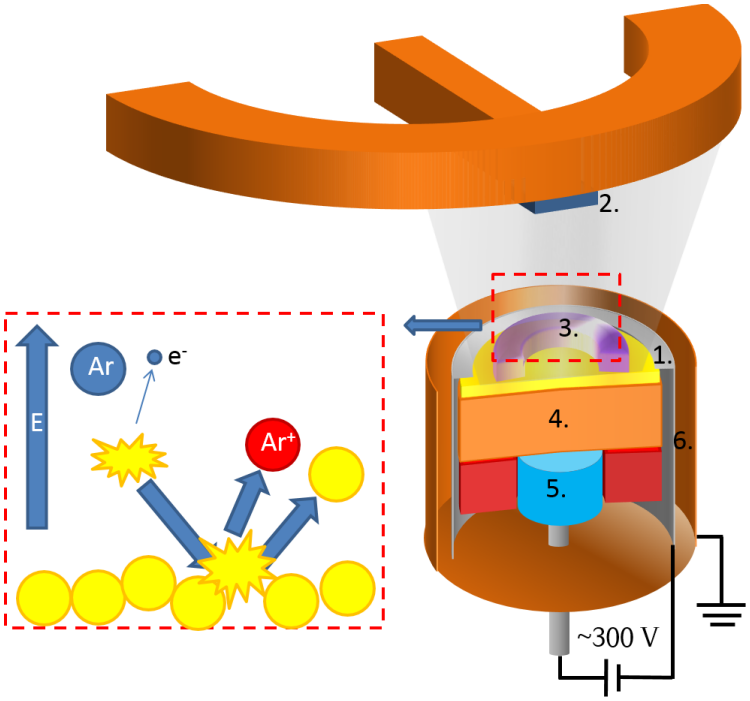

Figure 3.1: Cartoon demonstrating the internal mechanics of a DC magnetron sputter gun showing the position of the anode (1) and target material which forms the cathode (3). The substrate for deposition is attached to the anode and positioned in the plasma. Above the target, the field created by the ring magnets beneath the target (5) cause a high density plasma to be confined in a ring near the target surface. In order to prevent damage to the radial magnets and ensure a uniform contact, a thick copper buffer is placed between them and the target (4). The apparatus is surrounded by grounded shields (6) to drain the significant static charges which can build up during deposition which are separated from the target material by ceramic spacers.

is primarily concerned with films in the sub-micron range, it is far more important that any deposition technique used produces films with a very low thickness tolerance. Therefore, samples in this research are all deposited using balanced magnetrons.

The system used for deposition in this research is a multi-source, high vacuum sputtering chamber. The system comprises a single growth chamber which can be evacuated to a pressure of 10^{-7} Torr (1.3×10^{-10} atm: partial pressures, H_2O 7×10^{-8} Torr, N_2 1×10^{-8} Torr, O_2 $< 0.1 \times 10^{-8}$ Torr) using a combination of an oil-based mechanical pump and a helium based cryopump. The pressure can be further decreased to a base of 10^{-9} Torr using a nitrogen based trap to condense residual water vapour

from the atmosphere. Due to the surface sensitivity of this research, the greatest threat to sample quality is the presence of oxygen or water as residual gases in the growth environment as these can easily bond to interfaces and quench interfacial coupling. Oxygen is easily captured by the cryopump. However, the low molecular weight of water makes it hard to capture. Therefore, all samples in this research were grown using the nitrogen trap in order to remove residual water. Utilising the nitrogen trap, the total chamber pressure can be reduced to $2-3\times10^{-8}$ Torr (partial pressures, H_2O 1.4×10^{-8} N_2 1×10^{-8} O_2 1×10^{-9}).

3.1.2 Sublimation

Molecules such as fullerenes with high molecular weight and low inter-molecular binding energy can easily be evaporated without resorting to plasma or beam techniques. Sublimation of C_{60} occurs between 700 and 900 K in atmosphere and significantly lower in UHV. [156] Dissociation of C_{60} cages occurs primarily due to C_2 emission at 10.8 ± 0.3 eV .[157] Coalescence of C_{60} can occur at 1073 K but has only been observed at such low temperatures in nanopeapod structures. [158] Full coalescence of isolated molecules occurs around 1500 K. The large gap in energy between inter-molecular and inter-atomic forces, and the resulting difference in temperature required for sublimation and cage destruction in this system make it easy to deposit via evaporation without changing chemical composition. A detailed review of the sublimation rates and vapour pressures of solid C_{60} at various temperatures can be found in [159].

C_{60} crystals are loaded into an alumina crucible which sits in a tungsten filament inside a copper shield completely sealed save a small aperture through which the molecular vapour may escape, figure 3.2. It is vital when depositing C_{60} that the molecular plume be strictly confined since the higher scattering cross-section of the large and massive C_{60} molecule increases the diffusion of material throughout the deposition chamber due to random walks. The copper shield is externally water cooled to prevent excessive heating of the surrounding components throughout the long growth times. A quartz microbalance is located inside the shield just off the escape aperture, 5 cm from the crucible, to collect material from the plume in order to monitor the sublimation rate.

During sublimation, a current of between 19-25 A is passed through the tungsten filament causing it to heat to several hundred degrees Kelvin. The quartz balance allows the deposition rate to be monitored and the filament current adjusted to maintain a

stable rate. This monitoring was vital to account for variations in the vapour pressure of the molecules. Over the course of 3 hrs, the deposition rate can vary by 30%. The throw distance between the crucible and the substrate is 10 cm.

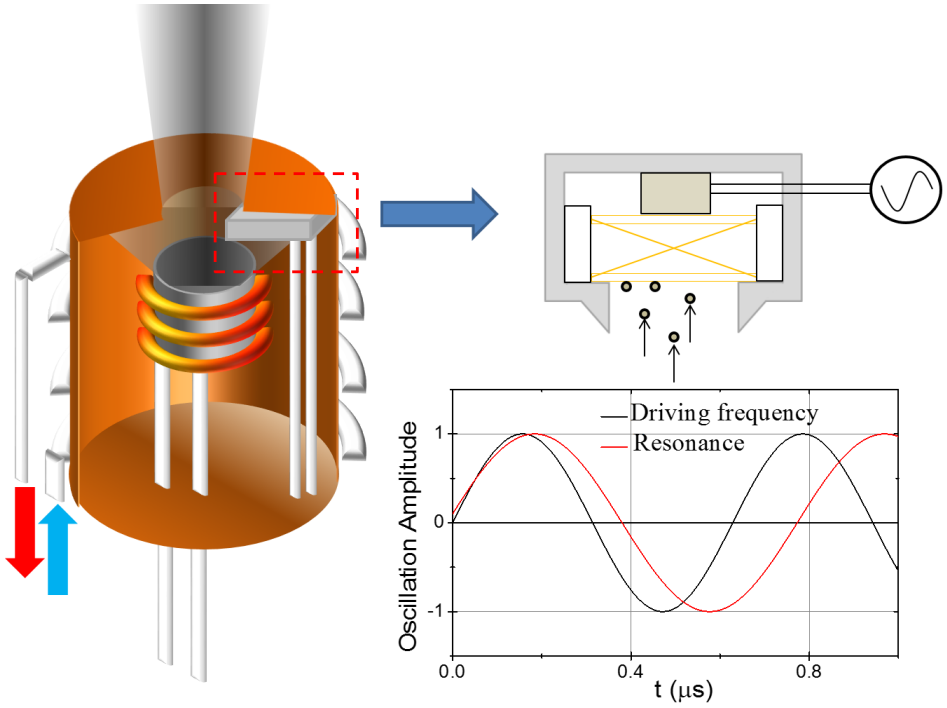

Figure 3.2: Illustration of the evaporation source interior. The crucible sits within a high resistance W coil. Water is cycled around the outside of the copper shield to prevent overheating. The quartz balance sits in the molecular plume. A quartz crystal is driven at resonance by a piezo electric motor. As matter adheres to the crystal, the resonant frequency changes. The phase difference between the driving frequency and the resonant frequency provides a measure of the total mass adhered to the crystal.

C_{60} is unstable to oxidation and can degrade very quickly under ambient conditions. A key cause of degradation is photo-assisted oxidation and decomposition. [160] Without photons to excite reactive species, C_{60} is quite stable at room temperature and pressure. When heated above 473 K in the presence of atmospheric oxygen, C_{60} undergoes irreversible oxidation forming an epoxide and amorphous fullerene-oxide precursors which lead to full breakdown of the C_{60} cages and oxidation to CO_2 at around 930 K. [161] Even at low temperatures and without photo-oxidation, the intercalation of oxygen into C_{60} crystals can occur even if reduction to CO_2 does not occur until it

is illuminated or heated. [162]

By necessity of the deposition system, the fullerenes used in this study are exposed to air regularly when being loaded into the evaporation system and when the UHV chamber is opened to remove samples. This could cause serious problems if irreversible oxidation were allowed to occur. Such contamination is prevented through the deposition method itself. Firstly, the molecules which are used as a source are prepared in macroscopic crystals. Due to the smaller number of lattice defects and smaller surface area to volume ratio, larger crystals are known to be more stable to oxygen intercalation. [156] Secondly, the crucible is contained in a near sealed container, the only opening being the aperture through which the molecular plume will be delivered to the substrate. This means the molecules are stored in darkness even when the UHV chamber is opened to atmosphere. Even though oxygen may intercalate into the C_{60} crystals, it will not cause irreversible oxidation. In studies of both powders and thin films, the concentration of oxygen in C_{60} which has been exposed to atmospheric conditions is shown to drop at 400 K and reaches near pristine levels by 450 K. [163] This is the peak desorption temperature for both graphite and C_{60} and is notably far below the temperature required for irreversible oxidation in the absence of light at 930 K. Before evaporation but after the chamber has been fully evacuated, the crucible is heated to a temperature just below the sublimation temperature. This ensures the C_{60} molecules are fully outgassed before reaching the temperature at which irreversible oxidation would occur.

Over time, degradation of the source molecules is inevitable. Incomplete outgassing of the source before sublimation or exposure to small amounts of light will result in the build up of C_{60} polymers or fragments as well as quantities of soot comprising a mixture of various carbon allotropes and oxides. [164] These compounds are often more vulnerable to oxidation and oxygen intercalation and will speed up further degradation of the remaining C_{60}. However, the precautions taken: high vacuum, minimizing exposure to light, outgassing below sublimation to remove intercalated oxygen; when using this growth system allow us to deposit high purity C_{60} for several weeks using the same source molecules. Degradation of the source molecules can be monitored by observing the decline of sublimation rates over time as more stable carbon allotropes and polymers begin to dominate.

3.1.3 Co-deposition of RE Alloys

When creating thin films of alloys, there are a number of available choices for the growth method. Perhaps the most controllable is co-deposition, using multiple sputter guns angled toward a single substrate which sputter simultaneously to produce an alloy where the proportions of the different phases is determined by the relative growth rates. This is only possible where sputter guns can be angled to produce a co-deposition plasma. Where this is not possible, alloyed targets provide an alternative. While the structure of an alloyed target cannot necessarily be transferred to a substrate, the ratio of materials in the target and their relative melting points will influence the final alloy. The mass of the species in an alloy will cause some variation in composition between target and substrate due to variations in scattering with the sputter gas and 'resputtering' (deposition of lighter species back onto the sputter target due to scattering with the sputter gas) which will supress the Co concentration slightly at 24 mTorr. [165] The heat of vaporization of Gd is 305 kJ/mol and Co 375 kJ/mol. [166] The rate of evaporation and energy of ejected atoms is related to the heat of vaporisation since this determines the ion energy required to overcome the binding energy of the lattice. Co and Gd will evaporate at similar rates with the Gd deposition rate slightly increased by its lower binding energy.

CoGd alloys in this research were deposited from a composite target comprising a Co medallion doped with Gd foil. By calculating the proportion of the racetrack intersected by the Gd foil, it is possible to approximate the final ratios of the alloy. This allows the ratio to be adjusted between growths to optimise the critical temperature. The optimisation is detailed in section 5.2.

3.1.4 Thin Film Deposition

Samples used in this research are deposited on p-doped silicon with either native oxide or thermal oxide surfaces. Both substrates have one polished side. Substrates with native oxide are used when the transport characteristics of the samples will not be measured. These native oxides will be on the order of 10 Å. [167] Substrates with thermal oxides are used when there is the potential for current to shunt through the substrate during transport measurements. The thermal oxide is generated to a thickness of $\approx$ 100 nm maintaining similar roughness to unoxidised wafers but with a thick insulating barrier.

Metals such as cobalt or organic materials such as C_{60} deposited directly on to silicon have increased surface roughness due to surface tension between substrate and film which can cause aggregation, lattice stress and stacking errors. Tantalum seed layers have been shown to reduce roughness in Co films and improve inter-layer coupling. This is most clearly demonstrated in exchange bias systems where, as in this research, interfacial coupling is key. The priming of a substrate with a Ta layer of less than 5 nm not only creates a metal surface with near atomic flatness but also seeds the lattice of Co layers, inducing a body-centred cubic crystal structure with a (111) surface. This is useful for interfacial studies since, in BCC structures, a (111) plane has a higher number of atoms per unit area at the surface. [168]

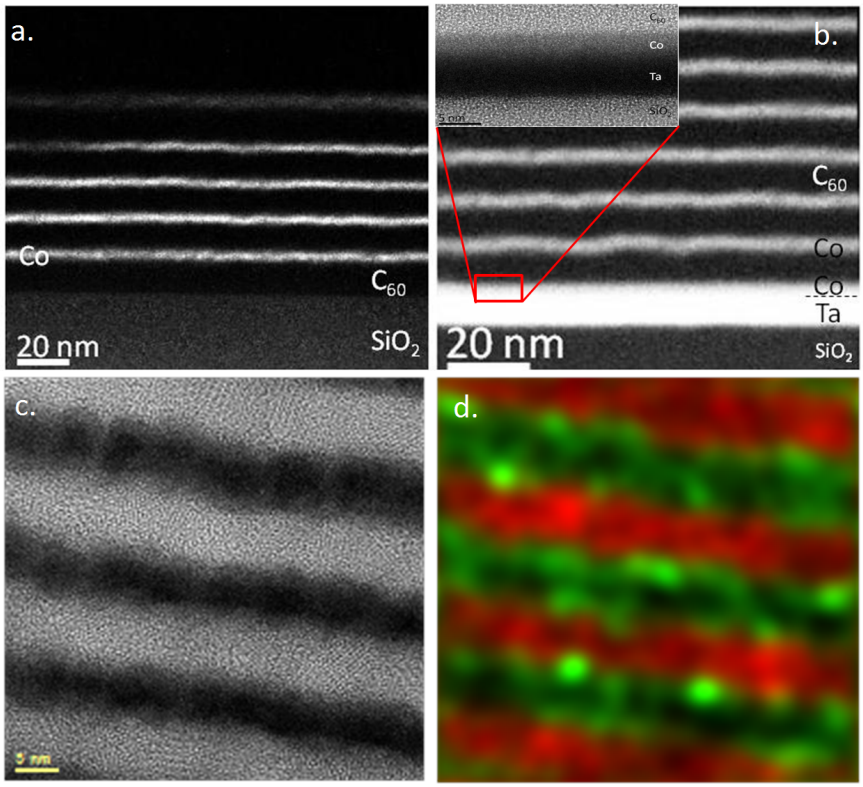

Figure 3.3: a. TEM of CoC_{60} multilayer with no Ta seed and b. an identical multilayer using a Ta seed with the first three layers magnified to show the smooth interfaces obtained by using the seed. TEM c. and Fourier analysis d. of a CoC_{60} multilayer showing the distinction of the layers and polycrystallinity. Cross-sectional TEM performed at University of York by Daniel Gilks and Vlado Lazarov a.-b. and Luis Hueso and David Ciudad at CIC NanoGUNE c.-d. and included in the Supplementary Information of [169]

In super-lattices of Co and C_{60}, Ta seeding produced crystallinity in Co layers above 3 nm, figure 3.3. Co layers deposited on C_{60} showed some crystallinity when over 5 nm thick irrespective of the presence of a Ta seed. C_{60} layers were highly amorphous in all cases as evidenced by the lack of structural peaks in X-Ray diffraction studies. In multilayers of up to ten repeats, there was no evidence of significant intermixing between Co and C60 layers or progressive increase in roughness from layer to layer. This is a vital consideration in hybrid layers and vertical junctions. Control of the 'ill-defined' layer has been a persistent problem in organic spintronic architectures so the apparent resistance of C_{60} to Co intercalation makes these structures ideal for studying interfaces. [102]

Metal layers are deposited from DC sputter guns operating at currents of 50 mA and powers of 12 - 20 W. Argon is used as a sputter gas and is injected at a constant rate of 24 standard cubic centimetres per minute (SCCM) which, balanced against a cryo pump, maintains a constant chamber pressure of 2.3 - 2.5 mTorr. This pressure is chosen both to ensure a sputter rate which is not so slow as to unduly expose the layer to residual oxygen and not so fast as to lack sufficient control over the thickness, and also to ensure the surface tension of metal films in the argon atmosphere promotes complete wetting without introducing stresses into the film as it grows. A 20mT field is applied across the substrate during growth to ensure magnetic anisotropy is uniaxial with an easy axis set at growth.

When fullerenes are sublimated, the key consideration is minimizing interfacial contamination. While UHV conditions slow oxidation, exposing a surface to these conditions for long time periods can still lead to oxidation of a surface. It is, therefore, necessary to minimize the time any surface is exposed. In addition, fullerenes, due to their large cross-section and comparatively low kinetic energy, are more likely to scatter from sputter gas atoms than are metal atoms. If evaporation is performed in the sputter gas the longer flight time of molecules would result in undue oxidation of fullerenes. Thus, during sublimation, the flow of sputter gas is turned off and the delay between the end of the growth of a metal layer and the start of the growth of the fullerene layer is kept below 10 s.

Finally, even if a sample is grown in ideal conditions, both Co and C_{60} will quickly oxidize in atmosphere. It is necessary to protect these materials from atmospheric contamination by covering them with a layer of material which will be inert to atmo-

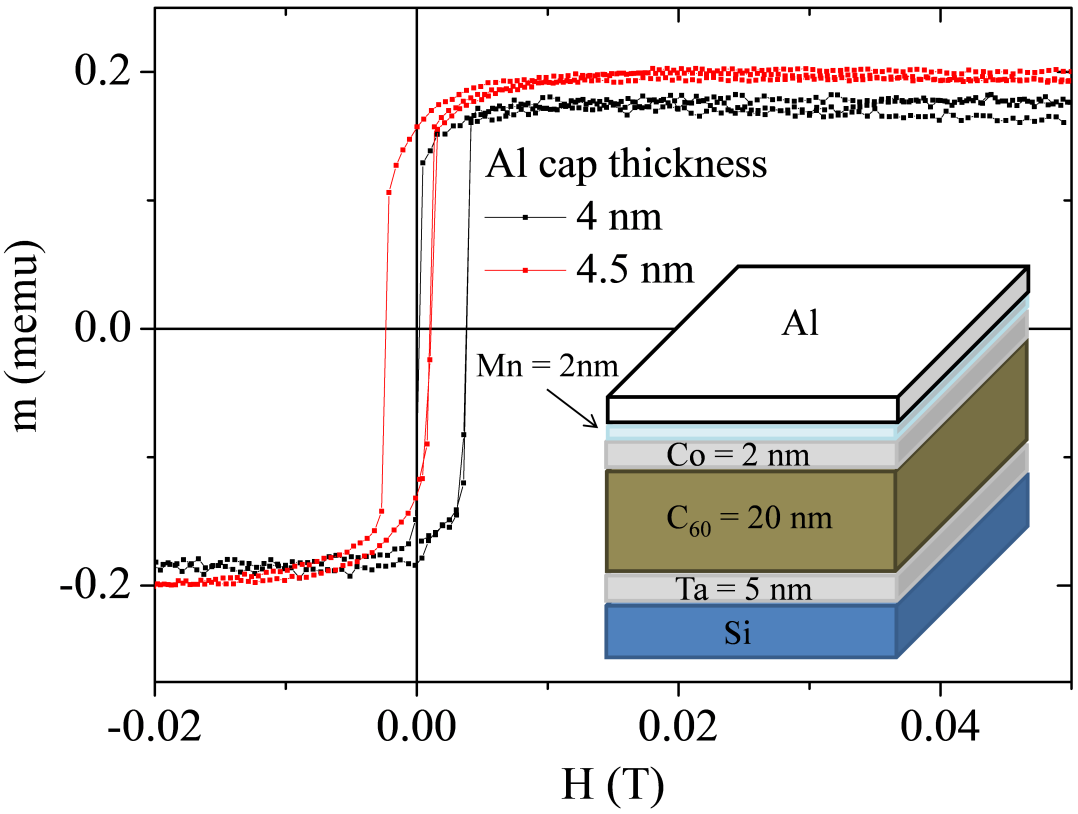

Figure 3.4: Hystersis loops for two examples of samples prepared for XMCD. The sample structure is indicated in the bottom right corner. Samples were cooled from 300 K to 120 K in an applied field of 50 mT. Note that Al caps of less than 4 nm produced hysteresis loops with clear exchange bias due to the penetration of oxygen. Mn, included in these structures as a probe of local magnetism, increases the roughness and oxygen affinity of layers below the Al cap. Samples without this layer were also stable with caps thicker than 4.5 nm.

sphere. Aluminium oxidises in air to form amorphous Al_2O_3 which is inert, low density, insulating and transparent. The penetration of oxygen into aluminium metal becomes stable over a time period of a week due to the expansion of the Al lattice which occurs during oxidation with oxygen penetrating to a maximum depth of $\approx$ 22 Å. [170] This makes aluminium an ideal capping material to protect sensitive structures. However, aluminium metal caps have been observed to deposit poorly on carbon surfaces. Aluminium poorly wets carbon surfaces causing beading during deposition such that aluminium caps which should provide an effective barrier to oxidation become porous. Aluminium layers deposited on graphite are shown to produce 3D clusters up to 25 Å

in diameter and an interfacial region of Al-C bonds up to 18 Å. [171] Diffusion of Al into C_{60} has also been observed. Diffusion of aluminium atoms into interstitial lattice sites in C_{60} occurs during deposition at room temperature for Al layers up to 10 Å and C_{60} layers of 6 ML. [172] This, coupled with the intrinsic roughness of C_{60} layers, makes it hard to get full aluminium coverage to the depth of 22 Å as would be required to prevent oxidation without depositing excessively thick capping layers.

When measuring magnetometry in these samples, the negligible signal an aluminium cap would give makes it preferable to deposit very thick caps for the protection of magnetic layers. In such samples, caps were grown between 15-20 nm.

Caps grown on metal layers deposited onto C_{60} were stable to oxygen above 4.5 nm, figure 3.4. The effectiveness of thin film caps was determined by growing CoC_{60} bilayers and measuring hysteresis loops below 291 K. CoO is antiferromagnetic with a Néel temperature of 291 K. If a crystalline layer of CoO has grown on top of Co at remanence it will create exchange bias.

3.1.5 Junction Deposition

Measurements of the conductivity of C_{60} layers were performed using four point measurements with a crossed electrode configuration, figure 3.5. These are deposited using shadow masks selected in-situ using separable sample and mask mounts which can be detached and moved independently. In junctions, Ta seed layers are not used. This is because, while the shadow masks are kept in place with spring loaded mounts, it is possible for masks to shift slightly when the sample mounts are moved. A conducting seed layer could potentially create a short which shunts current through non-polarized channels.

In transport samples it was necessary that caps were non-conducting. These caps were optimized by determining the maximum thickness at which the resistance of the capping layer was not measureable indicating full oxidation, determined to be 2.5 nm. The deposition of electrodes on top of fullerene layers in these structures prevents diffusion and island formation of Al on C_{60} such that thinner Al caps are stable to oxygen.

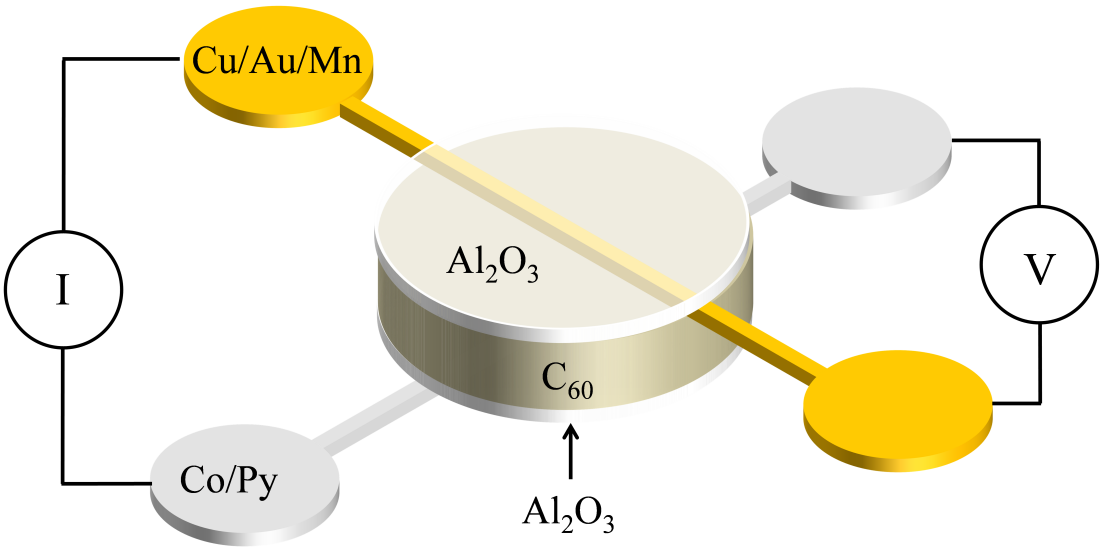

Figure 3.5: Example of a single barrier junction used in this research. The lower electrode is made from a magnetic material to inject spin polarized current. Insulating barriers are used in some junctions to preserve polarization and decouple the ferromagnet from the molecular layer. The top electrodes are deposited from non-magnetic materials and capped with an aluminium layer. Electrodes are 100 μm wide. Measurements are made in a four point configuration.

3.2 Magnetometry

Vibrating Sample Magnetometry relies on simplistic principles of magnetic induction as described in Faraday's law

$$-\frac{d\varphi}{dt} = \varepsilon, \tag{3.1}$$

where φ is the magnetic flux through a given surface and ε is electromotive force. In attempting to quantify the volume magnetization of a given finite object, a simple method for transforming the magnetization into a measureable voltage is to move the object within a coil of wire, creating a current whose magnitude is proportional to the rate at which the object is moved, its size and shape (as described by its demagnetization field) and its magnetization. The flux density, $\mathbf{B}$, within the sample can be expressed as the superposition of the magnetic field, $\mathbf{H}$, and the sample magnetization, $\mathbf{M}$,

$$\mathbf{B} = \mu_0(\mathbf{H} + \mathbf{M}) \tag{3.2}$$

For the special case of a spherical sample, the internal magnetic field, $\mathbf{H}_i$ measured

anywhere inside the sample is given by

$$\mathbf{H}_i = \mathbf{H}_{ext} - N\mathbf{M} \tag{3.3}$$

where $\mathbf{H}_{ext}$ is the external or applied field and N is a demagnetizing factor and depends on the sample shape and orienatation, in this case $N = \frac{1}{3}$. The correction $-N\mathbf{M}$ to the field is known as the demagnetizing field, $\mathbf{H}_d$. Outside the sample, $\mathbf{M} = 0$ and

$$\mathbf{B} = \mu_0\mathbf{H} \tag{3.4}$$

However, the field, $\mathbf{H}$, measured at a point outside the sample volume will comprise contributions from any external magnetic moments, such as the uniform field applied by a solenoid $\mathbf{H}_{app}$, and the magnetic moment of the sample itself, often called the stray field $\mathbf{H}_{stray}$

$$\mathbf{H} = \mathbf{H}_{app} + \mathbf{H}_{stray} \tag{3.5}$$

The relationship between $\mathbf{B}$, $\mathbf{H}$ and $\mathbf{M}$ is shown in figure 3.6. When the sample is vibrated at a known frequency within a loop of wire, the stray field produced by the sample magnetic moment will oscillate producing a current in the coil. Only this component of the total flux density, $\mathbf{B}$, will oscillate at the known frequency and can be isolated from all other surrounding electronics, RF interference, thermal fluctuations or magnetic contamination. Isolation of the sample signal is achieved using a band pass filter/amplifier such as a lock-in amplifier. This outputs the product of the measured signal, V_s, oscillating at a frequency ω_s and some reference signal, V_r oscillating at a known frequency ω_r and with phase φ_s and φ_r respectively

$$V_{Lock\text{–}In} = V_s V_r \sin(\omega_s t + \varphi_s)\sin(\omega_r t + \varphi_r) \tag{3.6}$$

which can be expanded to

$$V_{Lock\text{–}In} = \frac{1}{2}V_r V_s\Big[\cos([\omega_s - \omega_r]t + \varphi_s - \varphi_r) - \cos([\omega_s + \omega_r]t + \Delta\varphi_s + \varphi_r)\Big] \tag{3.7}$$

If the signal is passed through a band pass filter, the signal will be zero except in the case that $\omega_s = \omega_r \pm \delta\omega$ where $\delta\omega$ is the band-width of the filter. Where this is the case, the final signal, V, will be

$$V = \frac{1}{2} V_r V_s \cos(\varphi_s - \varphi_r) \tag{3.8}$$

In VSM measurements, the reference signal is provided by the vibration controller such that any voltage in the induction coils which oscillates at the same frequency will produce a net DC voltage when averaged over a period several times greater than the oscillation period while oscillations at other frequencies will be rejected.

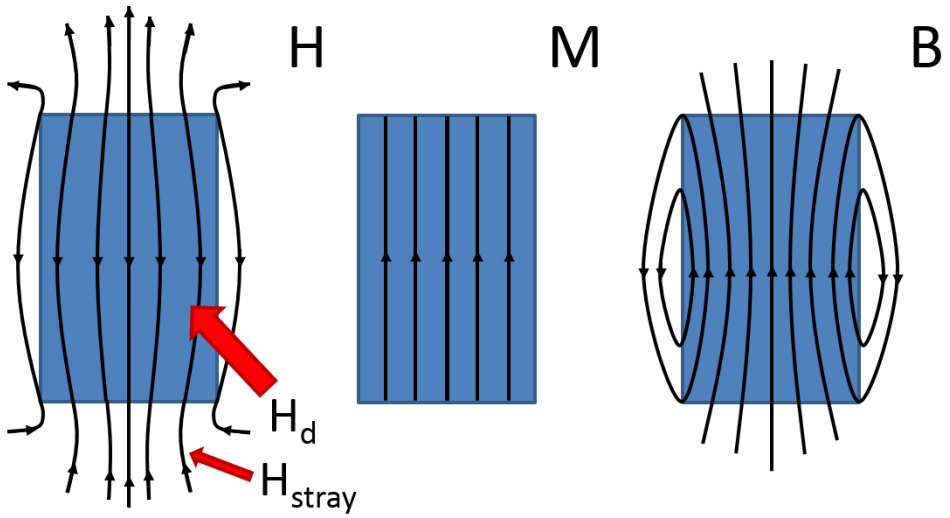

Figure 3.6: Illustration of the relationship between **B**, **M** and **H** following the manner of reference [173]. It is the flux density in the detection coil which is measured by the VSM, $\varphi = \int \int \mathbf{B} \cdot d\mathbf{A}$.

The sample oscillates within the range of the detection coils in a resonant regime. We can see that the rate of change of flux in the detection coils will oscillate at the same frequency. This method allows very small sample moments to be observed even in a relatively noisy environment.

Conventional VSM magnetometry presented in this research was performed using an Oxford Instruments MagLab VSM, shown in figure 3.7, which provides temperature control over a range of 305 to 1.5 K. Temperature control is provided by liquid helium gas, fed into the variable temperature insert (VTI) by a needle valve, and a DC resistance heater located at the base of the VTI. The VTI is maintained at vacuum by a rotary pump, this is vital since the main components of air: water vapour, nitrogen and oxygen, all freeze at the base temperature of the VTI: that is 1.5 K; and could

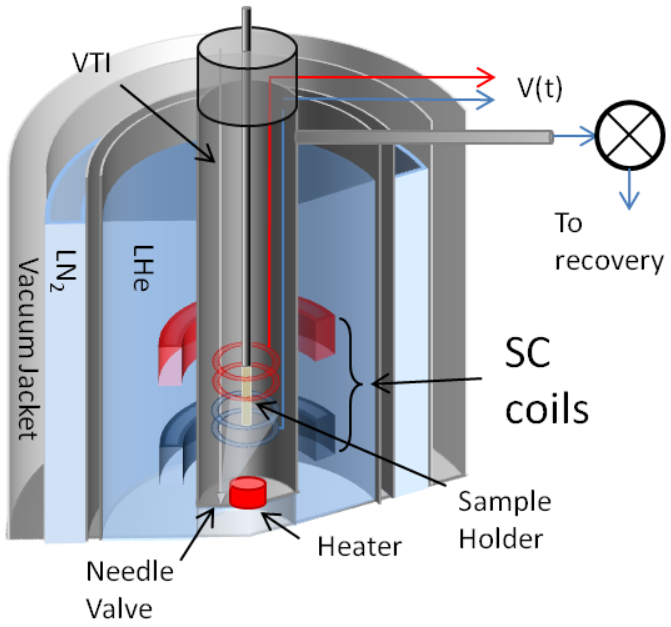

Figure 3.7: Representation of the Oxford Instruments Vibrating Sample Magnetometer used in this research highlighting key components.

block key components. The sample is held on a Polyether etherketone (PEEK) paddle, chosen for its low absorption of water by volume (0.1% in 24 hrs), high tensile strength (90-100 MPa), resistance to thermal degradation and high thermal conductivity (0.25 W/m K) in comparison to other members of the polyaryletherketone (PAEK) family. [174] This paddle is attached to a carbon fibre rod which attaches to the vibration motor outside the VTI. An LN_2 jacket and outer vacuum jacket ensures that rime and extreme thermal gradients cannot interfere with the control assembly at the top of the VTI or cause fast boil off of liquid cryogens.

SQUID magnetometry is performed in an LOT-QuantumDesign MPMS 3 SQUID VSM. The cryogenic system here uses dry cooling with a closed torus surrounding the sample chamber through which helium is fed. This system has a base temperature of 1.8 K and a max temperature of 400 K. Samples are attached to quartz paddles with low temperature varnish and held using a carbon fibre rod. For high temperture measurements, a specialised sample paddle with a built in contact heater can be attached to the sample with a high thermal conductivity adhesive in order to reach temperatures of 1000 K.

3.2.1 AC Susceptibility

While conventional VSM measurements provide time averaged information about the magnetization of a material, it provides limited information about the magnetization dynamics. Magnetization can be described in terms of the magnetic susceptibility, χ

$$M(H) = \chi H, \tag{3.9}$$

or, in the case of ferromagnets, susceptibility can be described as a tensor

$$\chi_{ij}^{d} = \frac{\partial M_i}{\partial H_j}. \tag{3.10}$$

As the applied field is changed, different parts of the hysteresis loop can be accessed and the susceptibility changes. The susceptibility at different points can be measured by creating a small oscillation in the field. The magnetization can then be described as a combination of DC and AC components

$$M = \chi(H_{DC} + H_{AC}sin\omega t). \tag{3.11}$$

The susceptibility, χ, is a complex quantity

$$\chi(\omega, H) = \chi'(\omega, H) - i\chi''(\omega, H). \tag{3.12}$$

The AC magnetization can then be described by a phase, φ

$$M_{AC} = \chi(\omega, H)H_{AC}sin\omega t(cos\varphi - isin\varphi). \tag{3.13}$$

This phase change describes the lag between the change in the AC field and the AC magnetization and characterises dissipation or viscosity of the magnetic system. Thus, at low frequency, the AC susceptibility closely follows the DC susceptibility. At higher frequencies, changes in the phase can be detected by measuring relative magnitudes of the real and imaginary components of the AC magnetization.

For low DC fields, the susceptibility of some disordered systems such as spin glasses shows a first order transition at the freezing temperature, T_f, defined as the temperature at which different spin configurations are no longer thermally degenerate. This transition is similar to the Néel temperature of antiferromagnets and occurs due to the 'freezing' of moments into a random, disordered state. An example of such as transition

is shown in figure 3.8. This shows the glass transition in a CuMn spin glass. It is important to note that higher DC fields lead to progressive broadening of the susceptibility peak, discussed in detail in reference [175].

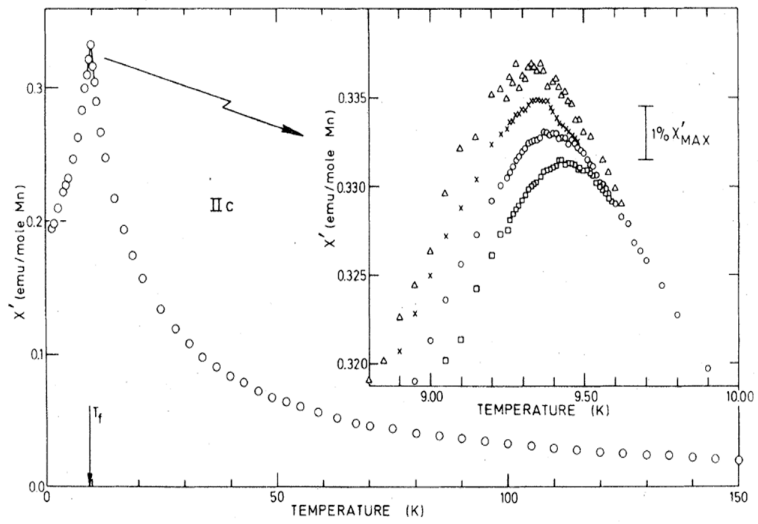

Figure 3.8: Example of the real part of the AC susceptibility in a CuMn alloy. The freezing of the spins below the glass transition temperature can be observed as a cusp at the transition temperature. The inset shows the dependence of the transition on the AC field frequency: squares, 1.33 kHz; circles 234 Hz; crosses, 10.4 Hz; triangles, 2.6 Hz. Figure from [176].

3.3 Raman Spectroscopy and Photo-Luminescence

Raman spectroscopy in this research is performed using a Horiba LabRam HR800 Raman Microscope. A schematic is shown in figure 3.9. This makes three laser frequencies available for illuminating samples on a motorized Marzhauser stage. The beam is filtered and collimated to occlude any contaminant light and create a sufficiently narrow beam to map sample features. An optical microscope is used to focus the beam. The reflected beam is passed through a beam splitter such that the reflected portion can be isolated and sent to a diffraction grating. A CCD detector mounted on a worm motor can scan across the diffraction pattern and isolate components of the spectrum. The resolution at the nth maximum is determined by the chromatic resolving power, $\Delta\lambda$, of the grating:

$$nN = \frac{\lambda}{\Delta\lambda} \tag{3.14}$$

Where N is the line density of the grating. Two gratings can be used with line densities of 600 or 1800. As mentioned in section 3.1.2, photo-assisted degradation and oxidation is a significant problem for molecular devices. During Raman spectroscopy, it is possible for the higher energy lasers, blue and green, to cause what is often termed photo-bleaching. That is the degradation of fluorescence due to chemical changes in the sample induced by photons.

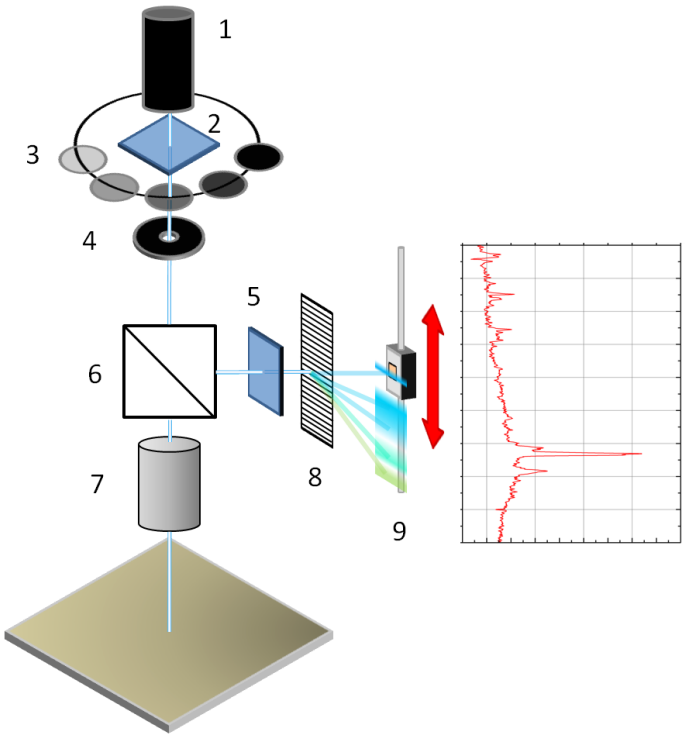

Figure 3.9: Diagram of the workings of the Horiba Raman microscope. The laser (1) is directed through a chromatic filter (2) to remove contaminant light and through one of a set of intensity filters mounted on a rotating plate (3). The hole (4) acts to collimate the light before it reaches the sample. After this, the beam passes through a beam splitter (6) and a microscope (7). Light reflected from the sample is directed toward a diffraction grating (8) through a band pass filter (5) which removes contaminant light. The resultant pattern is analysed by a 1024 detector CCD (9).

The wavelength dependence of the diffraction pattern is accommodated by calibrating the CCD worm motor using a standard silicon sample. Silicon produces a well

defined first order Raman peak at 520 cm^{-1} at 300 K. Because the peak is narrow and changes little as a function of impurity concentration, it is an ideal standard for calibration. [177] Using this and the zero-shift Rayleigh peak, it is possible to convert the CCD motor position to a wavenumber/wavelength/energy axis as per requirement.

While it is not possible to prevent photo-induced degradation entirely without using a lower energy laser, it is possible to significantly reduce the proportion of molecules destroyed by this process. Firstly, an automated shutter ensures that, during measurement, the beam is only incident on the sample while data is being recorded. This eliminates unnecessary flux which might damage the sample while the CCD is moving or data is being stitched. Second, a selectable filter is placed between the beam and the sample which can reduce the beam flux by several orders of magnitude. Optimal results are usually obtained for intensities of 0.1 mW. Finally, the choice of capping material can protect the molecules not only from atmospheric stress but also from evaporation, by decreasing the exposed surface area, and reduce the overall intensity of the beam. However, it is important to note that long exposure times are just as injurious to sample quality as high intensities with the additional factor that if the sample has poor thermal conductivity, heat from the beam will build up in small region of the sample and lead to small areas of evaporation or chemical changes such as oxidation. It is, therefore, always necessary to balance low intensity against short exposure times. Raman scattering is a relatively rare event with $\approx 10^{-7}$ % of photons undergoing Stokes scattering. [152]

One way to significantly improve the signal to noise ratio in Raman samples is to ensure the molecular layer is deposited on top of a conductor. This is because, when conducting surfaces are not perfectly smooth, the scattering of photons with free electrons in the conductor surface can produce surface plasmons which oscillate at the same frequency as the incident light. These plasmons amplify the electric field in a region approximately equal to the photon wavelength near the conductor surface increasing the magnitude of the molecular dipole oscillations described in equation 2.108. This process is known as surface enhanced Raman scattering. [178] These considerations provide important information about how to construct samples for Raman.

While the Horiba microscope has mostly been used for Raman spectroscopy, the detector makes no distinction between photon scattering and other photon sources or scattering processes in the sample. This can be problematic when unexpected high

energy events lead to noise spikes or when contaminant light leads to distortion of the Raman spectrum, but it also allows the instrument to be used to investigate luminescent phenomena without changing any aspect of the set up. Any of the lasers can be used to create an excitation provided they produce photons of high enough energy and a UV light can also be installed to provide illumination where none of the lasers suffice. Because the focal optics for the detector act on the reflected portion of the light independent of the incident portion, there is no need to use a focused or collimated light source to perform photoluminescence experiments.

3.4 I1011 and BOREAS Beamlines

The XMCD technique is employed in this research to probe the magnetic and electronic structures of hybridized composites, specifically CoC60. XMCD data was recorded at the BL29-BOREAS beamline in the ALBA facility, Barcelona, and the I1011 beamline at the MAXII facility, Lund. Both systems are similarly structured according to the diagram in figure 3.10. X-Rays are produced using an undulator, a set of alternating magnetic poles mounted on rails which can be moved relative to one another to produce a helical field vector. Synchrotron electrons entering the undulator undergo a spiral motion, producing X-Rays with a polarization vector determined by the arrangement of the magnets in the undulator. Since the emitted photons conserve angular momentum, left or right handed spirals can be used to generate opposite circular polarization while changing the gap between the rails in the undulator can change the radius of the spiral and, therefore, the peak energy output. Moving the rails such that the electrons undergo a wave like motion with no spiral can produce linearly polarized light. [137]

Undulator radiation is monchromated to narrow the spectrum and allow high resolution spectroscopy. Monochromation is achieved using a variable line spacing (VLS) reflection grating which disperses the spectrum without loss of polarization. [180] The desired energy can then be selected using a focusing mirror. In both the BOREAS and I1011 beamlines, three gratings are available, optimized for different energy ranges. The monochromated beam can then be focused and collimated using X-Ray mirrors into a beam of ≈ 0.1 mm (BOREAS) or 0.2×0.8 mm (I1011) before being directed into the endstation. At BOREAS, the HECTOR endstation is used for all data presented in this research. At I1011, the UHV in-situ endstation is used. In both systems, the experimental chamber is evacuated using a cryo-pump to 10^{-10} mbar in order to

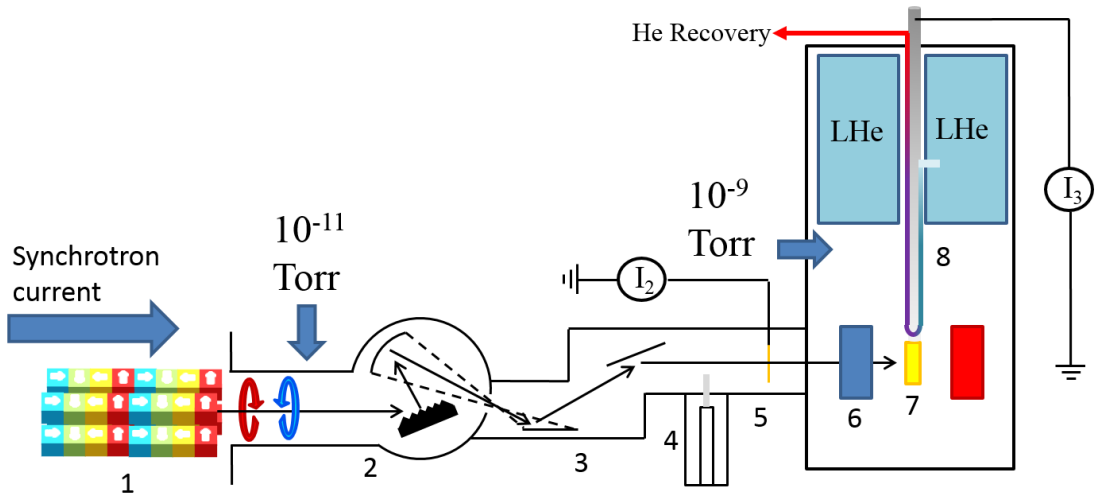

Figure 3.10: Simplified schematic of the BOREAS beamline [179]. Circularly polarized X-Rays are generated at the undulator (1) and directed into the monochromator array (2). The monochromated X-Rays are then collimated and focused using an array of mirrors (3). An attenuation grating can be inserted (4) to control the beam intensity. The beam is then passed through a gold calibration grating (5) which records a baseline TEY for the beam intensity, I_2, before being directed into the sample chamber. Coils are arranged to apply a field parallel to the beam direction (6) with the sample mounted on a conducting plate (7) which is attached to an external ammeter to detect the sample TEY, I_3. The plate can be cooled by the cold finger cryostat (8) with liquid helium contained in a built in reservoir. The entire endstation is mounted on a scaffold with 3-deminsional mobility afforded by worm motors. The chamber moves independent of the sample mount to allow the beam to scan across the sample.

minimize interaction of the beam with bodies other than the sample and reduce sample decay. Samples are observed in TEY by mounting them on a conducting paddle with a connection to ground and a picoammeter to measure the flow of free electrons from the sample surface. Because Si, C_{60} and Al_2O_3 all have high resistivities, a drain contact is made to improve conductivity between the sample surface and the paddle. In both cases, samples are introduced to the experimental chamber via a loadlock to protect the vacuum of the beamline. In the BOREAS beamline, a field is applied from a set of fixed coils in the plane of the beam. Fields can be applied up to 6 T. In the I1011 beamline, hollow core rotating coils can apply fields up to 0.6 T in almost any direction limited only by those positions at which the coils obscure the beam path. [181] In the BOREAS beamline, a cold finger cryostat can be used to control the sample

temperature with a base of 2 K.

3.4.1 Transport XMCD

Observing the effects of charge and spin polarized transport on the NEXAFS of C_{60} required current channels to be effectively separated. Since the drain current is on the order of pico amps and the current driven in junctions is on the order of nano amps, there is a danger that the channels could be mixed with source current escaping to ground or drain current escaping to source meter ground.

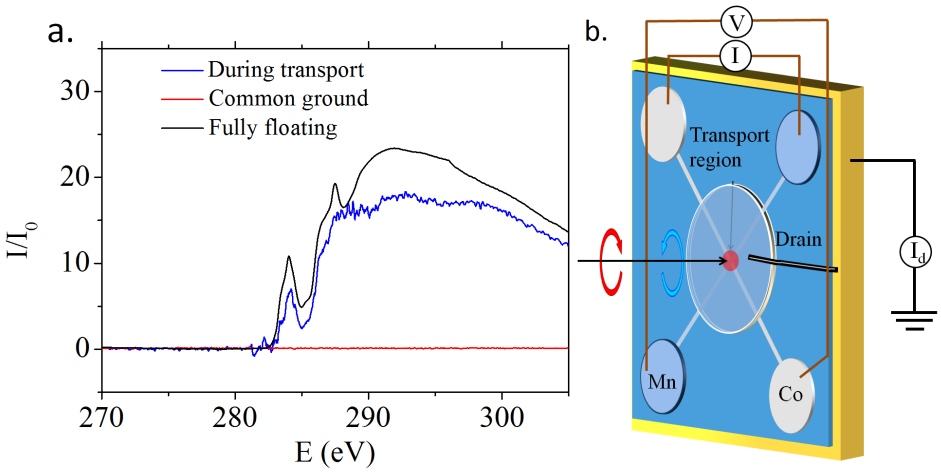

Figure 3.11: a. Comparison of the signal from a C_{60} layer with different contacts showing the difference in the signal to noise ratio. The blue curve is K-edge when the sample is set up as shown on the right. The black is when all contacts are removed save the drain contact. The red is when I and V on the diagram are connected to a common ground. b. Schematic of the junction on the sample plate. The insulating SiO_2 substrate separates the gold plate from the junction. A drain contact to the C_{60} layer is made using a piece of carbon tape covered with colloidal silver. The carbon tape is separated from the probed region by 1 mm to ensure it does not contaminate the C_{60} K-edge. The junction centre is located by triangulating the Mn and Co edges.

The drain contact for junctions is made directly to the central C_{60} island with a strip of conducting carbon tape coated with colloidal silver. This provides an adequately conducting channel for the drain current to escape. Current and voltage measurement contacts must be left floating while the edge is measured, else the drain current escapes into the instrument ground. Noise from the aerial effect of floating contacts increases

noise in all measurements. It is thus necessary to completely disconnect all contacts where possible, see figure 3.11.

3.5 CRISP and POLREF Beamlines

PNR experiments were performed at the ISIS pulsed muon and neutron facility using the CRISP and POLREF beamlines whose basic layout is illustrated is figure 3.12. Both beamlines use a variable aperture chopper disc to define a wavelength band of 0.5 to 6.5 Å for CRISP and 1-15 Å for PORLEF. An electromagnet can provide fields up to 0.8 T and a cryostat can be used to control sample temperature down to a base temperature of 2 K. The sample is angled by means of worm motors in the case of CRISP or by angling a bench containing the sample, collimation slits and analyser all at once in the case of POLREF. Neutrons are detected by a He^3 detector in which He^3 captures incident neutrons and undergoes decay into a hydrogen and tritium nucleus, which are easily detected by their charge.

As detailed in section 2.8, much of the physics of XRR can be applied to neutron reflectivity. This means that we can scan Δq by varying the angle of the detector with respect to the sample surface as in equation 2.86. However, unlike XRR, there is no way to monochromate the neutron beam in PNR. Neutrons are produced via spallation of a target with a high energy proton beam [183] and have a broad range of energies meaning that, for any given detector angle, neutrons of a broad range of q values can be detected. To solve this problem, PNR utilises time of flight detection.

Firstly, the highest and lowest energy neutrons are removed using a chopper built from a nimonic alloy of Ni, Cr and Co which is chosen for its high tensile strength and melting point, allowing it to be used for fast rotating components. The chopper is essentially a spinning disc with holes cut into it which rotates in phase with the proton beam pulse. The holes allow a range of neutron velocities to be selected from the spallation event since fast neutrons will arrive at the chopper earlier than slow neutrons. It also allows the gamma flash, a burst of gamma rays which occurs as a result of spallation, to be blocked and prevented from interfering with the measurement. The selected range of neutron velocities is called a frame. The frame spectrum is monitored by a beam monitor placed just after the chopper, marked in figure 3.12 as 4. A second monitor, 6, is located before the sample which is used to normalise the intensity of the reflectivity spectrum since the flux of different neutron velocities is not equal. Once the

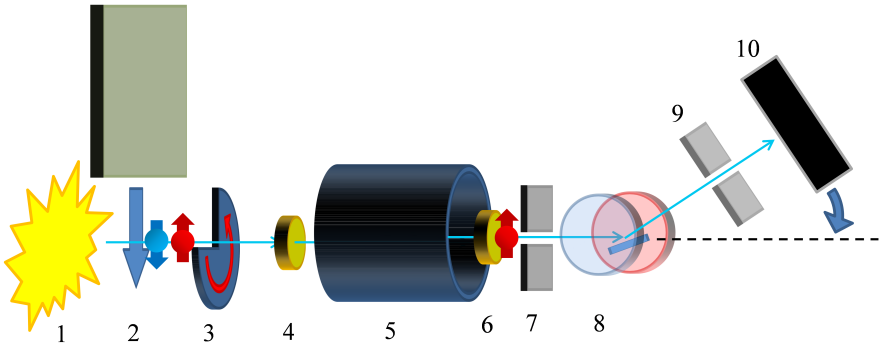

Figure 3.12: Simplified diagram of the POLREF beamline. [182] 1. The impact of a proton beam on a spallation source produces neutrons. This beam can be blocked by a Gd shutter (1) allowing the beam to be "turned off" by the user. A nimonic chopper (2) spins with identical period to the beam pulse enabling it to isolate specific parts of the spallation pulse called frames. After the chopper, a beam monitor (4) detects the passage of neutrons providing the start time for calculating the time of flight. Neutrons then pass through a spin flipper (5), comprising a magnet array and set of polarising mirrors which isolate a particular polarisation of neutrons. The neutrons are then detected a second time by another monitor (6) to calculate their intial momentum. The beam is then collimated by a slit (7) and directed toward the sample which sits between the coils of an electromagnet (8) and can be mounted into a cryostat for low temperature measurements. From the sample onward the entire apparatus is mounted on a motorized stage allowing it to be raised at a well defined angle to the beam path. The reflected beam is passed through a second set of slits (9) and finally impacts the detector (10). The angle of reflection and the time of flight recorded by monitors 4 and 6 is used to calculate the change in Q_z.

velocities of the incident neutrons is established, the time taken for them to traverse the beamline is known and neutrons of different q can be distinguished by the time they arrive at the detector. Thus, for a given angle, the reflectivity spectrum can be built up by measuring the amplitudes by which neutrons of various q are scattered from the sample. [184]

The beam width of the POLREF beamline is $\approx$ 6 by 3 cm meaning samples with a large surface area are required to achieve high counts. The flux of POLREF is 107 $cm^{-2}s^{-1}$ allowing a sample with dimensions 2 by 2 cm to be measured over a time period of 1.5 hrs.

Reflectivity data is fit using the GenX optical matrix package created by M Björk. [185] Spectra are simultaneously fit for spin up to spin up scattering amplitude and spin

down to spin down. Interlayer variation means that fitting the entire superlattice is infeasible in GenX due to the high possible number of degrees of freedom. To minimize degrees of freedom in the final fit, individual layer thickness and interfacial roughness are fit using XRR spectra. VSM measurements are used to determine the volume magnetization normalized for the entire film. In the final fit, the remaining free parameters are the magnetic moment per atom in each layer (while the total magnetization was fixed by VSM) and the density and interdiffusion roughness of the interfacial layers. The magnetic moment per atom is free to vary but the sum total of all moments in the film are tied to the volume magnetization. The fit optimization is performed using the inbuilt differential evolution tools in GenX and identified by a figure of merit calculated from the logarithmic sum of the residuals:

$$\mathrm{FOM} = \frac{1}{\mathrm{N}-1}\sum_{\mathrm{i}} |\log(\mathrm{M_i}) - \log(\mathrm{S_i})| \tag{3.15}$$

Where N is the total number of points, $\mathrm{M_i}$ is the measured value and $\mathrm{S_i}$ the simulated value. Once a minimum was established, the region of conformational space was explored with various valid combinations of magnetic moment per C_{60} cage to determine whether the minima observed were local or general. The fits generated a magnetic profile of each sample, revealing how magnetic moment varied layer to layer. These profiles could then be graphically represented to show the sample structures. The imaginary part of the neutron scattering cross-section, which describes magnetic components, is used to plot the mixing of magnetic layers and to weight the moment per atom determined by the best fit.

3.6 Low Temperature and Conventional Transport

Transport measurements are made using both constant current (Keithley 6221) and constant voltage (Keithley 2400) sources using a crossed electrode configuration in a four point measurement. Room temperature measurements are performed with spring-loaded pins as contact points. Low temperature transport is performed using ultra-pure aluminium contacts bonded to electrode pads using a wedge bonder. Both contact methods penetrate the sample film.

Low temperature transport is performed using an Oxford Instruments He^4 wet cryostat. The system uses a variable temperature insert (VTI) cooled through the

expansion of helium gas from a liquid helium reservoir to a base temperature of 1.5 K. The temperature can be controlled using a resistance heater and an automated needle valve to restrict helium gas flow. The temperature is monitored with a CERNOX thermometer inserted into the sample holder which enabled the sample temperature to be recorded with a resolution of 0.1 K during cooling. It is important to note that there will be a difference in the actual and recorded sample temperature due to the finite separation between Cernox and sample. This will depend on cooling rate and time. The cooling rate used in this research is 4 K/min and results in a 3 K difference between heating and cooling curves. The sample head is attached to a low temperature hollow stick which carries the electrical channels. The total resistance of the channels and Al wire contacts was $\approx$ 220 Ω. Thermal EMF was eliminated by measuring 8 points, four positive and four negative, for each resistance versus temperature data point. The frequency of this oscillation was less than 10 Hz. The voltage applied for each data point in section 5.4 was 10 $\pm$ 0.002 mV.

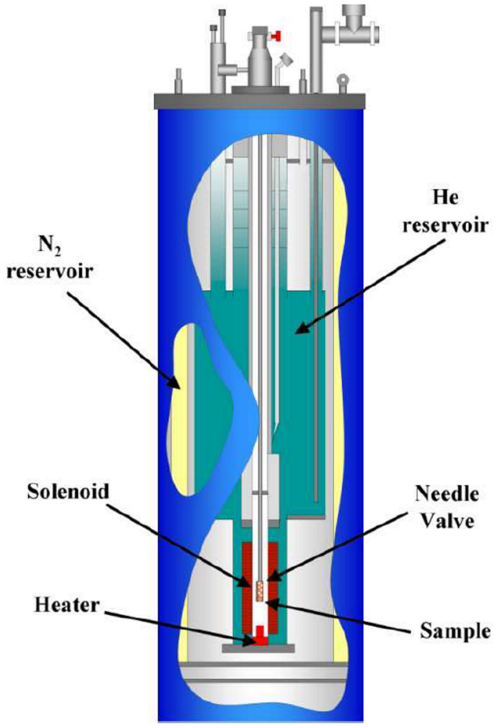

Figure 3.13: Illustration of the Oxford instruments cryostat used in this research reproduced from [186].

Chapter 4

Interfacial Hybridization in Cobalt C_{60} Composites

4.1 Introduction

As discussed in section 2.4, the overlap of metallic and molecular orbitals at material interfaces can lead to significant changes in molecular band-structure. However, a fairly underexplored notion is that this effect might be reciprocal and the transfer of charge, changes in interfacial potential and alignment of fermi levels might alter the characteristics of a metal. There are a few key factors which should limit this effect. First, metals cannot support internal potentials and when an external potential exists screening is far greater in metals than molecular solids. Where a point charge is inserted into a metal, the Coulomb potential will be damped over the Thomas-Fermi screening length, k_0

$$k_0^2 = 4\pi e^2 N(E_F), \tag{4.1}$$

where e is the electron charge and $N(E_F)$ is the density of states at the Fermi level. In a dielectric medium, the permittivity affects how far electrostatic interactions persist. In C_{60} the relative permittivity is around 5 allowing the effects of charges to propagate small polarizations of molecules over several nanometers. [187] Locally, the band structure of molecules is strongly coupled to the molecular structure such that when bonds are formed or when dipolar interactions cause distortions of molecular symmetry, the band structure is altered through Jahn-Teller distortions or changes to electron affinity. [188] When molecules bond to a metal surface, the changes to molecular band structure and alignment of Fermi-levels implicit in the description of a spinterface in section 2.4 is stabilized by the formation of an interfacial dipole. This surface dipole is screened in both metal and molecule. [189] One might expect from the different screening processes in metal and molecule that the impact of this interfacial dipole on the electronic structure of the metal would be minimal since screening in the metal will occur over a few Å while polarizations may propagate several nanometers in molecules. However, when the surface of a hybridized metal/molecule interface is probed, significant changes in the density of states can be observed. [190]

In a metal-molecule contact, the alignment of Fermi levels might change the contact resistance and, therefore, influence conductance of molecular devices. In magnet-molecule contacts, changes in the interfacial DOS of a ferromagnetic material could significantly alter the magnetic properties of a device. The effect of such interfaces has been studied extensively from the perspective of magnetic interface states in molecules,

particularly the study of MR in LSMO/Alq_3 by Barraud et al [17] and the use of such interfaces as spin filters by Raman et al [34], but not from the perspective of the changes in the magnetic properties of the metal. The following chapter discusses the characterisation of magnet-molecule interfaces with a focus on the properties of the ferromagnet: including magnetic moment, net magnetization and anisotropy.

4.2 Magnetometry of Ferromagnet/C_{60} Bilayers

Bilayers were deposited using the joint sublimation/DC sputtering deposition chamber described in section 3.1.1 and 3.1.2. The relative coupling strengths of the three transition metal ferromagnets were studied by comparing 5 nm films deposited using identical methods in UHV conditions onto silicon dioxide substrates with a seed layer comprising 3 nm of Ta. This ensured that the interfaces of each sample type were as consistent as possible.

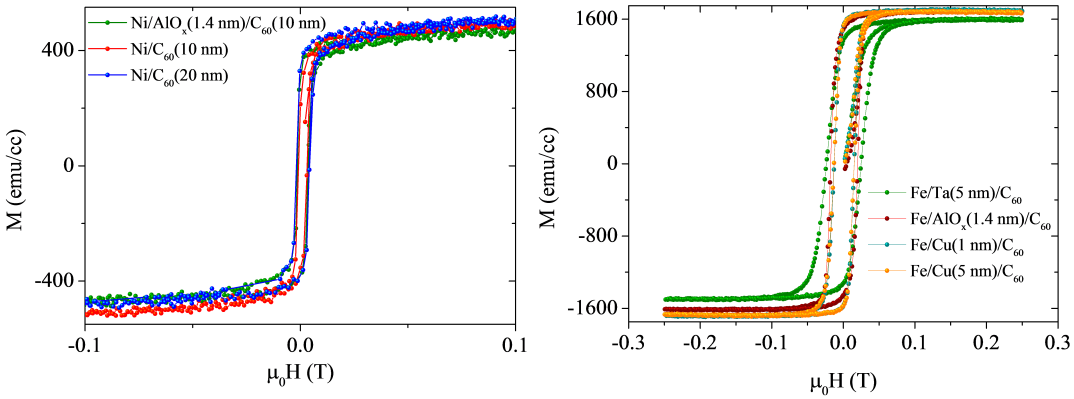

Figure 4.1: a. Hysteresis loops of NiC_{60} showing the lack of a trend in magnetization with C_{60} thickness. b. Various spacer layers tested in FeC_{60} bilayers. Ta was found to cause damage to the metal layer and cause erroneous magnetization reduction. Alumina was an effective spacer but was excluded due to the danger of overoxidation during the reactive sputtering process used to deposit the oxide from a metallic target. Cu was found to provide the best spacer with bulk values for the magnetization of iron achieved when the spacer was 5 nm thick.

For each metal, a set of samples were used to build up increasingly thick C_{60} layers to observe changes in magnetization (figure 4.2). Control samples were fabricated by de-coupling the metal and molecule using a conducting spacer layer. A layer of copper sputtered between the metal and molecule layers screens any interfacial interactions.

Bulk properties are recovered when the spacer layer is extended to 5 nm (figure 4.1).

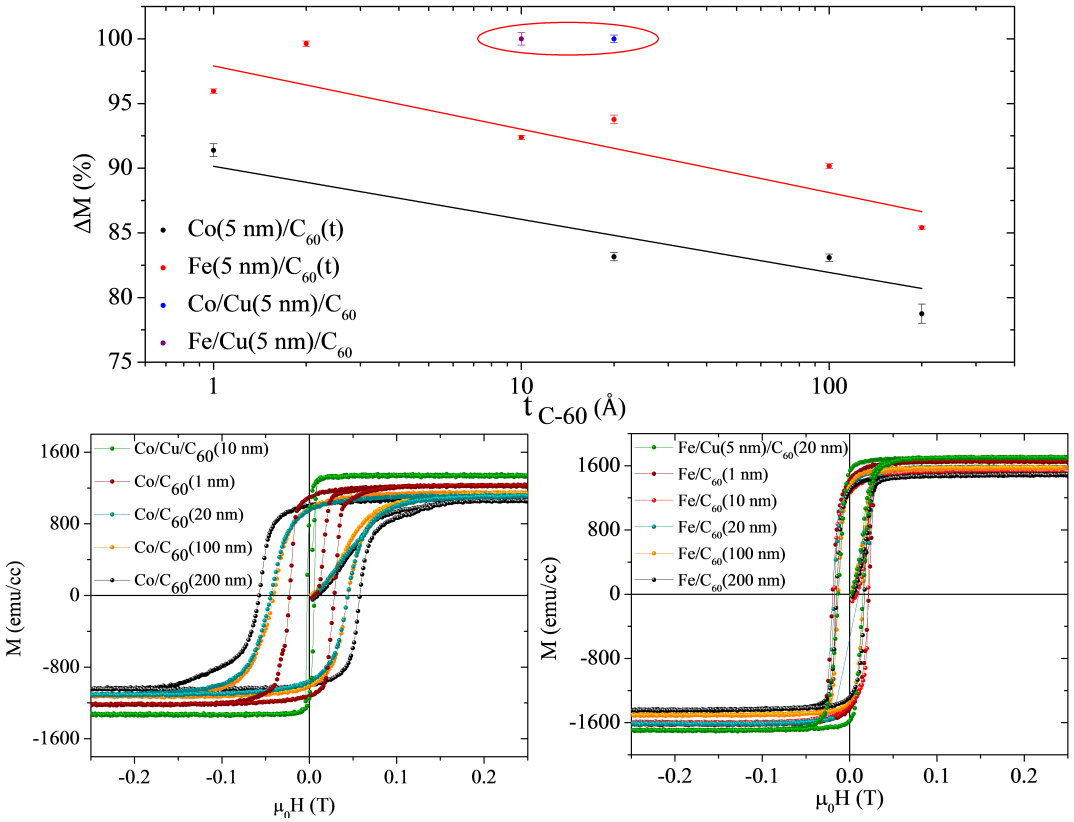

Figure 4.2: a. Percentage reduction of volume magnetization of 5 nm layers of Co and Fe as a function of C_{60} thickness for Co (black) and Fe (red). The reduction in magnetization is significantly greater for all thicknesses of C_{60} in Co than Fe. Both metals recover bulk values, of 1440 and 1708 emu/cc respectively, when a Cu spacer layer of 5 nm is placed between the magnetic material and the C_{60} layer. Hysteresis loops of Co (b.) and Fe (c.), taken at 100 K using a VSM, show a significant increase in the coercivity of Co layers as the C_{60} layer is built up which does not occur for Fe. In both materials, magnetization reduction shows an inverse exponential dependence on C_{60} layer thickness.

The formation of the hybrid interface was shown to reduce the volume magnetization of both Co and Fe. In Ni, no correlation was observed. As thicker C_{60} layers were deposited, a greater reduction in magnetization was observed. The dependence of magnetization reduction on C_{60} thickness was such that additional C_{60} had less impact on magnetization the further it was from the interface. However, measureable changes could still be seen for C_{60} layers 100-200 nm thick indicating that the interaction

between molecules and metal is not limited to the first few monolayers as was suspected. Of Co and Fe, Co showed the most pronounced reduction in magnetization with a maximum observed change of 21% corresponding to a total change of 270 ± 10 emu/cc for a 200 nm C_{60} layer.

As discussed in theoretical models of spin hybridization induced polarized states (SHIPS), the different population of spin split bands in ferromagnets leads to asymmetric broadening of molecular orbitals. [17] The transfer of majority spin electrons into the SHIPS would result in a preferential depopulation of the majority spin band in the ferromagnet and an overall reduction of the total magnetic moment of the film. The differences in the magnetization reduction in Fe, Co and Ni may be due to differences in density of states or s-d mixing in these three metals. Further DFT simulation would be needed to complete a model of interfacial coupling in all three metals.

4.3 XAS and XMCD of Co/C_{60} Interfaces

As discussed in section 2.4, hybridization of molecular and metallic orbitals at interfaces is expected to alter the band structure of the molecule, broadening and shifting the degenerate orbitals to match Fermi levels at the interface. Additionally, Boyen et. al. indicate that changes in metal DOS can be expected due to the formation of interfacial dipoles at metal molecule contacts. [190] In order to probe for changes in DOS, spin population and hybridization, XAS and XMCD were used to analyse bilayer structures of Co/C_{60}. As discussed in section 2.9, TEY measured XAS is a surface sensitive technique due to the limited escape depth of Auger electrons from a film. It is also an element specific technique which can isolate specific transitions in a spectrum by monochromating the probing X-Ray beam and tuning it to resonant core transitions. It is, therefore, possible for XAS to analyse the L transition for surface layers of a Co film and the K-transition of C_{60} in a single sample.

XMCD allows the population and polarization of these bands to be probed. The sum rules for transition metals allow the absolute moment per atom of the surface layers of Co to be determined by fitting the L-2 and L-3 transitions in order to observe any drop in moment associated with the loss of majority spins to the molecules. [139] Such specific information cannot be gained from the carbon edge in C_{60} due to the lack of a spin-orbit split core level and weaker spin-orbit coupling. However, the curvature of the C_{60} molecule means it has higher spin-orbit coupling than other carbon allotropes.

[136] Dichroism in the K-edge is indicative of orbital moment. [132] Since C_{60} is usually diamagnetic, any dichroism in the π edges at zero field indicates some induced polarization of the π-orbitals even though a magnetic moment per atom cannot be calculated. Examples of the use of carbon XMCD can be found in [134] where orbital moment in amorphous carbon films with magnetism induced by an Fe film is studied using XMCD or in [132] where π electron ferromagnetism is observed using XMCD. In addition, XAS is a probe of available states as core electrons can only be excited into unoccupied states in higher energy bands. Observing the magnitude of different peaks in the C K-edge provides insight into how these bands are occupied and therefore how much charge is present in the molecule or how the band structure had been altered by interaction with the metal.

Bilayer structures were prepared on thermally oxidized silicon substrates with Ta seed layers and Al caps. Co layers were deposited at 10 nm to maximize cobalt signal. Since XAS probes only upper layers, the additional thickness with respect to bilayers used in magnetometry would not have a significant effect since the surface will dominate the signal. The auger escape depth in cobalt is expected to be approx 1.5 nm. [191] Capping layers in these structures were kept to 2.5 nm so as not to excessively reduce electron yield from the lower layers by exceeding escape depth. While a cap of this thickness could be stable, [171] there is an increased risk that oxygen could penetrate the sample. Oxygen penetration could be monitored at the Co edge. CoO has well characterised double peaks due to the formation of bonds involving d electrons. [192]

Two systems with different C_{60} layer thicknesses were observed in order to probe different layers, figure 4.3. A discontinuous, 5 nm layer was used to allow the interfacial molecular layers to be observed. A 20 nm layer was used to measure a continuous C_{60} layer with thickness far greater than the expected 3 ML escape depth for TEY in order to observe C_{60} far from the interface. [145]

The first peak at 284.5 eV corresponds to the LUMO. [130] In the thin layer, the next peak to appear is at 288 eV, close to the ionization potential at 289 eV. This may either be the LUMO +3 or a localised σ exciton similar to that observed at the onset of the σ resonance in other carbon allotropes. [126] [131] The broad features between 290 and 310 eV are the σ-orbital resonances. [125] In the thicker C_{60} layer, the LUMO +1 and +2 peaks are also clearly visible at 286 eV and 286.8 eV respectively while in the thinner layer these peaks are not visible. Reductions of peak intensity in carbon

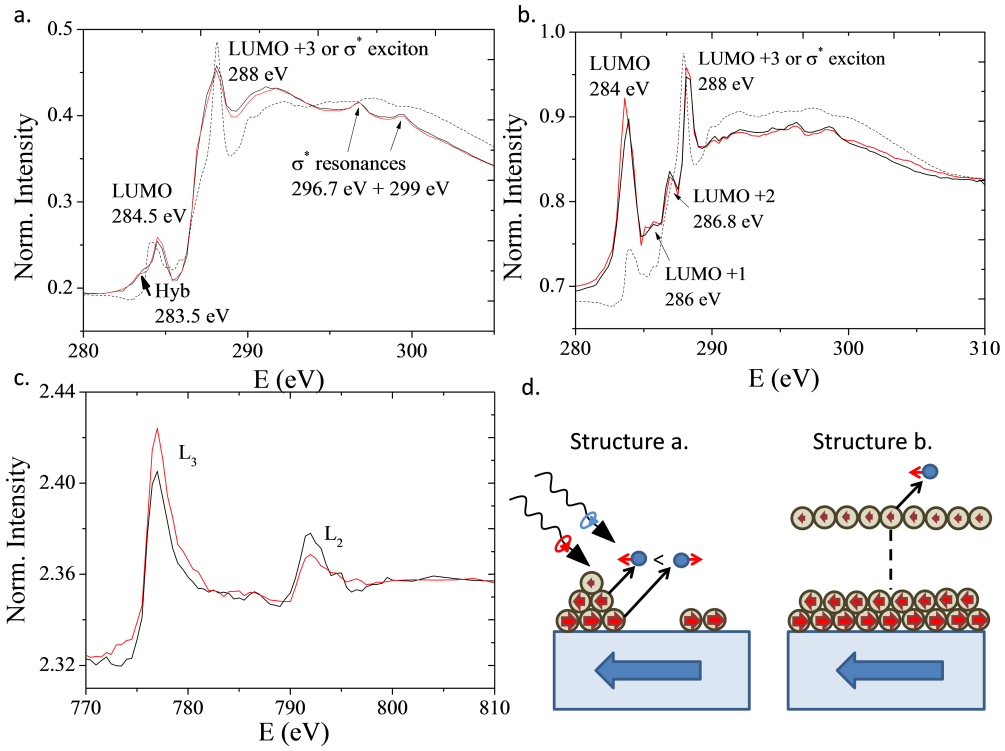

Figure 4.3: a. XAS at the C-edge for a 5 nm discontinuous C_{60} layer deposited on cobalt for opposite polarizations. b. The C-edge for a 20 nm C_{60} layer on cobalt. The dotted line is the spectrum obtained from a 99.99% pure C_{60} film deposited on silicon oxide. c. The XAS at the Co edge for a 10 nm Co film with 5 nm of C_{60} deposited over it. While some signal was lost due to attenuation in the carbon layer, the polarization of the L-2 and L-3 peaks is clearly visible. d. Schematic of the samples and emission processes expected for XMCD measurement in the samples shown in a. and b. The Alumina caps are omitted for simplicity.

NEXAFS are observed for ultrathin C_{60} films on Au, though to a lesser extent. Changes in the recombination process of the core-hole exciton such as increase in participator events involving the metal may play a role in supressing these peaks. [97] The key feature which emerges is the shoulder of the LUMO derived peak. This has previously been traced to partially occupied hybridized interface states forming just below the C_{60} LUMO. The peak emerges due to the shift of the core-level binding energy due to charge transfer from the metal into the molecular LUMO. [193] [194] [36] The $\frac{m_l}{m_s}$ ratio for the cobalt layer calculated from the sum rules for transition metals, equation 2.101, is 0.41 as compared to the expected bulk value of 0.099. [139] Without precise

knowledge of the occupancy of the 3d band, which is infeasible in this case due to the expected changes induced by hybridization, it is not possible to determine whether this change is due to alterations in the band structure due to hybridization or a change in spin polarization due to majority spin transfer. What is clear, however, is that the magnetic moment of the surface cobalt is altered by the presence of C_{60} and the absence of splitting of the L-2 and L-3 peaks precludes the involvement of oxide species.

Density Functional Theory simulations performed at the University of Liverpool by Gilberto Teobaldi provide further support for a spinterface interpretation of these effects. [169] Simulations for four C_{60} cages relaxing onto 2ML of cobalt indicate interfacial hybridization would result in metallic hybrid states appearing below the LUMO with a definite polarization. Distortion of the 3d band in cobalt and the transfer of majority spin electrons is predicted to cause a total loss of 3.7 μ_B for every C_{60} cage added. The moment in C_{60} cages is expected to oscillate but is anti-ferromagnetically coupled closest to the interface with a maximum moment of 0.02 μ_B per atom or 1.2 μ_B per cage. The full details of these calculations can be found in the supplementary information of [169].

4.4 PNR of Co/C_{60} Multiplayers

While XMCD provides element specific information about magnetic moments, it provides limited depth resolution. The clear difference between XMCD signals for different C_{60} thicknesses indicates some variation in magnetic moment in fullerenes at different proximity to the interface but does little to determine length scales and does not allow calculations of moment per atom. In addition, observations in magnetometry that the reduction in magnetic moment of a ferromagnet is inversely related to total fullerene layer thickness indicating that there is (reduced) interaction between metal and molecule over a tens of nm. Polarized Neutron Reflectivity, section 2.8, allows the mapping of this magnetic profile.

The large penetration depth of neutrons, owed in part to their lack of charge, means they can easily be used to probe films many hundreds of nanometers thick while the de Broglie wavelength of slow neutrons, ≈ 0.5 - 15 Å, makes them able to explore a material with sub-nanometer resolution. Coherent scattering of neutrons produces interference patterns to which the formalism of XRR described in section 2.7 can be applied. The different reflectivity spectra obtained when scattering neutrons of opposite polarization

from a magnetic material provide detailed information about the magnetic structure.

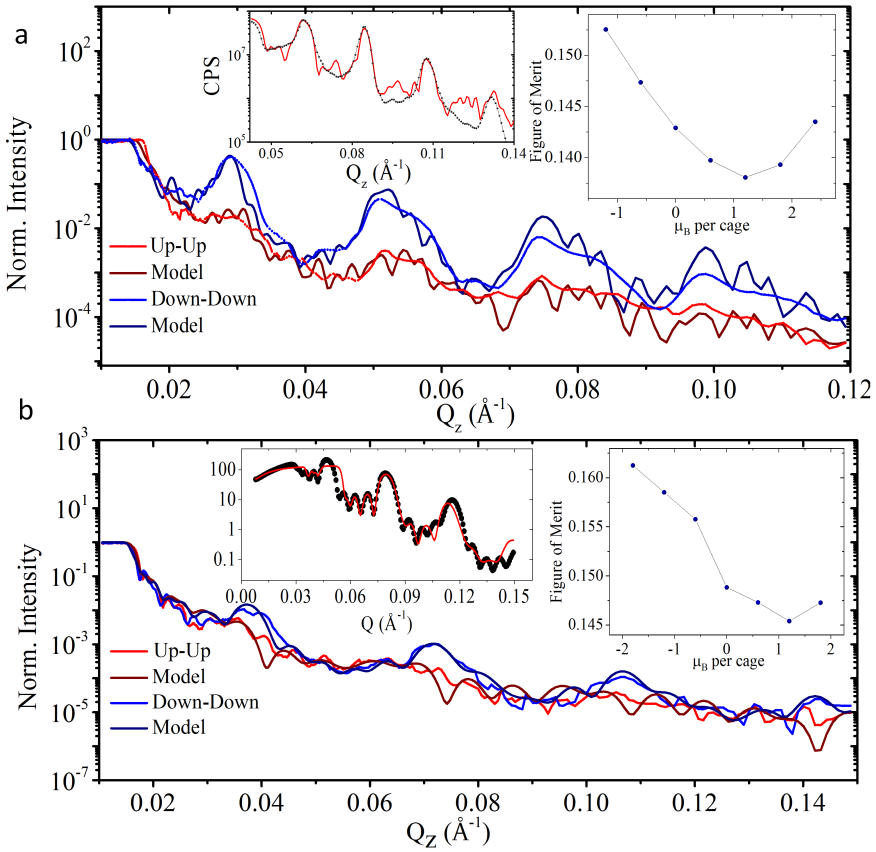

Figure 4.4: a. PNR data and fits obtained using structural information from XRR (inset) and magnetic information from VSM. Free parameters were the μ_B per atom in each layer and the interdiffusion of the interfaces. The inset shows the landscape of the FOM for various plausible values of μ_B per C_{60} cage indicating the optimum is achieved at 1.2 μ_B per cage. b. Fit for the 5 layer sample with insets showing the FOM landscape and XRR data. While exploring the FOM landscape, the moment of other layers is adjusted in parallel by tying the total magnetization to the VSM value of 137 emu/cc (for all layers including C_{60} ensuring all simulations have physical significance.

Determining the expected changes in reflectivity for a magnetic material is not trivial but there are some broad predictions which can be made. The critical edge and Kiessig fringes will provide information about the material averaged density and magnetization, the signal decay will provide information about interface roughness and the length scale of magnetic distributions, Bragg peaks will be dependent on the

interlayer correlation of the multilayer. To probe the magnetic distribution within the film, maximum contrast between polarizations must be achieved in Bragg peaks. This requires the development of a superlattice with sufficiently high correlation between repeats that the reflectivity at the maxima in the modified Bragg equation, 2.90, is close to unity.

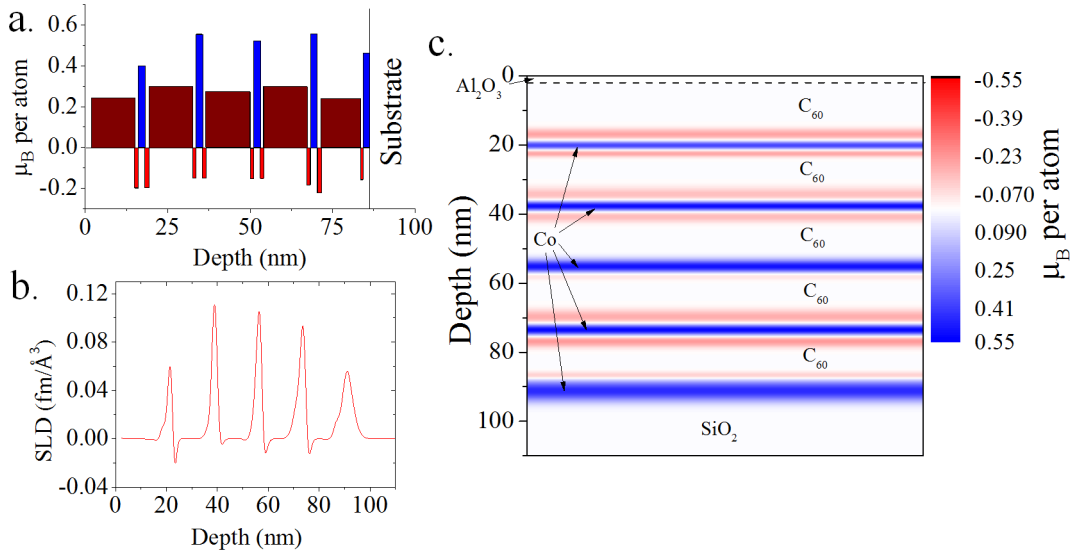

Figure 4.5: Colour plot (c.) showing the magnetic profile of the five layer sample. The interface between each successive layer is modelled as a Gaussian fitted using the imaginary component of the depth dependent SLD (b.) used in the best fit. The SLD is isolated and normalised for each layer then multiplied by the moment for that layer to model intermixing. Clearly evident are the anti-ferromagnetically coupled interfacial regions which flank all but one of the Cobalt layers. The C_{60} layers each have a positive magnetic moment which is too small to be seen here but has a significant effect on the FOM. In the pre-correction profile (a.), the C_{60} layer moments are multiplied by ten to show the variations between layers.

Multilayer structures of Co/C_{60} were developed using the same method as the bi-layers discussed in section 4.2. The thicknesses of layers were guided by reflectivity simulations using the Python GenX package [185] to provide maximum contrast in Bragg peaks when interfacial moments were changed. These simulations were performed by Dr Oscar Cespedes and indicated an optimum structure of Ta(5 nm)/[Co(4 nm)/C_{60} (21 nm)] × 10/Al(3 nm). A second structure with thinner C_{60} and Co layers was also chosen in order to determine what effect total layer thickness would have on the magnetic profile. This structure was optimised with five layers: Ta(5 nm)/[Co(2

nm)/C_{60} (13 nm)] x 5/Al (3 nm). These superlattices were grown on 2 x 2 cm silicon dioxide substrates. The larger surface area is designed to maximize the sample signal since the beam width is 3 x 6 cm with a total flux of 107 $cm^{-2}s^{-1}$. Reflectivity is displayed in figure 4.4.

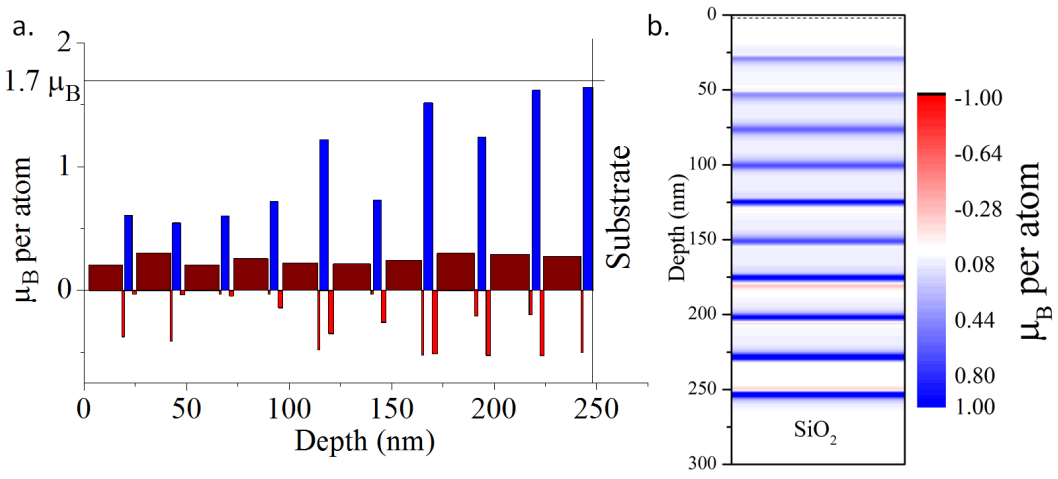

Figure 4.6: a. Profile of the ten layer sample used showing the absolute moment per atom in each layer from the best fit. Note that the moment per atom of all layers is significantly lower on average for the top five layers. As in figure 4.5, C_{60} moments per atom are multiplied by ten in order to show the differences between layers. b. Colour map of the SLD corrected moment per atom in the ten layer multi-layer. Due to their increased thickness, Cobalt layers have magnetic properties closer to bulk while interfacial magnetism is comparatively lower. However, reversal of the interfacial magnetization is still observable in some interfaces.

These structures were measured in the POLREF beamline at the ISIS pulsed muon and neutron facility discussed in section 3.5. Samples were measured at saturation, determined using VSM, with applied fields of 150 mT in the ten repeat structure and 50 mT in the five repeat structure and fitted using the GenX package. [185] Depth profiles are shown in figures 4.5 and 4.6. In each fit, there is clear evidence that an interfacial region forms between Co and C_{60} with a moment below that of cobalt but anti-ferromagnetically coupled. In the ten layer structure, upper layers show smaller overall moments in all layers and in the SLD corrected profile only a few interfaces show a clear negative polarisation. This correlates with the idea that interface quality is key to strong coupling and large charge transfer, though roughness and disorder is shown to have additional effects discussed in section 4.5.

In the five layer structure, negative polarisation at all but one possible Co/C_{60} interfaces is supported by the fits. Both simulations agree that the average moment per atom in C_{60} cages is 1.2 ± 0.3 μ_B. The fit is more strongly supported in five layers than ten due to better correlation between layers where compound roughness is less significant. In all cases, the moment per atom in cobalt layers was below the bulk value of 1.7 μ_B supporting the conclusion of XMCD and DFT that there is a net transfer of majority spin electrons from the ferromagnet to fullerenes, supressing magnetization in the cobalt and inducing magnetism in coupled fullerenes. Due to limitations in DFT simulation of bulk molecular solids, the cause of the changes in polarisation between interfacial and bulk fullerenes is as yet unknown. However, since exchange interactions in C_{60} could not be strong enough to allow intrinsic ferromagnetism, it is expected that as interfacial coupling tends to zero away from the interface, charged fullerenes in the bulk will behave as paramagnets. C_{60} charge transfer composites such as N@C_{60} show paramagnetism similar to polarised atoms. [195]

4.5 Exchange Asymmetry and Dynamics of Co/C_{60} Interfaces

DOS, orbital symmetry and band structure are also related to exchange and anisotropy in ferromagnets as discussed in section 2.1. The strength of exchange interactions can be observed quite efficiently by measuring the temperature dependence of magnetization and deriving the Curie temperature which is proportional to the exchange integral

$$T_C = \frac{2zJ_{ij}j(j+1)}{3k_B}, \tag{4.2}$$

where T_C is the Curie temperature, z the distance between magnetic centres, J_{ij} the exchange integral, j the angular momentum quantum number and k_B the Boltzmann constant. [44] At high temperature, ferromagnets such as Co, Ni and Fe should obey the Curie-Bloch relation

$$\frac{M(T)}{M(0)} = \left(1 - \left(\frac{T}{T_c}\right)^{\alpha}\right)^{\beta}, \tag{4.3}$$

where M(T) is the saturation magnetization at temperature T, M(0) is the expected magnetization at 0 K, T_c is the Curie temperature and α and β are material specific

critical exponents.

A piece of the ten layer sample measured in section 4.4 was measured in a SQUID-VSM over a temperature range of 10 - 375 K in applied fields of 150 mT, above saturation at 300 K. The multilayers show an unexpected variation in magnetization with temperature at low temperatures (figure 4.7 left inset). Fitting a Curie-Bloch law above 173 K indicates the Curie temperature is supressed to 936 K from 1400 K (figure 4.7 left). By demagnetizing the multilayer and cooling in zero field, it is possible to observe a blocked state below 173 K (figure 4.7 right). Applying small fields, below saturation, multiple transitions can be observed as the multilayer is heated and when cooling, deviation from a Bloch's law is more significant with a suppression of magnetization occurring as the sample is cooled below the first transition at 205 K and increasing again below the last transition at 19.5 K. As shown in section 4.4, these multilayers are not consistent from layer to layer.

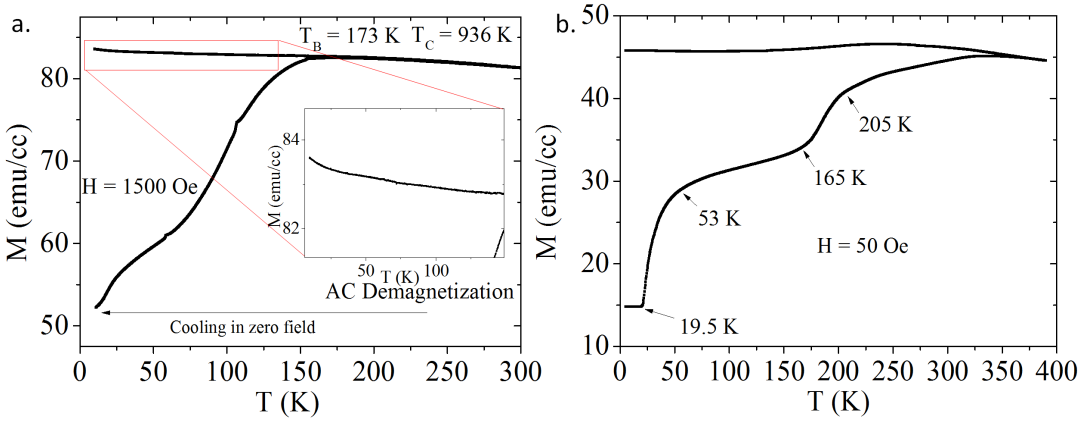

Figure 4.7: a. Zero-field cooled/field cooled measurement of a ten layer Co/C_{60} multilayer showing the blocked state below 173 K. The inset shows the upturn in magnetisation at low temperatures. b. Zero-field/field cooled measurement of the same sample using a 50 Oe applied field. Inflection points are picked out. A drop in magnetization is evident in the field cooled branch below 250 K.

To observe interfaces with greater consistency, trilayers were deposited with the structure Co(x nm)/C_{60} (18 nm)/Co(x nm). Zero-field/field cooled measurements were performed in order to observe the changes which occur in the transition temperatures, figure 4.8. In each case, the sample is demagnetized at 300 K before cooling in zero field. However, it was observed that even very small residual fields resulted in a significant

magnetization at low temperatures. Multiple transitions are still observable in samples with thicknesses above 0.8 nm. The transition temperature, T_r is taken as the first inflection point after the magnetization reversal as a clear inflection was observable in all but the thickest sample. The field applied was consistently 50 ± 1 Oe. The transition temperature decreases as the reciprocal of cobalt layer thickness once the layers become continuous after 0.5 nm (figure 4.8 left).

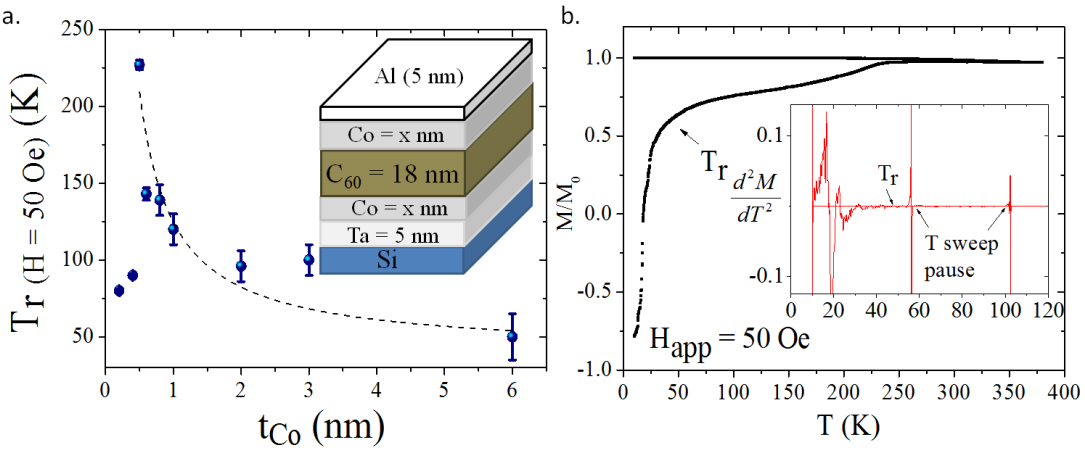

Figure 4.8: a. Dependence of transition temperature T_r on cobalt layer thickness fit to $\frac{T_0}{t}$. Below 0.5 nm, deviation from the fit can be explained by discontinuity of the cobalt film. The inset shows an illustration of the sample construction. b. Example ZFC/FC measured in a trilayer with 6 nm cobalt layers. The starting negative magnetization is due to a small residual field left after the demagnetization process. Demagnetization is performed by placing the sample in an oscillating field with a decaying magnitude. The transition temperature is picked out. The inset shows the second derivative of the ZFC branch. The transition is located by taking the second derivative of the zero-field branch and locating the first point after the transition at which the change in gradient is zero within a five point average.

Below this thickness, deviation from the fit can be traced to total film thickness being below the c-axis spacing of hcp cobalt. The appearance of additional transitions above 0.8 nm may be correlated to the film thickness exceeding the intrinsic roughness of C_{60} at 0.7 nm allowing the top cobalt layer to become continuous. By 20 nm, the cobalt films display near bulk behaviour. This behaviour is characteristic of interfacial effects like exchange bias where coupling of interfacial spin planes becomes less and less significant as ferromagnetic layers become thicker and bulk ferromagnetic properties begin to dominate behaviour as in equation 2.60 for exchange bias field or in the surface

term of the Stoner-Wohlfarth model, equation 2.30. [196]

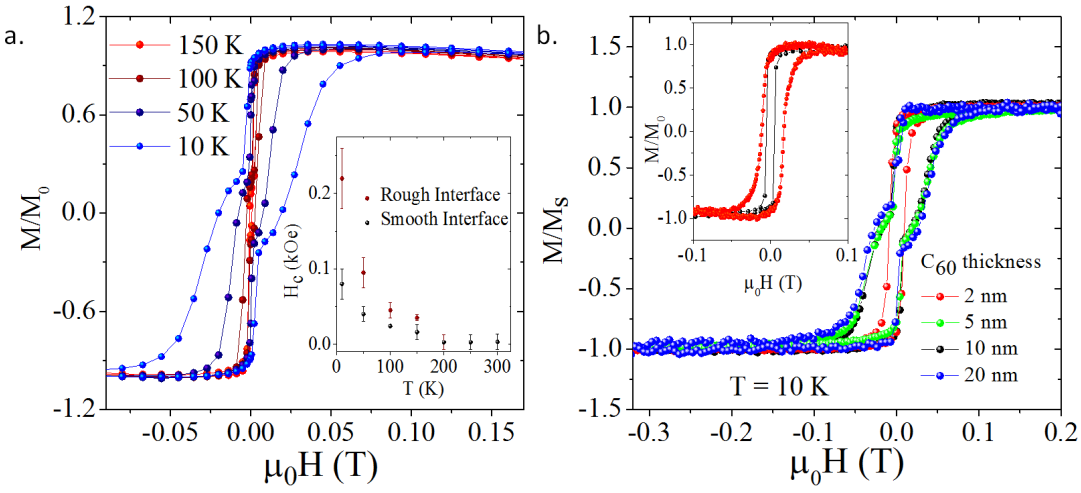

Figure 4.9: a. Hysteresis loops at various temperatures for a trilayer of Co(1.5 nm)/C_{60} (10 nm)/Co(1.5 nm) showing the emergence of two distinct loops at low temperatures. The two different coercivities can be traced to the different interfacial roughness for the upper and lower cobalt layers. The inset shows the coercivity for the isolated loops showing that they diverge after 200 K. b. Shows hysteresis loops at 10 K for trilayers of Co(1.5 nm)/C_{60} (x nm)/Co(1.5 nm). As the C_{60} layer is built up, the two magnetic layers decouple and show different coercivities, confirming this behaviour is related to interface morphology. The inset shows two hysteresis loops from bilayers with only a lower cobalt layer (black) [Co(0.8 nm)/C_{60} (20 nm)] or upper layer (red) [C_{60} (60 nm)/Co (2 nm)] showing that it is the upper interface which has the higher coercivity.

Further information on the exchange and anisotropy changes caused by interfacial hybridization can be obtained by observing the temperature dependence of hysteresis loops. Observations of trilayers show that, below 150 K, two distinct loops with different coercivity become apparent (figure 4.9 left). These correspond to the upper and lower layers where the different interfacial roughness created by depositing cobalt directly onto silicon dioxide or onto a C_{60} layer alters the anisotropy. This is confirmed by varying the thickness of the separating C_{60} layer. Building it up from discontinuity, one can see that the two loops emerge only when the C_{60} layer becomes continuous around 5 nm and the loops change little after this point (figure 4.9 right). While many organic materials might allow significant diffusion of sputtered metal, [102], the TEM characterisation of sputtered samples showed very small interdiffusion between

molecular and metal layers in C_{60}/Co, figure 3.3. Isolating individual layers confirms that the upper layers produce the higher coercivity (figure 4.9 right inset). This may simply be a result of increased surface roughness due to the C_{60} film since roughness has been observed to increase coercivity in thin Co films. [197] Increased coercivity is also observed in exchange biased systems as a result of interfacial frustration and disorder. [198] [38]

Indeed, hysteresis loops obtained from bilayers with only the upper layer also show asymmetry in the hysteresis loop when cooled in fields in excess of 1 T (figure 4.10). Asymmetry emerges below the T_r predicted from figure 4.8 and is larger in samples with thinner cobalt layers indicating this behaviour is also a result of interfacial hybridization. However, very thin samples, below 4 nm, do not show measurable asymmetry at 10 K, figure 4.11a. While asymmetry is retained when cooling fields are removed, it can be altered by applying large fields thereafter. In a trilayer sample, shown in figure 4.10d, the measured asymmetry is reduced after cycling the field to $\pm$ 2 T. This is very similar to the training effects observed in exchange biased bilayers which can be attributed to irreversible reorganisation at disordered interfaces, particularly the creation of anti-ferromagnetic domain walls. [199]

Out of plane measurements show that bilayers with cobalt layers below 4 nm have significant out of plane components of their anisotropy (figure 4.11b). This is confirmed by measuring the impact of C_{60} layers on exchange bias. Exchange bias relies on the formation of uniaxial anisotropy through interfacial coupling. An iridium manganese layer is deposited onto a cobalt layer which has been saturated in an applied field. Iridium manganese was chosen as it has been studied extensively in exchange biased bilayers produced using the same deposition system as used in this work. [200] The coupling between uncompensated spin planes in the anti-ferromagnetic iridium manganese alloy with the surface spins in the cobalt layer forms a uniaxial anisotropy which lies in the film plane. Higher interfacial roughness or strong out of plane anisotropy would be orthogonal to this in-plane symmetry breaking and no bias field or a reduced bias field would result. Measurements of these exchange bias bilayers deposited on top of 20 nm C_{60} layers show that cobalt layers below 4 nm deviate from the expected dependence on ferromagnet layer thickness (figure 4.11c).

Together, these results indicate that the interfacial hybridization produces some uniaxial anisotropy. This occurs after cooling cobalt/C_{60} interfaces of sufficient interfacial

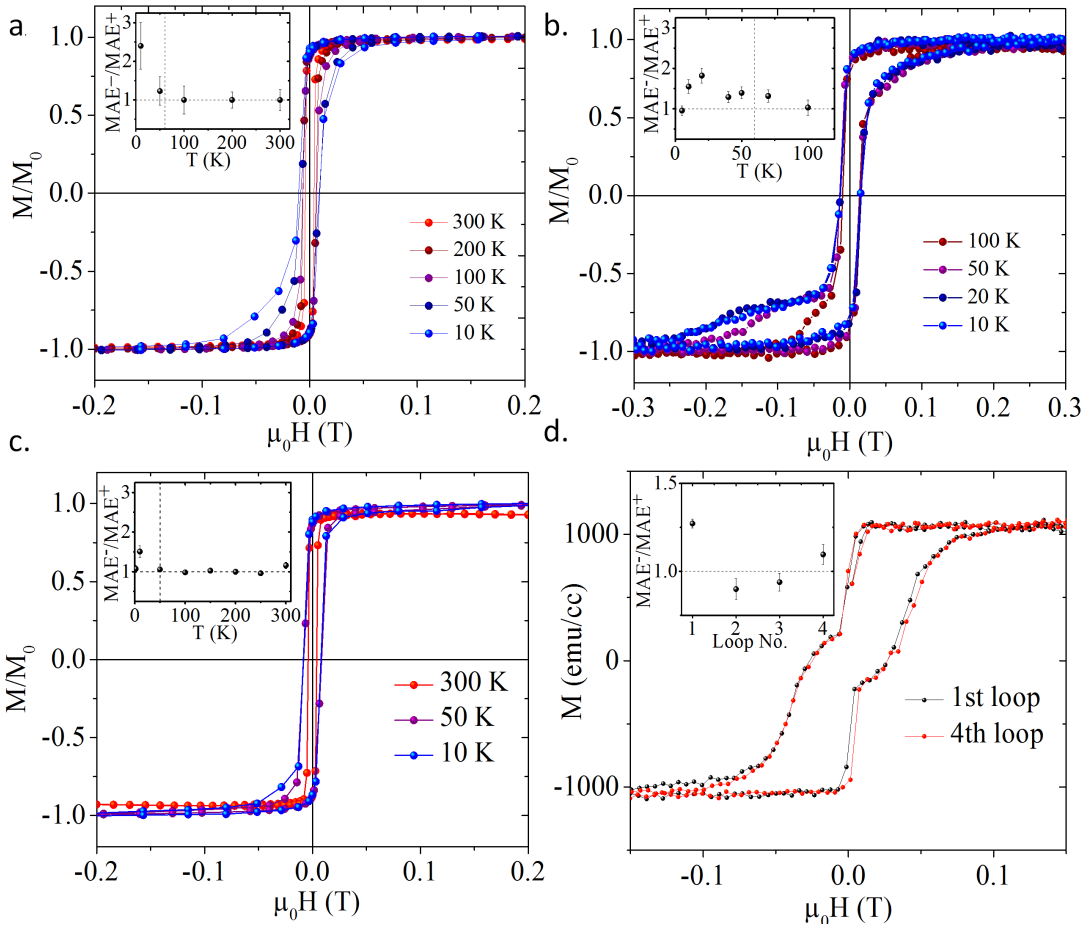

Figure 4.10: Hysteresis loops at various temperatures for bilayers of C_{60} (60 nm)/Co(x nm)/Al(10 nm) where x is 4 nm (a.) 5 nm (b.) and 8 nm (c.) cooled in 2 T. Asymmetry is evident at low temperatures when these structures are cooled in fields greater than 1 T. Insets show the asymmetry ratio calculated by integrating the positive and negative branches of the hysteresis loop. On each inset, the expected T_r from figure 4.8. Asymmetry is strongest in the thinnest layer and decreases as the cobalt layer becomes thicker. c. shows a trilayer structure of Co(1.5 nm)/C_{60} (60 nm)/Co(1.5 nm)/Al(10 nm) which has been cooled in 2 T to 10 K. A small asymmetry is evident which is marked in the inset. However, as the hysteresis loop is cycled to ± 300 mT, the asymmetry is reduced until it reaches unity.

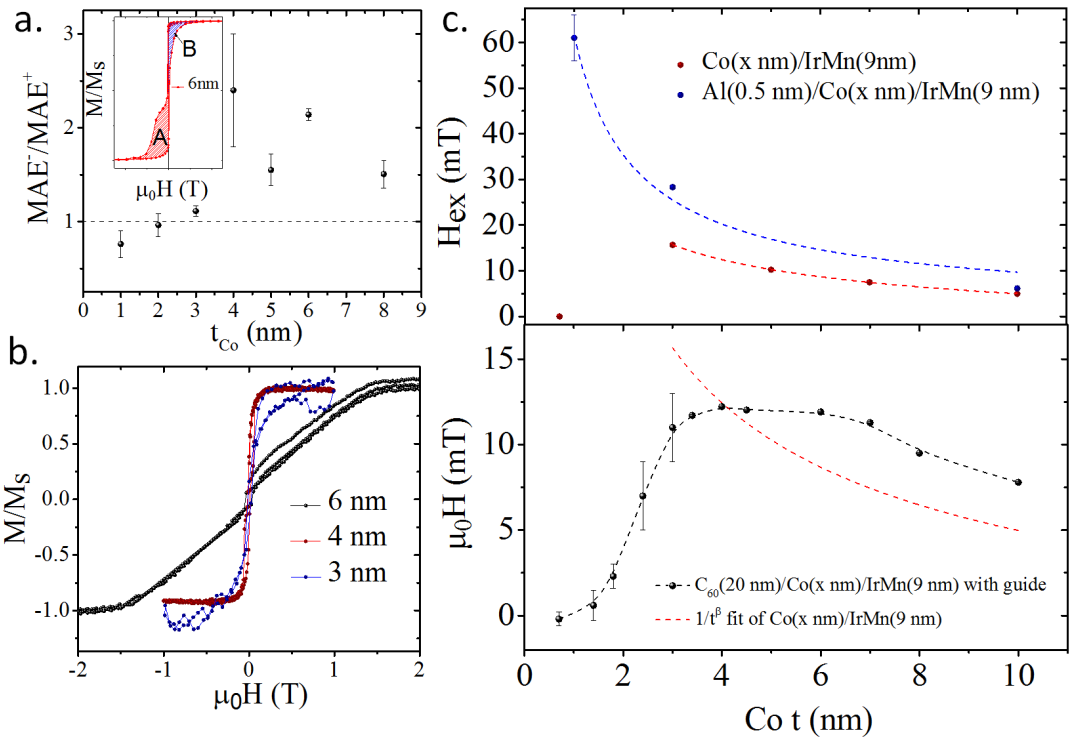

Figure 4.11: a. Shows the asymmetry measured in bilayers at 10 K after being cooled in 1 T as a function of cobalt layer thickness. The inset shows the method for calculating asymmetry in an example loop. b. Shows three such bilayers measured in an out of plane configuration. At 6 nm, a normal out of plane hysteresis loop is observed while cobalt layers of 4 nm and below show a significant out of plane anisotropy. c. Shows the control samples, exchange biased bilayers indicating the expected $\frac{1}{t_{Co}}$ dependence of bias field H_{ex} in these systems and similar systems where the roughness of a C_{60} layer has been mimicked by depositing a thin aluminium layer beneath the ferromagnetic layer. The lower panel shows the bias field in C_{60} (20 nm)/Co(x nm)/IrMn(9 nm)/Al(10 nm) as a function of cobalt thickness. The fit of the control samples is shown in red.

roughness in large applied fields. Asymmetric anisotropy is retained after this field is removed. These structures exhibit training effects similar to those seen in exchange biased systems indicating that disorder plays a role in asymmetry. [201] It is infeasible that charged C_{60} alone could possess magnetic order which could lead to exchange bias but as demonstrated in 4.3 and 4.4, there is an interfacial region with a metallic band structure and high moment per atom and anti-ferromagnetic coupling. That only the upper interfaces of trilayers have been shown to exhibit asymmetry implies that a disordered or frustrated interface is key.

Loop asymmetry which behaves much like exchange bias has been observed in composites of AF stacks of magnetic molecules coupling to an FM substrate. [113] The appearance of asymmetry without any measurable bias field sets this system apart from such hybrid systems where there are easily identifiable uncompensated spin planes. In Co/CoO nanoparticles, asymmetry is understood to be the result of the freezing of uncompensated moments in the anti-ferromagnetic CoO shell. This freezing provides an additional component of anisotropy which overcomes the Zeeman energy associated with those shell moments. Reference [202] details how transverse susceptibility measurements can be used to show that the energy barrier for magnetization reversal is asymmetric and does not reverse after saturation. This relies on uncompensated moments in a low susceptibility material such as anti-ferromagentic CoO being frozen in a particular configuration during field cooling and not being reconfigured by the reversal of the core or bulk ferromagnet. This has also been associated with the formation of glassy disordered states. [203]

However, this study has eliminated the formation of nano-particles since out of plane measurements reveal strong in-plane anisotropy emergent in films in excess of 4 nm and the formation of oxides is not indicated in XRR, XMCD and PNR which show no evidence of anti-ferromagnetically ordered oxide layers and the optimisation of aluminium caps discussed in section 3.1.4 prevents penetration of oxygen. It should also be noted that oxidised core-shell nanoparticles show exchange bias in addition to asymmetry where this system shows no bias field in any measured samples.

However, it is known from XMCD and PNR, section 4.3 and 4.4, that an interfacial region forms between cobalt and C_{60} which is anti-ferromagnetically coupled to the bulk ferromagnet. From magnetometry, section 4.2, it is known that interfacial hybridization between cobalt and C_{60} leads to magnetic hardening. In addition, the

supplementary information of reference [169] contains DFT simulations performed by Gilberto Teobaldi which indicate that molecule configuration and interatomic distance could have profound effects on the magnetic state of surface molecules and PNR measurements of ten layer multilayers observe lower net moment associated with rougher layers, as shown in figure 4.6, which indicate a more disordered magnetic state.

It is proposed that the ZFC/FC behaviour shows the freezing of this disordered interface in which a distribution of uncompensated moments exist as a result of charge transfer into SHIPS and inhomogeneous coupling across the interface due to roughness and disorder. The zero field branch begins with both the bulk ferromagnet and interface in a zero-net moment configuration whose coercivity rapidly decreases as the interface unfreezes and its contribution to the anisotropy energy disappears. In the field cooled branch, a distinctive low temperature behaviour observed, particularly the upturn in magnetization seen below T_r, is similar to that observed in surface spin glasses as they are frozen in a configuration dictated by external fields. [204] The asymmetry arises from these frozen moments and their contribution to the anisotropy which does not reverse with the bulk ferromagnet but can be reconfigured by sufficiently large fields as evidenced by the training effect observed in asymmetric loops. The fact that there is no measureable exchange bias, evidenced by the equal positive and negative coercivities, indicates that the bulk ferromagnet is not pinned by any interfacial coupling. Instead there is a distribution of pinning sites created by the frozen interfacial moments which affect the reversal dynamics.

Such a glassy or disordered state should be evident in susceptibility measurements. The increase in coercivity expected in a ferromagnet should be monotonically correlated to temperature while a phase transition to a glassy state should produce an inflection in susceptibility. Susceptibility measurements were performed on the ten repeat structure: [Co(4 nm)/C_{60} (17.8 nm) $\times$ 10] Al(3 nm). A multilayer was used to attempt to maximise the measureable signal since bilayers of the type used in figure 4.10 had poor signal to noise ratios in AC measurements. A DC field of 40 Oe is applied with an oscillating field of 10 Oe driven a 5 Hz. The susceptibility shows a clear transition around 170 K (figure 4.12 top and inset). This is higher than predicted for a 4 nm layer which may be correlated to the use of multilayers since ZFC/FC measurements of ten layer repeats also show a transition around 170 K (figure 4.7). In addition, spin glasses and dynamic disordered systems show ergodicity breaking effects, particularly a

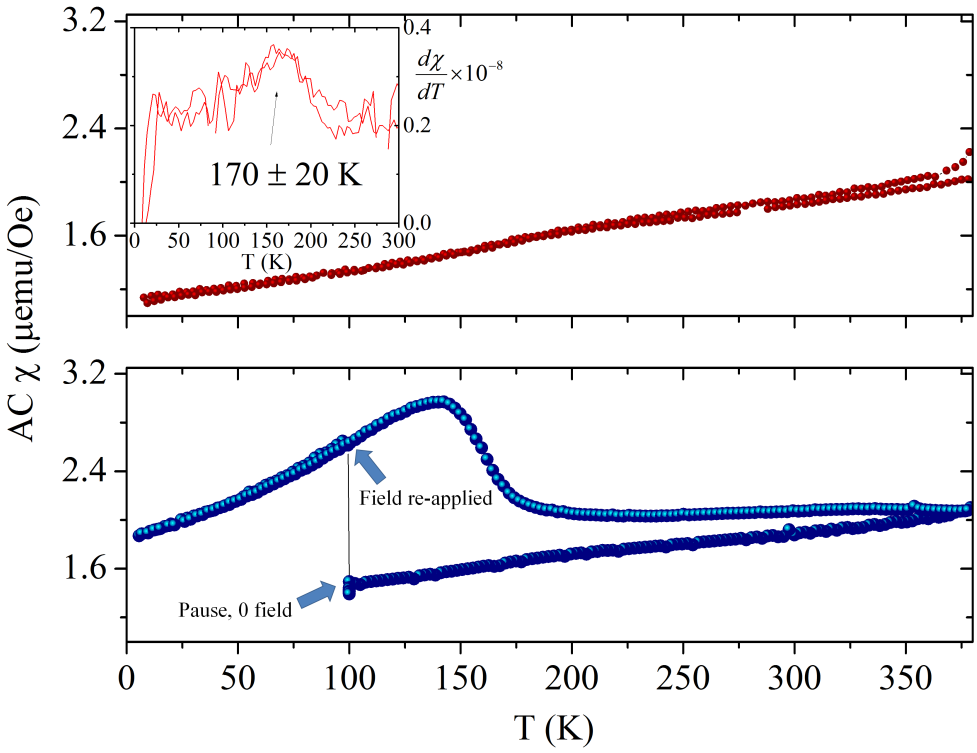

Figure 4.12: The top panel shows the AC susceptibility for a ten layer sample: Co(4 nm)C_{60} (17.8 nm) × 10 Al(3 nm). The inset shows the differential in order to highlight the inflection. The bottom panel shows the AC susceptibility with a pause at 100 K.

dependence of magnetic behaviour on waiting times. In particular, alloyed spin glasses such as CuMn are known to exhibit a dependence of susceptibility on the time the material is kept at a constant temperature in a constant field due to the relaxation of disordered states and resultant increase in stability over long timescales. [205] To further indicate the presence of a glassy state, the susceptibility measurements were repeated but with a pause at 100 K at which all external fields were set to zero and the temperature left stable for 90 minutes. When the external field is re-applied, it can be seen the susceptibility has increased (figure 4.12 bottom). Warming from low temperature, it is observed that there is a peak in susceptibility around the transition temperature which then swiftly settles back to its original value. This indicates that waiting below the transition temperature allows the disordered interfacial state to relax into a configuration determined by the ferromagnetic layers which would make it easier to magnetize the sample in this direction. The original susceptibilty is only recovered

when the interfacial moments unfreeze.

4.6 Conclusions and Discussion

Investigation of Co/C_{60} multilayers clearly indicates that the molecular layer introduces significant magnetic changes in cobalt layers. Firstly, the magnetization of the cobalt layer is reduced indicating a loss of majority spin electrons due to electron transfer from the cobalt 3d band into the spin split hybridized interface states formed between the molecular and ferromagnetic layers. The trend for magnetization reduction to increase for C_{60} layers up to 200 nm thick indicates that not only surface molecules are involved in the electron transfer process. This behaviour is surprising since the most distant molecules in such a layer are more than 100 hopping events from the interface (N.B the precise distribution of hopping distances is not known but modelling indicates that average distances of 1.4 nm produce good agreement with mobility data for thick C_{60} films) though the spin diffusion length in C_{60} films is on the order of 100 nm. [206] [27] XMCD confirms the presence of a hybrid band just below the energy of the LUMO indicating charge transfer. XAS for C_{60} layers up to 20 nm thick show the band structure recovers near bulk behaviour at a greater distance from the interface. This supports the notion of a spinterface like interaction where surface molecules form hybrid orbitals and have a radically different band structure, even becoming metallic as indicated in DFT simulations.

PNR builds up a depth profile of this system and reveals that there is a distribution of charge throughout the C_{60} layer with an average magnetic moment per cage of 1.2 μ_B. This supports the expectation from magnetometry on bilayers with very thick C_{60} layers that the whole C_{60} layer, not just interfacial molecules, are involved in the charge transfer process. However, the interfacial region, which extends between 1-2 nm from the cobalt surface, is anti-ferromagnetically coupled to the underlying ferromagnet and has a significantly higher moment and an average density which indicates involvement of both surface cobalt atoms and C_{60} cages. This is very similar to the proposed character of a spinterface as indicated by Sanvito in [32] where band bending is spin split due to polarization of the metal d band. However, the bulk C_{60} appears to follow the applied field which indicates a paramagnetic character expected for charged fullerenes. This will be further explored in Chapter 5. The mechanism for long range charge diffusion in C_{60} is, as yet, unknown.

Further investigation into the behaviours of the composite system reveals that, when the interfacial region is sufficiently disordered, a glassy state emerges below a T_r which is inversely proportional to cobalt layer thickness. This glassy state provides an asymmetric contribution to anisotropy, pinning regions of the composite against applied fields during the magnetization reversal process. It is not reversed when the bulk cobalt layer undergoes magnetization reversal but can be reduced through applying high fields to re-order the interfacial moments resulting in training effects. Interfacial coupling is not strong enough to create a measurable exchange bias indicating that the anisotropy energy of the glassy interface state is significantly less than the Zeeman energy associated with the bulk cobalt layer. AC susceptibility further supports the notion of a glassy state, showing ergodicity breaking effects wherein pausing below T_r to allow the disordered state to relax has a profound affect on the susceptibility. Further investigations should focus on rigorous susceptibility measurement and characterisation of the thermo-remanant relaxation of composites in order to define the distribution of relaxation times associated with interfacial moments as a function of temperature and correlate this to the observed transitions in ZFC/FC measurements. There is also the possibility of using muon spin relaxation measurements to confirm the existence of a spin glass or other disordered state by attempting to observe the well known Gaussian Kubo-Toyabe (GKT) relaxation behaviour. [207]

Chapter 5

Gd/C_{60} Hybridization

5.1 Introduction

While investigations into Co/C_{60} have shown that hybridization and charge transfer between transition metals and molecules can influence the magnetic properties of the metal as well as those of the molecules, there are a wide range of magnetic materials in everyday use to which the same principles would not necessarily apply. In section 4.2, Ni, Fe and Co were all shown to couple differently to the C_{60} molecular layer as evidenced by the different reductions of magnetization observed for equivalent complexes. It may, therefore, be expected that other metals will couple to C_{60} in unique ways producing novel compound materials which must be determined experimentally.

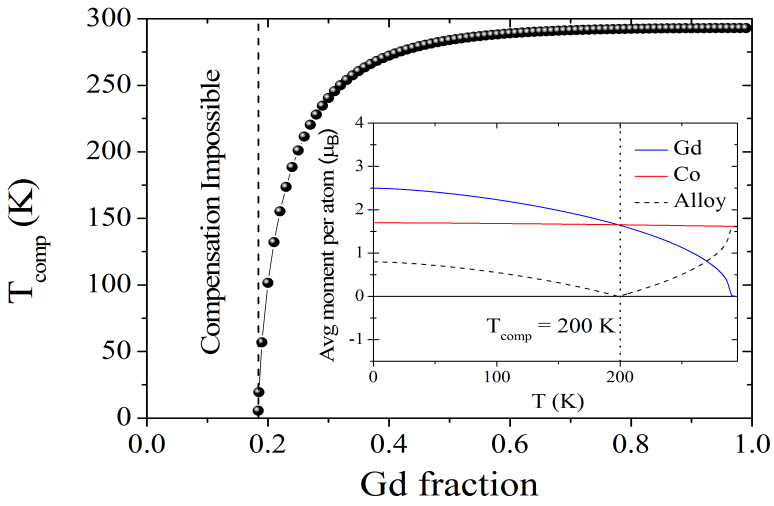

Figure 5.1: Dependence of the compensation temperature in a $Co_{1-x}Gd_x$ alloy, at which the zero net magnetization state is achieved, with composition calculated from an approximation in which critical exponents are similar for Gd and Co, the exact exponents can be found here [208]. The gadolinium fraction required for a given compensation temperature is slightly higher than predicted here (for example Kaiser et al found an alloy with a Gd fraction of 2.6 had a T_{comp} of 150 K where this model predicts this would be achieved by an alloy with Gd fraction 2.2 [209]) but variation due to imperfect mixing or deposition rate fluctuation produces larger variation in T_{comp} than the difference between simplified and realistic critical exponents. The inset shows the two Curie-Bloch model of the compensation for an x = 0.2 $Co_{1-x}Gd_x$ alloy with the net magnetization plotted as the mod-sum of the difference between the curves. Again, this is a simplification since gadolinium departs from Curie-Bloch behaviour below 50 K. [210] This model also assumes perfect mixing and homogeneity of the alloy but can be used to illustrate the mechanism.

Of particular interest for molecular control of magnetism are the lanthanides. These metals occupy the 4f transition block in the 6th period and progress from Lanthanum to Lutetium. Heavy lanthanide metal atoms, Gd and heavier, can have large moments due to unpaired electrons in the 4f shell. However, the 4f shell is highly localised in comparison to the 3d shell of the transition metals and is screened by its conduction electrons. [211] This prohibits any direct modification of the magnetism in lanthanides using the same principles outlined in chapter 4. As described in section 2.1.3 , rare earth atoms couple via the RKKY mechanism whereby indirect exchange occurs between atoms and is mediated by conduction electrons. [212] This means that while the magnetic 4f shell of rare earths cannot be directly manipulated with molecules, the interaction between those moments can be affected through the hybridization between molecular π orbitals and the RE conduction bands.

Investigation into rare earth magnets proceeded in two forms. First, the ferrimagnetic alloy CoGd was used as an ideal system to study the coupling of C_{60} to transition and rare earth metals. Co and Gd form an amorphous alloy where the two elemental sublattices are anti-ferromagnetically coupled. [213] Because Gd has a far higher moment per atom than Co, 7.55 μ_B as opposed to 1.7 μ_B, it dominates the magnetization at low temperature and overcomes the magnetostatic energy of the Co sublattice, forcing it to align against external fields. However, Gd has a far lower Curie temperature than Co, 293 K as opposed to 1400 K. If the Curie-Bloch curves for these two sublattices are plotted together, it can be seen that at some temperature, determined by the ratio of alloy components, the net magnetization of the two sublattices will be equal. At this temperature, called the compensation temperature, the net magnetization of the alloy will be zero (figure 5.1). However the transport polarization of the alloy at the compensation temperature is non-zero .[214] This makes it an ideal material for studying spin injection as the background magnetization of the alloy can be reduced or removed while still conferring a polarization to a host material. In this case, a compensated CoGd alloy would show whether the magnetic molecular layer mentioned in section 4.4 couples to the underlying magnetic structure or behaves paramagnetically and follows only an external field. By measuring the moment per atom of each layer using PNR above and below the compensation temperature, it is possible to see the polarization of those layers whose magnetism is induced by the cobalt sublattice flip. Paramagnetic components would be unaffected by this transition. The results of PNR

and magnetometry on these structures are outlined in section 5.2.

Second, the hybridization between a pure Gd film and C_{60} is studied using magnetometry to determine how hybridization between conduction bands in the rare-earth and the molecule LUMO affect RKKY coupling. Since the RKKY Hamiltonian is dependent on the conduction band structure (equation 2.42), which might be altered by band bending and hybridization, it is expected that strong interfacial coupling might affect the periodicity and magnitude of RKKY exchange in Gd resulting in changes to magnetic order. [54] The results of magnetometry on these structures are outlined in section 5.3. Resistance is measured in GdC_{60} films is also used to measure spin disorder scattering, section 5.4, and XAS is used to study the interfacial hybridization between Gd and C_{60}, section 5.5.

5.2 Hybridization in CoGd/C_{60} Multilayers: Magnetometry and PNR

CoGd alloys were sputtered from a composite target described in section 3.1.3. Thin Gd foil was pressed into the racetrack of a Co target covering a fraction of the sputtering surface which approximated the target ratio for the alloy. The target gadolinium fraction was 0.25 as this would produce a compensation temperature of $\approx$ 200 K. Variations in concentration due to the different conductivity, melting point or coverage of the gadolinium foil would still produce a compensation temperature between 10 - 300 K for variations of $\pm$ 0.05. Gadolinium content was varied by adding or removing sections of gadolinium foil to modify the compensation.

Deposition currents and chamber pressure were varied in order to vary deposition rate to achieve optimal mixing. The deposition rates for Gd doped Co targets were found to increase from 1.1 $Å s^{-1}$ (for undoped targets) to 2.1 $Å s^{-1}$ with an increase in distributed power from 16 W to 18 W. This is due to the higher resistivity of Gd (120 $\mu\Omega$cm at 300 K) [210] as opposed to Co (1.11 nΩcm at 295 K) [215] and the difference in the binding energy of the different metals as demonstrated by their melting points (1585 K for Gd and 1768 K for Co). The optimal results for isolated CoGd layers were achieved when 30 % of the Co target racetrack was covered by Gd foil and sputtering power was 18 W with a sputter gas pressure of 1.8 mTorr (figure 5.2a). This compensation temperature correlates to a gadolinium fraction of 0.21 $\pm$

0.01. Determining the exact fraction from the measured alloy density is not possible in this case due to the mixing of various phases with very different density and crystal structure in amorphous CoGd films. [213] This result is in good agreement with the results of the study by Hansen et al. [216]

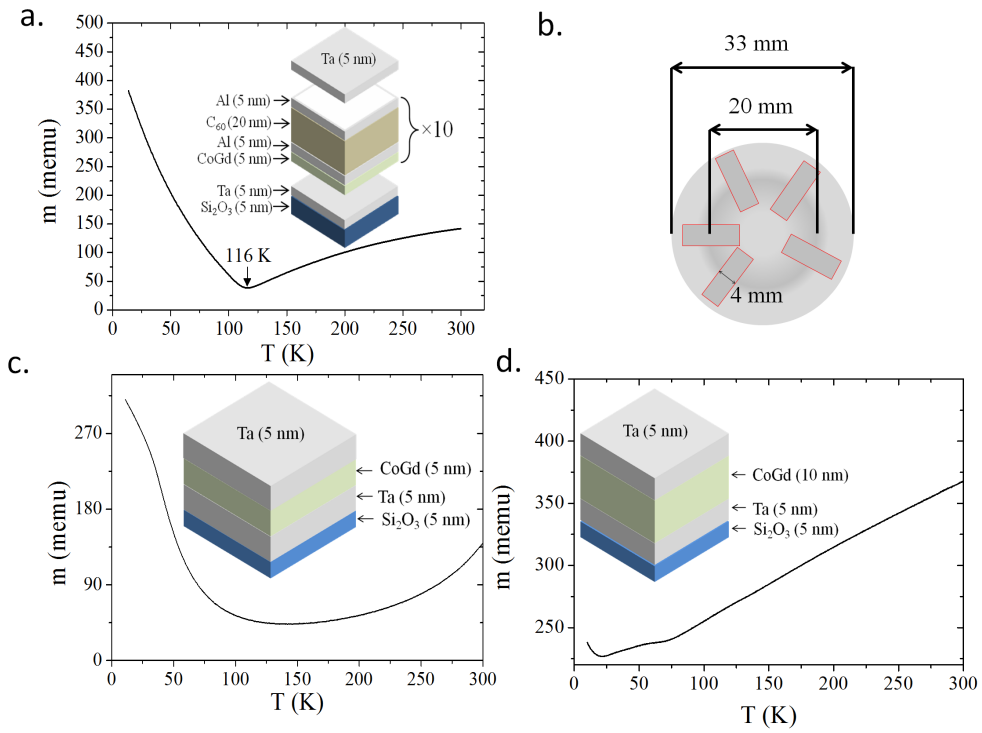

Figure 5.2: a. Moment vs Temperature for a multilayer structure shown in the inset measured via SQUID magnetometry. Zero magnetization is not achieved at any temperature but a clear minimum is observable at 116 K, the moment of the alloy at 295 K was 141 ± 2 emu/cc. Compensation temperature and moment indicate an alloy composition $Co_{1-x}Gd_x$ with an x value fo 0.21 ± 0.01. The doped target is illustrated in b. Gd foil is placed to cover the racetrack intersecting a total of 30 % of the racetrack circumference. c. Is a single layer of Gd flanked by a Ta seed and cap. The target coverage is identical to a. chamber pressure was 1.73 mTorr. All other multilayers deposited with a CoGd/Ta interface showed a reduced or no compensation. d. Shows the moment vs temperature curve for a 10 nm CoGd layer with Ta seed and cap deposited using a target with 25 % Gd foil coverage.

Capping material was found to influence the compensation behaviour. Samples which used heavy metals such as Ta as capping materials broadened the compensation (figure 5.2 c and d). Multilayers of CoGd/Al/C_{60} still showed good compensation in-

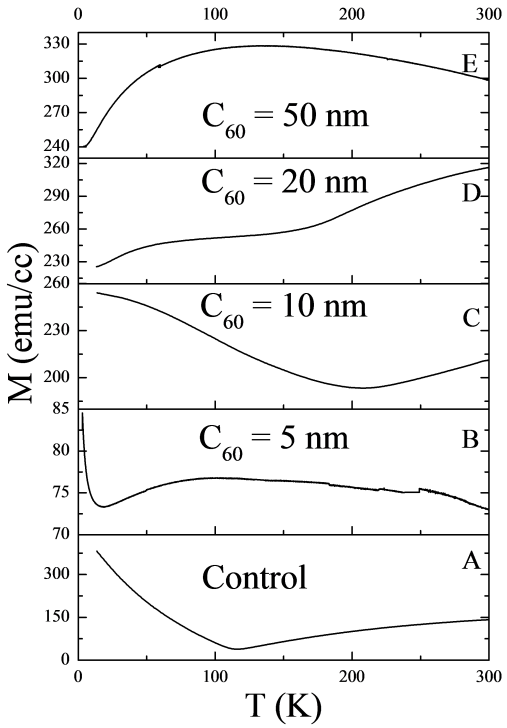

Figure 5.3: a. Moment vs Temperature curves recorded in applied fields of 0.1 T for ten layer multilayers of Ta(5 nm)/[CoGd(5 nm)/C_{60} (x nm)]x10/Al(5 nm). The control sample (A) has 10 nm of C_{60} separated from the CoGd layers by 5 nm of Al. The 5 nm (B) sample has a different alloy composition with 25 % coverage on the target, hence the lower magnetization.

dicating that the roughness of multilayer structures do not prevent compensation. All samples were measured using a SQUID VSM, moment vs temperature curves were recorded in applied fields of 0.1 T, above H_{sat}, to determine if compensation was achieved. Deposition of C_{60} changed the compensated fraction and temperature in all CoGd samples. The composition used in figure 5.2 a was used in multilayers with 10 nm and 20 nm of C_{60} and a composition with lower gadolinium concentration, 25 % intersection, was used in multilayers with 5 and 50 nm of C_{60}. Multilayers with up to 10 nm of C_{60} still showed a compensation point where the magnetization dipped below the value at 10 K. At 20 nm, the compensation is still present but does not go below the magnetization at 10 K indicating that while there may be a magnetic phase transition, there is not a true compensation. By 50 nm, no compensation is observable

(figure 5.3).

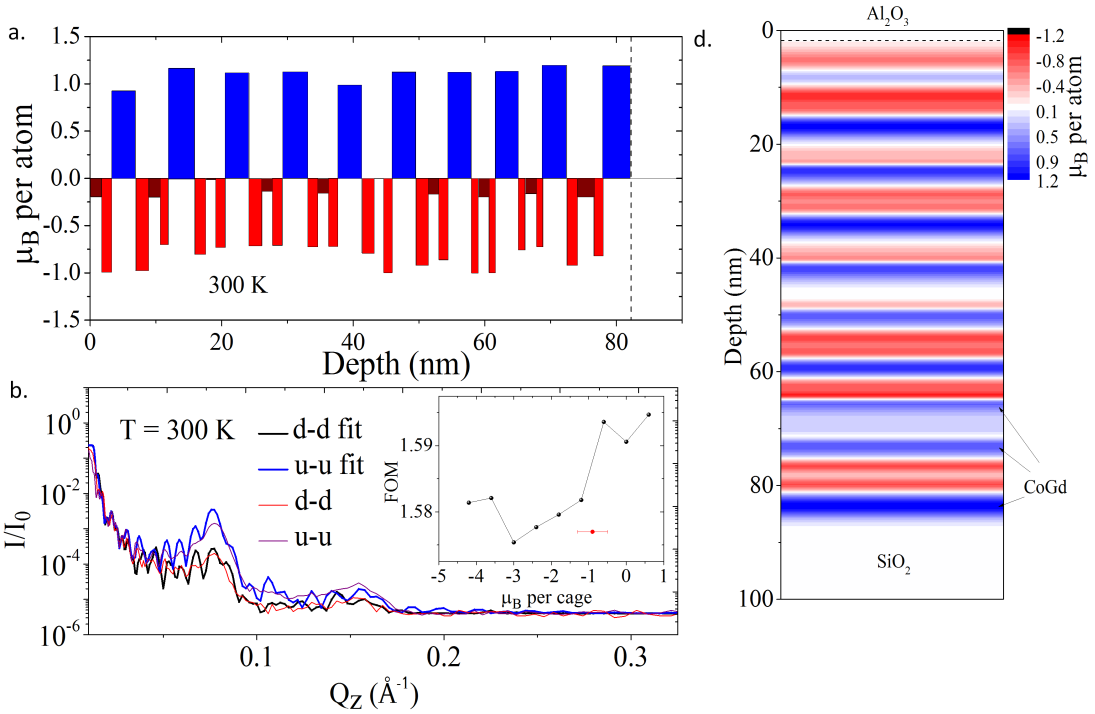

Figure 5.4: a. Magnetic profile of the ten layer multilayer Ta(5 nm)/[CoGd(5 nm)/C_{60} (5 nm)]x10/Al(5 nm) derived from fitting the polarized neutron reflectivity spectrum obtained at 300 K b. As in section 4.4, structural parameters were fixed from XRR such that only magnetic moment per atom was a free parameter. However, due to the very high neutron capture cross-section of Gd [217] the neutron scattering parameter b was also freed for the alloy layers since the alloy composition is not determined from XRR. The inset shows the local FOM landscape determined by varying all C_{60} moments, adjusting the alloy layer to maintain a constant magnetization within a small variance to achieve the best fit. The red point shows the FOM for the fit shown in panel b. which is obtained by allowing C_{60} layers to vary with respect to one another. d. Shows the magnetic profile corrected by the SLD to show gradual change as in section 4.4.

The multilayer in figure 5.3 B showed compensation at 18.5 K. While the compensated fraction was low ($\approx 10\%$) the overall moment was also low, 80 emu/cc at 4.2 K. Higher Gd concentrations quench Co moment leading to higher average magnetization near compensation. Since lower overall moment at the compensation point is preferable, this composition was selected. [216] [214] This multilayer was observed using PNR in applied fields of 0.1 T at 5 K, 18.5 K and 300 K. At 300 K, fitting the PNR spectrum

using the same method described in section 4.4 reveals a similar anti-ferromagnetic interfacial coupling to CoC_{60} (figure 5.4). The thinner C_{60} layers do not show clear evidence of paramagnetism and change the sign of their magnetization through the compensation point. This indicates that magnetic coupling propagates through these thin C_{60}, acting on spins beyond the first monolayer. The best fit predicts a moment per C_{60} cage in the bulk of 1.2 μ_B. However, exploring the FOM landscape shows that this may be a local minimum and the true moment may extend as high as 3 μ_B per cage, though this would not be expected to be stable due to Coulomb repulsion between cages.

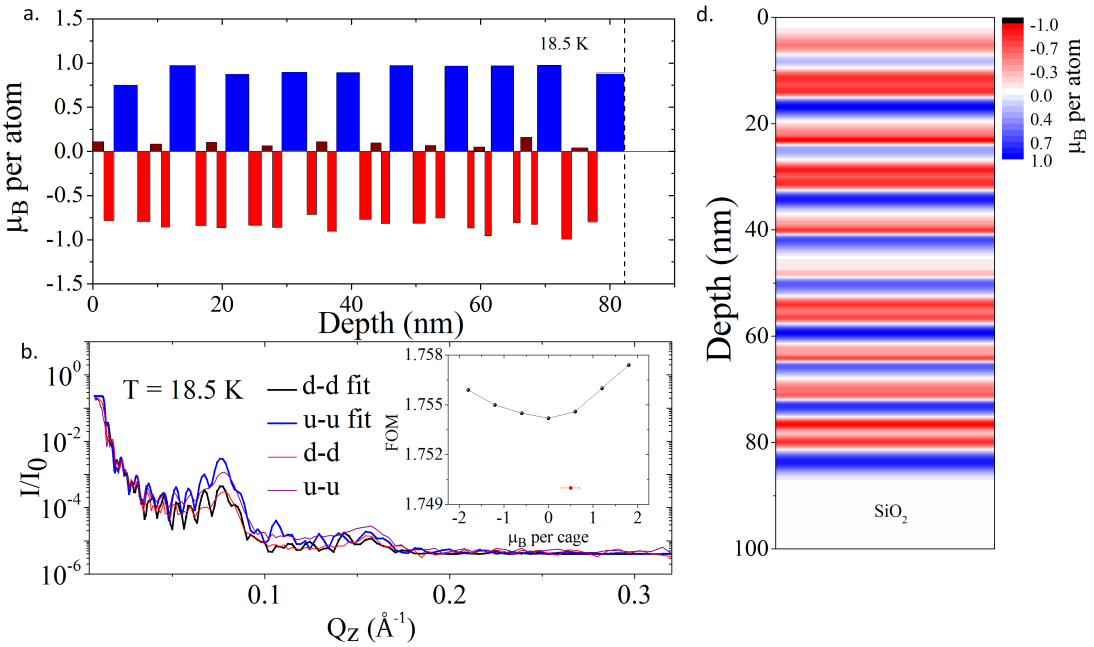

Figure 5.5: a. Magnetic profile at 18.5 K which is where the alloy compensates as shown in figure 5.3. b. Shows the spectra and fit. The inset shows the FOM. d. the corrected cross section. The FOM landscape indicates that the C_{60} moment is close to zero though allowing layers to vary with respect to each other produces a good fit with a positive moment, red data point.

At the compensation point it is immediately apparent that the C_{60} polarization has reversed (figure 5.5). However, the interfacial polarization is unchanged, averaged over the ML. The scattering density for the interfacial region is $0.049 \pm 0.009 Å^{-3}$ while the alloy has a scattering density of $0.040 \pm 0.006 Å^{-3}$ and C_{60} has a scattering density of 0.0014 ± 0.0001 indicating this interfacial region includes a high proportion of Co

and Gd atoms. The interfacial region extends for 1.5 ± 0.1 nm and the thickness is, at least within the significance of the fit, independent of temperature. Cooling below the compensation point, there is a recovery of the magnetic moment of the alloy while the polarization of the interfaces and C_{60} remains unchanged confirming that both the 5 K and 18.5 K spectra are in a Gd dominated regime (figure 5.6). Observing the SLD corrected profiles side by side, one can see that the greatest changes between the spectra recorded at 5 and 300 K occur in the interfacial and C_{60} region due to the reversal of the C_{60} polarization.

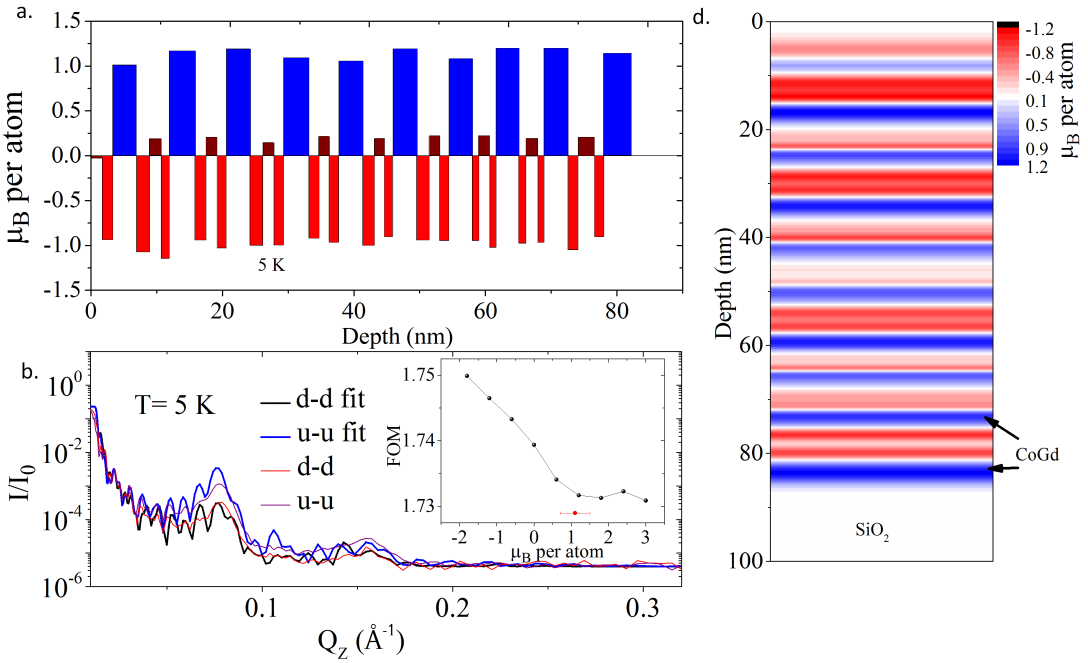

Figure 5.6: a. Magnetic profile at 5 K b. Shows the spectra and fit. The inset shows the FOM and d. the corrected cross section. Here, the FOM landscape shows a clear tendency toward positive moments.

The fitting procedure in these multilayers is the same as for the CoC_{60} system from section 4.4. Structural information is fixed by XRR and magnetic information by the mvT so that fewer free parameters are present in the fit. Despite this, the significance of this fit is lower than that for CoC_{60} due the necessity of leaving the neutron scattering parameter b free to accommodate the possible variation in alloy mixing. The FOM plots shown in figures 5.4, 5.5 and 5.6 show that a change in C_{60} polarization occurs between 5 and 300 K. This is clear evidence that there exists a preferential coupling of

the moment induced in C_{60} to the underlying Co sublattice while the screened moment of Gd 4f electrons contributes little to the C_{60} polarization. This study also indicates that the magnetic coupling of C_{60} moments extends up to 2.8 nm from the metal surface as indicated in the thickest C_{60} layer observed in this sample which still reverses its polarization when passing the compensation point.

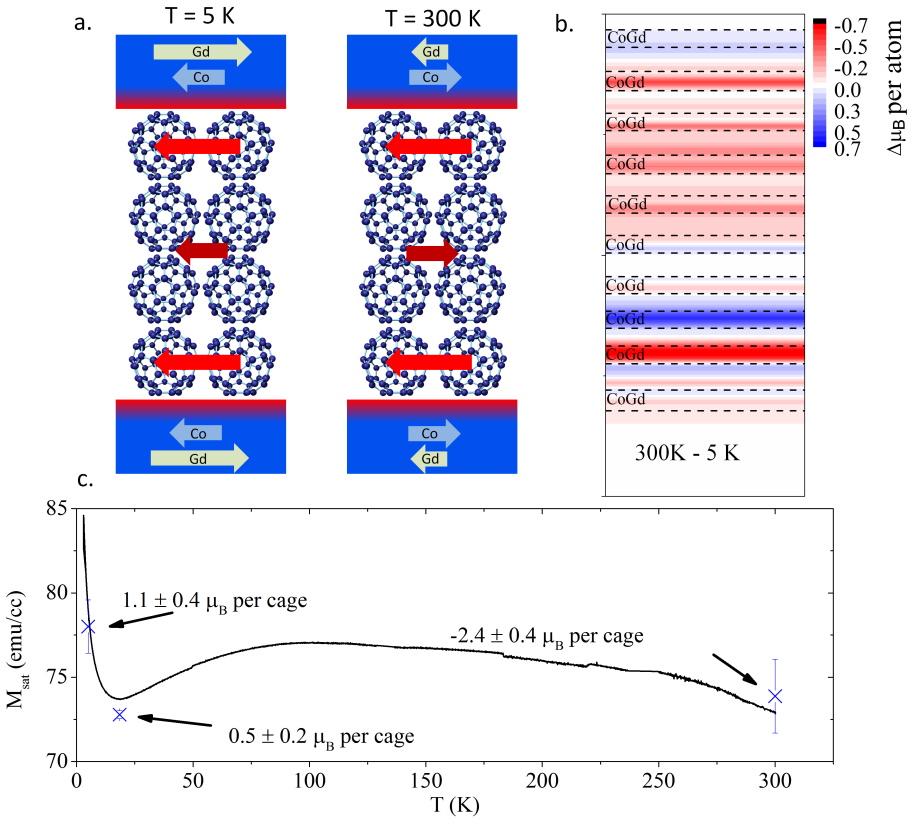

Figure 5.7: a. Simplified diagram of the layers of one unit of the CoGd multilayer showing the net moment of the Co and Gd sublattices at 5 and 300 K. The interfacial region includes the surface atoms of the CoGd layer (indicated in red) and the C_{60} layer. b. Difference between the SLD corrected magnetic moment profiles at 5 and 300 K. c. The predicted magnetisation of each fit (at 300, 18.5 and 5 K) compared to the MvT recorded in this sample using SQUID magnetometry. At each point the average C_{60} moment predicted by the best fit is shown. The error in the magnetization shows the deviation in magnetization allowed to produce a good fit when testing different C_{60} moments. C_{60} μ_B per cage are indicated for each point.

The behaviour of the interfacial region provides insight into interfacial coupling between molecule and alloy. Above and below the compensation temperature, an in-

terfacial region 1.5 ± 0.1 nm exists which is antiferromagnetically coupled to the rest of the alloy. The density and scattering length of this region indicates it includes both C_{60} and CoGd. This is interpreted as the result of the effect of hybridization on the surface atoms of the CoGd alloy and the transfer of spin polarized electrons into hybird interface states in the C_{60} analagous to the behaviour observed in 4. Since the magnetic moment of the interface changes little as a function of temperature, the antiferromagnetic coupling of interfacial moments to the rest of the alloy can be considered a general property of hybrid interfaces and not necassarily related to the direction of the moments in the Co sublattice. Beyond this interfacial region, C_{60} moments are shown to change sign when passing through the compensation point indicating these moments are coupled to one particular sublattice in the alloy, not only the net moment. The expected behaviour of each layer is detailed in 5.7.

5.3 GdC$_{60}$ Hybridization and Evidence for Magnetic Phase Transitions

The observation that C_{60} can lead to a significant modification of the compensation behaviour in CoGd alloys (figure 5.3) but did not appear to couple to 4f moments in the Gd sublattice raises an important question regarding the nature of the interaction between molecules and rare earth ferromagnets: namely, how might hybridization to conduction electrons alter magnetic structure? As mentioned in the introduction to this chapter (section 5.3), it is possible that the RKKY interaction which couples 4f moments together via intermediate conduction electrons could be modified by hybridization. Distortion of the 6s and 5d conduction bands in Gd could lead to alterations in magnetic coupling. To study the extent to which this occurred, it was necessary to move away from CoGd alloys and focus on the interaction between C_{60} and pure Gd. Gd was deposited using the DC magnetron sputtering method described in section 3.1.1 on silicon dioxide substrates at room temperature. These films are deposited close to their Curie temperature so the permanent magnet array will not necessarily set a well defined easy axis.

Gd is deposited from a 99.95% pure coin mounted in a DC magnetron. Deposition takes place in an atmosphere of argon at 2.8 mTorr with a bias of 308 V and a deposition power of 13 W. This produces a deposition rate of 1.53 Ås^{-1}. 3 nm Ta layers are used

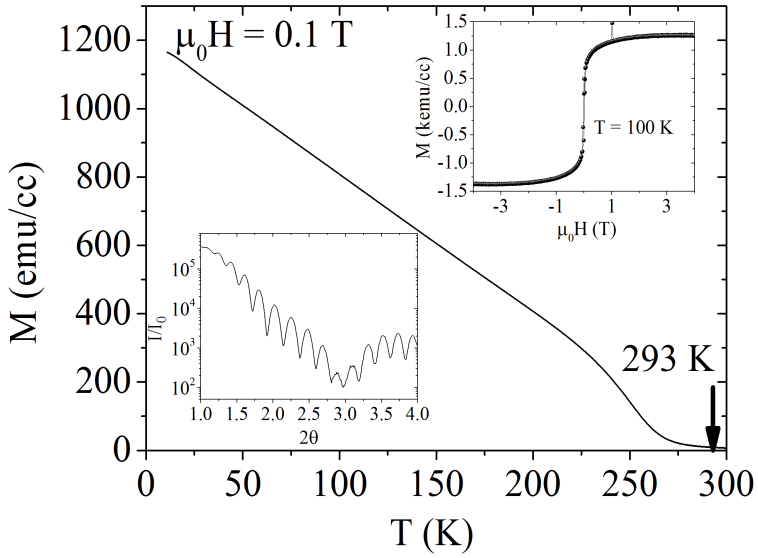

Figure 5.8: MvT of a 30 nm Gd metal film at 0.1 T recorded using a SQUID-VSM. Insets show hysteresis loop at 100 K and XRR recorded in the same film.

to seed an atomically flat surface to minimize roughness. A 30 nm metallic layer with a 5 nm Ta cap produced a T_C of 279.0 ± 0.5 K measured at 0.1 T with a saturation magnetization of 1370 ± 10 emu/cc at 100 K with a coercive field $H_C = 17 \pm 1$ mT (figure 5.8). This is lower than the expected T_C and M_{sat} for single crystal Gd. [210] However, the ordering temperature of Gd is known to be strongly depend on crystallinity. [217] This value of magnetization is in agreement with studies of Gd thin films sputter deposited at room temperature onto Ta seed layers (Scheunert et. al. give values of 1353 and 1274 emu/cc depending on deposition rate). [218] XRR showed RMS roughness of 1 – 2Å with no evidence of oxide layers.

C_{60} was deposited onto Gd films of varying thickness in order to assess the range of interfacial interactions in Gd and the effect hybridization would have on magnetization. The cap used in each case was a 20 nm layer of Al. Thin films of Gd were found to have significantly reduced magnetization in the presence of C_{60} at 100 K (figure 5.9). Recovery of bulk magnetization was achieved above 30 nm.

Hysteresis loops were recorded for Gd films of various thicknesses at 2 K (figure 5.10). Very thin films of 1 nm thickness showed superparamagnetic behaviour with high saturation magnetization but zero coercivity. This may be because the film is too thin to be continuous. However, whether or not it is continuous, it demonstrates that

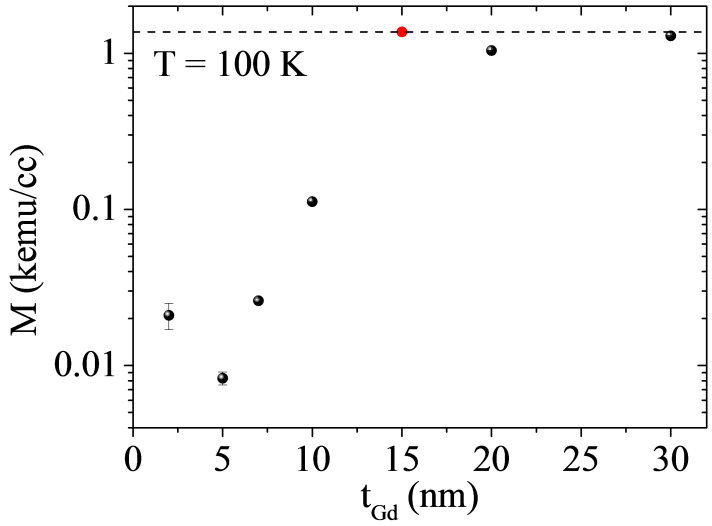

Figure 5.9: Saturation magnetization vs Gd film thickness for bilayers of Gd(xnm)C$_{60}$(20nm). Magnetization is determined by measuring hysteresis loops in a VSM at 100 K. The background is removed as a linear correction and the magnetization derived from the measured sample dimensions. The magnetization axis is plotted logarithmically to show the variation in magnetization in the thinnest films. The red point is the bulk value obtained in the control presented in figure 5.8.

the moment per atom of Gd does not decrease in the presence of C$_{60}$ since the superparamagnetic moment is still large. This indicates changes in the magnetic ordering are responsible for the suppression of magnetization rather than loss of 4f majority spins as was the case for Co/C$_{60}$, section 4.2. This is in line with the idea that 4f electrons are screened from direct interaction with by the conduction electrons. Therefore, the only change in moment per atom which could occur would be the small portion of the atomic moment associated with the outer shells, 0.55μ_B of the 7.55μ_B total. [219] Films up to 5 nm thick show very low remanance, < 30 emu/cc, and otherwise paramagnetic behaviour. Between 7 and 10 nm, an unexpected behaviour emerges in that the susceptibility of the Gd is significantly reduced even as magnetization begins to recover. Finally, by 20 nm, the hysteresis loop becomes bulk like, recovering full magnetization by 30 nm.

Measuring the moment as a function of temperature shows a magnetic transition at low temperature and reveals unexpected behaviour in films between 5-10 nm thick

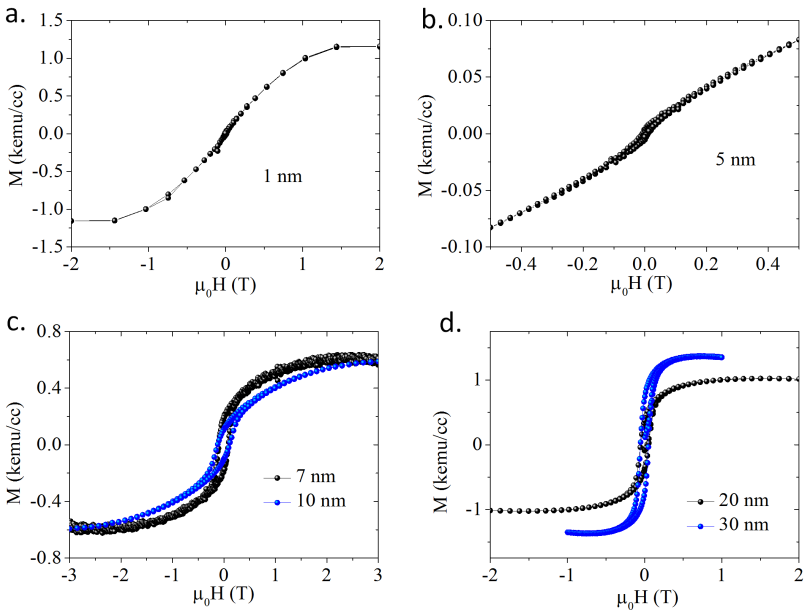

Figure 5.10: Hysteresis loops recorded at 2 K in a conventional VSM (c. 7 nm and d. 30 nm) and SQUID VSM from GdC_{60} bilayers Ta(3 nm)/Gd(x nm)/C_{60} (20 nm)/Al(20 nm). All samples were zero field cooled from 300 K before measurement.

(figure 5.11). Bilayers of GdC_{60} are cooled in zero field after demagnetization at 300 K. Gd films 7 and 8 nm thick show a zero magnetization state below 10 K in applied fields up to 50 mT. Up to 10 nm, Gd films show magnetic oscillations as a function of temperature below 10 K. The susceptibility of 7 and 10 nm films was determined from the derivative of the hysteresis curve at the coercivity (figure 5.12). Susceptibility is supressed with a clear transition occurring as the temperature is raised through the oscillations up to 10 K. The 30 nm film closely resembles studies of single crystal Gd at low fields. [218] [210] The change in behaviour above and below 10 nm may be related to the size induced phase change from hcp to fcc crystal structure observed in Gd thin films below 10 nm. [220]

The deviation from ferromagnetic behaviour at low temperatures, characterised by the downturn in in-plane magnetization, is attributed to the rotation of the easy axis in Gd as a function of temperature due to temperature dependent changes in the lattice constants of the Gd unit cell. [210] Neutron diffraction studies of Gd hcp single crystals demonstrate that the easy magnetization axis rotates with respect to the c axis, being fully aligned at room temperature but rotating to a maximum of 75° at 195 K

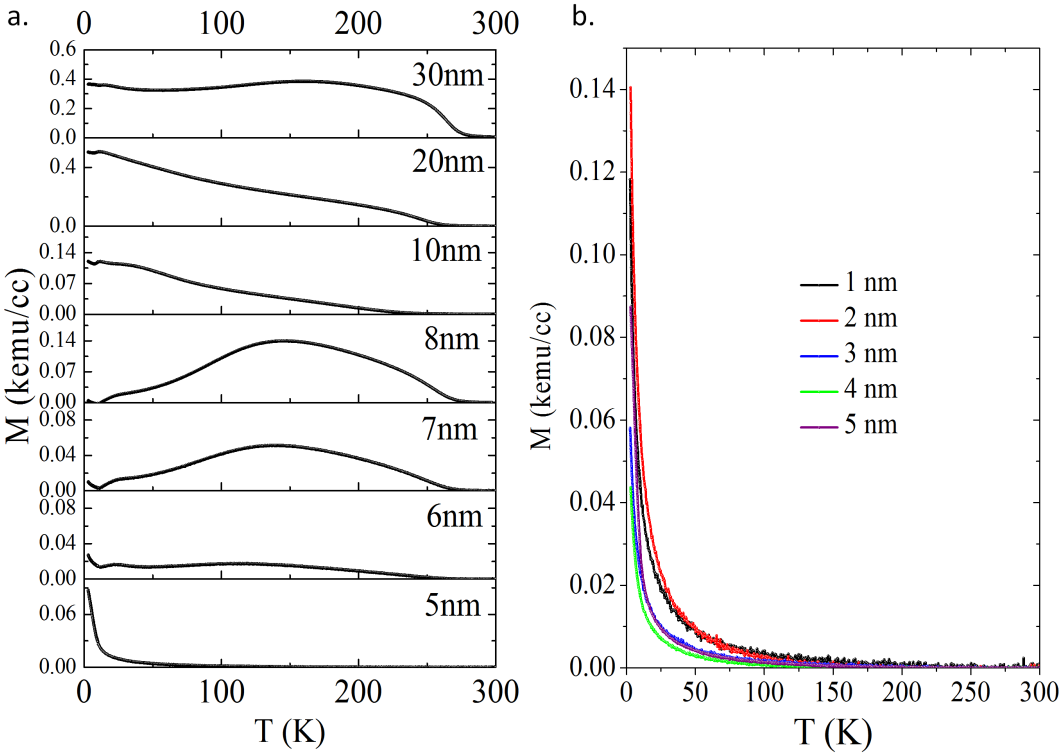

Figure 5.11: a. Moment vs temperature recorded for bilayers of Ta(3 nm)/Gd(x nm)/C_{60}(20 nm)/Al(20 nm) in applied fields of 50 mT. b. Below 5 nm, MvT curves fit well to Curie-Weiss law indicating paramagnetic behaviour.

before moving back to 30° at 4 K. [221] The canting of the easy axis and the resultant magnetization vs temperature behaviour prompted much discussion in the 1960s as to whether a spiralling magnetic state might emerge in Gd around 210 K where the transitions are most apparent. The much discussed result of Belov et al. [222] seemed to indicate a transition between a ferromagnetic state and a spiral spin structure which occurred at 210 K. However, later studies such as that by Graham [223] did not support this conclusion. However, the emergence of such a spiral state might well be supposed since Er, Ho and Dy all show spiral states close to their Néel temperatures. The lack of a helical phase in Gd is attributed to the lack of Kohn anomalies in the conduction electron momentum variation in the strength of inter-atomic interactions, see section 2.1.3. The coupling constants are stronger in Gd than any of the latter rare earths which exhibit helical or spiral phases and do not change sign for any q value. [40]

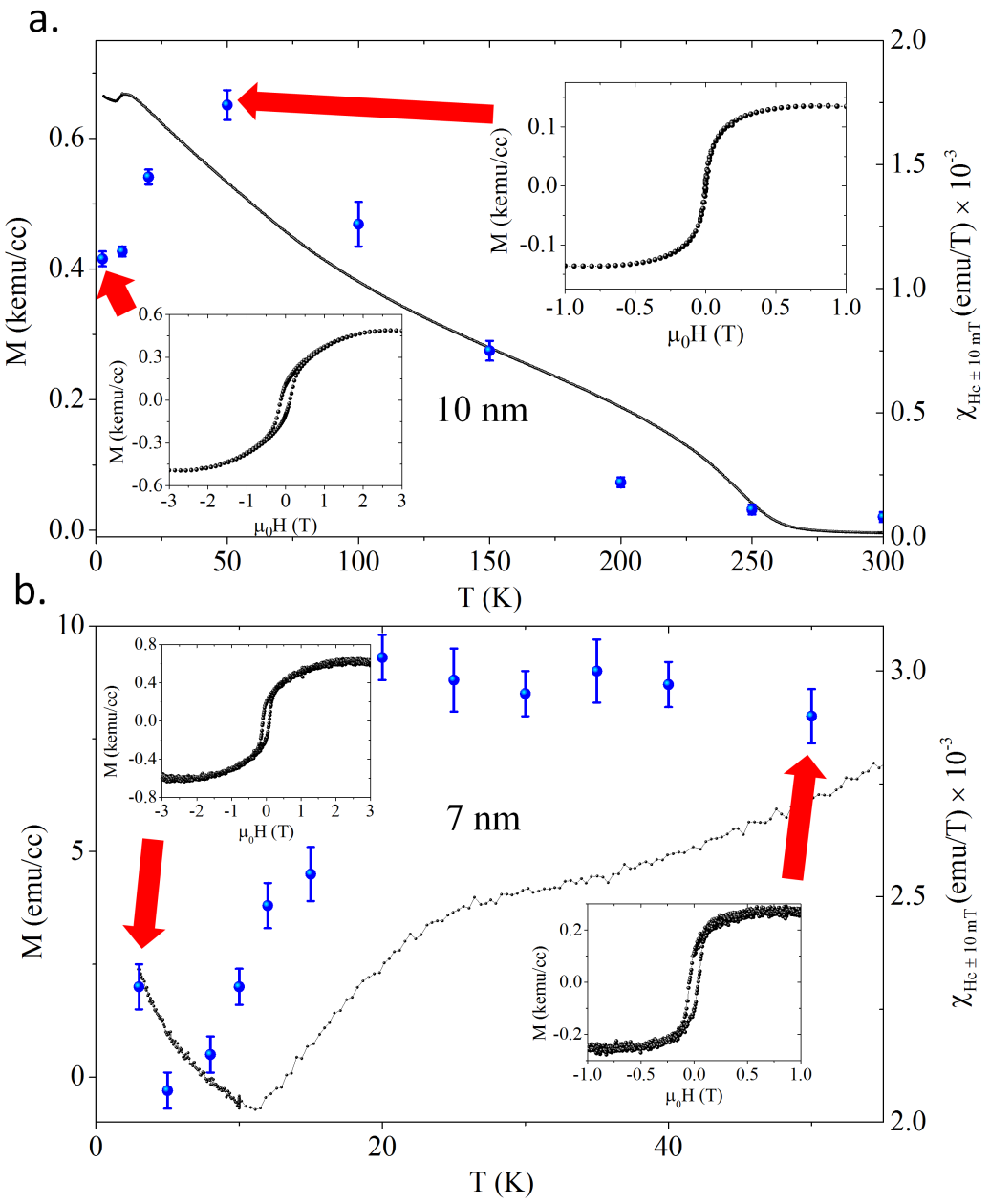

Figure 5.12: The 7 nm (a) and 10 nm (b) samples shown with susceptibility data. The blue data points show the susceptibility calculated at the coercive field for loops at various temperatures in each film while the black points show the magnetisation at 50 mT. In the case of the 7 nm film, the derivative was taken following adjacent averaging with an aperture of 10 in order to reduce the effect of thermal noise from the conventional VSM measurement. The insets show the hysteresis loops recorded at 3 K and 50 K.

The thinnest films, those below 5 nm, are paramagnetic at all available temperatures. Any correlation between film thickness and Curie point in thicker films is not clear, not least due to the broad ferro-para magnetic transition characteristic of Gd. However, the change in MvT dependence is indicative of some deviation from the usual conventional ferromagnetism in Gd.

The identifying features of anti-ferromagnetic and helical phases in rare earths have been studied in detail. [40] Other than the purely paramagnetic phases expected in films thinner than 5 nm, the candidates for the additional transitions are a wave-like anti-ferromagnetic phase and a spiral phase. It is also possible that neither state exist and the oscillation of the easy axis angle is altered, changing the susceptibility but not introducing any periodicity.

5.4 Resistance vs Temperature in GdC_{60} Films

Different spin ordering in rare-earth films can manifest as differences in the spin disorder scattering term of the conductivity. As discussed in the theory presented by Elliott and Wedgwood [224] and observed by Singh et al [225], the spin scattering is a probe of correlation in rare earths. In magnets where the order is a wavelike anti-ferromagnet or a spiral phase, the spin ordering is periodic but with a periodicity different to the crystal lattice. These different periodicities can alter the Brillouin boundary conditions and alter the resistivity of the metal. A rigorous treatment of this problem was first given by Miwa. [226] It is, therefore, possible to see magnetic transitions such as the spiral phases in Ho and Dy as peaks in the resistivity vs temperature curves of these metal films. Resistivity curves in zero-field cooled Erbium crystals show a characteristic hump in the resistivity just below the Néel temperature and additional transitions at 53 K and 20 K corresponding to the emergence of a wave-like periodic structure and a conical structure respectively (figure 5.13). These features are most visible in the c-axis where they manifest as clear, first order phase transitions. [227] The polycrystallinity of Gd films deposited in this study will make it impossible to observe first order phase transitions such as those seen in Erbium single crystals. However, it will still be possible to extract information about spin disorder from resistivity measurements.

Bilayer films of Gd(30 and 8 nm)C_{60}a-C(10 nm)Al(2 nm) were deposited for resistance measurements. The amorphous carbon layer (a-C) is used to stabilize the cap and prevent the diffusion and beading which would usually preclude the use of such

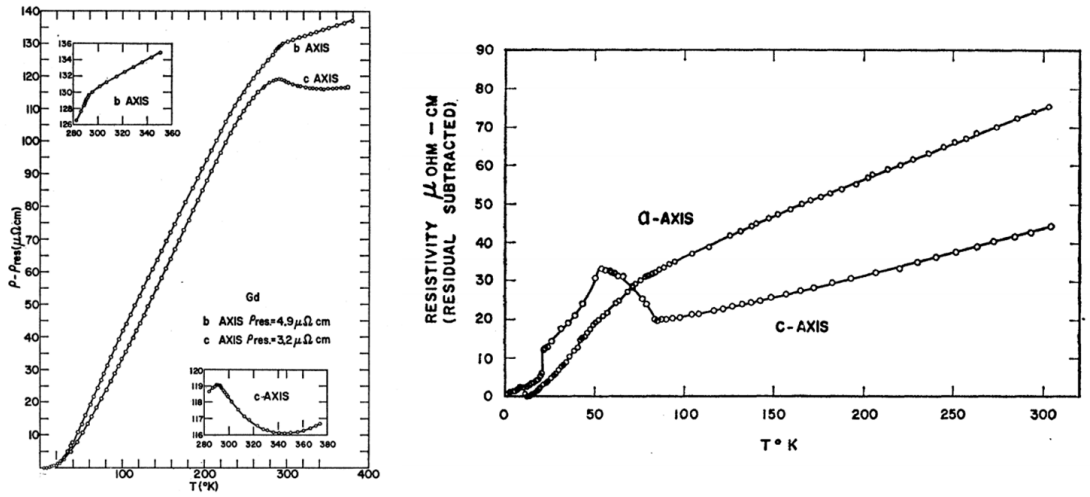

Figure 5.13: Figure adapted from [227] showing the resistivity of erbium as a function of temperature (right) and figure adapted from [210] showing the resistivity of Gd. The Néel temperature at 85 K is where the Erbium film undergoes a transition from a paramagnetic phase to an anti-ferromagnet. The paramagnetic transition in Gd at 293 K is evidenced by the broad maximum in the c-axis resistivity.

a thin Al cap on C_{60}. The cap is necessarily thin to prevent the shunting of applied current through metallic layers other than Gd which may distort the result. The film was wirebonded in four point van der Pauw configuration with Al wire and inserted into a He cryostat as described in section 3.6.

The resistance was measured using applied voltages of 0.4 mV (figure 5.14). Samples were cooled from 300 K in zero field. Measuring with increasing temperature from zero field, the 30 nm sample whose magnetisation vs temperature behaviour was closest to bulk Gd, showed some inflection at 20 K corresponding to the observed low temperature inflection in the MvT. The RvT curve in this sample is non-linear and there is no clear inflection at the Curie temperature. In the 8 nm sample, where the zero net magnetization state was observed at low temperatures, there is a complex RvT dependence with at least two transitions observable corresponding to the observed onset of the low temperature oscillations in the MvT and the paramagnetic transition. The low temperature peak occurs at 31.5 K and resembles the inflection in the c-axis resistivity of Gd in figure 5.13 near the Curie temperature. However, the hysteresis loops collected at 50 K in similar samples, figure 5.13, show that this is not a param-

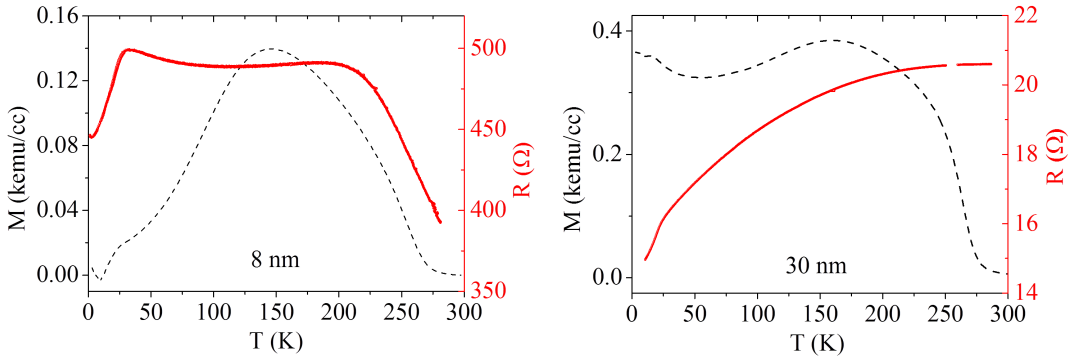

Figure 5.14: Resisitance vs Temperature curves for GdC_{60} bilayers of 30 nm (left) and 8 nm (right). Dotted line show the MvTs for equivalent samples.

agnetic transition. The steep decrease in resistivity above 190 K agrees with the MvT and seems to indicate the paramagnetic transition. The region between 31.5 and 190 K then represents an intermediate phase with increased susceptibility and resistivity. This intermediate phase bears many similarities to the periodic anti-ferromagnetic and spiral states in other rare earths such as Erbium and Dysprosium, though without the first order transitions observable in single crystals. However, this information can only indicate a greater spin disorder in this intermediate region, not the exact nature of that disorder. Neutron diffraction would be required to determine the exact nature of the intermediate state and identify spiral or other periodic structures.

5.5 XAS and XMCD in GdC_{60} Bilayers

XMCD was used to probe the bilayer interface and identify traces of hybridization in the NEXAFS of the carbon edge similar to the features found in CoC_{60} in section 4.3 (figure 5.15). Analysis of the M-4,5 transitions in Gd also determines whether or not there is any hybridization of the Gd 4f shell. A GdC_{60} bilayer was deposited with Gd(6 nm)/C_{60} (15 nm)/Al(3 nm) such that the magnetic behaviour should be at the thickness limit where the mvT oscillations emerge. The C_{60} was thinner than that used in magnetometry due to the limited escape depth of free electrons in XAS which also limited the cap thickness. The cap was deposited in the same manner as the CoC_{60} bilayers used in section 4.3. The bilayer was measured at saturation at both 4 K and 300 K. At 4 K, the applied field was 3 T and at 300 K was 1 T. The sample was placed

at 45 degrees to the polarization vector of the X-rays after being saturated in plane.

The XAS of Gd at the M-4,5 edge agrees with reports on pure Gd. [228] Though it should be noted that the shielding of 4f electrons means the XAS of the M transition in rare earths is usually unchanged in compounds. However, this does confirm that there is no hybridization between C_{60} and the 4f shell. The expectation value of the spin moment is calculated from the sum rules for the d-f core transition. A full discussion of the derivation of these sum rules can be found in [229] while the physical parameters are detailed in [228]

$$\int_{E_F}^{E}\left[(\mu^{+}_{M_5}-\mu^{-}_{M_5})-\frac{3}{2}(\mu^{+}_{M_4}-\mu^{-}_{M_4})\right]dE=\frac{N}{3N_h}(\langle\sigma_z\rangle+6\langle T_z\rangle), \tag{5.1}$$

where $\mu^{+,-,0}_{M_{4,5}}$ are the XAS with positive, negative and zero polarization at the M4 and M5 edges. N is the sum of the integrals of positive, negative and zero polarization spectra. N_h is the number of holes in the 4f band. $\langle\sigma_z\rangle$ and $\langle T_z\rangle$ are the expectation values of the spin and dipole moments respectively. The values of N_h and $\langle T_z\rangle$ are taken from the Hubbard corrected, generalized-gradient approximation found in [228]. The resultant spin moment, corrected for a 45° projection onto the polarization axis is 3.29 ± 0.02 μ_B per atom indicating moment is supressed even for high fields at low temperatures.

The carbon edge shows a clear peak at 283.5 eV, the position of the hybrid shoulder in the spectra in figure 4.3. At the expected LUMO energy, 284.5 eV, there is a small peak evident. Additional peaks appear at 285.3 and 286.4 eV. The 285.3 eV peak is attributed to C_{60} aggregation while the peak at 286.4 eV corresponds to the LUMO +1. [230] A higher order π^* peak is observable at 287.4 eV, which can be attributed to the LUMO +3, with an additional peak emerging at 289.7 eV, just below the ionization potential, which may be a bound σ^* exciton. [126] There is a feature below the LUMO (282 eV) observable just above the noise. At low temperature, the peak at 283.5 eV is split into two distinct peaks which can be attributed to the T_{1u} and T_{1g} symmetric orbitals which become degenerate at higher temperatures. [231] This indicates that this feature is the LUMO and the energy of the core hole exciton has been reduced as observed in hybridization with transition metals. [232] The magnitude of this peak with respect to the expected LUMO at 284.5 eV indicates a far greater number of C_{60} molecules experience a change in LUMO energy than was observed in Co/C_{60}.

At 300 K, many of the additional features in the carbon edge have been lost. The

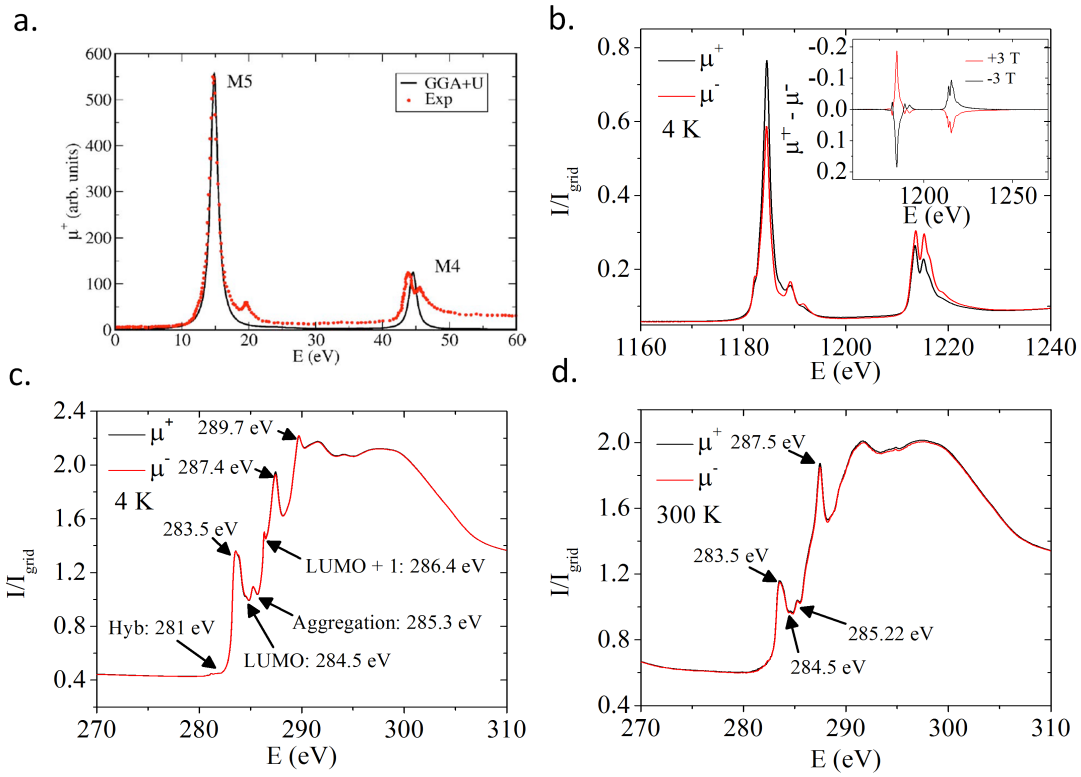

Figure 5.15: XMCD recorded in GdC_{60} bilayer films. a. is a figure adapted from the XMCD study of pure Gd performed by Abdelouahed et al [228] presented for comparison of the $M_{4,5}$ edges. The post-absorption peak structure in both M_5 and M_4 edges is due to core-hole exciton interactions in the 4f shell described in [228] b. Shows the XAS recorded with positive and negative polarization in Gd at 4 K. c. Shows the XAS for positive and negative polarizations at the carbon edge at 4 K. The two polarizations are almost coincident though there is some possible dichroism shown at 287.5 eV shown in the inset. d. Shows the C edge at 300 K.

peak at 283.5 eV and the aggregation peak at 285.3 eV are still present. The other higher order LUMO peaks have been subsumed into the σ* resonance though the peak at the onset of the σ* resonance, which may be a bound σ* exciton, is still present. There is no longer any evidence of splitting in the 283.5 eV peak though the FWHM of the peak is identical at both temperatures indicating thermal degeneracy has merged the two peaks.

A second bilayer was prepared with C_{60} (20 nm)/Gd(7 nm)/Al(3 nm). Due to the surface sensitivity of the XMCD technique, this arrangement provides more information on those carbon atoms closest to the interface. Indeed, this structure revealed a

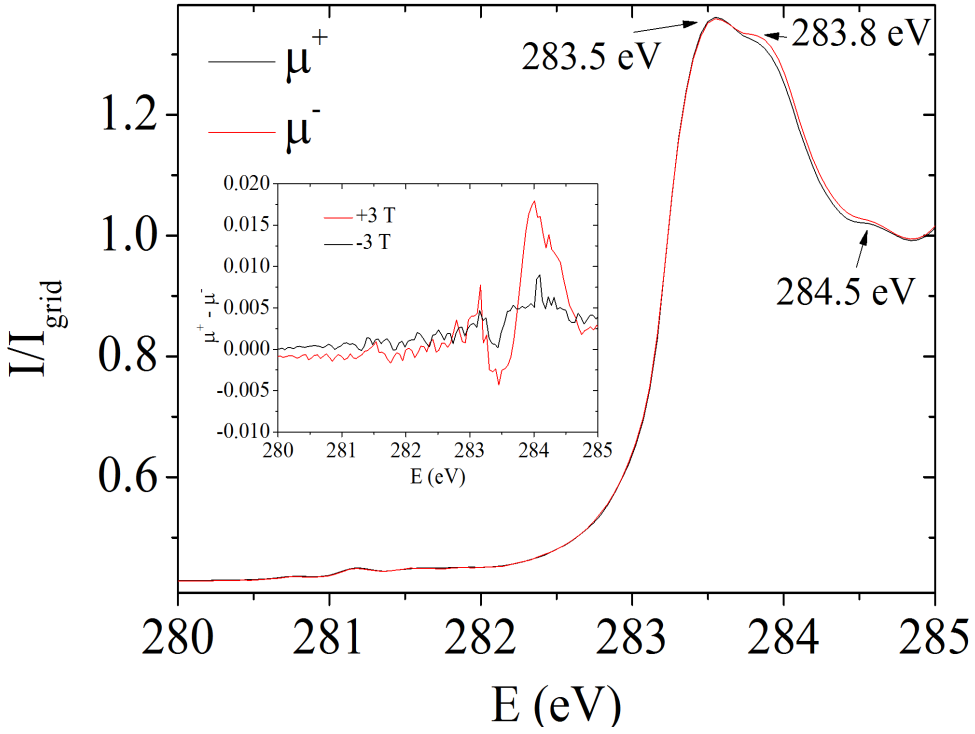

Figure 5.16: XAS in a field of +3 T at 4 K at the carbon edge for both polarizations. Focused on the near edge, it is possible to see it is divided into two peaks. The small features below the edge are also just visible above the background noise at this scale. The XMCD for positive and negative fields is shown in the inset. While the dichroism is evident above the noise in positive fields it does not fully reverse upon changing the sign of the field.

significant peak in the region of the small feature at 282 eV (figure 5.15). Though the effect of the core hole on the energy of the exciton is unknown, this peak falls 2.5 eV below the expected LUMO which should place it below the Fermi energy. [128] The appearance of this peak at the GdC_{60} interface is particularly significant when considering the transport dependent XMCD in section 6.5 which appears after applying a bias voltage to a C_{60} junction. The aggregation and LUMO +1 peaks, 285.3 and 286.4 eV, are entirely absent while a π^* peak is still observable at 287.1 eV as well as the σ^* peak at 289 eV. It is argued that the peak at 282 eV is due to the formation of interfacial hybrid orbitals with energy close to or potentially below the Fermi energy as described in section 2.4. The arrangement of layers in the structure measured in figure 5.16 makes it possible to probe the first ML of C_{60} which would be obscured in figure 5.15 due to the limited escape depth of photoelectrons in C_{60}. The NEXAFS in figure 5.16,

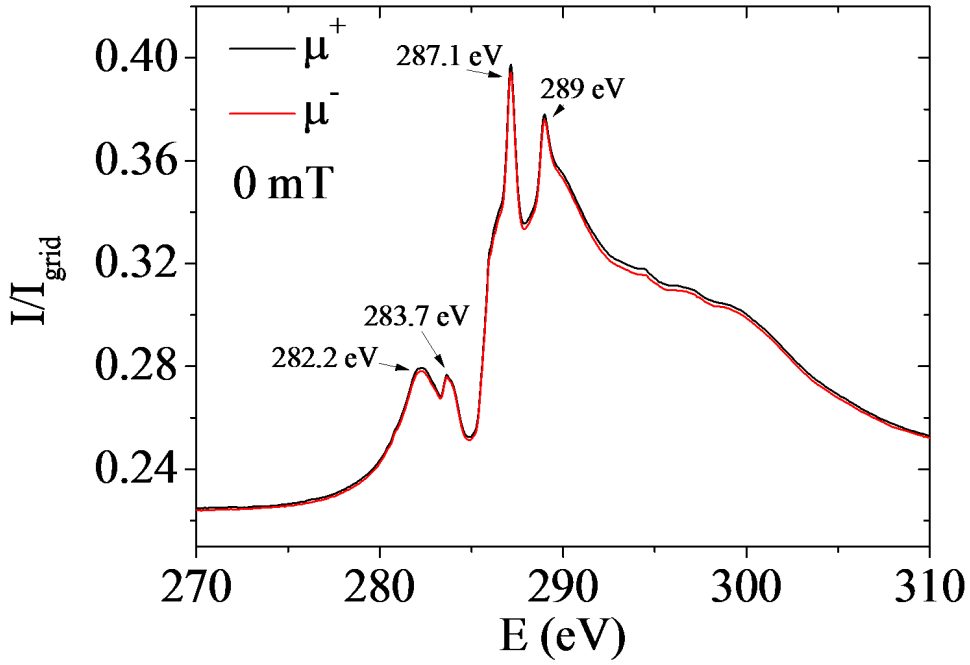

Figure 5.17: XAS at the carbon edge for the bilayer C_{60} (20 nm)/Gd(7 nm)/Al(3 nm) recorded at 5 K in zero field after cooling in zero field from 300 K.

does not resemble graphite [131] or amorphous carbon [233] precluding a graphitic or amorphous surface layer as the origin of the modified edge. Another possibility is that diffusion of Gd into the C_{60} surface results in a metallic state, similar to the metallic states observed in alkali metal doped solid C_{60} above its transition temperature. [234]

5.6 Conclusions and Discussion

The study of CoGd alloys clearly demonstrated that C_{60} can have a profound effect on the compensation behaviour of ferrimagnetic alloys. Control multilayers showed normal compensation indicating it is not the roughness of C_{60} surfaces which is responsible for the modification and very thin C_{60} layers do not eliminate compensation indicating the introduction of impurities is not responsible. The dependence of the compensation behaviour on total C_{60} thickness points to a hybridization process as observed in CoC_{60} multilayers, where the transfer of electrons into the molecular layer as well as the for-

mation of hybrid interface states modifies magnetic properties. However, extrapolating the loss of Co moment due to charge transfer defined in chapter 4 does not explain the behaviour since a transfer of majority spin electrons from Gd is not possible due to screening of the 4f orbital. PNR investigation reveals a complex interfacial structure with a broad interfacial region anti-ferromagnetically aligned to the bulk alloy. The density of this region indicates it is comrpises the surface atoms of the CoGd alloy and interfacial molecules with a total thickness of 1.5 $\pm$ 0.1 nm. This AF coupled region is present above and below the compensation temperature. The ferromagnetic coupling between metal and molecule persists up to 2.8 nm in the C_{60} layer as is evidenced by the fact that the molecular layer switches its polarization through the compensation point. The C_{60} layer is polarized against the Co magnetization indicating the AF coupling observed in section 4.4 extends into this layer.

However, Gd is not inert to interaction with C_{60} as shown in the study of GdC_{60} bilayers. While the superparamagnetic thin layers show saturation close to the bulk value, thicker layers show heavily supressed magnetization. This indicates that while the moment per atom of Gd may be unchanged, at least in the 4f shell, the magnetic order in thin films is altered by interaction with C_{60}. The proposed mechanism for this interaction is a modification of the conduction bands of Gd which influences the magnitude and sign of the RKKY interaction.

While pure Gd shows conventional ferromagnetism owing to the strength of the inter-atomic interactions, most of the heavy lanthanides do not and undergo complex transformations from ferromagnetic to anti-ferromagnetic and paramagnetic phases with increasing temperature involving wave-like, spiral and conical magnetic phases. [40] While Gd shows a canting of the angle of its easy axis away from the c axis in hcp structures, it does not usually show periodic magnetic order, though spiral phases are observed in various Gd-transition metal alloys. [235] Introducing a C_{60} interface gives rise to new magnetic behaviours which have some characteristics in common with the periodic anti-ferromagnetic phases of Ho, Er, and Dy. This involves new low temperature features in the MvT of alloys between 5 and 10 nm accompanied by clear transitions in the susceptibility at the same temperatures. In addition, the resistivity of bilayer films shows unexpected behaviour which can be explained as changes in the spin-disorder scattering due to magnetic phase transitions. In particular, the resisitivity of a GdC_{60} film with an 8 nm Gd layer, which showed the most significant changes

in magnetic moment at low temperature, between the paramagnetic transition at 190 K and the onset of the low temperature magnetization features at 31.5 K indicates some intermediate, disordered phase. Detailed information as to the nature of this intermediate phase will require an additional technique, such as neutron diffraction, to determine whether there are momentum dependent changes in exchange which might indicate Kohn anomalies. However, the polycrystallinity of the sputtered films here presented may prohibit the use of the coherent neutron scattering techniques used to confirm helical magnetic structures in Dy and Er. [236] [237]

XAS of GdC_{60} bilayers show evidence of hybridization at low temperatures, particularly the dominance of a peak at 283.5 eV and the emergence of a large peak at 282 eV when the first ML of the GdC_{60} interface is probed. XMCD could not be observed in this peak as in CoC_{60}. Higher order charge peaks in the carbon edge also indicate a significant charge transfer, though the exact charge per cage cannot be determined by NEXAFS alone. The Gd M transition shows no deviation from its expected structure save that the dichroism indicates a reduced moment per atom: $3.29 \pm 0.02\ \mu_B$ per atom where $7.55\ \mu_B$ is expected. [210]

Further investigation into the induced magnetization of fullerenes may require the use of other ferrimagnetic alloys though further investigation of hybridization with Gd may inform the selection of alloy compositions which show full compensation with thick C_{60} layers. Otherwise, insulating ferrimagnets may offer a possible solution provided hybridization with the transition metal sub-lattice can still be achieved. The possibility of inducing a helical state long debated but conclusively disproven in pure Gd is of particular fascination since it indicates the variety of complex behaviours which become accessible through molecular control of magnetism. It also demonstrates that the direct coupling of molecular orbitals to magnetic orbitals in metals is not the only route to altering magnetism. However, further study is needed to determine the exact nature of the introduced transitions and confirm the existence of a periodic magnetic structure, be it spiral, conical or wave-like. Improving the crystallinity of sputtered Gd films would be key to such a study since the rotation of the easy axis with respect to the c axis of hcp structures is likely to play a role in the low temperature transitions. Future study should include other lanthanides, especially Ho, Dy and Er to determine the effect hybridization has on the existent spiral and conical phases of these metals.

Chapter 6

Spectroscopy During Spin Transport in C_{60}

6.1 Introduction

The previous chapters have discussed the hybridization of molecular and metal orbitals at material interfaces as a method of constructing new and uniquely controllable materials for various spintronic and magneto-electronic applications. However, the bulk of molecular spintronics is concerned with the motion of electrons through molecules and molecular solids. The following chapter will outline research into methods of measuring spin injection into C_{60} using three different spectroscopy techniques which probe different energy scales: Raman spectroscopy which probes the low energy vibrational modes of the molecule and the role of vibronic coupling in spin-transport, photo-luminescence which probes the band gap of C_{60} and the role of excitons and their recombination and X-ray absorption spectroscopy which probes the band structure above the Fermi energy through core-hole excitation and the role of different orbitals in spin transport.

The Raman spectrum of C_{60} has been theoretically modelled in detail with the most accurate being the model of Schettino et al. [238] Ten Raman active modes are expected: the two A_g and eight H_g modes. Experimentally, there has been much discussion about the apparent duality of the Raman active mode frequencies, particularly the dominant $A_g(2)$ mode which, in solid C_{60} films, appears at both 1469 cm^{-1} and 1459 cm^{-1} often simultaneously in the same sample. [239] This doubling has variously been assigned to the photo-assisted intercalation of oxygen, [240] the formation of long-lifetime triplet states [241] and a photo-activated transformation from a rotationally disordered solid phase to an ordered solid phase. [239] Later observations made by Luo et al showed that the Raman spectrum, particularly the ratio between the dual $A_g(2)$ peaks, responded to applied fields which they attributed to the intermolecular coupling of triplet states in C_{60} dimers. [242]

The vibrational modes of C_{60} and their coupling, or lack of coupling, to spin-polarised excited states is a key line of enquiry in organic spintronics. The formation of electron-vibron quasi-particles described in Holstein's model for van der Waals bonded solids, discussed in section 2.3, is key to the transport of electrons between the localised states of C_{60} cages and the formation of a LUMO derived conduction band.[243] Because vibrational modes are strongly dependent on molecular symmetry and are largely intra-molecular, being mostly unaffected by weak inter-molecular forces, the coupling between vibrational modes and electrons can provide a very sensitive probe of electron transport and, potentially, spin transport. [244] A limitation of organic spintronics has

been the difficulties faced in applying common spectroscopic techniques to their study. [245] More specialized spectroscopic tools, such as a probe based on spin dependent Raman spectroscopy, may provide a method for investigating and clarifying some of the more controversial aspects of organic spintronics such as the mechanisms of spin transport and scattering [29], long spin diffusion length in C_{60} [246] or the unexpected lack of the Hanle effect in organic spintronic devices. [247]

A related persistent issue is the measurement of the spin population in organic materials. While MR devices can now be produced and measured to provide qualitatively consistent data, electrical measurements struggle to measure spin population or residence time for a spin polarized electron on a single molecular site. [29] The suggestion that spin polarization could affect recombination processes in organic opto-electronic devices provides a possible route toward a useful probe of spin population via photo-luminescence. [43]

Finally, core excitation spectroscopy techniques such as XAS have been applied to investigating numerous charge transfer processes including hopping. [129] In this context, XAS is a form of pump-probe technique with the 'pump' being the excitation of a core-hole exciton which then forms the probe for processes with a characteristic timescale equivalent to the core-hole exciton lifetime. These techniques are particularly useful in van der Waals bonded solids such as C_{60} because the intra-molecular structure is well preserved in the solid. A review of the use of core spectroscopies in various forms of nano-carbon was prepared by Brünwiler and is found in [128]. In C_{60} the 1s excitation to the LUMO forms an exciton which resides in the HOMO-LUMO gap while the width of the LUMO derived peak provides information on the vibronic coupling and resultant LUMO band-width. The transfer of charge in complexes or at interfaces has been studied in detail in the carbon K-edge including the data presented in section 4.3. [248] [249] However, XAS measurements during spin polarised transport have not been performed. The hopping of the excited core electron before recombination during transport can quench recombination channels, evident as a suppression of the peaks in the XAS corresponding to those channels. As pointed out by Brünwiler: since the core-hole exciton formed by excitation from the 1s level to the LUMO lies in the gap, there should be minimal diffusion of the excited electron to adjacent molecules in equilibrium conditions. However, Lof et al note that any change in the charge state of C_{60} produces a significant perturbation to the band structure. [77] Therefore, XAS

performed during transport should show significant changes in the LUMO and higher order peaks due to charge transfer only in the case that an external potential causes a hopping event before recombination of the core exciton providing potential insight into hopping time, recombination pathways and changes to the symmetry or orbital structure of the molecules.

6.2 Spin Dependence of Photoluminescence Quenching

The photoluminescence spectrum of C_{60} was studied using the Raman optics described in section 3.3. The excitons were generated using a 473 nm blue diode laser. The PL spectrum showed two peaks at 1.69 and 1.51 eV corresponding to the Frenkel exciton recombination and main phonon replica respectively (figure 6.1). [146] Exposure to a high intensity with the 473 nm laser over a period longer than one minute produced some change in Pl intensity due to bleaching. The beam intensity was restricted to $\approx$ 0.1mW. Scans which caused any visible photo-bleaching of the film on inspection were discounted from the data set.

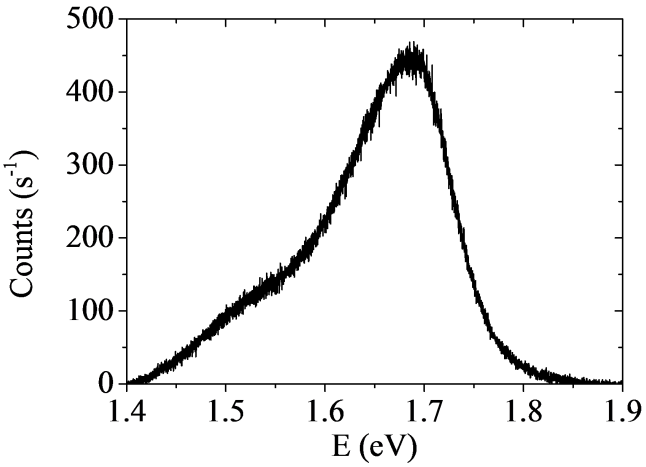

Figure 6.1: Typical photoluminescence recorded from a C_{60} film using a 473 nm laser. At 300 K, the only clear features are the Frenkel exciton at 1.69 eV and the phonon replica at 1.51 eV.

In order to determine the effect of hybridization on the luminescence, electrodes were deposited in a junction configuration onto a silicon dioxide substrate and a C_{60} layer deposited on top such that regions of hybridized C_{60} and pristine C_{60} could be identified on the same sample. The sample structure was Au(5 nm)/Co(5 nm)/C_{60} (20

nm)/Al(5 nm). Scans were taken in a regular grid pattern over the sample surface in the region of the junction allowing a map of the various features to be created. The position and ratio of the Ag(2) peaks were not found to vary over the sample surface though the intensity of the Ag(2) peak is highly supressed over the region of the Co electrode. The photoluminescence spectrum varied depending on the sample region. In particular, the PL was quenched over the Au and Co electrodes (figure 6.2). Applying a 250 mT field out of plane to the Co electrode further modifies the spectrum, reducing the PL quenching, but less so over the Co electrode than the Au electrode. The position of the highest peak in the PL was also observed to change slightly in different regions of the sample. Over the Co electrode, the Frenkel exciton exists at a slightly lower energy (1.68 eV) while over the Au electrode it exists at a slightly higher energy (1.7 eV).

PL quenching in proximity to metal surfaces is well known, having been studied in fatty acid films by Drexhage and explained in both classical and Quantum Electro-Dynamic theoretical frameworks by Chance. [250] [251] Two mechanisms are described. First, an exciton can decay without emitting a photon by dissipating energy into the nearby metal and second, the metal surface can act as a mirror to reflect the emitted radiation in the near field resulting in destructive interference. Kuhnke et al studied PL quenching of C_{60} films in proximity to Au and Ag films at various distances from the metal surface and found that non-radiative damping processes significantly altered exciton lifetime. [41] We expect that in close proximity to the metal interface, coupling of dipoles to surface plasmon modes is responsible for the PL quenching. A detailed description of the damping process, as determined by Kuhnke using the Persson and Lang model, is found in [252]. Simply, oscillations of magnetic and electric dipoles in proximity to a metal induces free electron motion, dissipating energy into the metal lattice.

The current experimental set up is not sufficient to distinguish the precise damping mechanisms since there is currently no means to detect exciton lifetime or surface plasmons in the underlying metal. Many different exciton decay mechanisms in C_{60} are discussed in literature which may or may not be affected by metal interfaces (such as the Herzberg-Teller mechanisms involved in singlet exciton decay [253], second harmonic generation [254], intermolecular charge transfer [255] or formation of triplet excitons [148]) but the study of Kuhnke already presents extensive detail on this subject. [41] The changes observed here all occur in the region of the Frenkel exciton at 1.69 eV and

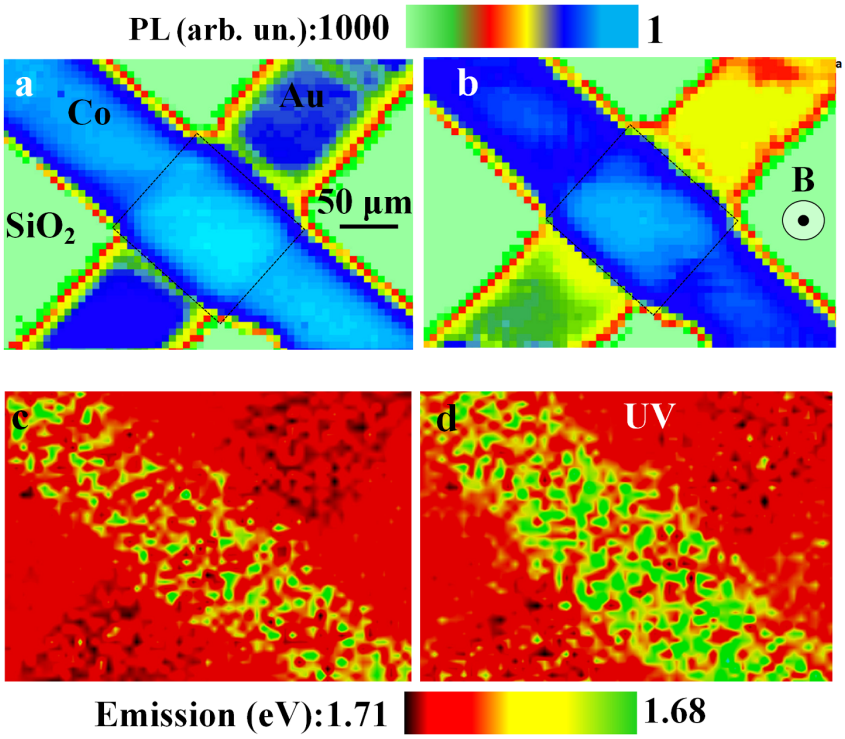

Figure 6.2: a. Map of the junction area showing the Co and Au electrodes. The PL intensity is quenched over the metal. b. Map of the same area with a magnetic field applied. Note that both electrodes show increased PL intensity but the Au electrode is increased by a larger fraction. c. Shows the Frenkel exciton energy with red and black being higher energy and green lower energy. d. Shows the Frenkel exciton energy while the junction is irradiated with UV light. This figure is a reproduction of figure 2 from [244] originally created by Dr Oscar Cespedes.

the phonon replica at 1.51 eV.

Despite the lack of detailed information regarding the quenching mechanism, this work can add to the canon of PL quenching the additional observation that quenching is greater over Co and Au. It is expected that this is evidence of the greater electron transfer from Co to C_{60} of 1.3 electrons per cage as opposed to Au of 0.2 electrons per cage.[94] There are several possible interpretations of the increased quenching. First, the DFT study referenced in [169] indicates metallic interface states in the fullerenes. Since the damping is distance dependent, creating metallic states in the first few ML of the molecular solid would effectively move the metal surface closer to a given dipole increasing the damping experienced by that dipole. Second, the greater transfer of charge

into the fullerene layer might suppress PL by reducing unoccupied LUMO states, decreasing quantum efficiency, and providing additional damping mechanisms through the coupling of oscillating dipoles to stable charged fullerenes. In a more complex picture, additional charge may also affect the radiative decay of excitons by altering the available decay paths, such as the decay of the singlet exciton via vibronic, inter-molecular exchange. [253] The spin polarization of transferred electrons could also suppress the formation of singlet excitons in favour of triplets with a much longer lifetime. [43] [148] More detailed information regarding the decay mechanisms involved could be obtained by measuring the separation dependence of PL quenching. This would require a single monolayer of C_{60} separated from the metal surface by an insulating barrier of well-known thickness analogous to the Kuhnke study.

Further insight is provided by the application of an out of plane field of 250 mT. The application of this field increases PL over the metal electrodes. However, while PL over the Au electrode recovers to 40% of its unquenched value, the recovery over Co is only 10%. Two key differences between these regions can be considered. First, hybridization between Au and C_{60} is weak and involves only a small electron transfer of 0.2 electrons per cage as opposed to 1.3 in Co. Second, the ferromagnetism of the Co electrode induces magnetic ground states in C_{60} such that the partially occupied hybrid bands are spin split and couple anti-ferromagnetically at the interface as discussed in detail in chapter 4. It is clear that the difference in PL is couched in the magnetic coupling between Co and C_{60}.

It is convenient to first consider the recovery of PL over the Au electrode. Investigations of recombination of singlet excitons in C_{60} indicate that an electric dipole transition is forbidden and the recombination occurs either through a magnetic dipole transition or through a Herzberg-Teller mechanism. [148] [41] The interaction between magnetic and electric dipoles and metallic surface has a complex orientation dependence. The review by Barnes gives some detail of the expected energy loss mechanisms for different electric dipole orientations. [256] Assuming orthogonality between the electric and magnetic dipole solutions, a transition from an isotropic distribution of orientations to a perpendicular orientation of magnetic dipoles should lead to a larger fraction of radiated energy and a lower energy loss to surface plasmon modes (figure 6.3). This is supported by the early discussion of magnetic dipole orientation by Lukosz and Kunz, though their discussion is more focused on partially reflective semiconductors

and is not a direct comparison. [257] The orientation dependence of magnetic dipole decay is well known, to the extent that Noginova et al have proposed its application as a probe of local magnetism in the near field. [258]

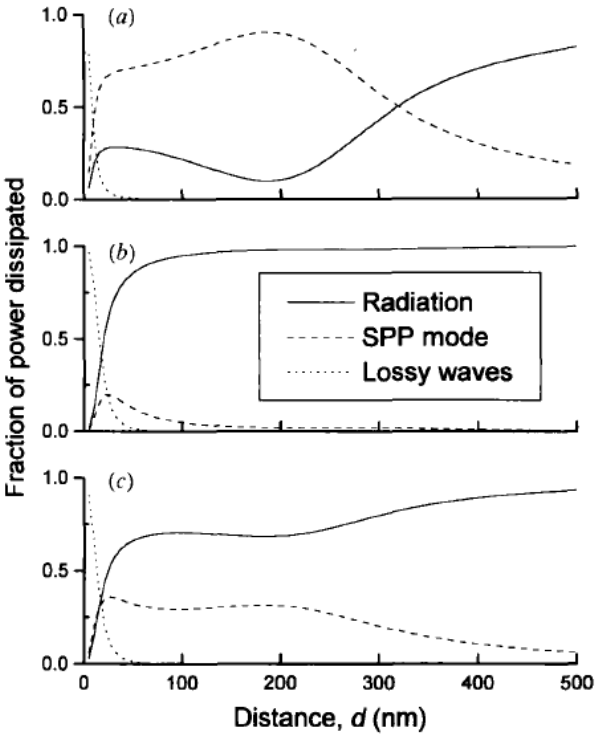

Figure 6.3: Figure taken from [256] showing the different mechanisms by which power may be dissipated from an electric dipole depending on its orientation to and distance from a metal surface a. perpendicular orientation, b. parallel and c isotropic. It is assumed that magnetic dipoles would be orthogonal. The "lossy waves" are electron density oscillations distinct from SPs described by Ford and Weber in [259]

In the case of the Co electrode, a field of 250 mT is insufficient to saturate the magnet out of plane. The small recovery can then be assigned to a small rotation of the magnetization vector perpendicular to the metal surface while it remains mostly in plane. The interfacial magnetic states in the C_{60} described in chapter 4 are coupled to the Co magnetization. Thus, in this region the magnetic dipoles are still mostly in the parallel regime and lose a higher portion of their energy to surface plasmons and lossy waves in the metal.

Finally, we must consider the PL peak position. Becker et al have observed shifts

in PL peak emission in the polymer PPV on aluminium films. [260] This is attributed to wavelength dependent changes in quantum efficiency as a result of interference between the evanescent waves in the metal film and the emission from the polymer. While interference cannot be discounted in this set up, the prior discussion points toward non-radiative decay paths as being dominant where the PL is quenched. Instead, the PL peak shift is attributed to phonon-induced spin flip events. As discussed, the spin polarized charge transfer between Co and C_{60} would increase the formation of triplet excitons or triplet charge transfer states which reduces recombination at the Frenkel exciton energy. [43] The triplet state is far longer lived than the singlet (lifetime is typically milliseconds rather than the 1.8 μs expected for radiative decay of singlet excitons). [261] [262] However, electron spin resonance (ESR) studies of the dynamics of the triplet exciton indicate an intermolecular recombination process mediated by polarons which can enhance photoluminescence. [263] It is, therefore, expected that phonon induced recombination will increasingly dominate photoluminescence where quenching is due to triplet formation either due to spin flip events from phonon scattering or because of the coupling of excitons and phonons to create polarons which facilitate intermolecular decay processes. However, as the detailed understanding of photo-physics in C_{60} thin films is not yet matched in CoC_{60} composites, this conclusion is not yet confirmed. The larger shift in PL peak position observed during UV radiation at 6 eV can be interpreted as either an increased charge transfer from the metal due to the photo-electric effect, further increasing polarization and triplet formation in C_{60}, or an increase in recombination events due to photo-induced intermolecular charge transfer facilitated by UV photons. [255]

The presence of metal layers clearly quenches PL as expected from the literature but this study adds the observation that the magnetic coupling between Co and C_{60} produces greater quenching and shifts the PL peak to lower energies. While a few possible explanations have been presented here, future study may reveal precisely how the transfer of spin polarized electrons into C_{60} can affect recombination pathways and the coupling of magnetic dipoles to metal films. A detailed understanding of the spin dependence of optical properties in C_{60} would be vitally important to spintronic applications of C_{60} since mechanisms for manipulating exciton lifetimes in molecular films will also allow manipulation of conductivity in optoelectrical devices. [43]

6.3 Raman Spectra of C_{60} During Transport

A 20 nm film of C_{60} was used to provide a reference for further measurements (figure 6.4). This control used a 5 nm Al cap requiring slightly higher laser intensity to produce a good signal to noise ratio. Because of the threat of photo-assisted polymerization or oxygen diffusion, all measured changes in the Raman spectrum were compared in multiple scans at the same point in order to establish if changes occurred solely due to the action of the laser. [240] [264] All spectra are composed of multiple acquisitions with a minimum of three scans used to filter out transient peaks.

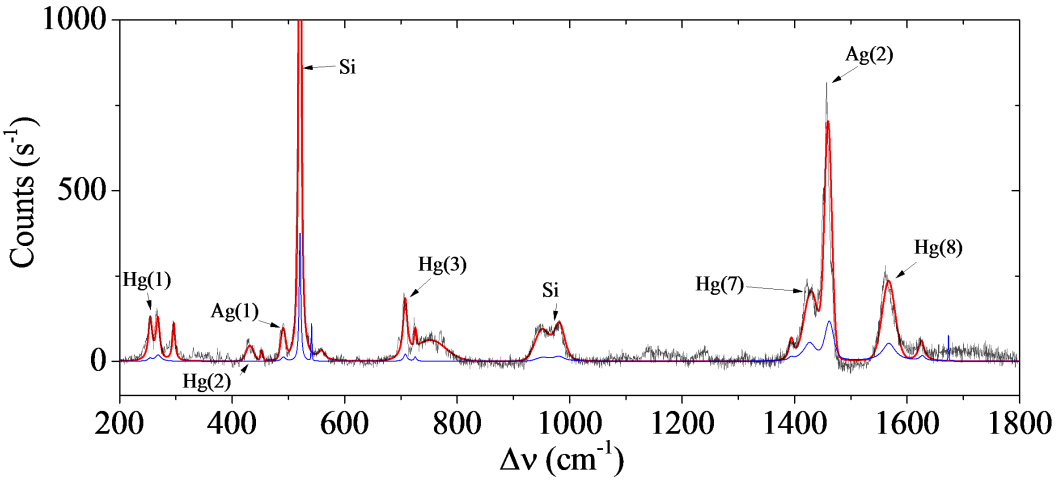

Figure 6.4: Spectra collected from a 20 nm C_{60} film. The black line is the original data and the red line a fit taking into account all discernible peaks. The blue line is the signal recorded using a blue laser at 473 nm, the other data is collected using a green laser at 532.01 nm. Seven of the expected ten peaks are observable. Hg (4,5,6) are of typically low intensity and may well be subsumed into other features or background noise. [153] The substrate peaks at 521 cm^{-1} and 970 cm^{-1} are clearly identified. [177] The splitting of the Hg (1) peak and negative offset of the Hg (8) peak are indicative of some degree of polymerization. [265] The additional peaks can be traced to either the formation of amorphous carbon regions during the deposition of the cap or the presence of aluminium oxide in the cap. [266] [267]

Junctions for Raman spectroscopy were deposited using shadow mask deposition detailed in section 3.1.5. C_{60} sublimation was performed using a filament current of 21.5 A which resulted in a film growth rate of 0.8 - 1.2 $Ås^{-1}$ in an atmosphere of less than 0.01 mTorr and water vapour and oxygen partial pressures of less than 10^{-8} Torr and 10^{-9} Torr respectively. The structure was Co (5 nm)/AlO_x (1.4 nm)/C_{60} (40

nm)/AlO_x (1.4 nm)/Au (5 nm) where the bottom cobalt layer comprises the bottom electrode and the top Au layer the top electrode.

The double alumina barriers decouple both interfaces from the C_{60}. This ensures that any effects observed will be solely a property of charges involved in transport and not interfacial potentials. The barrier between the Co electrode and C_{60} has the additional advantage of conserving the polarization of the Co electrode during spin injection. Each barrier is deposited using plasma oxidation. A 1.4 nm Al layer was first deposited before raising the partial pressure of oxygen to create an oxygen plasma which is maintained for 40 s. The process of producing tunnel barriers for C_{60} devices in this apparatus was optimised by May Wheeler. [268] The ideal gas flows determined through this optimisation were 16 SCCM of argon and 76 SCCM of oxygen creating a total chamber pressure of 7.2 mTorr. Because the upper alumina barrier provides an effective barrier to C_{60} oxidation and the deposition of further Al capping layers only risks creating additional current pathways, no further cap was deposited.

These junctions were entirely linear within the limit of $\pm$0.2V. Higher bias was not used since it was observed that this could cause irreversible changes in the junction resistivity which was attributed to the penetration of the alumina tunnel barriers by pinholes. The resistivity of the double barrier junction was 1.51 $\pm$ 0.01 MΩ. Wheeler observed small but detectable MR in similar junctions with C_{60} layers up to 60 nm thick at low temperatures and 20 nm thick at room temperature. The study performed by Zhang et al also indicates spin diffusion lengths up to 100 nm at room temperature. [246] The magnetic electrode is grown such that the magnetocrystalline easy axis lies along the electrode length. The electrode is also magnetized using a permanent magnet at 250 mT prior to measurement.

Raman spectra were acquired at different points on the IV with constant current densities from a DC source (figure 6.5). Negative currents inject non-polarized electrons from the Au electrode. Positive currents inject electrons from the Co electrode with a net spin polarization. The junction area is $10^4 \mu m^2$. When current flows from the magnetic electrode, the Ag(2) peak is clearly split with a dominant main peak, identified as Ag(2) at 1466 cm^{-1}, and a smaller sub-peak, Ag(2)' at 1459 cm^{-1}. The positions of these two peaks vary as a function of current direction but are separated by $\approx$ 10 cm^{-1}.

The appearance of the Ag(2)' peak is dependent on both the current set point and

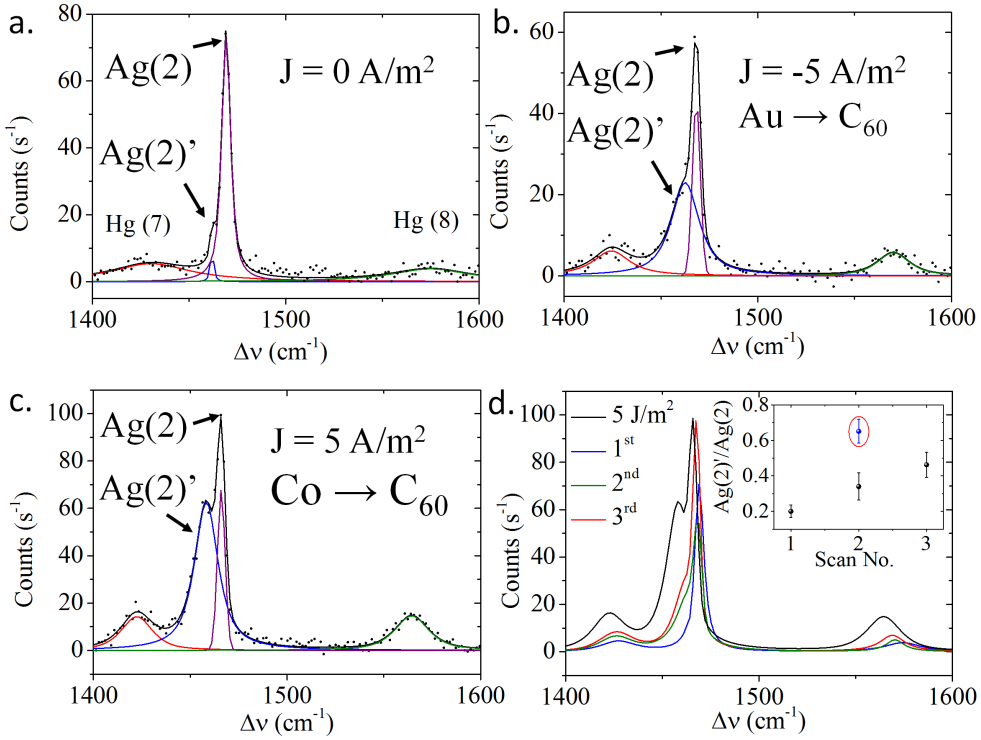

Figure 6.5: Raman scans of the region of the Ag(2) peak with different current densities. Each peak region is fitted with the Hg(7) and Hg(8) peaks and the split Ag(2) peak. a. Zero current flow. Note that while the Ag(2)' peak is still present, its intensity is near the level of background noise. b. Negative current, electrons are coming from the Au electrode and are unpolarized. c. Positive current with a net polarization from the Co electrode. d. 0 current density scans taken at various points to check for irreversible photo-polymerisation. Scan 1 was taken in the pristine state. Scan 2 after all subsequent current dependence scans were completed and scan 3 after leaving the junction attached to an external ground in a dark cabinet for 2 minutes. The inset shows the ratio of the Ag(2) peaks. The red circled blue data point is the ratio during transport with a current density set point of 5 J/m^2 corresponding to the data in c. and the black curve in d.

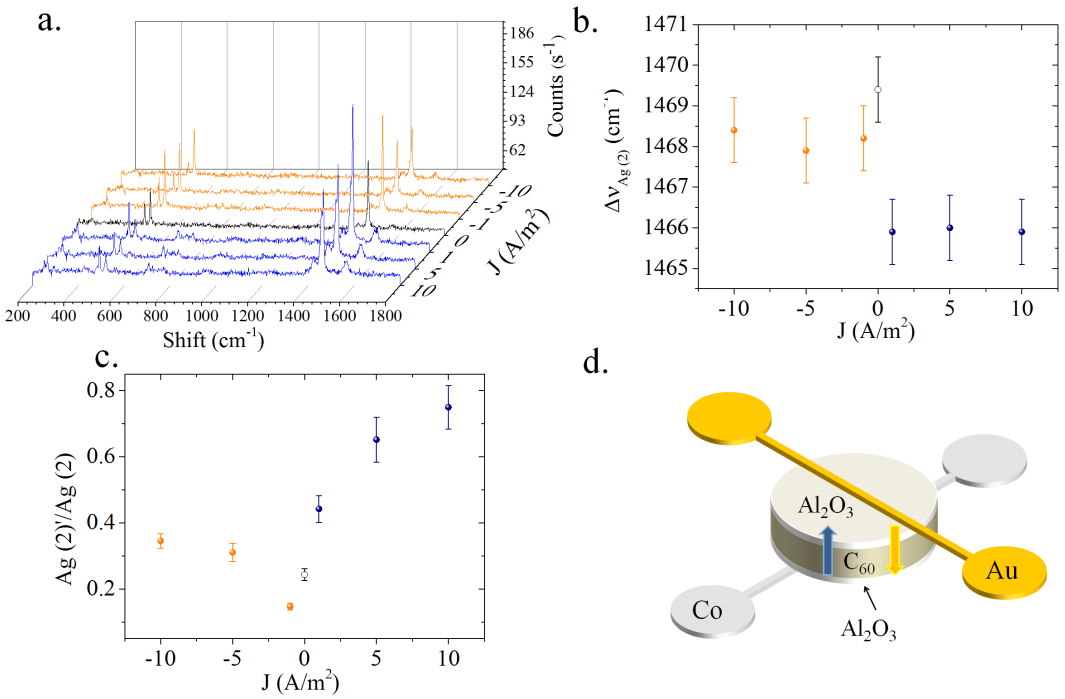

Figure 6.6: a. Raman spectra recorded from the junction Co (5 nm)/AlO_x (1.4 nm)/C_{60} (40 nm)/AlO_x (1.4 nm)/Au (5 nm) for different current densities. Orange denotes current sourced from the Au side and blue from the Co side. b. Shows the position of the Ag (2) peak for these current densities. c. shows the ratio between the Ag(2)' and Ag(2) peak. d. Shows the junction structure with colour coded arrows denoting the flow of negative charge.

the sign of the current. When no bias is applied and current density is zero, the Ag(2)' peak is almost at the level of noise. With current sourced from the Au electrode, the relative magnitude of the Ag(2)' peak increases. When a current sourced from the Co electrode, The Ag(2)' peak is significantly increased. The pump-probe study by Jeoung et al points to new Raman peaks emerging as a result of the triplet exciton in C_{60}, one of which appears at 1461 cm^{-1}. [241]

The study by Akers et al [239] indicated that the split Ag(2) peak could not be attributed to a triplet state because of the lack of triplet-triplet absorption and the fact that there was no observed depletion of the C_{60} ground state equivalent to the excitation of triplets. The contemporaneous study by Sauvajol et al [42] showed that the split Ag(2) peak could be progressively excited with increasing pump laser pulse power and was wholly reversible but only at low temperature. This agrees with an

earlier study which attributed the new peak to triplet excited C_{60} at 40 K. [269] Notable in all these studies is that the lower wavevector of the Ag(2) peak is attributed to a lowering of the symmetry of the molecule. The formation of a molecular dipole due to exciton formation should lower the symmetry of the molecule, giving rise to the additional peak. However, the relative magnitude of the Ag(2)' peak is greater when the current is sourced from the Co electrode, even when the current density is identical.

In an extended band scheme, the population of triplet and singlet excitons should occur with a 3:1 ratio when one or fewer electrodes have a net spin polarisation independent of the current direction. This assumes that the population of singlets and triplets exists at equilibrium over long time periods. However, this assumption fails if there are spin selective recombination processes.

Since electrons sourced from the Co or Au electrode should result in equal numbers of triplet excitons, it follows that the greater polarisation of electrons when the current is sourced from Co is responsible for the difference in the Raman spectra. The study of organic opto-electronic devices in high magnetic fields by Wang et al showed that spin polarized currents affect the number of singlet and triplet charge transfer states. That is, states formed by intermolecular interaction between electrons and holes on different molecules. [43] In C_{60}, intersystem crossing from singlets to triplets occurs easily since the energy difference between the triplet and singlet is smaller than the hopping energy: 0.37 eV in comparison to 0.5 eV. [150] Where electrons are spin polarised, charge transfer states and intersystem crossing processes may lead to a higher population of triplets. Alternately, intermolecular interactions may affect the mobility of spin polarised electrons leading to a larger number of C_{60} anions or trapped excitons when injected electrons are spin polarised.

Further study of the dependence of the Ag(2) peaks proceeded un-systematically so as to exclude photoassisted transformations (figure 6.6). Alternating negative and positive current densities were used and zero current measurements were taken before and after to observe irreversible changes. While some photo-polymerization has clearly occurred, as can be seen from the appearance of the Ag(2)' peak after measurement (figure 6.5 d), this cannot account for the intensity of the Ag(2)' peak when a current is sourced. In addition, the expected depletion of the ground state is observed as the Ag(2) peak is reduced with respect to the Ag(2)' peak. Finally, a displacement of the Ag(2) peak is observed which only occurs when the current is sourced from the magnetic

electrode. These results confirm that the Raman spectrum in the region of the Ag(2) pentagonal pinch mode is dependent on current and that the relative magnitude of the Ag(2)' peak is dependent on the injection of spin polarised electrons.

6.4 Photoluminscence of C_{60} During Transport

Following this observation, measurements of the PL during transport were performed in order to determine whether there was a reduction of the PL which might betray the presence of long-lifetime triplets (figure 6.7). A double barrier junction was deposited with the structure: Py (30 nm)/AlO_x (1.4 nm)/C_{60} (20 nm)/AlO_x (1.4 nm)/Au (5 nm). Py has the advantage of a slightly higher spin polarisation (40% over 37.5%) [270] [271] and is more resistant to oxidation than Co reducing the risk associated with accidental over oxidation of the barrier. [272] PL spectra were recorded in the junction intersection using a 473 nm laser. The metal interfaces still reduced the peak intensity but the oxide barrier also served to separate the interfaces, reducing quenching. The application of an out of plane field is observed to increase the PL intensity both with and without bias in a manner analogous to section 6.2. The exception to this is when an out of plane field is applied while a current is sourced from the Py electrode.

On sourcing a current through the junction from the Py side, the PL intensity was observed to drop. This might be understood in terms of the negative photoluminescence effect. This occurs when there is some method of carrier extraction from a semiconductor, such that all the excitons generated by incident light do not necessarily recombine to produce luminescence leading to a departure from Kirchhoff's Law. [273]

As discussed in section , when electrons are spin polarised, intermolecular interactions may lead to different hopping times and different singlet/triplet populations due to intersystem crossing and charge transfer states. The extraction of electrons or holes from a localised exciton would reduce PL in the same manner as the NPL mechanism described above. However, the lack of a significant change in the PL intensity when a current is sourced form the Au electrode indicates this is dependent on the spin polarisation of electrons. Greater generation of triplet charge transfer states would reduce PL intensity since recombination of triplet excitons is spin forbidden and decay must occur via intersystem crossing instead producing phosphorescent emission. [262] This is illustrated in figure 6.7b.

A spin polarized exciton can be created or can decay in the absence of a magnetic

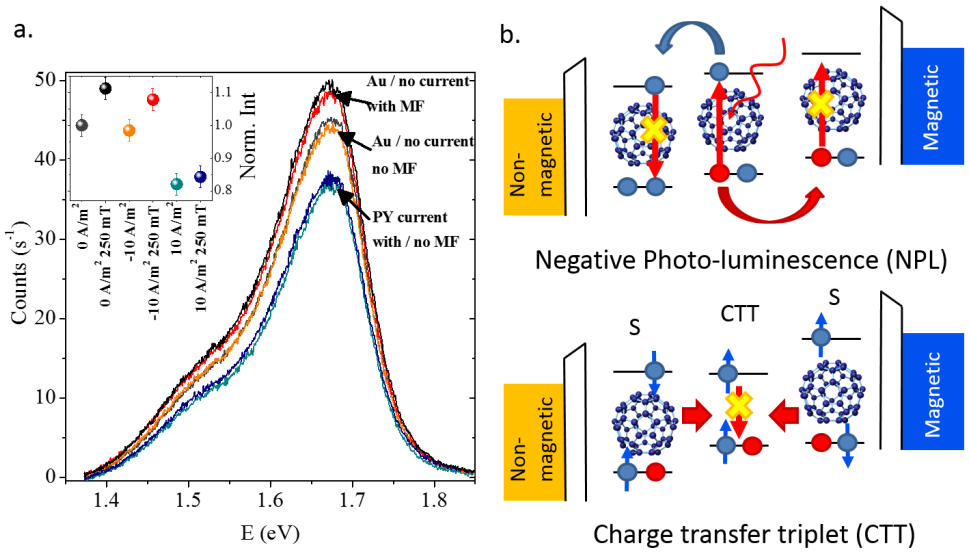

Figure 6.7: a. PL spectra recorded from the junction centre at different current setpoints and applied fields. The inset shows the intensity of the Frenkel peak normalized to the zero-current, zero-field intensity. b. Shows a diagram of the NPL mechanism in organic materials, the photo-excited carrier is extracted due to the bias before recombination. If electron hopping times are spin dependent, this process would be different depending on the sign of the current. The lower panel shows two non-polarised excitons interacting to create a triplet state through charge transfer. The triplet cannot recombine due to the Pauli exclusion principle and must decay via intersystem crossing to a spin singlet. This figure is a partial reproduction of figure 3 from [244]

field through the absorption or emission of a circularly polarized photon through spin-orbit coupling. [274] This makes circularly polarized luminescence spectroscopy (CPL) an efficient method of determining spin polarization in many semiconductors. [275] However, the emission of circularly polarized photons during recombination is generally facilitated by spin-orbit coupling of the electronic states in question. [276] In C_{60} low spin-orbit coupling should make it unfavourable for spin polarized excitons to recombine through the emission of polarized photons.

It is notable, however, that the curvature of the C_{60} molecule increases spin orbit coupling compared to other carbon allotropes. [136] Measurement of the fraction of luminescent photons with CPL would determine the extent of recombination of spin polarized excitons. [150] Morphology is known to profoundly affect the decay of ex-

citons in many organic crystals, including C_{60}, particularly the decay of singlets into triplets, trapping of excitons and spin-flip events which may affect the magnitude of PL reduction due to spin injection. [277] [278] These effects will affect the PL reduction during spin injection making it difficult to determine the exact polarization of the injected current.

The use of spin-polarized electron transfer has already been employed to improve the performance of organic photo-voltaic cells by increasing carrier lifetime through exploiting spin-forbidden recombination in a manner very similar to the model proposed here. [279] This is supported by the fact that the recovery of PL intensity with out of plane fields does not occur when the current flows from the Py electrode. The effect of proximity to metal interfaces, as discussed in section 6.2, is to provide non-radiative decay paths for excitons and to damp the oscillation of magnetic or electric dipoles such that energy is lost to the metal surface. When magnetic dipoles are aligned perpendicular to the surface, the non-radiative decay of excitons is lessened and there is a recovery of radiative decay paths. However, if radiative decay paths are spin-forbidden, there should be no recovery of PL with magnetic dipole orientation, only a reduction of energy dissipated into the metal which would not affect the PL intensity.

6.5 XAS with Simultaneous Transport

As described in section 6.1, core-hole excitation spectroscopies are a useful probe of charge transfer dynamics and band-structure: dynamics because of the use of the core-hole exciton as a local probe with a characteristic timescale given by its lifetime; and band-structure because of its element specific excitation allowing the contribution of different elements to be distinguished. XAS has been used in C_{60} to probe charge transfer complexes and interfacial hybridization but has yet to be applied to probing spin transport in fullerene solids. [128]

Junctions were deposited in a single barrier configuration: Ta (3 nm)/Co(30 nm)/AlO_x (1.4 nm)/C_{60} (15 nm)/Mn (3 nm)/Al(4.5 nm), see figure 2.10 for the attenuation expected here. This structure was intended to allow observation of C_{60} molecules close to the tunnel barrier and the transport of spin polarized electrons through the molecular layer. The thin Mn electrode was included as a paramagnetic probe of local magnetism though in practice its roughness and small signal precluded this use. The inclusion of the Ta seed layer was required to seed the Co layer, and was found to improve the yield

of intact tunnel barriers during sample optimisation. While it is possible that the Co and Ta shadow masks did not entirely overlap, the factor 10 difference in the thickness should ensure that polarized electrons from Co are significantly involved in transport. The junction had a resistance of 320 kΩ at room temperature indicating that both C_{60} molecular film and tunnel barriers were intact. Applied voltages were kept below 100 mV in order to avoid breakdown of the barrier.

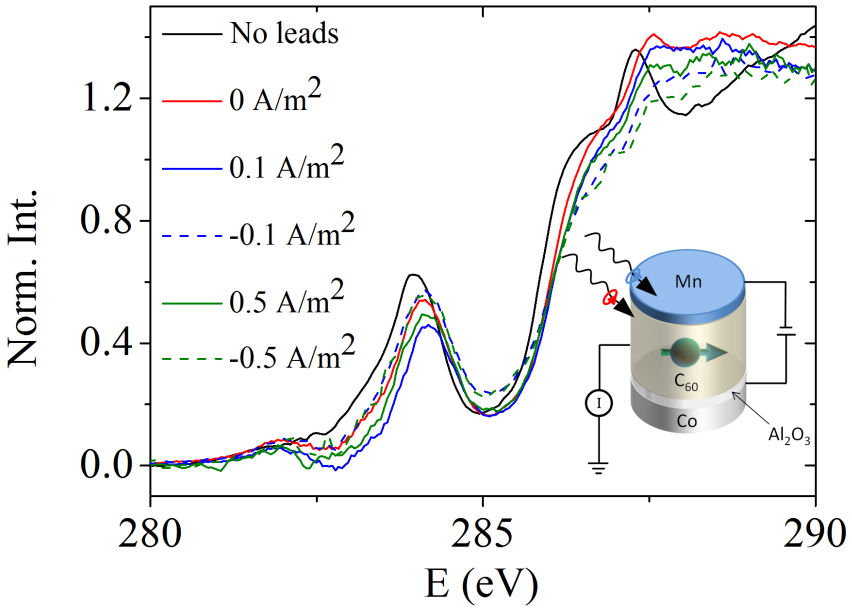

Figure 6.8: The carbon K-edge recorded for the C_{60} junction at various current setpoints. The black line shows the signal when the sample is isolated from the current source. The red when the current source is attached but no current is sourced. The dotted lines show the equivalent negative current densities for the blue and green lines. Positive current densities source a polarized current from the Co electrode, negative source a current from the Mn electrode.

The junction was attached to a gold coated plate with isolated transport contacts in a four point configuration. A drain contact was made between the molecular film and the gold coated plate using conducting carbon tape with a coating of colloidal silver to improve conductivity. This plate was then attached to a motorized arm in the endstation of the BOREAS beamline in the ALBA synchrotron. The four transport contacts were threaded through a shielded cable and contacted to a floating current source. The drain contact was threaded through a separate cable and the TEY measured by a nanovoltmeter between the drain and ground. See figure 3.11. The lifetime

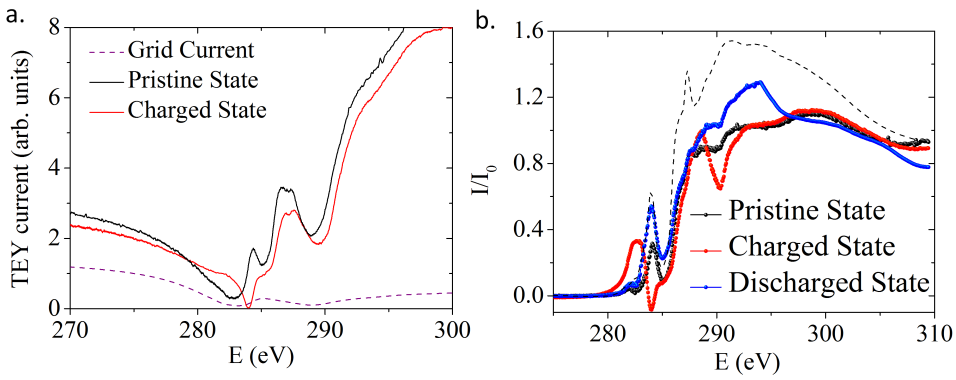

Figure 6.9: Carbon K-edge recorded before application of an external bias (pristine) after the application and removal of a bias but before grounding (charged). a. shows the un-normalized TEY current and the TEY current measured at the Au calibration grid. b. shows the normalized TEY current in the different states and the recovery of the intial state (discharged) after connected the electrodes to a common ground. The dotted black line in b. shows the signal obtained from a pure C_{60} film without contacts.

of the C 1s exciton in C_{60} is estimated to be 6 ± 3 fs while the hopping time at room temperature is predicted to be around 40 ps making the core-hole exciton a probe of the instantaneous state of the C_{60} molecule during transport. [129] [280]

During transport, the noise level in the NEXAFS was significantly increased due to TEY signal draining into the electrodes or injected current escaping into the drain contact. Noise was higher when the current was sourced from the Mn electrode due to the junction asymmetry. At room temperature before electrical contact was made, the carbon edge showed the LUMO at 284 eV and a second peak at 287 eV which may be attributed to the LUMO +2. [231] A small feature is observable in the pre-edge structure at 282 eV which can be attributed to hybridization and charge transfer and also appears in GdC_{60} in section 5.5. With the electrodes attached, the edge appears shifted by 0.2 eV with a clear separation between the LUMO and the feature at 282 eV. The peak at 287 eV is lost in the noise near the σ resonance. Sourcing a positive current, with electrons moving into C_{60} from the Co, the LUMO appears slightly suppressed while a negative current produces no change with respect to the zero current edge. This may indicate some occupation of the LUMO during transport though it is difficult to draw this conclusion due to the increased noise, figure 6.8. The connection of electrical contacts clearly does affect the edge due to the draining of TEY current.

A very clear change occurs when the bias is removed. After sourcing a current and removing the external bias without making a connection to ground, the edge is modified, figure 6.9. This modification is identical whether the current is positive or negative and persists for periods in excess of 30 minutes during measurement.

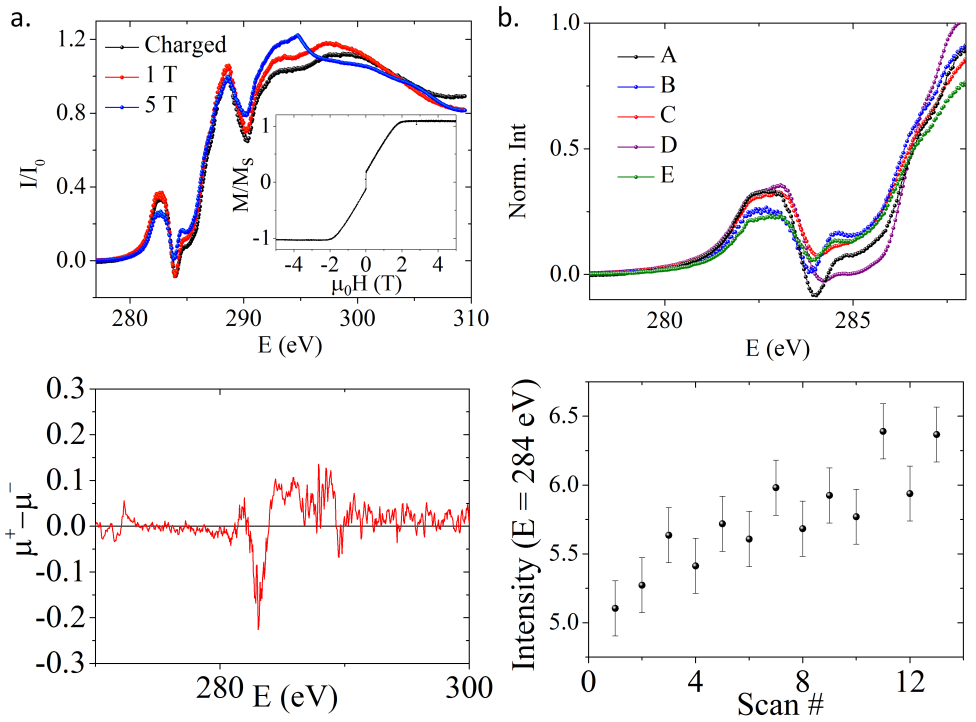

Figure 6.10: a. Carbon K-edge observed in the modified state after pulses of out of plane fields. b. Zoom of the LUMO region in various states: A Shows the state immediately after charging. B After a 5 T out of plane field pulse. C Shows the state after discharging and recharging without further magnetization of the Co electrode following B. D Shows the result of discharging, saturating the Co electrode in plane with a 5 T field and recharging. E shows the result of demagnetizing the electrode using an oscillating in plane field. c. Dichroism measured in the charged state, averaged over 23 scans, the most significant difference is measured in the 282 eV peak. d. The normalised intensity at 284 eV for progressive scans showing some affect of the beam. However, the total affect after 12 scans is only 1.5 cps while the change induced by demagnetization is more than 4 cps between two consecutive scans.

The modification is characterised by a suppression of the LUMO peak to zero intensity while the peak at 282 eV becomes dominant. It is vital before attempting to analyze this edge to address some artefacts introduced by normalization. Because hy-

drocarbon contamination is common the normalization signal obtained from the gold grid has an absorption peak in the region of the carbon edge. For large signals, this has the effect of reducing the intensity of the LUMO at 284.5 eV. In most measurements, this constant reduction is negligible. However, in the case that the LUMO is significantly suppressed, the sample absorption at 284.5 eV can drop below the grid absorption producing an apparently negative peak when the signal is normalised. This also occurs at the ionization threshold at 290 eV where there is an inflection in the absorption at the normalization grid which caused the unexpected negative peak at 290 eV in the normalized data. [230] Thus, while the exact intensity of the LUMO peak and ionization threshold cannot be considered accurate, it is clear from the un-normalized signal that the LUMO suppression is real. The LUMO can be restored to its initial state by connecting the electrodes, briefly, to a common ground. This process is completely reversible and repeatable indicating a non-destructive yet significant change of the C_{60} band structure.

The modified edge shows dichroism in the 282 eV peak, figure 6.10, indicating a significant orbital moment associated with this state. The edge is also dependent on the magnetization of the Co electrode. This becomes apparent when out of plane field pulses are used to partially demagnetise the magnetic electrode. The out of plane hysteresis loop for the Co electrode has a remanant fraction of 0.17 so that it can be partially demagnetized through out of plane saturation.

The carbon edge shows progressive recovery of the LUMO as the Co electrode is demagnetized though it never recovers its initial state since the electrode could not be fully demagnetized in this way. In plane demagnetization was attempted by oscillating applied fields in a decaying sine wave which also proved effective. If connected to an external ground and then recharged with an applied voltage, a similar edge is recovered to that seen after a 5 T out of plane field. If the electrode is saturated in plane, the edge returns to something close to its fully suppressed character though with some modification which has not yet been explained. Prolonged exposure to the beam induces some change in the modified edge which can be attributed either to depletion of the modified state through increased participator recombination of core-holes or by radiolysis of C_{60} cages. [128] It should be noted that in TEY detection, magnetic fields can affect the detected current due to the Hall effect, demagnetization of the Co electrode may have a similar effect due to changes in the stray field.

Since no such changes are observed during transport, one must conclude that the modification of the carbon edge occurs as equilibrium is re-established following the removal of an external voltage. Considering the low current densities used, it is surprising that the LUMO is suppressed to effectively zero. An approximate calculation of the density of electrons in the C_{60} layer when the current density is 0.1 A/m2, one can see that only an approximate 1 % of molecules should host an extra charge per second. The post-transport edge indicates that, at the very least, to the limit of the escape depth, 100 % of the molecules are in a modified state. Since the expected photo-electron escape depth from C_{60} layers is 3 ML, this would be explained if $\approx$ 100 % of the molecules in the top 3 ML of the C_{60} layer were in the modified state. [145] The feature at 282 eV has the same approximate width (2.0 $\pm$ 0.5 eV) and the same peak energy as the feature observed in C_{60} Gd in figure 5.16. In section 5.5, this peak emerged in the first ML of C_{60} in contact with a Gd layer.

In this modified state, the excitation of core-hole excitons is dominated by a transition to a lower energy state lying 2.5 eV below the LUMO exciton. The LUMO exciton itself would usually reside in the band gap due to the effect of the core-hole meaning that the first exciton in the modified edge exists below the unmodified Fermi Energy. [128] [281] This indicates that the excitation is either into holes created by the transfer of electrons out of the HOMO or that the LUMO and Fermi Energy of the molecule have been supressed by more than 2.5 eV. A drop in the Fermi Energy and LUMO of C_{60} is observed in some charge transfer complexes and in some metal/C_{60} interfaces. [282] [283] However, without photoemission spectroscopy to observe the relative positions of the HOMO no conclusion can yet be drawn. What can be determined is that the removal of external bias following transport induces a persistent, modified state in C_{60}.

C_{60} and other molecular semiconductors have been considered as key components of multi-organic memory devices due to their implied ability to trap charge in non-volatile states over long timescales. [284] [285] For C_{60}, this is usually realised by distributing the molecules in an insulating matrix such as poly-4-vinyl phenol (PVP) or in 'double-float' gated devices where the trap is a film lying between two tunnel barriers to form a gate for transistors. [286] [287] [288] During measurement, we did not observe the transport hysteresis characteristic of such devices, indicating that while charge trapping may occur, this system does not exhibit the bistability observed in

true C_{60} memory devices. In thin films, trapped charges are observed to occur due to boundaries (such as crystalline domains) and varying electronic coupling (such as metal-organic boundaries). [289] [290] [291] [284] In C_{60} self-trapping states can also appear due to the effect of excitons on molecular symmetry and on site Coulomb interactions meaning certain charge states can localise themselves by distorting their host molecule. [292]

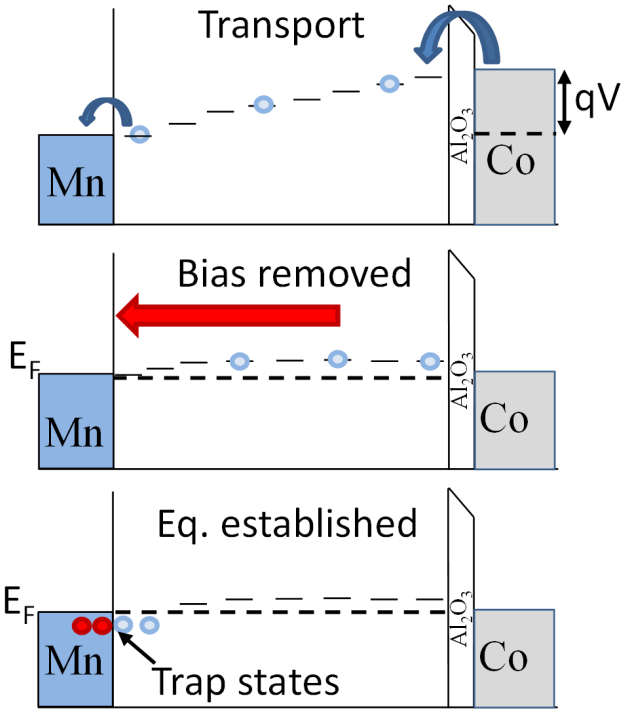

Figure 6.11: A basic schematic of the proposed mechanism. During transport (here shown from the Co electrode) charges move through the LUMO derived band via the variable range hopping mechanism. On removing the external bias, the molecular layer contains localised charges which then attempt to achieve equilibrium by flowing into the metal electrodes. Some of these charges become trapped in interface states. The origin of the trap states is unknown but possibilities are: 1. self trapping of charges in interfacial states as detailed in [292] facilitated by the interfacial interactions between Mn and C_{60} or 2. trapping of charge in modified interface states induced by a change in the oxidation state of the Mn electrode due to the presence of MnO_2 clusters as detailed in [293].

Another possibility is that the Mn electrode has formed an oxide during sputtering. Manganese oxides are semiconductors, n or p type depending on the stoichiometry,

with band gaps of approximately 1 eV. The most common natural oxide is manganese dioxide, MnO_2. As described in section 2.4, depending on the work function of the electrode, electrons could move from the HOMO of the C_{60} to create holes near the Fermi-energy. Transitions to these holes would create a new resonance in the NEXAFS. However, MnO_2 has been observed to play a very different role in electrolytic capacitors wherein charging and discharging of the capacitor through thin MnO_2 electrodes leads to a reversible change in the Mn oxidation state which alters the distribution of ions in the electrolyte. This mechanism was studied in detail by Toupin, [293]. The conclusions drawn in this study are not easily extrapolated to organic semiconductors. However, the presence of MnO_2 in this sample could not be entirely ruled out. Future study should determine whether clusters of MnO_2 are present and play any role in charge storage.

While it is not possible to draw any certain conclusion from the observations shown here, these results support the conjecture that shallow trap states emerge at the interface between the Mn electrode and C_{60}. A shallow trap would escape observation in electrical measurements since a small voltage would be sufficient to allow electrons to escape. On removing this external potential, the C_{60} would retain its instantaneous state. That is, it would retain the charges which were localised at molecular sites when the bias was turned off. A charged organic layer connected to metal electrodes is a non-equilibrium state and the establishment of equilibrium would require the redistribution of charge i.e by draining into the Mn electrode. Thus, charges may become trapped in interfacial states as they drain into the metal electrode. This mechanism is outlined the illustration of figure 6.11. While it is not understood as yet how these trap states emerge, this reorganisation of charge results in a significant modification of the charge distribution at the C_{60} manganese interface producing the observed persistent, modified edge seen in the XAS. Redistribution of charges through an organic layer in this manner has been observed, though at a far slower rate, in PVP-C_{60}. [287]

The interaction between Mn and C_{60} is known to induce a magnetic ground state in Mn. The polarisation of hybrid interface states due to this magnetic interaction could explain the dichroism observed in the carbon K-edge near the interface. [35] A more detailed study of MnC_{60} thin films via XAS or PES in an analogous fashion to the CoC_{60} study presented in chapter 4 would be needed to establish the exact nature of the interfacial interaction and its role in the modified edge. The response of

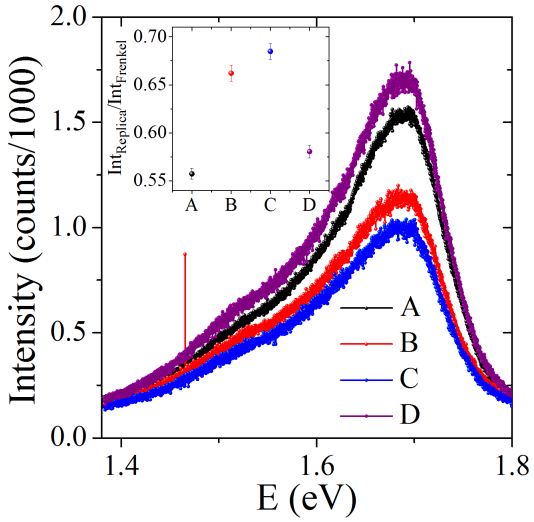

Figure 6.12: Photo-luminescence recorded in an identical structure to those used in figures 6.8-6.10. A Initial state before any bias is applied. B Measurement while 30 mV is applied. C After removing the 30 mV bias. D After connecting electrodes to a common ground. The inset shows the ratio of the replica to the Frenkel exciton peak in each instance.

the modified state to the magnetization state of the Co electrode, provided potential artefacts in the TEY current can be removed, indicates that the local magnetic field plays a role in the interfacial trapping and maintaining spin polarized charge.

Measurement of the photoluminescence in an identical device using a 473 nm diode laser as an excitation source showed that PL intensity is suppressed following external bias and that this state is also persistent after the bias has been removed, figure 6.12. In the modified state, the replica peak height is increased with respect to the Frenkel exciton indicating a greater fraction of recombination events occur due to phonon scattering. This behaviour is analogous to the changes in PL intensity observed in section 6.4 though here it has been observed to persist in the absence of applied voltage. The relative change in the phonon replica peak intensity and the stray field dependence of the carbon edge can be used to infer that spin polarization at the Mn/C_{60} interface plays a role in charge trapping and LUMO suppression. Attempts to measure the carbon edge in large applied fields showed edge changes in control samples due to the effect of large magnetic fields on Auger electrons and were thus discounted though a non-magnetic device measured in various applied fields would represent a more con-

trolled study of the field dependent behaviour if these artefacts could be removed.

6.6 Conclusions and Discussion

Measurements of the PL reduction over metal electrodes in a junction-like configuration show that the interfacial coupling and charge transfer, which is stronger in Co that Au, increases the well-known phenomenon of PL quenching in C_{60}. The response of the PL quenching to external fields can be understood by reference to the orientation dependence of dipole coupling to surface plasmons in metal films. This makes PL quenching a potential useful probe of interfacial magnetism and charge transfer in molecule/metal composites. Future research can utilise this method to compare charge transfer from different metals. The shift of the PL peak in different areas of the sample may be due to changes in the quantum efficiency of the conversion of singlet excitons to triplets or changes in the decay paths of these different excitons. To resolve this issue, two studies are proposed. First, a study of the distance dependence of the PL quenching and shift performed by depositing C_{60} monolayers on a Co film separated by a spacer of known width. The separation dependence can be used to determine the nature of the energy transfer from excitons to metal in a manner analogous to the study by Kuhnke et al. [41] Secondly, measurement of exciton lifetimes would allow conversion of singlet excitons to long lived triplets or non-radiative decay of excitons to be distinguished.

Observations of the Raman spectra, particularly the Ag(2) pentagonal pinch mode peak, agree with the arguments of Sauvajol at al [42] that the emergence of the Ag(2)' peak is related to lowering of moelcular symmetry. Here, the injection of spin polarised electrons increases the magnitude of the Ag(2)' peak indicating increased formation of C_{60} anions or triplet states when injected electrons are spin polarised. This is supported by PL observations which show suppression of peak intensity as a result of spin injection. This shows that carrier recombination can be controlled in C_{60} through spin injection. Control of exciton recombination in this manner is a key step in the use of organic materials such as C_{60} in opto-electric devices. [43] It is also possible that PL reduction can be used as a measure of the polarization of injected electrons provided CPL can be used to determine the proportion of spin forbidden transitions which occur via emission of a polarized photon.

Finally, XAS observations during transport reveal only small modifications of the

LUMO which are difficult to distinguish due to increased noise. This indicates that the number of molecules instantaneously hosting an additional charge during transport is very small. However, on removing the external bias, a significant modification of the K-edge is observed in the region of the LUMO which persists over long timescales exceeding 30 minutes. This modified edge responds to the magnetisation state of the magnetic electrode in a manner whcih suggests it is influenced by external fields. It is proposed that this observation uncovers interfacial charge trapping which occurs as the molecular film redistributes localised charges in order to establish equilibrium. The nature of the interfacial coupling between Mn and C_{60} is not well understood but C_{60} has been observed to introduce a magnetic ground state in Mn indicating there is a significant exchange of charge between these two materials. [35] PL measurements support the notion that there are spin polarised electrons at the interface since recombination via phonon scattering is proportionally increased. Future research will focus on determining the nature of the interfacial coupling between Mn and C_{60} in order to determine the nature of the trap states and μSR characterisation of the 'charged' state to determine its potential as a spin storage device.

Chapter 7

Conclusion

7.1 Summary

This thesis has discussed the interfacial interactions between fullerenes and ferromagnetic metals from both the transition metal and Lanthanide blocks and the application of different spectroscopic techniques to the investigation of spin injection and transport in hybrid organic-inorganic devices.

In chapter 4, the magnetic interactions between the three ferromagnetic transition metals were investigated through volume magnetometry and it was determined that interfacial hybridization and electron transfer result in a depletion of the majority spin population of the ferromagnet and the formation of a magnetic interfacial layer of fullerenes. This manifests as a reduction of the magnetization of Fe and Co layers with increasingly thick C_{60} deposited on top and a magnetic hardening of Co layers. Magnetization reduction was shown to be dependent on the total C_{60} layer thickness up to 200 nm thick indicating long range diffusion of charge in C_{60} films.

Using Co/C_{60}, which was found to exhibit the strongest effect with a maximum observed magnetization reduction of 270 $\pm$ 10 emu/cc, this interaction was investigated using the sensitive tools of PNR and XMCD. XAS at the carbon K-edge showed a peak which emerged below the LUMO when the C_{60} layer was 5 nm thick indicating the presence of an interfacial hybrid state expected from the literature. [36] [37] This supports a spinterface interpretation of interfacial hybridization in this system in which the broadening and energy shift of molecular orbitals is spin dependent when the substrate is ferromagnetic. [32] This is further supported by PNR which shows a magnetic interface, anti-ferromagnetically coupled to the underlying ferromagnet. PNR also indicates a moment in the C_{60} layer of 1.2 μ_B per cage, a value supported by DFT simulation. [169]

Investigations of the temperature dependence of the magnetic behaviour of Co/C_{60} hybrid complexes revealed a blocked state at low temperatures and a deviation from Bloch's law in the field cooled behaviour. This is shown to be inversely proportional to ferromagnet layer thickness indicating that interfacial interactions with the C_{60} layer are responsible. Magnetometry of Co/C_{60} composites at various temperatures show the emergence of hysteresis loop asymmetry at low temperatures. Observations of the temperature dependence of the ferromagnet AC susceptibility show both a possible transition near the ZFC-FC critical temperature, T_r, but also ergodicity breaking effects wherein allowing the system to relax over long periods significantly alters the

observed susceptibility. A tentative comparison between the behaviour of this system and ferromagnet-spin glass interfaces is made. [202] [203] The magnetic hardening of the Co layer and the emergence of asymmetry in the low temperature loop is postulated to be due to the freezing of uncompensated moments in the disordered magnetic interface. The magnetic disorder is expected to occur due to the distribution of different fullerene orientations and Co-C atomic distances at the interface.

In chapter 5, the ferrimagnetic RE-TM alloy CoGd is used as a spin injector for C_{60}. PNR measurements show that the magnetic C_{60} molecules are coupled to the Co sublattice as they reverse their magnetization as the alloy passes through its compensation point. However, the preparation of CoGd/C_{60} complexes revealed that the inclusion of C_{60} modifies the compensation behaviour of the alloy. In Gd/C_{60} composites, it was found that the assumption that the screened 4f orbital would be unaffected by hybridization with C_{60} layers was incorrect and that the magnetization of Gd was affected by interaction with a fullerene layer. As well as reducing the magnetization of Gd, hybridization was found to have unexpected effects on the magnetisation vs temperature behaviour of the complex with zero net magnetization states appearing at low temperatures for films between 6 and 10 nm. Susceptibility measurements also show possible phase transition associated with the inflections in the MvT curves for these films. XAS at the carbon K-edge in Gd/C_{60} shows a peak at 282 eV, below the LUMO indicative of hybridization. These results indicate hybridization between the Gd conduction bands and the C_{60} LUMO indirectly influences the magnetic order of Gd thin films through the RKKY interaction. The unusual MvT behaviour and possible additional phase transitions are interpreted as an intermediate, disordered state between the ferromagnetic and paramagnetic phases of Gd analogous to the helical or anti-ferromagnetic phases of Dy, Er and Ho. [40] This conclusion is supported by measurements of the resistance of Gd/C_{60} complexes at various temperatures, which show an increase in resistivity in the intermediate temperature range indicated by magnetometry. If an intermediate, disordered state did occur in Gd/C_{60}, such a change in resistivity would be expected due to increased spin disorder scattering. [224]

In chapter 6, three different spectroscopy techniques are applied to the measurement of spin injection into C_{60} films. Photoluminescence quenching was observed for C_{60} films deposited over metals as expected from the literature. [41] However, PL quenching was more significant over Co than Au. This is attributed to the greater electron transfer

from Co to C_{60}. The response of PL quenching to external fields also showed a complex dependence which is potentially explained by the orientation dependence of the coupling between electric and magnetic dipoles and metal surfaces. [256]

The Raman spectrum of C_{60} was found to have a reversible dependence on spin injection with the long debated splitting of the Ag(2) peak correlating to the injection of spin polarised electrons. The appearance of the Ag(2) double peak, here labelled Ag(2) and Ag(2)', is attributed to lowering of molecular symmetry in the fullerene layer though it is acknowledged that there is an irreversible component which arises from photo-assisted polymerization. [244] [42] [239]

PL measurements during transport show a PL reduction when spins are injected by tunnelling from a magnetic electrode. This reduction is interpreted as a spin dependent negative photo-luminescence related to increased charge transfer triplet formation or electron spin dependent hopping times for polarons.

Finally, XAS of a C_{60} layer during transport shows a significant change in K-edge NEXAFS when external bias is removed. The LUMO peak is supressed to zero and a strong peak emerges at 282 eV. This state is persistent over periods of at least 30 minutes and shows a possible response to the magnetization of the ferromagnetic electrode. This is interpreted as the result of accumulation of charge in interfacial trap states between the C_{60} and a manganese electrode as charge is redistributed in the fullerene layer following the removal of external bias and equilibrium is established. Possible reasons for these trap states were proposed including self-trapping states due to moelcular distortion or reversible changes in the oxidation state of MnO_2 clusters in the electrode. [292] [293] This conclusion is currently tentative but the trapping of charge in fullerene layers is not unexpected from the literature. [285] [292] However, this would be the first time it has been observed in a pure C_{60} layer using XAS. The dichroism observed in these interfacial states also raises the intriguing notion of using these trap states for spin storage in organic devices.

7.2 Outlook

Molecular and organic electronics is not likely to overtake metal-oxide-semiconductor technology on the merits of its ability to mimic MOSFET devices.[2] However, since that first observation of the spintronic potential of organic materials [13] organic and molecular materials have been shown to provide new functionalities which are not

possible in their inorganic counterparts. [14]

This is particularly apparent in the study of interfacial hybridization. Beginning with observations of spin injection and anomalies in magnetoresistance [13] [89] [33] to interpretation of these anomalies [17] [32] and the development of spinterface physics to the implementation of the effect in new devices [34], the study of interfacial interactions is a model for how the complexity of molecules and their interactions, which may first manifest as problems to be overcome, can be applied to gain new functionality. However, implementation relies on detailed information and understanding of the processes of interfacial hybridization, charge transfer and spin injection which, for now, must be gathered through experiment. The work presented in chapters 4 and 5 demonstrate the degree of magnetic customization attainable in molecular-metallic composites. While it is well known that hybridization and charge transfer can affect molecules, this research shows that one can apply molecular layers to manipulate itinerant ferromagnetism in metals. Future research should expand on the two examples used in this research to explore the coercivity enhancing effects seen in section 4.2 to determine the limits of this effect. In particular it would be valuable to explore whether the BH product of transition-metal C_{60} composites can be engineered to rival rare-earth/transition-metal permanent magnets.

The results in chapter 5 also show that molecules could provide a route to controlling periodic magnetic structures or inducing them in materials which do not normally exhibit periodic structure. As interest in chiral magnetic phases has grown in the wake of Skyrmion research, [294] the prospect of inducing chiral states in rare-earths through interfacial hybridization could be developed into a useful tool for engineering bespoke materials for research and application. To do this, further research is required into the Gd/C_{60} system to determine the nature of the disordered intermediate phase. Neutron diffraction would be a useful study since this method allows magnetic order to be probed as a function of scattering vector q, potentially revealing Kohn anomalies if periodic structures are present. [236] However, even if periodic order is not present in Gd/C_{60} the simple fact that RKKY coupling in rare earths can be manipulated by molecules opens up a wealth of potential composites which might exhibit induced periodic order. To be useful for applications, molecule-metal composites must be found where periodic order can be induced in a material which has desirable properties not available in materials which intrinsically show chiral magnetic order or the chiral ordering must

be externally manipulatable by altering the interfacial interactions between metal and molecule in a non-destructive way, i.e with a gate voltage.

The results shown in chapter 6 present new spectroscopic tools for analysing charge transfer and spin injection in molecule-metal composites. The dependence of PL quenching on electron transfer and induced magnetism makes this a useful method for comparing various molecule metal contacts and can act as a complimentary technique to magnetometry in determining whether there is a net transfer of charge into the molecular layer without resorting to XAS, though XAS would still be required to determine what changes occur in the electronic structure as a result of charge transfer. The correlation between the Ag(2)' peak magnitude and the spin injection makes it a potential probe of spin polarised carriers in organic spintronic devices using C_{60} while the spin dependence of PL reduction in C_{60} junctions confirms that spin injection can be used to reduce carrier recombination in C_{60} which is vital for efficient opto-electronic devices. Finally, the striking changes which occur in the carbon NEXAFS following transport are an intriguing glimpse into charge trapping which has never been observed in this way in C_{60} before. The question now arises that, if this modified edge is evidence of charge trapping, how can it be manipulated? C_{60} has been used as part of multi-organics to store charge before [287] and self trapping of electrons is expected to occur in C_{60} solids [292] but can this interfacial charge trapping provide additional functionality to composite devices? Particularly fascinating is the prospect of storing spin polarised charge at the interface between C_{60} thin films and magnetic layers creating a spin capacitor utilising interfacial hybridization.

In conclusion, this research has shown that C_{60} is an effective tool for manipulating magnetism and spin in a range of applications: 3d ferromagnets, RE magnets potentially including chiral magnets, spin injection and potentially spin storage. C_{60} is an ideal system for studying these phenomena due to its simplicity, robustness and desirable chemical and electrical properties, but one of the great advantages of molecular and organic materials is the sheer variety of behaviours accessible to researchers. In the future, it is my hope that a vast array of molecules, produced to order by synthetic chemical processes, can act as a molecular toolbox for spintronic researchers and engineers to provide the ideal materials for any application.

References

[1] T. Maughan, The dystopian lake filled by the world's tech lust (2015), www.bbc.com/future/story/20150402-the-worst-place-on-earth

[2] Editorial, Does molecular electronics compute?, *Nat. Nanotech.* **8**, 377 (2013)

[3] M. Lapedus, 5 nm fab challenges (2016), www.semiengineering.com/5nm-fab-challenges

[4] C. W. Tang and S. A. VanSlyke, Organic electroluminescent devices, *Appl. Phys. Lett.* **51** (1987)

[5] S. R. Forrest, The path to ubiquitous and low-cost organic electronic appliances on plastic, *Nature* **428**, 911 (2004)

[6] J. M. Tour, Molecular electronics. Synthesis and testing of components, *Acc. Chem. Res.* **33**, 791 (2000)

[7] S. J. Tans, A. R. M. Verschueren and C. Dekker, room-temperature transistor based on a single carbon nanotube, *Nature* **393**, 49 (1998)

[8] J. Martínez-Blanco, C. Nacci, S. C. Erwin, K. Kanisawa, E. locane et al., Gating a single-molecule transistor with individual atoms, *Nat. Phys.* **11**, 640 (2015)

[9] K. S. Novoselov, A. K. Geim, S. V. Morozov, D. Jiang, Y. Zhang et al., Electric field effect in atomically thin carbon films, *Science* **306** (2004)

[10] F. Schwierz, Graphene transistors, *Nat. Nanotech.* **5**, 487 (2010)

[11] S. A. Wolf, D. D. Awschalom, R. A. Buhrman, J. M. Daughton, S. von Molnár et al., Spintronics: a spin-based electronics vision for the future, *Science* **294**, 1488 (2001)

[12] S. Sanvito, Molecular spintronics, *Chem. Soc. rev.* **40**, 3336 (2011)

[13] V. Dediu, M. Murgia, F. C. Matacotta, C. Taliani and S. Barbanera, Room temperature spin polarized injection in organic semiconductor, *Solid State Comm.* **122**, 181 (2002)

[14] Editorial, Why going organic is good, *Nat. Mat.* **8**, 691 (2009)

[15] C. Iacovita, M. V. Rastei, B. W. Heinrich, T. Brumme, J. Kortus et al., Visualizing the spin of individual cobalt-pthalocyanine molecules, *Phys. Rev. Lett* **101** (2008)

[16] E. Carlegrim, A. Kanciurzewska, P. Nordblad and M. Fahlman, Air-stable organic-based semiconducting room temperture thin film magnet for spintronics applications, *Appl. Phys. Lett.* **92** (2008)

[17] C. Barraud, P. Seneor, R. Mattana, S. Fusil, K. Bouzehouane et al., Unravelling the role of the interface for spin injection into organic semiconductors, *Nat. Phys.* **6**, 615 (2010)

[18] H. Kusai, S. Miwa, M. Mizuguchi, T. Shinjo, Y. Suzuki et al., Large magnetoresistance in rubrene-Co nano-composites, *Chem. Phys. Lett.* **448**, 106 (2007)

[19] M. Gobbi, F. Golmar, R. Llopis, F. Casanova and L. E. Hueso, Room-temperature spin transport in C_{60} based spin valves, *Adv. Mater.* **23**, 1609 (2011)

[20] L. E. Hueso, J. M. Pruneda, V. ferrari, G. Burnell, J. P. Valdés-Herrera et al., Transformation of spin information into large electrical signals using carbon nanotubes, *Nature* **445**, 410 (2007)

[21] H. W. Kroto, J. R. Heath, S. C. O'Brien, R. F. Curl and R. E. Smalley, C_{60}: Buckminsterfullerene, *Nature* **318**, 162 (1985)

[22] J. Cami, J. Bernard-Salas, E. Peeters and S. E. Malek, Detection of C_{60} and C_{70} in a young planetary nebula, *Science* **329**, 1180 (2010)

[23] W. Krẗschmer, L. D. lamb, K. Fostiropoulos and D. R. Huffman, Solid C_{60}: a new form of carbon, *Nature* **347**, 354 (1990)

[24] R. C. Haddon, A. F. Hebard, M. J. Rosseinsky, D. W. Murphy, S. J. Duclos et al., Conducting films of C_{60} and C_{70} by alkali-metal doping, *Nature* **350**, 320 (1991)

[25] A. F. Hebard, M. J. Rosseinsky, R. C. Haddon, D. W. Murphy, S. H. Glarum et al., Superconductivity at 18 k in potassium-doped C_{60}, *Nature* **350**, 600 (1991)

[26] G. Brumfiel, Misconduct finding at Bell Labs shakes physics community, *Nature* **419**, 419 (2002)

[27] X. Zhang, S. Mizukami, T. Kubota, Q. Ma, M. Oogane et al., Observation of a large spin-dependent transport length in organic spin valves at room temperature, *Nat. Comm.* **4** (2012)

[28] A. Rosén and B. Wästenberg, Calculations of the ionization thresholds and electron affinities of the neutral, positively and negatively charged C60-"follene-60", *J. Chem Phys.* **90** (1989)

[29] V. A. Dediu, L. E. Hueso, I. Bergenti and C. Taliani, Spin routes in organic semiconductors, *Nat Mat* **8**, 707 (2009)

[30] J. C. Scott, Metal-organic interface and charge injection in organic electronic devices, *J. Vac. Sci. Tech.* **21** (2003)

[31] H. Ishii, K. Sugiyama, E. Ito and K. Seki, Energy level alignment and interfacial electronic structures at organic/metal and organic/organic interfaces, *Adv. Mat.* **11** (1999)

[32] S. Sanvito, The rise of spinterface science, *Nat. Phys.* **6**, 563 (2010)

[33] O. Cespedes, M. S. Ferreira, S. Sanvito, M. Kociak and J. M. D. Coey, Contact induced magnetism in carbon nanotubes, *J Phys: Condens Matter* **16**, L155 (2004)

[34] K. V. Raman, A. M. kamerbeek, A. Mukherjee, N. Atodiresei, T. K. Sen et al., Interface-engineered templates for molecular spin memory devices, *Nature* **493**, 509 (2013)

[35] F. A. Ma'Mari, T. Moorsom, G. Teobaldi, W. Deacon, T. Prokscha et al., Beating the stoner criterion using molecular interfaces, *Nature* **524**, 69 (2015)

[36] T. L. A. Tran, P. K. J. Wong, M. P. de Jong, W. G. van der Wiel, Y. Q. Zhan et al., Hybridization-induced oscillatory magnetic polarization of c 60 orbitals at the c 60/ fe (001) interface, *Appl. Phys. Lett.* **98** (2011)

[37] T. R. Ohno, Y. Chen, S. E. Harvey, G. H. Kroll and J. H. Weaver, C_{60} bonding and energy-level alignment on metal and semiconductor surfaces, *Phys. Rev. B* **44** (1991)

[38] M. Ali, P. Adie, C. H. Marrows, D. Greig, B. J. Hickey et al., Exchange bias using a spin glass, *Nat. Mat* **6**, 70 (2007)

[39] J. Jensen and A. R. MacKintosh, *Rare Earth Magnetism: Structures and Excitations*, Clarendon Press (1991)

[40] R. E. Watson, A. J. Freeman and J. P. Dimmock, Magnetic ordering and the electronic properties of the heavy rare-earth metals, *Phys. Rev.* **167** (1968)

[41] K. Kuhnke, R. Becker, M. Epple and K. Kern, C_{60} exciton quenching near metal surfaces, *Phys. Rev. Lett.* **79** (1997)

[42] J. L. Sauvajol, F. Brocard, Z. Hricha and A. Zahab, Raman spectroscopy of C_{60} solid films, *Phys. Rev. B* **52** (1995)

[43] J. Wang, A. Chepelianskii, F. Gao and N. C. Greenham, Control of exciton spin statistics through polarization in organic optoelectronic devices, *Nat Comm* **3** (2012)

[44] S. Blundell, *Magnetism in Condensed Matter*, Oxford University Press (2001)

[45] E. C. Stoner, Collective electron ferromagnetism i, *Proceedings of the royal society of london. Series A, mathematical and physical sciences.* **165** (1937)

[46] C. P. Bean and J. D. Livingston, Superparamagnetism, *Jour. Appl. Phys.* **30** (1959)

[47] M. T. Johnson, P. J. H. Bloemen, F. J. A. Broeder and J. J. de Vries, Magnetic anisotropy in metallic multilayers, *Rep. Prog. Phys.* **59**, 1409 (1996)

[48] P. Bruno, *Ferienkurse des Forschungzentrum Jülich*, Forschungzentrum Jülich GmbH (1993), (Physical origins and theoretical models of magnetic anisotropy)

[49] G. H. O. Daalderop, P. J. Kelly and M. F. H. Schuurmans, Magnetic anisotropy of a free-standing Co monolyaer and of multilayers which contain Co monolayers, *Physical Review B* **50** (1994)

[50] N. L, anisotropie magnétique superficielle et surstructures d'orientation, *J. Phys. Radium* **15**, 225 (1954), a useful discussion in english can be found in [44].

[51] C. Tannous and J. Gieraltowski, The Stoner-Wohlfarth model of ferromagnetism, *Eur. J. phys.* **29**, 475 (2008)

[52] E. C. Stoner and E. P. Wohlfarth, A mechanism of magnetic hysteresis in heterogeneous alloys, *Philosophical Transactions of the Royal Society of London. Series A, Mathematical and Physical Sciences.* **240** (1948)

[53] I. D. Hughes, M. Däne, A. Ernst, W. Hergert, m Lüders et al., Lanthanide contraction and magnetism in the heavy rare earth elements, *Nature* **446**, 650 (2007)

[54] M. A. Runderman and C. Kittel, Indirect exchange coupling of nuclear magnetic moments by conduction electrons, *Phys. Rev.* **96** (1954)

[55] L. Bogani and W. Wernsdorfer, Molecular spintronics using single-molecular magnets, *Nat. Mat.* **7**, 179 (2008)

[56] M. N. Leuenberger and D. Loss, Quantum computing in molecular magnets, *Nature* **410**, 789 (2001)

[57] J. F. Janak, Uniform susceptibilities of metallic elements, *Phys. Rev. B* **16** (1977)

[58] H. H. Wickman, A. M. Trozzolo, H. J. Williams, G. W. Hull and F. R. Merritt, Spin-3/2 iron ferromagnet: its mössbauer and magnetic properties, *Phys. Rev.* **155** (1967)

[59] C. G. Barraclough, R. L. Martin, S. Mitra and R. C. Sherwood, Paramagnetic anisotropy, electronic structure and ferromagntism in spin S = 3/2 manganese(ii) pthalocyanine, *Jour. Chem. Phys.* **53** (1970)

[60] J. Kanamori, Superexchange interaction and symmetry properties of electron orbitals, *J. Phys. Chem. Solids* **10**, 87 (1959)

[61] K. Awaga, T. Sugano and M. Kinoshita, Ferromagnetic intermolecular interaction in the galvinoxyl radical: cooperation of spin polarization and charge-transfer interaction, *Chem. Phys. Lett.* **141** (1987)

[62] M. S. Paul and C. Veyret, Ferromagnetic ordering in an organic compound: DI - (2,2,6,6-tetramethyl-4 piperidinol-1 oxyl)(TANOL suberate), *Phys. Lett.* **45A** (1973)

[63] T. Sugano, Magnetic phase transitions in organic radicals, *Polyhedron* **20**, 1285 (2001)

[64] A. Benoit, J. Flouquet, B. Gillon and J. Schweizer, The antiferromagnetic structure of tanol suberate, *Jour. Mag. Mag. Mat.* **31-34**, 1155 (1983)

[65] R. Chiarelli, M. A. Novak, A. Rassat and J. L. Tholence, A ferromagnetic transition at 1.48 K in an organic nitroxide, *Nature* **363**, 147 (1993)

[66] K. Awaga and Y. Maruyama, ferromagnetic and antiferromagnetic intermolecular interactions of organic radicals, α-nitronyl nitroxides. ii, *J. Chem. Phys* **91** (1989)

[67] K. Itoh and M. Kinoshita, *Molecular Magnetism: New magnetic materials*, KODANSHA Ltd. and Taylor and Francis (2000)

[68] H. M. McConnell, Ferromagnetism in solid free radicals, *Jour. Chem. Phys.* **39** (1963)

[69] S. J. Blundell and F. L. Pratt, Organic and molecular magnets, *J. Phys. Condens. Matter* **16**, R771 (2004)

[70] H. M. McConnell, Comments on "organic ferromagnetism", *Proc. Robert A. Welch Found. Conf. Chem. Res.* (1967), not available in print but adequately explored in: [67]

[71] K. Yamaguchi, H. Namimoto, T. Fueno, T. Nogami and Y. Shirota, Possibilities of organic ferromagnets and ferrimagnets by the use of charge-transfer(CT) complexes with radical substituents. Ab initio MO studies., *Chem. Phys. Lett.* **166** (1990)

[72] P.-M. Allemand, K. C. Khemani, A. Koch, F. Wudl, K. Holczer et al., Organic molecular soft ferromagnetism in a fullerene C_{60}, *Science* **253** (1991)

[73] T. Kambe, Y. Nogami and K. Oshima, Annealing effects on the magnetic and structural properties of single-crystal TDAE - C_{60}, *Phys. Rev. B* **61** (2000)

[74] W. I. F. David, R. M. ibberson, J. C. Matthewman, K. Prassides, T. J. S. Dennis et al., Crystal structure and bonding of ordered C_{60}, *nature* **353**, 147 (1991)

[75] W. I. F. David, R. M. Ibberson, T. J. S. Dennis, J. P. Hare and K. Prassides, Structural phase transitions in the fullerene C_{60}, *Europhys. Lett.* **18**, 219 (1992)

[76] J. H. Weaver, J. L. Martins, T. Komeda, Y. Chen, T. R. Ohno et al., Electronic structure of solid C_{60}: Experiment and theory, *Phys. Rev. Lett.* **66** (1991)

[77] R. W. Lof, M. A. van Veenendaal, B. Koopmans, H. T. Jonkman and G. A. Sawatzky, Band gap, excitons and coulomb interaction in solid C_{60}, *Phys. Rev. Lett.* **68** (1992)

[78] S. Saito and A. Oshiyama, Cohesive mechanism and energy bands of solid C_{60}, *Phys. Rev. Lett.* **66** (1991)

[79] C. Wen, J. Li, K. Kitazawa, T. Aida, I. Honma et al., Electrical conductivity of a pure C_{60} single crystal, *Appl. Phys. Lett.* **61** (1992)

[80] R. Könenkamp, G. Priebe and B. Pietzak, Carrier mobilities and influence of oxygen in C_{60} films, *Phys. Rev. B* **60** (1999)

[81] R. A. Marcus, On the theory of oxidation-reduction reactions involving electron transfer. I, *Jour. Chem. Phys.* **24** (1956)

[82] R. A. Marcus, Electron transfer reaction in chemistry. Theory and experiment, *Rev. Mod. Phys.* **65** (1993)

[83] Z. Shuai, L. Wang and C. Song, *Theory of Charge Transport in carbon Electronic Materials*, Springer (2012)

[84] I. I. Fischuk, A. Kadashchuk, S. T. Hoffman, S. Athanasopoulos, J. Genoe et al., Unified description for hopping transport in organic semiconductors including both energetic disorder and polaronic constributions, *Phys. Rev. B* **88** (2013)

[85] T. Holstein, Studies of polaron motion: Part 1. the molecular-crystal model, *Ann. Phys.* **8**, 325 (1959)

[86] S. Saito and A. Oshiyama, Cohesive Mechanism and Energy Bands of Solid C_{60}, *Phys. Rev. Lett.* **66**, 2637 (1991)

[87] H. Li, B. C.-K. Tee, J. J. Cha, Y. Cui, j W chung et al., Hihg-mobility field-effect transistors from large-area solution-grown aligned C_{60} single crystals, *Jour. Am. Chem. soc.* **134**, 2760 (2012)

[88] T. L. A. Tran, T. Q. Le, J. G. M. Sanderink, W. G. van der Wiel and M. P. de Jong, The multistep tunneling analogue of conductivity mismatch in organic spin valves, *Adv. Func. Mat.* **22** (2012)

[89] Z. H. Xiong, D. Wu, Z. V. Vardeny and J. Shi, Giant magnetoresistance in organic spin-valves, *Nature* **427**, 821 (2004)

[90] K. Tsukagoshi, B. W. Alphenaar and H. Ago, Coherent transport of electron spin in a ferromagnetically contacted carbon nanotube, *Nature* **401** (1999)

[91] M. S. Ferreira and S. Sanvito, Contact-induced spin polarization in carbon nanotubes, *Phys. Rev. B* **69** (2004)

[92] A. J. Maxwell, P. A. Brühwiler, D. Arvanitis, J. Hasselström and N. Mårtensson, C 1s ionisation potential and energy referencing for solid C_{60} films on metal surfaces, *Chem Phys Lett* **260**, 71 (1996)

[93] J. B. Neaton, M. S. Hybertsen and S. G. Louie, Renormalization of molecular electronic levels at the metal-molecule interfaces, *Phys. Rev. Lett.* **97** (2006)

[94] X. Lu, M. Grobis, K. H. Khoo, S. G. Louie and M. F. Crommie, Charge transfer and screening in individual C_{60} molecules on metal substrates: a scannign tunneling spectroscopy and theoretical study, *Phys. Rev. B* **70** (2004)

[95] S. M. Sze and K. K. Ng, *Physics of semiconductor devices*, John Wiley and Sons, 3rd edition (2007)

[96] R. T. Tung, Chemical bonding and fermi level pinning at metal-semiconductor interfaces, *Phys Rev Lett* **84** (2000)

[97] A. J. Maxwell, P. A. Brühwiler, A. Nilsson and N. Mårtensson, Photoemission, autoionization and x-ray-absorption spectroscopy of ultrathin-film C_{60} on Au(110), *Phys Rev B* **49** (1994)

[98] A. R. Rocha and S. Sanvito, Resonant magnetoresistance in organic spin valves (invited), *Jour. Appl. Phys.* **101** (2007)

[99] A. R. Rocha, V. M. Garcia-suárez, S. W. Bailey, C. J. Lambert, J. Ferrer et al., Towards moelcular spintronics, *Nat Mat* **4**, 335 (2005)

[100] N. Atodiresei, J. Brede, P. Lazíc, V. Caciuc, G. Hoffmann et al., Design of the local spin polarization at the organic-ferromagnetic interface, *Phys. Rev. Lett.* **105** (2010)

[101] S. L. Kawahara, J. Lagoute, V. Repain, C. Chacon, S. Rousset et al., Large magnetoresistance through a single molecule due to a spin-split hybridized orbital, *Nano Lett.* **12**, 4558 (2012)

[102] V. Dediu, L. E. Hueso, I. Bergenti, A. Riminucci, F. Borgatti et al., Room-temperature spintronic effects in Alq_3-based hybrid devices, *Phys. Rev. B* **78** (2008)

[103] W. H. Meiklejohn and C. P. Bean, New magnetic anisotropy, *Phys. Rev.* **105** (1957)

[104] R. L. Stamps, Mechanisms for exchange bias, *J. Phys. D: Appl. Phys.* **33**, R247 (2000)

[105] C. Leighton, J. Nogués, B. J. Jönsson-Åkerman and I. K. Schuller, Coercivity enhancement in exchange biased systems driven by interfacial magnetic frustration, *Phys. Rev. Lett.* **84** (2000)

[106] D. Mauri, E. Kay, D. Scholl and J. K. Howard, Novel method for determining the anisotropy constant of MnFe in a NiFe/MnFe sandwich, *Jour. Appl. Phys.* **62** (1987)

[107] D. Mauri, H. C. Siegmann, P. S. Bagus and E. Kay, Simple model for thin ferromagnetic films exchange coupled to an antiferromagnetic substrate, *Jour. Appl. Phys.* **62** (1987)

[108] A. E. Berokowitz and K. Takano, Exchange anisotropy- a review, *Jour. Mag. Mag. Mat.* **200**, 552 (1999)

[109] A. P. Malozemoff, Heisenberg-to-Ising crossover in a random-field model with uniaxial anisotropy, *Phys. Rev. B* **37** (1988)

[110] M. Kiwi, Exchange bias theory, *Jour. Mag. Mag. Mat.* **234**, 584 (2001)

[111] T. C. Schulthess and W. H. Butler, Coupling mechanisms in exchange biased films (invited), *Jour. Appl. Phys.* **85** (1999)

[112] M. D. Stiles and R. D. McMichael, Model for exchange bias in polycrystalline ferromagnet-antiferromagnet bilayers, *Phys. Rev. B* **59** (1999)

[113] M. Gruber, F. Ibrahim, s Boukari, H. Isshiki, L. Joly et al., Exchange bias and room-temperture magnetic order in molecular layers, *Nat Mat* **14**, 981 (2015)

[114] K. Bairagi, A. Bellec, V. Repain, C. Chacon, Y. Girard et al., Tuning the magnetic anisotrop at a molecule-metal interface, *Phys. Rev. Lett* **114** (2015)

[115] S. Foner, Versatile and sensitive vibrating-sample magnetometer, *Review of Scientific Instruments* **30** (1959)

[116] R. L. Fagaly, Superconducting quantum interference device instruments and applications, *Rev. Sci. Intrum* **77** (2006)

[117] H. Weinstock, A review of SQUID magnetometry applied to nondestructive evaluation, *IEEE Trans. Mag.* **27** (1991)

[118] R. C. Jaklevic, J. lambe, A. H. Silver and J. E. Mercereau, Quantum interference effects in jospehson tunneling, *Phys. Rev. Lett* **12** (1964)

[119] J. Daillant and A. Gibaud, *X-ray and neutron reflectivity*, Springer (1999)

[120] D. Attwood, *Soft X-Rays and Extreme Ultra-Violet radiation: Principles and Applications*, Cambridge University Press (1999)

[121] S. K. Sinha, E. B. Sirota, S. Garoff and H. B. Stanley, X-ray and neutron scattering from rough surfaces, *Phys. Rev. B* **38** (1988)

[122] M. Sugawara, M. Kondo, S. Yamazaki and K. Nakajima, Exact determination of supperlattice structures by small-angle x-ray diffration method, *Appl. Phys. Lett.* **52**, 742 (1988)

[123] G. P. Felcher, R. O. Hilleke, R. K. Crawford, J. Haumann, R. Kieb et al., Polarized neutron reflectometer: A new instrument to measure magnetic depth profiles, *Rev. Sci. Instrum.* **58** (1987)

[124] C. J. Kinane, *The interplay of magnetism and structure in patterned multilayer thin films*, Ph.D. thesis, University of Leeds (2008)

[125] Y. Saito, H. Shinohara and A. Ohshita, Electron energy loss spectrum near carbon K-edge in solid C_{60}, *Jpn. J. Appl. Phys.* **30** (1991)

[126] D. Kondo, K. Sakamoto, H. Takeda, F. Matsui, K. Amemmiya et al., Unoccupied molecular orbitals of C_{60} molecules adsorbed on Si(001)-(2 $\times$ 1) and Si(111)-(7 $\times$ 7) surfaces studied by nexafs, *Surface Science* pp. 337–342 (2002)

[127] R. C. Haddon, L. E. Brus and K. Raghavachari, Electronic structure and bonding in icosahedral C_{60}, *Chem Phys Lett* **125** (1986)

[128] P. A. Brünwiler, O. Karis and N. Mårtensson, Charge-transfer dynamics studied using resonant core spectroscopies, *Rev. Mod. Phys.* **74**, 703 (2002)

[129] P. A. Brüwiler, A. J. Maxwell, P. Rudolf, C. D. Gutleben, B. Wästberg et al., C 1s autoionization study of electron hopping rates in solid C_{60}, *Phys. Rev. Lett* **71** (1993)

[130] S. Krummacher, M. Biermann, M. Need, A. Liebsch and W. Eberhardt, Close similarity of the electronic structure and electron correlation in gas-phase and solid c_{60}, *Phys. Rev. B* **48** (1993)

[131] P. A. Brühwiler, A. J. Maxwell, C. Puglia, A. Nilsson, S. Andersson et al., π^* and σ^* excitons in C 1s Absorption of Graphite, *Phys. Rev. Lett* **74** (1995)

[132] H. Ohldag, T. Tyliszczak, R. Höhne, D. Spemann, P. Esquinazi et al., π-electron ferromagnetism in metal-free carbon probed by soft x-ray dichroism, *Phys. Rev. Lett* **98** (2007)

[133] G. Y. Guo, What does the K-edge x-ray magnetic ciruclar dichroism spectrum tell us?, *J Phys: Condens Matter* **8**, L747 (1996)

[134] H.-C. Mertins, S. Valencia, W. Gudat, P. M. Oppeneer, O. Zaharko et al., Direct observation of local ferromagnetism on carbon in C/Fe multilayers, *Europhys. Lett.* **66** (2004)

[135] M. Weser, Y. Rehder, K. Horn, M. Sicot, M. Fonin et al., Induced magnetism of carbon atoms at the graphene/Ni(111) interface, *Appl. Phys. Lett.* **96** (2010)

[136] D. Huertas-Hernando, F. Guinea and A. Brataas, Spin-orbit coupling in curved graphene, fullerenes, nanotubes and nanotube caps, *Phys. Rev. B* **74** (2006)

[137] G. van der Laan and A. I. Figueroa, X-ray magnetic circular dichroism - a verstaile tool to study magnetism, *Coordination Chem. Rev.* **277-278**, 95 (2014)

[138] T. Funk, A. Deb, S. J. George, H. Wang and S. P. Cramer, X-ray magnetic circular dichroism - a high energy probe of magnetic properties, *Coordination Chemistry Reviews* **249**, 3 (2005)

[139] C. T. Chen, Y. U. Idzerda, H. J. Lin, N. V. Smith, G. Meigs et al., Experimental confirmation of the X-ray magnetic circular dichroism sum rules for iron and cobalt, *Phys. Rev. Lett.* **75** (1995)

[140] B. T. Thole, P. Carra, F. Sette and G. van der Laan, X-ray circular dichroism as a probe of orbital magnetization, *Phys. Rev. Lett.* **68** (1992)

[141] S. S. Dhesi, G. van der Laan, P. Bencok, N. B. Brookes, R. M. Galéra et al., Spin- and orbital-moment compensation in the zero-moment ferromagnet $\mathrm{sm_{0.974}gd_{0.026}al_2}$, *Phys. Rev. B* **82** (2010)

[142] M. van Veenendaal, J. B. Goedkoop and B. T. Thole, Polarized x-ray flourescence as a probe of ground state properties, *Phys. Rev. Lett* **77** (1996)

[143] E. Hartmann, X-ray flourescence yields for light emitter atoms: carbon, *At. Mol. Opt. Phys.* **21**, 1173 (1988)

[144] M. Klasson, J. Hedman, A. Berndtsson, R. Nilsson and C. Nordling, Escape depths of X-ray excited electrons, *Physica. Scripta* **5**, 93 (1972)

[145] E. Rotenberg, C. Enkvist, P. A. Brühwiler, A. J. Maxwell and N. Mårtensson, Local-field effect on photoemission of $\mathrm{c_{60}}$, *Phys. Rev. B* **54** (1996)

[146] J. L. Sauvajol, Z. Hricha, N. Coustel, A. Zahab and R. Aznar, Photoluminescence of solid $\mathrm{C_{60}}$, *J. Phys. Condens. Matter.* **5**, 2045 (1993)

[147] K. Yabana and G. F. Bertsch, Frobidden transitions in the absorption spectra of $\mathrm{c_{60}}$, *Chem Phys Lett* **197** (1992)

[148] T. W. Ebbesen, Y. Mochizuki, K. Tanigaki and H. Hiura, Direct observation of c_{60} exciton, *Europhys. Lett.* **25** (1994)

[149] E. L. Shirlet, L. X. Benedict and S. G. Louie, Excitons in solid c_{60}, *Phys. Rev. B* **54** (1996)

[150] J. W. Arbogast, A. P. Darmanyan, C. S. Foote, Y. Rubin, F. N. Diederich et al., Photophysical properties of C_{60}, *J. Phys. Chem.* **95**, 11 (1991)

[151] C. V. Raman and K. S. Krishnan, A new type of secondary radiation, *Nature* **121**, 501 (1928)

[152] C.-S. Wang, Theory of Stimulated Raman Scattering, *Phys. Rev.* **182**, 181 (1969)

[153] M. Matus and H. Kuzmany, Raman spectra of single-crystal C_{60}, *Appl. Phys. A* **56**, 241 (1993)

[154] J. P. Lowe and K. A. Peterson, *Quantum Chemistry*, Elsevier Academic Press, 3rd edition edition (2006)

[155] P. J. Kelly and R. D. Arnell, Magnetron sputtering: a review of recent developments and applications, *Vacuum* **56**, 159 (2000)

[156] H. Werner, M. Wohlers, D. Bublak, J. Blöcker and R. Schlögl, Interaction of molecular oxygen with solid C_{60}, *Fullerene Science and Technology* **1**, 457 (2006)

[157] S. Tomita, J. U. Andersen, K. Hansen and P. Hvelplund, Stability of buckminsterfullerene, C_{60}, *Chem. Phys. Lett.* **382**, 120 (2003)

[158] Y.-H. Kim, I.-H. Lee, K. J. Change and S. Lee, Dynamics of fullerene coalescence, *Physical Review Letters* **90** (2003)

[159] V. Piacente, G. Gigli, P. Scardala, A. Giustini and D. Ferro, Vapor pressure of C_{60} buckminsterfullerene, *Journal of Physical Chemistry* **99**, 14052 (1995)

[160] G. H. Kroll, P. J. Benning, Y. Chen, T. R. Ohno and J. H. Weaver, Interaction of O_2 with C_{60}: photon-induced oxidation, *Chem. Phys. Lett.* **181**, 112 (1991)

[161] A. M. Vassallo, L. S. K. Pang, P. A. Cole-Clarke and M. A. Wilson, Emission FTIR study of C_{60} thermal stability and oxidation, *J. Am. Chem. Soc.* **113**, 7820 (1991)

[162] V. Vijayakrishnan, A. K. Santra, T. Pradeep, R. Seshadri, R. Nagarajan et al., Interaction of nitrogen and oxygen with C_{60}, *J. Chem. Soc. Chem. Commun.* **2**, 198 (1992)

[163] H. Werner, T. Schendel-Niedrig, M. Wohlers, D. Herein, B. Herzog et al., Reaction of molecular oxygen with C_{60}: Spectroscopic studies, *J. Chem. Soc. Faraday Trans.* **90** (1994)

[164] J. A. Nisha, V. Sridharan, J. Janaki, Y. Hariharan, V. S. Sastry et al., Studies of C_{60} oxidation and products, *J. Phys, Chem.* **100**, 4503 (1996)

[165] S. M. Rossnagel, I. Yang and J. J. Cuomo, Compositional changes during magnetron sputtering of alloys, *Thin Solid Films* **199**, 59 (1991)

[166] D. R. Lide, *CRC Handbook of Chemistry and Physics*, CRC Press, 87th edition (2006)

[167] M. Morita, T. Ohmi, H. Hasegawa, M. Kawakami and M. Ohwada, Growth of native oxide on a silicon surface, *Jour. App. Phys.* **68**, 1272 (1990)

[168] Y.-T. Chen, Y. C. Lin, S. U. Jen, J.-Y. Tseng and Y. D. Yao, Effect of Ta seed layer on crystalline structure and magnetic properties in an exchange-biased co/irmn system, *Jour. Alloys and Compounds* **509**, 5587 (2011)

[169] T. Moorsom, M. Wheeler, T. M. Kahn, F. A. Ma'Mari, C. Kinane et al., Spin-polarized electron transfer in ferromagnet/C_{60} interfaces, *Phys. Rev. B* **90** (2014)

[170] I. Olefjord and A. Nylund, Surface analysis of oidized aluminium, *Surface and Interface Analysis* **21**, 290 (1994)

[171] C. Hinnen, D. Imbert, J. M. Siffre and P. Marcus, An in situ XPS study of sputter-deposited aluminium thin films on graphite, *Appl. Surface Science* **78**, 219 (1994)

[172] D. W. Owens, C. M. Aldao, D. M. Poirier and J. H. Weaver, Charge transfer, doping, and interface morphologies for Al - C_{60}, *Phys. Rev. B* **51** (1995)

[173] J. M. D. Coey, *Magnetism and Magnetic Materials*, Cambridge University Press (2009)

[174] D. Kemmish, *Update on the Technology and Applications of Polyaryletherketones*, iSmithers Rapra Publishing (2010)

[175] V. Canella and J. A. Mydosh, Magnetic ordering in gold-iron alloys, *Phys Rev B* **6** (1972)

[176] C. A. M. Mulder, A. J. van Duyneveldt and J. A. Mydosh, Susceptibility of the CuMn spin-glass: Frequency and field dependences, *Phys. Rev. B* **23** (1981)

[177] J. H. P. Jr, D. W. Feldman and M. Ashkin, Raman scattering by silicon and germanium, *Phys. Rev.* **155** (1967)

[178] A. Campion and P. Kambhampati, Surface enhanced raman scattering, *Chem Soc Rev* **27**, 241 (1998)

[179] M. Valvidares, J. Herrero and P. Gargiani, Bl29-boreas (2014), www.cells.es/en/beamlines/bl29-boreas

[180] M. C. Hettrick and S. Bowyer, Variable line-spacing gratings: new designs for use in grazing incidence spectrometers, *Appl. Optics* **22** (1983)

[181] I. A. Kowalik, G. Öhrwall, B. N. Jensen, R. Sankari, E. Wallén et al., Description of the new i1011 beamline for magnetic measurements using synchrotron radiation at MAX-lab, *Journal of Physics: Conference Series* **211** (2010)

[182] C. Kinane, www.isis.stfc.ac.uk/instruments/polref, retrieved: April 2016.

[183] C. C. Wilson, A guided tour of ISIS the UK spallation neutron source, *Neutron News* **6** (1995)

[184] J. Penfold, R. C. Ward and W. G. Williams, A time-of-flight neutron reflectometer for surface and interfacial studies, *J. Phys. E: Sci Instrum* **20**, 1411 (1987)

[185] M. Björk and G. Andersson, GenX: an extensible X-ray reflectivity refinement program utilizing differential evolution, *J. App. Cryst.* **40**, 1174 (2007)

[186] N. A. Porter, *Magnetoresistance in n-type Silicon*, Ph.D. thesis, University of Leeds (2010)

[187] G. Chern, H. Mathias, L. R. Testardi, L. Seger and J. Schlenoff, Low-frequency dielectric permittivity of C_{60}, *Jour. Superconductivity* **8** (1995)

[188] V. de Coulon, J. L. Martins and F. Reuse, Electronic structure of neutral and charged C_{60} clusters, *Phys. Rev. B* **45** (1992)

[189] X. Lu, M. Grobis, K. H. Khoo, S. G. Louie and M. F. Crommie, Charge transfer and screening in individual C_{60} molecules on metal substrates: A scanning tunneling spectroscopy and theoretical study, *Phys. Rev. B* **70** (2004)

[190] H.-G. Boyen, P. Ziemann, U. Wiedwald, V. Ivanova, D. M. Kolb et al., Local density of states effects at the metal-molecule interfaces in a molecular device, *Nat. Mat.* **5**, 394 (2006)

[191] K. Röll and C. Hammer, Determination of the depth resolution in auger depth profiling measurements, *Thin Solid Films* **57** (1979)

[192] M. Magnuson, S. M. Butorin, J. H. Guo and J. Nordgren, Electronic structure investigation of CoO by means of soft x-ray scattering, *Phys. Rev. B* **65** (2002)

[193] T.-C. Tseng, C. Urban, Y. Wang, R. Otero, S. L. Tait et al., Charge-transfer-induced structural rearrangements at both sides of organic/metal interfaces, *Nat Chem* **2**, 374 (2010)

[194] K.-D. Tsuei, J.-Y. Yuh, C.-T. Tzeng, R.-Y. Chu, S.-C. Chung et al., Photoemission and photoabsorption study of C_{60} adsorption on Cu(111) surfaces, *Phys. Rev. B* **56** (1997)

[195] T. A. Murphy, T. Pawlik, A. Weidinger, M. Höhne, R. Alcala et al., Observation of atomlike nitrogen in nitrogen-implanted solid C_{60}, *Phys. Rev. Lett.* **77** (1996)

[196] C. Leighton, M. R. Fitzsimmons, A. Hoffmann, J. Dura, C. F. Majkrzak et al., Thickness-dependent coercive mechanisms in exchange-biased bilayers, *Physical Review B* **65** (2002)

[197] Y. P. Zhao, R. M. Garnache, G. C. Wang, T. M. Lu, G. Palasantzas et al., Effect of surface roughness on magnetic domain wall thickness, domain size, and coercivity, *J. Appl. Phys* **89** (2001)

[198] C. Leighton, J. Nogués, B. J. Jönsson-Åkerman and I. K. Schuller, Coercivity enhancement in exchange biased systems driven by interfacial frustration, *Phys. Rev. Lett* **84** (2000)

[199] T. Hauet, J. A. Borchers, P. Mangin, Y. Henry and S. Mangin, Training effect in an exchange bias system: the role of interfacial domain walls, *Phys. Rev. Lett.* **96** (2006)

[200] M. Ali, C. H. Marrows, M. Al-Jawad, B. J. Hickey, A. Misra et al., Antiferromagnetic layer thickness depedence of the IrMn/Co exchange-bias system, *Phys. Rev. B* **68** (2003)

[201] M. Ali, C. H. Marrows and B. J. Hickey, Onset of exchange bias in ultrathin antiferromagnetic layers, *Phys. Rev. B* **67** (2003)

[202] S. Chandra, H. Khurshid, M.-H. Phan and H. Srikanth, Asymmetric hysteresis loops and its dependence on magnetic anisotropy in exchange biased Co/CoO core-shell nanoparticles, *Appl. Phys. Lett* **101** (2012)

[203] G. H. Jaffari, S. R. Ali, S. K. Hasanain, G. Güntherodt and S. I. Shah, Stabilization of surface spin glass behaviour in core-shell $Fe_{67}C_{33}$ – $cofe_2o_4$ nanoparticles, *J. Appl. Phys.* **108** (2010)

[204] S. Chandra, H. Khurshid, W. Li, G. C. Hadjipanayis, M. H. Phan et al., Spin dynamics and criteria for onset of exchange bias in superspin glass $Fe/\gamma - Fe_2O_3$ core-shell nanoparticles, *Phys. Rev. B.* **86** (2012)

[205] L. Lundgren, P. Svedlindh, P. Nordblad and O. Beckman, Dynamics of the relaxation-time spectrum in a CuMn spin-glass, *Phys. Rev. Lett.* **51** (1983)

[206] A. Nigam, G. Schwabegger, M. Ullah, R. Ahmed, I. I. Fishchuk et al., Strain induced anisotropic effect on electron mobility in c_{60} based organic field effect transistors, *Appl. Phys. Lett* **101** (2012)

[207] D. R. Noakes, G. M. Kalvius, R. Wäppling, E. Schreier, A. Krimmel et al., Search for a spin glass state in $PrAu_2Si_2$ by μSR, *Solid State Comm.* **131**, 87 (2004)

[208] K. K. Aliev, I. K. Kamilov and A. M. Omarov, Static critical behaviour of gadolinium, *Sov. Phys. JETP* **94**, 153 (1988), (translation from the American Institute of Physics)

[209] C. Kaiser, A. F. Panchula and S. S. P. Parkin, Finite tunneling spin polarization at the compensation point of rare-earth-metal-transition-metal alloys, *Phys. Rev. Lett.* **95** (2005)

[210] H. E. Nigh, S. Legvold and F. H. Spedding, Magnetization and electrical resistivity of gadolinium single crystals, *Phys. Rev.* **132** (1963)

[211] G. Crecelius, G. K. Wertheim and D. N. E. Buchanan, Core-hole screening in lanthanide metals, *Phys. Rev. B* **18** (1978)

[212] A. T. Hindmarch and B. J. Hickey, Direct experimental evidence for the ruderman-kittel-kasuya-yosida interaction in rare-earth metals, *Phys. Rev. Lett.* **91** (2003)

[213] W. M. Hubbard, E. Adams and J. V. Gilfrich, Magnetic moments of alloys of gadolinium with some of the transition elements, *J Appl Phys* **31** (1960)

[214] A. D. Naylor, G. Burnell and B. J. Hickey, Transport spin polarization of the rare-earth transition-metal alloy $Co_{1-x}Gd_x$, *Phys. Rev. B* **85** (2012)

[215] J. W. C. de Vries, Temperature and thickness dependence of the resistivity of thin polycrystalline aluminium, cobalt, nickel, palladium, silver and gold films, *Thin Solid Films* **167**, 25 (1988)

[216] P. Hansen, C. Clausen, G. Much, M. Rosenkranz and K. Witter, Magnetic and magneto-optical properties of rare-earth transition-metal alloys containing gd, tb, fe, co., *J. Appl. Phys.* **66** (1989)

[217] G. Leinweber, D. P. Barry, M. J. Trbovich, J. A. Burke, N. J. Drindak et al., Neutron capture and total cross-section measurements and resonance parameters of gadolinium, *Nuclear Science and Engineering* **154**, 261 (2006)

[218] G. Scheunert, W. R. Hendren, C. Ward and R. M. Bowman, Magnetization of 2.6 t in gadolinium thin films, *Appl. Phys. Lett.* **101** (2012)

[219] R. M. Moon, W. C. Koehler, j W Cable and H. R. Child, Distribution of mganetic moment in metallic gadolinium, *Phys. Rev. B* **5** (1972)

[220] X. G. Liu, D. Y. Geng, Q. Zhang, J. J. Jiang, W. Liu et al., Microstructure and magnetic properties of graphite-coated Gd nanocapsules, *Appl. Phys. Lett.* **94** (2009)

[221] G. Will, R. Nathans and H. A. Alperin, Neutron diffraction investigation of a gadolinium single crystal, *J. Appl. Phys.* **35** (1964)

[222] K. P. Belov and A. V. Ped'ko, "helical" antiferromagnetism of gadolinium, *Soviet Physics JETP* **15** (1962)

[223] C. D. G. Jr, Some magnetic properties of gd single crystals, *J. Appl. Phys.* **34** (1963)

[224] R. J. elliott and F. A. Wedgwood, Theory of the resistance of the rare earth metals, *Proc. Phys. Soc.* **81**, 846 (1963)

[225] R. L. Singh and D. J. W. Geldart, Critical behaviour of the electrical resistance of holmium near the neél temperature, *Solid State Comm.* **20**, 501 (1976)

[226] H. Miwa, Electrical resisitivity associated with screw-type spin arrangements, *Prog. Theor. Phys.* **28** (1962)

[227] R. W. Green, S. Legvold and F. H. Spedding, Magnetization and electrical resistivity of erbium single crystals, *Phys. Rev.* **122** (1961)

[228] S. Abdelouahed, N. Baadji and M. Alouani, Electronic structure and x-ray magnetic circular dichroism of gadolinium beyond the local spin density approximation, *Phys. Rev. B* **75** (2007)

[229] G. van der Laan and B. T. Thole, X-ray-absorption sum rules in jj-coupled operators and ground-state moments of actinide ions, *Phys. Rev. B* **53** (1996)

[230] A. Patnaik, K. K. Okudaira, S. Kera, H. Setoyama, K. Mase et al., Polarized near-edge x-ray-absorption fine structure spectroscopy of C_{60}-functionalized 11-amino-1-1undecane thiol self-assembled monolayer: Molecular orientation and evidence for C_{60} aggregation, *J. Chem Phys.* **122** (2005)

[231] L. J. Terminello, D. K. Shuh, F. J. Himpsel, D. A. Lapiano-Smith, J. Stöhr et al., Unfilled oritals of C_{60} and C_{70} from carbon K-shell X-ray absorption fine structure, *Chem. Phys. Lett.* **182** (1991)

[232] P.-Y. Cheng, M.-R. Chiang, Y.-L. Chan, Y.-J. Hsu, P.-C. W et al., Deep Co penetration and spin-polarization of C_{60} molecules at hybridized Co-C_{60} interfaces, *Appl. Phys. Lett.* **104** (2014)

[233] A. Gutiérrez, J. Díaz and M. F. López, X-ray absorption spectroscopy study of pulsed-laser-evaporated amorphous carbon films, *Appl. Phys. A* **61**, 111 (1995)

[234] C. T. Chen, L. H. Tjeng, P. Reudolf, G. Meigs, J. E. Rower et al., Electronic states and phases of K_xC_{60} from photoemission and x-ray absorption spectroscopy, *Nature* **352**, 603 (1991)

[235] H. R. Child and J. W. Cable, Magnetic structure properties of Gd-Y and Gd-Sc alloys, *J. Appl. Phys.* **40** (1969)

[236] M. K. Wilkinson, W. c Koehler, E. O. Wollan and J. W. Cable, Neutron diffraction investigation of magnetic ordering in dysprosium, *J Appl. Phys* **32** (1961)

[237] M. Habenschuss, C. Stassis, S. K. Sinha, H. W. Deckman and F. H. Spedding, Neutron diffraction study of the magnetic structure of erbium, *Phys. Rev. B* **10** (1974)

[238] V. Schettino, M. Pagliai, L. Ciabini and G. Cardini, The vibrational spectrum of fullerene C_{60}, *J. Phys. Chem. A.* **105**, 11192 (2001)

[239] K. L. Akers, C. Douketis, T. L. Haslett and M. Moskovits, Raman spectroscopy of C_{60} solid films: A tale of two spectra, *J. Phys. Chem.* **98**, 10824 (1994)

[240] P. Zhou, A. M. Rao, K.-A. Wang, J. D. Robertson, C. Eloi et al., Photo-assisted structural transition and oxygen diffusion in solid C_{60} films, *Appl. Phys. Lett.* **60** (1992)

[241] S. C. Jeoung, D. Kim, S. Kim and S. K. Kim, Triplet state raman spectra of C_{60} and C_{70}, *Chem. Phys. Lett.* **241**, 528 (1995)

[242] Z. Luo, Z. Cheng, Y. Luo, B. H. Loo, A. Peng et al., Photoassisted magnetization of fullerene C_{60} with magnetic-field trapped raman scattering, *J. Am. Chem. Soc.* **134**, 1130 (2012)

[243] V. Coropceanu, J. Cornil, D. A. da Silva Filho, Y. Olivier, R. Silbey et al., Charge transport in organic semiconductors, *Chem. Rev.* **107**, 926 (2007)

[244] T. Moorsom, M. Wheeler, M. T. Khan, F. A. Ma'Mari, G. Brunell et al., Effects of spin doping and spin injection in the luminescence and vibrational spectrum of C_{60}, *Appl. Phys. Lett.* **105** (2014)

[245] C. Boehme and J. M. Lupton, Challenges for organic spintronics, *Nat Nanotech* **8**, 612 (2013)

[246] Z. Zhang, S. Mizukami, T. Kubota, Q. Ma, M. Oogane et al., Observation of a large spin-dependent transport in organic spin valves at room temperature, *Nat Comm* **4** (2013)

[247] A. Riminucci, M. Prezioso, C. Pernechele, P. Graziosi, I. Bergenti et al., Hanle effect missing in a prototypical organic spintronic device, *Appl. Phys. Lett.* **102** (2013)

[248] F. Schiller, M. Ruiz-Osés, J. E. Ortega, P. Segovia, J. Martínez-Blanco et al., Electronic structure of C_{60} on Au(887), *J. Chem. Phys.* **125** (2006)

[249] E. Sohmen, J. Fink and W. Krätschmer, Electronic structure studies of undoped and n-type doped fullerene C_{60}, *Europhys. Lett.* **17** (1992)

[250] K. H. Drexhage, Influence of a dielectric interface on a flourescence decay time, *Jour. Luminescence* **1,2**, 693 (1970)

[251] R. R. Chance, A. PRock and R. Silbey, Molecular flourescence and energy transfer near interfaces, *Adv. Chem. Phys.* **37** (1978)

[252] B. N. J. Persson and N. D. Lang, Electron-hole-pair quenching of excited states near a metal, *Phys. Rev. B* **26** (1982)

[253] F. Negri, G. Orlandi and F. Zerbetto, Interpretation of the vibrational structure of the emission and absorption spectra of C60, *J. Chem Phys* **97** (1992)

[254] B. Koopmans, A.-M. Janner, H. T. Jonkman, G. A. Sawatzky and F. van der Woude, Strong bulk magnetic dipole induced second-harmonic generation from C_{60}, *Phys. Rev. Lett.* **71** (1993)

[255] S. Kazaoui, R. Ross and N. Minami, Intermolecular charge-transfer excitation in C_{60} films: Evidence from luminescence and spectroscopy, *Phys. Rev. B* **52** (1995)

[256] W. L. Barnes, Fluorescence near interfaces: the role of photonic mode density., *J. Modern Optics* **45** (1998)

[257] W. Lukosz and R. E. Kunz, Fluorescence lifetime of magnetic and electric dipoles near a dielectric interface, *Optics Communications* **20** (1977)

[258] N. Noginova, G. Zhu, M. Mavy and M. A. Noginov, Magnetic dipole based systems for probing optical magnetism, *J. Appl. Phys.* **103** (2008)

[259] G. W. Ford and W. H. Weber, Electromagneic interactions of molecules with metal surfaces, *Phys. Rep.* **113** (1984)

[260] H. Becker, S. E. Burns and R. H. Friend, Effect of metal films on the photoluminescence and electroluminescence of conjugated polymers, *Phys. Rev. B* **56** (1997)

[261] W. Guss, J. Feldmann, E. O. Göbel, C. Taliani, H. Mohn et al., Flourescence from X traps in C_{60} single crystals, *Phys. Rev. Lett.* **72** (1994)

[262] D. Dick, X. Wei, S. Jeglinski, R. E. Benner, Z. V. Vardeny et al., Transient spectroscopy of excitons and polarons in C_{60} films from femtoseconds to milliseconds., *Phys. Rev. Lett.* **73** (1994)

[263] P. A. Lane, L. S. Swanson, Q.-X. Ni and J. Shinar, Dynamics of photoexcited staes in C_{60}: an optically detected magnetic resonance, ESR, and light-induced ESR study, *Phys. Rev. Lett.* **68** (1992)

[264] A. M. Rao, P. Zhou, K.-A. Wang, G. T. Hager, J. M. Holden et al., Photoinduced polymerization of solid C_{60} films, *Science* **259**, 955 (1993)

[265] T. Wågberg, P. Jacobsson and B. Sundqvist, Comparative raman study of photopolymerized and pressure-polymerized C_{60} films, *Phys Rev B* **60** (1999)

[266] A. C. Ferrari and J. Robertson, Interpretation of raman spectra of disordered and amorphous carbon, *Phys. Rev. B* **61** (2000)

[267] M. Kadleíková, J. Breza and M. veselý, Raman spectra of synthetic sapphire, *Microelectronics Journal* **32**, 955 (2001)

[268] M. Wheeler, *Manipulation of fullerene* C_{60} *spintronic devices via ferromagnetic resonance*, Ph.D. thesis, University of Leeds (2014)

[269] P. H. M. van Loosdrecht, P. J. M. van Bentum and G. Meijer, Raman scettering in electronically excited C_{60}, *Chem. Phys. Lett.* **205** (1993)

[270] S. Lepadatu, M. C. Hickey, A. Potenza, H. Marchetto, T. R. Charlton et al., Experimental determination of spin-transfer torque nonadiabaticity parameter and spin polarization in permalloy, *Phys. Rev. B* **79** (2009)

[271] S. K. Upadhyay, A. Palanismai, R. N. Louie and R. A. Buhrman, Probing ferromagnets with andreev relfection, *Phys. Rev. Lett.* **81** (1998)

[272] M. R. Fitzsimmons, T. J. Silva and T. M. Crawford, Surface oxidation of permalloy thin films, *Phys. Rev. B* **73** (2006)

[273] C. T. Elliott, Negative luminescence and its applications, *Phil. Trans. R. Soc. Lond. A* **359**, 567 (2001)

[274] E. L. Ivchenko, Spectroscopy of spin-polarized excitons in semiconductors, *Pure and Appl. Chem.* **67** (1995)

[275] R. Fiederling, M. Keim, G. reuscher, W. Ossau, G. Schmidt et al., Injection and detection of a spin-polarized current in a light emittign diode, *Nature* **402**, 787 (1999)

[276] F. S. Richardson and J. P. Riehl, Circularly polarized luminescence spectroscopy, *Chem Rev* **77** (1977)

[277] V. K. Thorsmølle, R. D. Averitt, J. Demsar, D. L. Smith, S. Tretiak et al., Morphology effectively controls singlet-triplet exciton relaxation and charge transport in organic semiconductors, *Phys. Rev. Lett.* **102** (2009)

[278] D. M. Pai, J. F. Yanus and M. Stolka, Trap-controlled hopping transport, *J. Chem. Phys* **88**, 4714 (1984)

[279] Y. Zhang, T. P. Basel, B. R. Gautam, X. Yang, D. J. Mascaro et al., Spin-enhancement organic bulk heterojunction photovoltaic solar cells, *Nat Comm* **3** (2012)

[280] R. A. Cheville and N. J. Halas, Time-resolved carrier relaxation in solid C_{60} thin films, *Phys. Rev. B* **45** (1992)

[281] B. Wästberg, S. Lunell, C. Enkvist, P. A. Brühwiler, A. J. Maxwell et al., 1s x-ray-absorption spectrocopy of C_{60}: the effects of screening and core hole relaxation, *Phys. Rev. B* **50** (1994)

[282] R. Macovez, P. rudolf, I. Marenne, L. Kjeldgaard, P. A. Brühwiler et al., Electronic surface reconstruction and correlation in the fcc dimer phases of RbC_{60}, *Phys. Rev. B* **75** (2007)

[283] A. J. Maxwell, P. A. Brühwiler, D. Arvanitis and J. Hasselström, Electronic and geometric structure of C_{60} on Al(111) and Al(110), *Phys. Rev. B* **57** (1998)

[284] L. G. Kaake, P. F. Barbara and X. Y. Zhu, Intrinsic charge trapping in organic and polymeric semiconductors: a physical chemistry perspective, *J Phys Chem Lett* **1**, 628 (2010)

[285] J. C. Scott and L. D. Bozano, Nonvoltaile memory elements based on organic materials, *Adv. Mat.* **19**, 1452 (2007)

[286] S. Paul, A. Kanwal and M. Chhowalla, Memory effect in thin films of insulating polymer and C_{60} nanocomposites, *Nanotechnology* **17**, 145 (2006)

[287] A. Nakajima and M. Uchino, Charge redistribution in a charge storage layer containing C_{60} molecules and organic polymers for long electron retenetion, *Appl. Phys. Lett.* **101** (2012)

[288] H.-C. Chang, C. Lu, C.-L. Liu and W.-C. Chen, Single-crystal C_{60} needle/CuPc nanoparticle double floating-gate for low-voltage organic transistors based non-volatile memory devices, *Adv. Mat.* **27**, 27 (2014)

[289] K. Horiuchi, S. Uchino, S. Hashii, A. Hashimoto, T. Kato et al., Variable range hopping in a C_{60} field-effect transistor, *Appl. Phys. Lett.* **85** (2004)

[290] Y. Zhou, S.-T. Han, P. Sonar and V. A. L. Roy, Nonvolatile miltilevel data storage memory deivce from controlled ambipolar trapping mechanism, *Scientific reports* **3** (2013)

[291] J. H. Kang, D. da Silva Filho, J.-L. Bredas and X.-Y. Zhu, Shallow trap states in pentacene thin films from molecular sliding, *Appl. Phys. Lett.* **86** (2005)

[292] M. Matus, H. Kuzmany and E. Sohmen, Self-trapped polaron exciton in neutral fullerene c_{60}, *Phys. Rev. Lett.* **68** (1992)

[293] M. Toupin, T. Brousse and D. Bélanger, Charge storage mechanism of MnO_2 electrode used in aqueous electrochemical capacitor, *Chem Mater* **16**, 3184 (2004)

[294] S. Mühlbauer, B. Binz, F. Jonietz, C. Pfleiderer, A. Rosch et al., Skyrmion lattice in a chiral magnet, *Science* **323** (2009)